HIGH-POWER, HIGH-REPETITION-RATE PICOSECOND OPTICAL PARAMETRIC OSCILLATORS FOR THE VISIBLE TO MID-INFRARED

Steven French

A Thesis Submitted for the Degree of PhD
at the
University of St Andrews

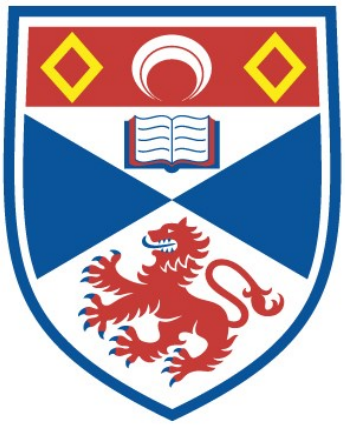

1997

Full metadata for this item is available in
St Andrews Research Repository
at:
http://research-repository.st-andrews.ac.uk/

Please use this identifier to cite or link to this item:
http://hdl.handle.net/10023/14890

This item is protected by original copyright

High-Power, High-Repetition-Rate Picosecond Optical Parametric Oscillators for the Visible to Mid-Infrared

Steven French, B.Sc, M.Sc.

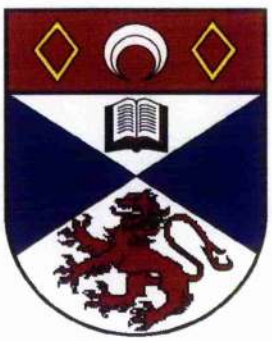

J. F. Allen Physics Research Laboratories
School of Physics and Astronomy
University of St Andrews
Fife, Scotland

A thesis submitted to the University of St Andrews
in application for the degree of Doctor of Philosophy

September 1996

ProQuest Number: 10166535

All rights reserved

INFORMATION TO ALL USERS
The quality of this reproduction is dependent upon the quality of the copy submitted.

In the unlikely event that the author did not send a complete manuscript
and there are missing pages, these will be noted. Also, if material had to be removed,
a note will indicate the deletion.

ProQuest 10166535

Published by ProQuest LLC (2017). Copyright of the Dissertation is held by the Author.

All rights reserved.
This work is protected against unauthorized copying under Title 17, United States Code
Microform Edition © ProQuest LLC.

ProQuest LLC.
789 East Eisenhower Parkway
P.O. Box 1346
Ann Arbor, MI 48106 – 1346

TL C134

To Mum, Dad and Lorraine

We are, we are romanced in fascination,
Sinfully sated in every incantation, typically
Farcical in every situation, but look what,
you can do with a little ***Imagination.***

The Wonder Stuff - 1993.

Picosecond Ti:sapphire pumped optical parametric oscillator

This photograph demonstrates the sum frequency mixing process that takes place in the 30 mm long Lithium triborate (LBO) optical parametric oscillator. The sum frequency mixing occurs between the resonant signal wave and the single pass pump. This photograph was taken at a wavelength of 528 nm, and represents an output power of 25 mW.

Declaration

I, Steven French, hereby certify that this thesis, which is approximately 60,000 words in length, has been written by me, that it is the record of work carried out by me and that it has not been submitted in any previous application for a higher degree.

Date 12/11/96 Signature of candidate.....

I was admitted as a research student in October 1993 and as a candidate for the degree of Ph.D in October 1994; the higher study for which this is a record was carried out in the University of St. Andrews between 1993 and 1996.

Date 12/11/96 Signature of candidate.....

I hereby certify that the candidate has fulfilled the conditions of the Resolution and Regulations appropriate for the degree of Doctor of Philosophy in the University of St. Andrews and that the candidate is qualified to submit this thesis in application for that degree.

Date 12/11/96 Signature of supervisor.....

In submitting this thesis to the University of St. Andrews I understand that I am giving permission for it to be made available for use in accordance with the regulations of the University Library for the time being in force, subject to any copyright vested in the work not being affected thereby. I also understand that the title and abstract will be published, and that a copy of the work may be made and supplied to any bona fide library or research worker.

Date 12/11/96 Signature of candidate.....

Publications

Journal Publications

Ti:sapphire-pumped picosecond optical parametric oscillator based on LiB_3O_5,

M. Ebrahimzadeh, S. French, W. Sibbett, and A. Miller,

Opt. Lett. **20**, (2), 166 (1995).

Non-critically phase-matched, Ti:sapphire-pumped picosecond optical parametric oscillator using LiB_3O_5,

M. Ebrahimzadeh, S. French, W. Sibbett, and A. Miller,

Appl. Phys B. **60**, 443 (1995).

Design and performance of a singly-resonant picosecond LiB_3O_5 optical parametric oscillator synchronously-pumped by a self-mode-locked Ti:sapphire laser,

M. Ebrahimzadeh, S. French, and A. Miller,

J. Opt. Soc. Am. B **12**, 2180 (1995).

High-power, high - repetition - rate picosecond optical parametric oscillator for the near - to mid - infrared,

S. French, M. Ebrahimzadeh, and A. Miller,

Opt. Lett. **21**, (2), 131 (1996).

High-power, high-repetition-rate picosecond optical parametric oscillators for the near-to mid-infrared,

S. French, M. Ebrahimzadeh, and A. Miller,

J. Mod. Opt. **43**, (5), 929 (1996).

High-power, high-repetition-rate picosecond optical parametric oscillator tunable in the visible,

S. French, M. Ebrahimzadeh, and A. Miller,

Opt. Lett. **21**, (13), 976 (1996).

Visible picosecond pulse generation in a frequency-doubled optical parametric oscillator based on LiB_3O_5,

S. French, M. Ebrahimzadeh, and A. Miller

Opt. Commun. **128**, 166 (1996).

Conference Publications

Picosecond LiB_3O_5 Optical parametric oscillator synchronously-pumped by a 81-MHz Ti:sapphire laser,

M. Ebrahimzadeh, S. French, W. Sibbett, and A. Miller,

Paper WG4, Advanced Solid State Lasers Conference (ASSL), Memphis Tn, January 1995.

S. French, M. Ebrahimzadeh, W. Sibbett, and A. Miller,

Picosecond LiB_3O_5 optical parametric oscillator synchronously-pumped by a 81-MHz Ti:sapphire laser,

Proceedings on Advanced Solid-State Lasers, Bruce H. T. Chai and Stephen A. Payne, eds, (Optical Society of America, Washington, DC. 1995), Vol 24, pp. 167-171.

High-power, widely tunable, Ti:sapphire-pumped picosecond LiB_3O_5 OPO,

M. Ebrahimzadeh, S. French, W. Sibbett, and A. Miller,

Paper CTuE5, Conference on Lasers and Electro-Optics (CLEO), Baltimore, May 1995.

Picosecond Optical Parametric Oscillation in $KTiOAsO_4$,

S. French, M. Ebrahimzadeh, and A. Miller,

Post Deadline Paper CPD47, Conference on Lasers and Electro-Optics (CLEO), Baltimore, May 1995.

High-power, high-repetition-rate picosecond optical parametric oscillators for the near-to mid-infrared,

S. French, M. Ebrahimzadeh, and A. Miller,

Paper 1-5, Twelfth National Quantum Electronics Conference (QE-12), Southampton, September 1995.

Visible picosecond pulse generation in a frequency-doubled optical *parametric oscillator based on LiB_3O_5,*

S. French, M. Ebrahimzadeh, and A. Miller,

Paper WF16, Advanced Solid State Lasers Conference (ASSL), San Francisco Ca, January 1996.

S. French, M. Ebrahimzadeh, and A. Miller,

Visible picosecond pulse generation in a frequency-doubled optical parametric oscillator based on LiB_3O_5,

OSA trends in Optics and Photonics on Advanced Solid-State Lasers, Stephen A. Payne and Clifford Pollock, eds, (Optical Society of America, Washington, DC. 1996), Vol 1, pp. 141-146.

Multiple wavelength generation in a picosecond optical parametric oscillator based on non-critically-phase-matched LiB_3O_5,

S. French, M. Ebrahimzadeh, and A. Miller,

Paper CWF15, Conference on Lasers and Electro-Optics (CLEO), Anaheim, May 1996.

Intracavity-frequency-doubled picosecond optical parametric oscillator based on non-critically-phase-matched LiB_3O_5,

S. French, M. Ebrahimzadeh, and A. Miller,

Paper CThA6, Conference on Lasers and Electro-Optics (CLEO), Anaheim, May 1996.

Multiple wavelength generation in a picosecond optical parametric oscillator based on non-critically-phase-matched LiB_3O_5,

S. French, M. Ebrahimzadeh, and A. Miller,

Paper NME14, International Nonlinear Optics Conference, Maui, Hawaii, July 1996.

Efficient picosecond pulse generation in the visible in a frequency-doubled optical parametric oscillator based on LiB_3O_5,

S. French, M. Ebrahimzadeh, and A. Miller,

Paper WA4, International Quantum Electronics Conference (IQEC), Sydney, Australia, July 1996.

Magazines

Laser Focus World, February 1995, page 13.

Opto & Laser Europe, March 1996, page 7.

Abstract

High-Power, High-Repetition-Rate Picosecond Optical Parametric Oscillators for the Visible to Mid-Infrared

S. French

J. F. Allen Physics Research Laboratories, School of Physics and Astronomy, University of St Andrews, Fife, Scotland.

This thesis describes the design, configuration and operation of picosecond optical parametric oscillators (OPOs) tunable from the visible to mid infrared. These systems were based on the materials LiB_3O_5 (LBO) and $KTiOAsO_4$ (KTA), and were pumped by a self-mode-locked Ti:sapphire laser at a repetition rate of 81 MHz.

The initial design of the picosecond parametric oscillator was based on a 16 mm long crystal of LBO. This system produces transform-limited signal pulses with durations of ~720 fs. Total average output powers of up to 90 mW over a signal (idler) tuning range of 1.374-1.530 μm (1.676-1.828 μm) have been generated at 1.3 times the 900 mW threshold.

The system performance was improved by the use of a new LBO crystal of length 30 mm. This system was continuously tunable from 1.160 to 2.185 μm. Up to 690 mW of output power has been generated for 2 W of input pump power at 5 times threshold. For this output power a depletion of 52 % was achieved with a corresponding external extraction efficiency of 34.5 %.

Picosecond pulse generation in the visible by external single-pass frequency-doubling of the LBO OPO to provide picosecond pulses in the 584-771 nm range has been demonstrated. Conversion efficiencies as high as 18 % have been demonstrated, with output powers in excess of 65 mW being measured, when utilising a combination of type I and type II temperature-tuned non-critical phase-matching in LBO. The pulse width of the second harmonic was in the region of 840-880 fs.

A further new source of tunable high-repetition-rate picosecond pulses for the visible has also been demonstrated, which is based on an internally-doubled, Ti:sapphire-pumped OPO that uses temperature-tuned LBO both as the OPO and

SHG crystal. Oscillation has been obtained for an input pump power of 700 mW with output powers in excess of 320 mW being generated, representing conversion efficiencies of as much as 16 %. The system is continuously tunable from 584 to 771 nm and can provide transform-limited visible pulses with durations of 840-880 fs across the available range.

The ability to tune beyond wavelengths of 2.5 μm was also required. To this end a new source of tunable picosecond pulses for the near - to mid - infrared has been developed which is based on the material KTA. Oscillation has been obtained for input pump powers as low as 230 mW. The system produces total output powers in excess of 403 mW with conversion efficiencies of 31 % at 5.2 times threshold. Transform-limited signal (idler) pulses of 1.02 (2.9) ps have been generated over the tuning range 1.139-1.281 (2.377-3.160) μm.

Contents

Chapter 1 *Introduction*

Contents Page

1.1 Introduction

Tunable ultrashort laser pulses in different regions of the optical spectrum are highly desirable for many applications. The study of numerous ultrafast phenomena such as carrier relaxation dynamics in semiconductors, [1] time-domain rotational and vibrational spectroscopy of molecules, and time-resolved measurements of many photoexcitation processes require ultrashort optical pulses with picosecond and femtosecond temporal durations [2, 3, 4, 5].

Before the recent surge in the development of ultrafast optical parametric oscillators (OPOs), optical sources capable of generating such pulses were traditionally based on conventional mode-locked laser gain media with extended fluorescence bandwidths such as the dye [6-15] or colour-centre lasers [16-19]. More recently, the application of novel passive nonlinear mode-locking techniques has enabled the generation of ultrashort pulses from vibronic laser gain media, most notably the Ti:sapphire laser [20-26]. While these techniques have proved highly effective in providing optical pulses with durations from a few femtoseconds to hundreds of picoseconds, the tuning range available to many of these systems is often limited to, at best, a few hundred nanometers or so. Moreover, with the exception of colour-centre lasers and some newly-emerging vibronic systems, the wavelength coverage of most of the existing tunable lasers is confined mainly to the visible spectrum.

Tunable ultrashort optical pulses in these wavelength regions have also been generated using a number of methods including nonlinear frequency conversion techniques based on difference frequency mixing [27-29], seeded parametric amplification [30-32] , or continuum generation [33, 34]. However, the need for two or more independent pump pulse trains, with the consequent demands on temporal synchronism, or the requirement for more than one amplification stage,

generally leads to added system complexity, higher cost, and relatively low overall conversion efficiencies. This may not be optimal for many experiments. In the following section a discussion is given of the methods used for generating ultrafast pulses in the visible and infrared before the recent developments in ultrafast OPOs. Figure 1.1 shows the tuning ranges available from the sources described above. In the following section a review of the development in synchronously-pumped picosecond optical parametric oscillators is given.

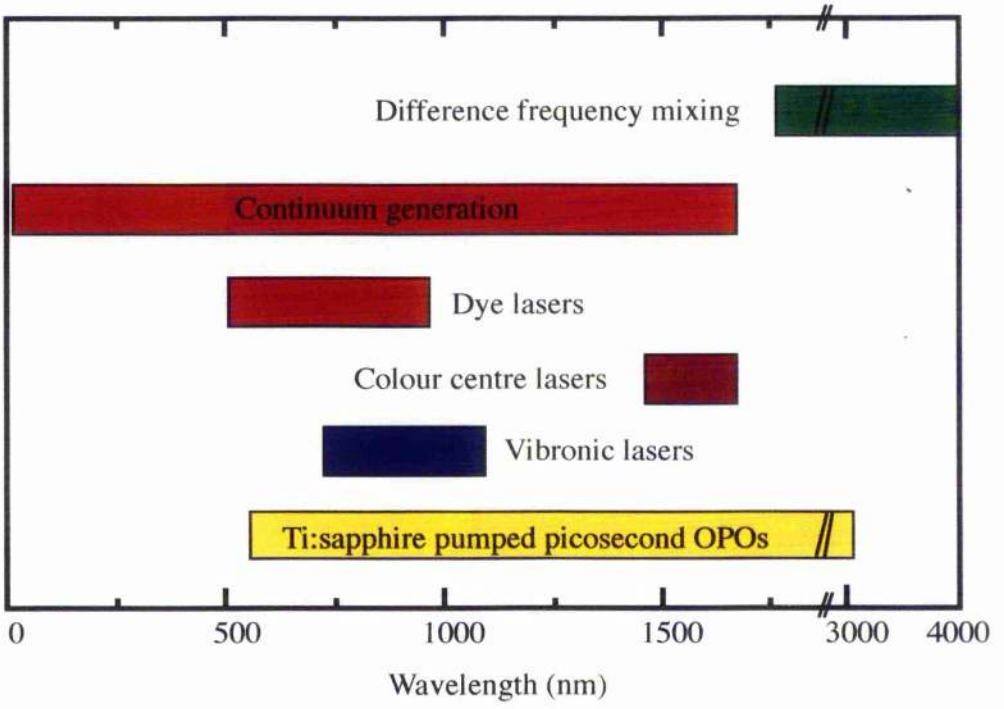

Figure 1.1
Comparison of the tuning ranges available in the visible and infrared from conventional ultrafast laser sources and optical parametric osillators.

1.2 Synchronously-pumped Optical Parametric Oscillators

The synchronously-pumped optical parametric oscillator (OPO) offers a highly attractive alternative for the generation of ultrashort pulses in new wavelength regions. In addition to its unrivalled spectral versatility and high efficiency, it is solid-state in design, long-lived, and relatively simple to implement, thus avoiding several of the disadvantages associated with other approaches. In addition, unlike the conventional mode-locked lasers where pulse formation and duration is ultimately limited by the fluorescence bandwidth of the gain medium, a large degree of selectivity in pulse duration is available with the OPO by suitable choice of pump pulse length and nonlinear crystal. As such, the OPO is

capable of providing optical pulses throughout the temporal spectrum from the nanosecond to the femtosecond regime. The output pulses from the OPO also exhibit lower timing jitter relative to the pump pulses than synchronously-pumped lasers with gain storage, because of the instantaneous nature of parametric gain. This property makes the synchronously-pumped OPO highly suited for high-resolution pump-probe spectroscopy.

The potential of synchronously-pumped OPOs for the generation of ultrashort optical pulses in new wavelength regions was demonstrated more than two decades ago. In 1972 Burneika and co-workers proposed a synchronously-pumped OPO configured so that the cavity lengths of the OPO and mode-locked pump laser were equal [35]. In the same work, the researchers demonstrated an optical parametric amplifier (OPA) using KDP which was synchronously-pumped by the second harmonic of a mode-locked Nd:YAG laser. However, for many years a lack of suitable pump sources of sufficient intensity ($\approx$ 100 kW) and nonlinear materials of desirable optical and mechanical characteristics limited the operation of synchronously-pumped OPOs either to doubly-resonant oscillator (DRO) configurations [36-40] or to the pulsed mode-locked singly-resonant regime, [41-45]. Whereas DROs have the benefit of reduced oscillation thresholds, the requirement for the simultaneous resonance of both parametric waves in one cavity generally leads to poor amplitude and frequency stability of the output. For this reason, singly-resonant oscillators (SROs) are desired, albeit at the expense of higher thresholds. Furthermore, ultrafast measurements with high signal-to-noise ratio generally require truly continuous sources at high repetition rates with the output consisting of identical pulses. These requirements are generally not met in pulsed synchronously-pumped OPOs where both the intensity and duration of the mode-locked pulses can vary across the pulse envelope and the output does not constitute a truly repetitive pulse train. Consequently, up until recently interest in OPOs as practical tunable ultrafast sources remained largely limited. However, the emergence of new materials with large nonlinearities and high damage thresholds and novel pump sources of high intensity and good beam quality has now enabled the generation of highly stable and truly continuous ultrashort pulse trains at high repetition rates, using OPOs.

In 1989, Edelstein et al demonstrated the first cw femtosecond SRO based on KTP [46]. To access the high peak intensities necessary for oscillation, the KTP crystal was pumped at the intracavity focus of a colliding-pulse mode-locked dye laser. This approach was subsequently extended to an externally-pumped

oscillator by Mak et al [47], where increased signal powers of up to 30 mW were demonstrated. Soon after, the emergence of the self-mode-locked Ti:sapphire laser as the pump source brought about marked improvements in the performance of femtosecond OPOs with regard to output power, pulse duration, stability, and reduced system complexity [48-54].

During the same period, much effort has been expended in the development of similar OPOs for the picosecond time domain. These efforts have been driven by the recognition that optical pulses with picosecond temporal durations are also of interest for many experiments because they offer a suitable compromise between spectral and temporal resolution not available with femtosecond pulses. Moreover, many ultrafast phenomena such as photochemical isomerization, electronic relaxation, and molecular rotation occur on the picosecond time-scale. To date, several cw synchronously-pumped picosecond SROs based on KTP and LBO have been successfully demonstrated by a number of investigators [55-61]. The pump sources used in these experiments have been almost entirely based on the cw mode-locked Nd:YAG or Nd:YLF lasers and their second harmonic. The attainment of short pump pulses of sufficient intensity has in most cases also necessitated the use of coupled-cavity techniques [55-57] or external pulse compression [58, 59]. Frequency-doubling of these systems to provide continuous train of picosecond pulses in the green also requires external enhancement configurations [55-58]. These requirements place additional demands on pump laser stability and lead to additional system complexity and higher cost.

The work in this thesis involves the development of cw picosecond synchronously-pumped OPOs based on a self-mode-locked Ti:sapphire laser as the pump source. One of the major advantages of the Ti:sapphire laser as the pump source is that its tunability permits wavelength tuning in picosecond OPOs without resorting to angle-tuned phase-matching. This is particularly useful when temperature phase-matching is not available as a means of wavelength tuning. On the other hand, the combination of a tunable pump and temperature-tuning allows access to a particular set of pump, signal and idler wavelengths, thus providing a multi-parameter tuning capability. This may be useful in applications such as pump-probe spectroscopy or wavelength multiplexing. The self-mode-locked Ti:sapphire laser is also capable of generating average powers in excess of 2 W, which enables efficient and high-power operation of OPOs. Commercial self-mode-locked Ti:sapphire lasers (e.g. Spectra-Physics, Tsunami) can now provide output pulses with durations from 100 fs to 5 ps through the

choice of intracavity optics and can be configured for femtosecond or picosecond operation in a few hours. As such, they also represent highly cost-effective pump sources for OPOs operating in the picosecond and femtosecond time domain. The first demonstration of the use of this laser in the femtosecond domain was by Kafka et al in 1994 [64], with a subsequent fuller description given in 1995 [63].

The potential of Ti:sapphire lasers as pumps for picosecond OPOs has been previously demonstrated [64]. By using a KTP crystal cut for type II non-critical phase-matching (NCPM) along the x-axis (θ=90°, ϕ=0°), tunable 1.2 ps pulses were generated over a wavelength range 1.05-1.21 μm and 2.28-2.87 μm by tuning the Ti:sapphire pump laser. The extent of the tuning to date in Ti:sapphire-pumped picosecond OPOs is shown in Figure 1.1 [65-71]. This can be seen to more than match the tuning available from conventional sources.

1.3 Outline of the work in the thesis

The work described in this thesis involves the development of picosecond sources tunable from the visible to mid infrared.

In Chapter 2 the operation of the self-mode-locked Ti:sapphire laser used as the pump source for the optical parametric oscillators described in this thesis is discussed. Chapter 3 describes the most important features relating to the construction of picosecond optical parametric oscillators including what features govern the choice of nonlinear crystal used as the parametric gain medium.

Chapters 4 to 7 describe the development of five separate systems to provide picosecond pulses from the visible to the mid infrared. Chapter 4 describes the initial Ti:sapphire-pumped OPO constructed, which was based on the nonlinear crystal LBO. A full temporal and spectral characterisation of the system is given. This OPO produced adequate performance characteristics, but improvements could be made. In Chapter 5 an improved LBO OPO is described, this device displayed significant improvements to the previous device, which allowed the investigation of many more interesting features. In Chapter 6 the output from the LBO system is extended into the visible by both extracavity and intracavity frequency-doubling the LBO OPO. In Chapter 7 tuning further into the infrared is accessed by the construction of a KTA OPO.

Chapter 8 provides conclusions to the thesis and outlines the achievements in system design, construction and characterisation.

References

1. See for example, A. Tomita, J. Shah, J. E. Cunningham, S. M. Goodnick, P. Lugli, and S. L. Chuang, Physical Review B **48**, 5708 (1993)

2. See, for example, G. R. Fleming, P. G. Wolynes, Phys. Today **43** (5), 36 (1990); D. H. Auston, Phys. Today **43** (2), 46 (1990)

3. See for example, M. Nisoli, A. Cybo-Ottone, S. De Silvestri, V. Magni, R. Tubino, S. Luzzati, A. Musco, and D. Commoretto, Solid State Communications, **86**, 583 (1993)

4. J. Shah, B. Deveaud, T. C. Damen, W. T. Tsang, A. C. Gossard, and P. Lugli, Phys. Rev. Lett. **59**, 222 (1987)

5. W. -Z. Lin, R. W. Schoenlein, J. G. Fujimoto, and E. P. Ippen, IEEE J. Quantum Electron. **24**, 267 (1988)

6. R. L. Fork, B. I. Greene, and C. V. Shank, Appl. Phys. Lett. **38**, 671 (1981)

7. E. P. Ippen, C. V. Shank, and A. Dienes, Appl. Phys. Lett. **21**, 348 (1972)

8. H. Vanherzeele, R. Torti, and J.-C. Diels, Appl. Opt. **23**, 4182 (1984)

9. M. C. Nuss, R. Leonhardt, and W. Zinth, Opt. Lett. **10**, 559 (1985)

10. M. D. Dawson, T. F. Boggess, D. W. Garvey, and A. L. Smirl, Opt. Commun. **60**, 79 (1986)

11. J. Dobler, H. H. Shultz, and W. Zinth, Opt. Commun. **57**, 407 (1986)

12. M. D. Dawson, T. F. Boggess, and A. L. Smirl, Opt. Lett. **12**, 254 (1987)

13. M. D. Dawson, T. F. Boggess, and A. L. Smirl, IEEE J. Q. El. Lett

14. P. M. W. French, and J. R. Taylor, Opt. Lett. **13**, 470 (1988)

15. M. D. Dawson, T. F. Boggess, and A. L. Smirl, Opt. Lett. **12**, 590 (1987)

16. L. F. Mollenauer and R. H. Stolen, Opt. Lett. **9**, 13 (1984)

17. F. M. Mitschke and L. F. Mollenauer, Opt. Lett. **12**, 407 (1987)

18. J. Mark, L. Y. Liu, K. L. Hall, H. A. Haus, and E. P. Ippen, Opt. Lett. **14**, 48 (1989)

19. F. Ouellette and M. Piché, Opt. Commun. **60**, 99 (1986)

20. J. Goodberlet, J. Wang, J. G. Fujimoto, and P. A. Schulz, Opt. Lett. **14**, 1125 (1989)

21. D. E. Spence and W. Sibbett, J. Opt. Soc. Am. B **8**, 2053 (1991)

22. D. E. Spence, P. N. Kean, and W. Sibbett, Opt. Lett. **16**, 42 (1991)

23. R. E. Bridges, R. W. Boyd, and G. P. Agrawal, Opt. Lett. **18**, 2026 (1993)

24. G. Cerullo, S. De Silvestri, V. Magni, and L. Pallaro, Opt. Lett. **19**, 807 (1994)

25. For example, the *Spectra Physics Tsunami* laser, Tsunami, Mode-locked Ti:sapphire Laser User's Manual, Spectra Physics Lasers, Inc. 1330 Terra Bella Avenue, Mountain View, Ca 94039-7013, U.S.A.

26. J. D. Kafka, M. L. Watts, and J. W. Pieterse, IEEE J. Quant. Electron. **28**, 2151 (1992)

27. D. S. Moore, and S. C. Schmidt, Opt. Lett. **12**, 480 (1987)

28. V. Petrov, and F. Seifert, Opt. Lett. **19**, 40 (1994)

29. M. Cavallari, G. M. Gale, F. Hache, L. I. Pavlov, and E. Rousseau, Opt. Commun. **114**, 329 (1995)

30. J. Y. Zhang, J. Y. Huang, Y. R. Shen, and C. Chen, J. Opt. Soc. Am. B **10**, 1758 (1993)

31. R. Danielius, A. Piskarskas, A. Stabinis, G. P. Banfi, P. Di Trapani, and R. Righini, J. Opt. Soc. Amer. B **10**, 2222 (1993)

32. U. Emmerichs, H. J. Bakker, and H. Kurz, Opt. Commun. **111**, 497 (1994)

33. R. L. Fork, C. V. Shank, C. Hirlimann, R. Yen, and W. J. Tomlinson. Opt. Lett. **8**, 1 (1983)

34. W. H. Knox, J. Opt. Soc. Amer. B **4**, 1771 (1987)

35. K. Burneika, M. Ignatavichyus, V. Kabelka, A. Piskarskas, and A. Stabinis, IEEE J. Quantum Electron. **QE-8**, 574 (1972)

36. A. S. Piskarskas, V. Smil'gyavichyus, and A. Umbrass, Sov. J. Quantum. Electron. **18**, 155 (9988)

37. M. Ebrahimzadeh, G. P. A. Malcolm, and A. I. Ferguson, Opt. Lett. **17**, 183 (1992)

38. A. Piskarskas, V. Smilgevicius, A. Umbrass, A. Fix, and R. Wallenstein, Opt. Commun. **77**, 335 (1990)

39. G. T. Maker and A. I. Ferguson, Appl. Phys. Lett. **56**, 1614 (1990)

40. M. Ebrahimzadeh, G. J. Hall, and A. I. Ferguson, Opt. Lett. **16**, 1744 (1991)

41. L. J. Bromley, A. Guy, and D. C. Hanna, Opt. Commun. **70**, 350 (1989)

42. S. Burdulis, R. Grigonis, A. Piskarskas, G. Sinkevicius, V. Sirutakis, A. Fix, J. Nolting, and R. W. Wallenstein, Opt. Commun. **74**, 398 (1990)

43. R. Laenen, H. Graener, and A. Laubereau, Opt. Lett. **15**, 971 (1990)

44. M. Ebrahimzadeh, G. J. Hall, and A. I. Ferguson, Opt. Lett. **17**, 652(1992)

45. H. Zhou, J. Zhang, T. Chen, C. Chen, and Y. R. Shen, Appl. Phys. Lett. **62**, 1457 (1993)

46. D. C. Edelstein, E. S. Wachman, and C. L. Tang, Appl. Phys. Lett. **54**, 1728 (1989)

47. G. Mak, Q. Fu, and H. M. van Driel, Appl. Phys. Lett. **60**, 542 (1992)

48. Q. Fu, G. Mak and H. M. van Driel, Opt. Lett. **17**, 1006 (1992)

49. W. S. Pelouch, P. E. Powers, and C. L. Tang, Opt. Lett. **17**, 1070 (1992)

50. P. E. Powers, S. Ramakrishna, C. L. Tang, and L. K. Cheng, Opt. Lett. **18**, 1171 (1993)

51. J. D. Kafka, M. L. Watts, and J. W. Pieterse, in *Conference on Lasers and Electro-Optics*, Vol. 11 of 1993 OSA Technical Digest Series (Optical Society of America, Washington, D.C., 1993), paper CPD32

52. J. M. Dudley, D. T. Reid, M. Ebrahimzadeh, and W. Sibbett, Opt. Commun. **104**, 419 (1994)

53. T. J. Driscoll, G. M. Gale, and F. Hache, Opt. Commun. **110**, 638 (1994)

54. D. T. Reid, M. Ebrahimzadeh, and W. Sibbett, Opt. Lett. **20**, 55 (1995)

55. M. J. McCarthy and D. C. Hanna, Opt. Lett. **17**, 402 (1992)

56. A. Robertson, G. P. A. Malcolm, M. Ebrahimzadeh, and A. I. Ferguson, in *Conference on Lasers and Electro-Optics*, Vol. 12 of 1992 OSA Technical Digest Series (Optical Society of America, Washington, D.C., 1992), paper CPD15

57. S. D. Butterworth, M. J. McCarthy, and D. C. Hanna, Opt. Lett. **18**, 1429 (1993)

58. A. Robertson and A. I. Ferguson, Opt. Lett. **19**, 117 (1994)

59. J. Chung and A. E. Siegman, J. Opt. Soc. Am. B **10**, 2201 (1993)

60. Ch. Grasser, D. Wang, R. Beigang, and R. Wallenstein, J. Opt. Soc. Am. B **10**, 2218 (1993)

61. S. D. Butterworth, S. Girard, and D. C. Hanna, J. Opt. Soc. Am. B **12**, 2158 (1995)

62. J. D. Kafka, M. L. Watts and J. W. Pieterse, in *Conference on Lasers and Electro-Optics*, Vol. 8 of 1994 OSA Technical Digest Series (Optical Society of America, Washington, D.C., 1994), paper CWI6

63. J. D. Kafka, M. L. Watts, and J. W. Pieterse, J. Opt. Soc. Am. B **12**, 2147 (1995)

64. A. Nebel, C. Fallnich, R. Beigang, and R. Wallenstein, J. Opt. Soc. Am. B **10**, 2195 (1993)

65. M. Ebrahimzadeh, S. French, W. Sibbett, and A. Miller, Opt. Lett. **20**, (2), 166 (1995)

66. M. Ebrahimzadeh, S. French, W. Sibbett, and A. Miller, Appl. Phys B. **60**, 443 (1995)

67. M. Ebrahimzadeh, S. French, and A. Miller, J. Opt. Soc. Am. B **12**, 2180 (1995)

68. S. French, M. Ebrahimzadeh, and A. Miller, Opt. Lett. **21**, (2), 131 (1996)

69. S. French, M. Ebrahimzadeh, and A. Miller, J. Mod. Opt. **43**, (5), 929 (1996)

70. S. French, M. Ebrahimzadeh, and A. Miller, Opt. Lett. **21**, (13), 976 (1996)

71. S. French, M. Ebrahimzadeh, and A. Miller, Opt. Commun. **128**, 166 (1996)

Contents Page

2.1 Introduction

As discussed in Chapter 1, this thesis describes picosecond optical parametric oscillators that are pumped by a self-mode-locked Ti:sapphire laser. This pump source is an integral part of the entire operation, with the OPO performance being greatly influenced by the quality of the service it receives from the pump source. It is therefore necessary to discuss the properties and operational characteristics of the Ti:sapphire laser. In this chapter a full characterisation of the laser is given as well as a description of the suitability of Ti:sapphire as a laser gain medium. The chapter begins with a discussion of the properties of linear and nonlinear pulse propagation in transparent optical media, as is the case for lasers and OPOs. A description of the techniques used to measure the temporal and spectral characteristics of the output of ultrafast mode-locked lasers is also given, these techniques are equally usable for the characterisation of ultrafast OPOs and are used extensively throughout the work in this thesis.

2.2 Pulse propagation in linear and nonlinear media

In this section a description of pulse propagation in linear and nonlinear optical systems is given. These features are very important as they relate to the characteristics that will be present in an optical pulse after it has propagated through a length of such a system. The initial description will be concerned with a purely dispersive medium in which no nonlinear effects are present. A discussion of nonlinear propagation will then be given, which will involve the description of important features such as self phase modulation and self focussing.

2.2.1 Pulse Propagation in Linear Optical Media.

The variation of the speed of light with wavelength in a material results in the concept of dispersion. When an electric field acts on an optical material then the response of the medium will depend on the frequency of the interacting field. This occurrence is manifested as the dependence of the refractive index (n) of the medium on the optical field frequency (ω).

The variation of refractive index with wavelength (λ) is commonly expressed mathematically by the Sellmeier equation which is generally of the form:

$$n^2 = A + \frac{B}{(\lambda^2 + C)} + D\lambda^2 \qquad (2.1)$$

the refractive index is measured experimentally with the Sellmeier constants A, B, C and D being used to fit the empirical formula to the experimental data. For the vast majority of optical materials this equation will be valid from the visible to near infrared spectral regions. Outwith these region materials start to exhibit resonances, which results in the breakdown of the accuracy of the above equation. The wavelength range over which these equations are valid is ultimately dependent on the material in question. The variation of n and $dn/d\lambda$ with wavelength governs which spectral regime is being operated in, if both n and $dn/d\lambda$ decrease with wavelength then this is described as normal dispersion. In this dispersive regime blue light will travel more slowly and refract more strongly than red light. When operating close to an optical resonance these properties may be reversed such that both n and $dn/d\lambda$ increase with increasing wavelength with this situation being referred to as anomalous dispersion.

The different wavelength components of a pulse propagating in an optical medium travel at speeds given by $c/n(\lambda)$. The differences in the values of n for each spectral component of the pulses results in each wavelength portion travelling at a different speed. This therefore results in temporal dispersion of a pulse propagating in an optical medium. Whether pulse broadening or shortening results from propagation in a dispersive medium will depend on the properties of the material. Work on dispersion has led to the understanding of the situation. In a circumstance in which there is no attenuation, the nonlinear and anomalous dispersions can combine to produce pulse shapes which are periodic functions of distance. These pulses are known as solitons, with soliton propagation of light pulses in optical fibres now common place. In any ultrafast laser or optical parametric oscillator cavity elements can create a situation in

which nonlinearities and dispersion affect the characteristics of the output pulses. When designing a picosecond OPO the measurement of the intracavity dispersion must be undertaken. This may result in the necessity of the inclusion of a dispersion control element such as a prism sequence or Gires-Tournois interferometer (GTI) [1].

The material dispersion can be calculated by expanding the propagation constant, β, in a Taylor series about the central frequency, ω_0.

$$\beta(\omega) = \frac{\omega}{c} n(\omega) = \beta + \beta_1(\omega - \omega_0) + \beta_2(\omega - \omega_0)^2 + \beta_3(\omega - \omega_0)^3 + \ldots \quad (2.2)$$

The physical meanings of the coefficients in equation (2.2) relate to phase and group velocity [2]. The velocity of propagation of a region of constant phase is referred to as the phase velocity, v_ϕ, within an optical pulse the individual optical components will travel at different speeds. The group velocity, $v_g = d\omega/d\beta$ represents the velocity of the pulse envelope. This will, in general, change its form as it progresses within the medium. The coefficient β is related to the phase velocity, v_ϕ, by

$$\beta = \beta(\omega) = \frac{\omega_0}{v_\phi} \quad (2.3)$$

The group velocity is related to β and is given by

$$\beta_1 = \frac{1}{v_g} \quad (2.4)$$

where

$$\beta_1 = \frac{d\beta}{d\omega} = \frac{1}{c}\left(n + \omega\frac{dn}{d\omega}\right) = \frac{1}{c}\left(n - \frac{dn}{d\lambda}\right) \quad (2.5)$$

The group velocity (v_g) represents the propagation rate of the pulse envelope while the individual optical cycles within the envelope will progress with the phase velocity ($v\phi$). The term β_2 represents the group velocity dispersion (GVD) and is given by

$$\beta_2 = \frac{d}{d\omega}\left(\frac{1}{v_g}\right) = \frac{1}{c}\left(2\frac{dn}{d\omega} + \omega\frac{d^2n}{d\omega^2}\right) = \frac{\lambda^3}{2\pi c^2}\frac{d^2n}{d\lambda^2} \quad (2.6)$$

This term is used as a measure of the dispersion exhibited by an optical material and represents the change in shape experienced by a pulse as it travels

through a dispersive medium. In the situation where β_2 is zero then an optical pulse will propagate for an indefinite period without any modification to its temporal envelope. The term $\beta_2 = 0$ at approximately 1.3 μm, for many common optical materials. However generally higher-order terms of equation (2.2) are non-zero and so cannot be neglected in dispersion considerations. The third-order dispersion term β_3 is given by

$$\beta_3 = \frac{d^2}{d\omega^2}\left(\frac{1}{v_g}\right) = \frac{1}{c}\left(3\frac{d^2n}{d\omega^2} + \omega\frac{d^3n}{d\omega^3}\right) = \frac{-\lambda^4}{2\pi^2c^3}\left(3\frac{d^2n}{d\lambda^2} + \lambda\frac{d^3n}{d\lambda^3}\right) \qquad (2.7)$$

When extremely short pulses are required i.e. ~10 fs then the β_3 term becomes important and must be considered; in this work as pulse durations of no less than ~500 fs are used then all the work can be undertaken without addressing third order dispersion effects and hence all the discussions included here will deal only with the effects and correction of group velocity dispersion associated with the second derivative of phase with respect to frequency or second order dispersion.

The chromatic dispersion constant (D) of a system may be expressed as,

$$D = \frac{d\beta_1}{d\lambda} = -\frac{2\pi c}{\lambda^2}\beta_2 = -\frac{\lambda}{c}\frac{d^2n}{d\lambda^2} \qquad (2.8)$$

As discussed previously, when designing a picosecond OPO the consequence of GVD must be considered. It is highly desirable if a device for varying the intracavity GVD can be combined with other OPO cavity elements. The requirement to control the GVD has led to the development of several techniques. One of the most popular is the Brewster-angled prism sequence, which is illustrated in Figure 2.1. This approach have advantages over other schemes because of the fact that it has a lower insertion loss than, say a grating arrangement as well as greater spectral tunability than Gires-Tournois interferometers. If the optical path length through an optical system is given by, P, then the dispersion constant, D, is given by

$$D = \left(\frac{\lambda}{cL}\right)\frac{d^2P}{d\lambda^2} \qquad (2.9)$$

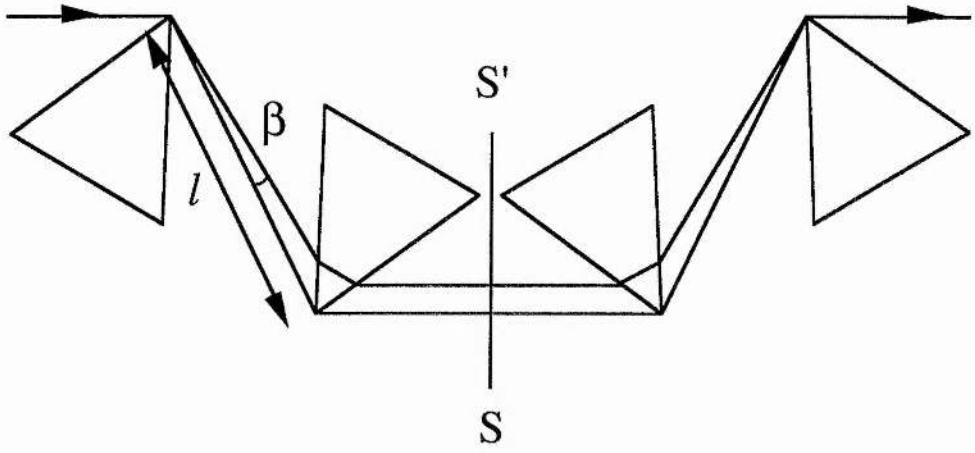

Figure 2.1
Four prism sequence to produce net negative GVD.

where L corresponds to the physical length of the optical path. For a single pass of the four prism sequence illustrated in Figure 2.1, it can be shown that [3],

$$\frac{d^2P}{d\lambda^2} = 4l\left\{\left[\frac{d^2n}{d\lambda^2} + \left(2n - \frac{1}{n^3}\right)\left(\frac{dn}{d\lambda}\right)^2\right]\sin\theta - 2\left(\frac{dn}{d\lambda}\right)^2\cos\theta\right\} \quad (2.10)$$

where n represents the refractive index of the prism material. Commonly in laser and OPO cavity configurations, including those described in this thesis, θ is of the order of the angular deviation of the ray bundle, this means that cosθ is approximated equal to unity and the term lsinθ is of the order of the beam spot size of 2mm. Providing $\frac{d^2n}{d\lambda^2}$ is not excessively large compared with $\left(\frac{dn}{d\lambda}\right)^2$, equation (2.10) shows that the prism sequence will produce a net negative GVD for sufficiently large values of l. Varying the value of l can change the amount of GVD produced by the prism sequence. The total dispersion present within a cavity including a prism sequence may be calculated by using equations (2.9) and (2.10) in combination with equation (2.8).

The degree to which an optical pulse propagating in a dispersive material is influenced by GVD will depend upon the dispersion of the material and the initial pulse characteristics [4]. A pulse with constant instantaneous frequency across its temporal profile is known as an unchirped pulse, or bandwidth (transform)-limited pulse. As this pulse travels through a dispersive medium it will undergo a broadening irrespective of the sign of β_2. In the visible spectral region many optical materials have positive dispersion, i.e. $\beta_2 > 0$, this results in a reduction in refractive index with wavelength. Operation in a positively

dispersive regime results in longer wavelength optical components travelling faster than shorter wavelength components. The influence of GVD will result in an initially unchirped pulse experiencing a re-distribution of its spectral components, which will attain a relative delay with respect to one another. The instantaneous frequency change present across the pulse will cause it to become chirped. After movement through a positive dispersive medium an initially unchirped pulse will have become linearly 'up' chirped, with the instantaneous frequency increasing linearly from the front to the back of the pulse. The reverse effect is true for propagation through a negatively dispersive regime in which a bandwidth limited pulse will become 'down' chirped.

If the initial pulse is itself frequency chirped then this will lead to pulse shape characteristics being more complicated. It is beneficial to define a pulse chirp parameter (C), with $C>0$ for up chirped pulses, and $C<0$ for down-chirped pulses. Determination of whether a pulse experiences temporal broadening or narrowing depends on the sign of C and β_2. Pulse broadening will occur if the quantity $C\beta_2 >0$, implying that the sign of both chirp and dispersion must be the same. If the product $C\beta_2 <0$ then chirp and dispersion have opposite signs and pulse narrowing will occur until some minimum pulse duration is reached, C will then change sign and pulse broadening will commence. For negative dispersion systems in which $\beta_2<0$ this effect can be understood by the following argument. When a pulse is initially up-chirped ($C>0$) its blue spectral components are delayed with respect to its red spectral components. In systems where, $\beta_2<0$, blue light travels faster than red, this results in the blue components of an up-chirped pulse catching up with the red components. A minimum pulse duration will be obtained when the delay between the spectral components of the pulse reaches zero. Subsequent propagation will result in pulse broadening, because the red components now trails the blue, as the pulse becomes down chirped.

2.2.2 Nonlinear Pulse Propagation.

In this section the combination of GVD and the nonlinear spectral broadening effect, self phase modulation (SPM) will be discussed.

When an optical pulse travels through a transparent dielectric material its electric field will interact with that medium via its response force, the result of this is that a macroscopic polarisation (P) is generated in the material. Interaction between optical field and atomic structures produces a distortion in the electron-charge clouds in solids and a reorientation of the axes of molecules

in liquids. If a sufficiently high electric fields interacts with an optical material then the response of that material may become nonlinear. This response may be expressed as the series expansion [5],

$$P = \chi_{(1)}\varepsilon_0 E + \chi_{(2)}\varepsilon_0 E^2 + \chi_{(3)}\varepsilon_0 E^3 + ... \qquad (2.11)$$

where $\chi_{(1)}$ is the linear susceptibility and $\chi_{(2)}$ and $\chi_{(3)}$ are higher-order nonlinearities in the dielectric response of the material.

Different nonlinear phenomena are associated with different terms in equation 2.11. Phenomena such as second harmonic generation and optical parametric oscillation are related to the E^2 term. This term becomes zero in centrosymmetric materials, in comparison to the E^3 term that is present in practically all optical materials. The two main properties resulting from the nonlinearity associated with the E^3 term are self phase modulation (SPM) and self focusing. This results in the E^3 term having a large bearing on the characteristics of the optical pulses that are generated from ultrashort pulse lasers and OPOs.

2.2.3 Nonlinear refractive index

The refractive index has a nonlinear dependence on field strength described by

$$n = n_0 + n_2 I(t) \qquad \text{where, } n_2 = \frac{\chi_{(3)}}{2\varepsilon_0 n_0} \qquad (2.12)$$

where n_2 is the nonlinear refractive index and n_0 is the linear refractive index. The field associated with an intense optical field can itself produce a modulation in the refractive index, this results in an intensity dependence of the refractive index referred to as the optical Kerr effect. The magnitude of n_2 is determined by a multitude of physical mechanisms, acting over a broad temporal range, however it is generally always positive.

2.2.4 Self Phase Modulation

Self phase modulation is the change in the phase of an optical pulse due to the nonlinearity of the refractive index of the medium through which it is propagating. This phenomena was first observed by Shimizu [6] who observed that after passing through a liquid filled cell an initially unmodulated laser spectrum had a modulation extending both above and below the laser frequency this was attributed to the intensity-dependent refractive index. When an optical pulse propagates through a nonlinear material it will encounter a refractive index change governed from equation (2.12) of

$$\Delta n=n(t)-n_0+n_2I(t) \tag{2.13}$$

where I(t) is the temporal intensity pulse profile. The pulse intensity variation will result in the pulse experiencing a time-varying phase shift. A pulse passing through a length (L) of a nonlinear material will experience a phase shift of

$$\Delta\phi(t) = kL\Delta n(t) = \frac{2\pi L}{\lambda} n_2 I(t) \tag{2.14}$$

where λ is the pulse wavelength. This phase shift will induce a instantaneous frequency chirp of

$$\Delta\omega = \frac{d}{dt}\left(\Delta\phi(t)\right) = \frac{2\pi n_2}{\lambda}\frac{dI(t)}{dt} \tag{2.15}$$

Figure 2.2 shows how nonlinear chirp can result in a change in instantaneous frequency for a gaussian intensity pulse profile. The dependence of $\Delta\omega$ on the temporal gradient of the pulse intensity coupled with in general $n_2 > 0$ leads to the leading edge of the pulse experiencing a red shift since in this region $\Delta\omega < 0$, the trailing edge of the pulse will encounter a blue shift as in this region $\Delta\omega > 0$. The central region of the pulse will experience an approximately linear chirp. The temporal pulse intensity profile will remain unchanged in non dispersive media, however in dispersive media the combined effects of group velocity dispersion and SPM will cause envelope distortion. These effects can results in several temporal effects such as pulse broadening or soliton propagation.

Solitons are optical pulses that propagate through a dispersive, nonlinear medium with an invariant pulse shape. Several reports of solitonic propagation have been made [7], such effects occur at regions of anomalous dispersion in a material, where a balancing between the dispersion and SPM are reached. The pulse shortening process in ultrashort pulse laser and OPO systems can be

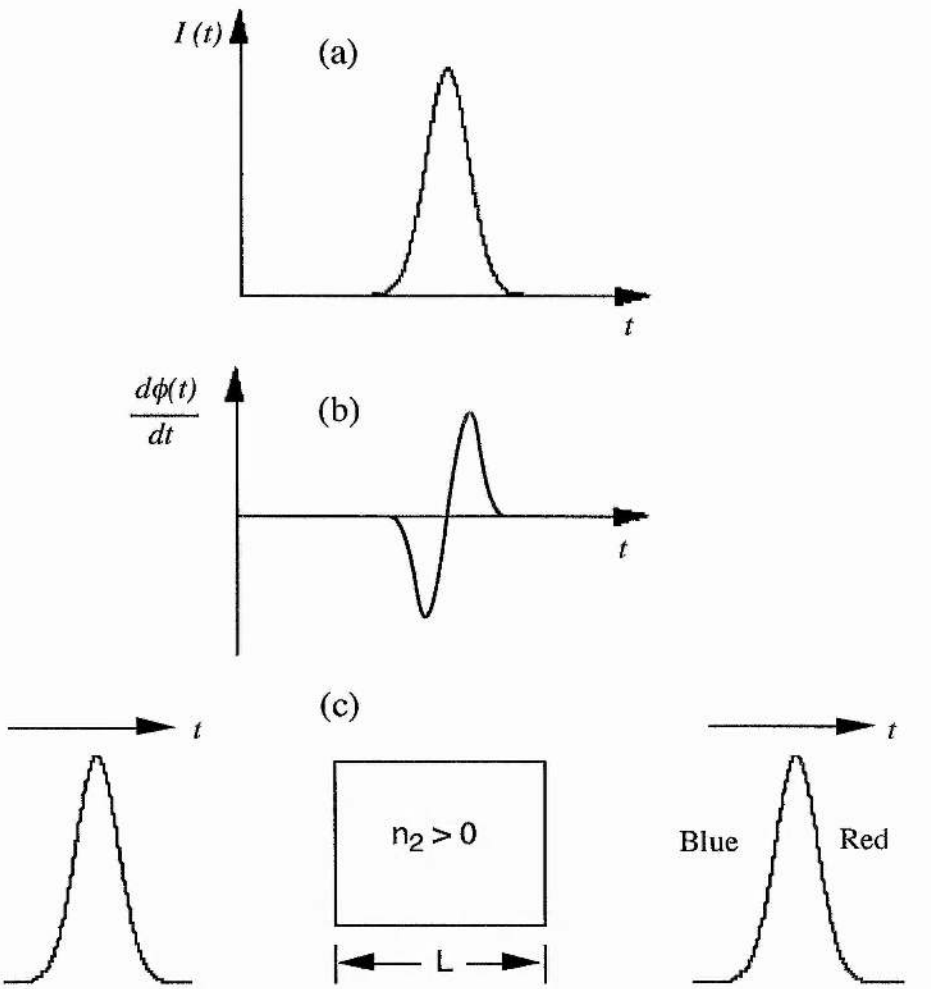

Figure 2.2
(a) Pulse intensity envelope. (b) Change in instantaneous frequency. (c) Arrangement to observe self phase modulation.

described by a soliton approach in which the GVD is varied by using a prism sequence. When an optical pulse is present in such a system it will be encounter the effects of SPM, this will result in the creation of new frequency components and will lead to the pulse becoming up chirped. If negative dispersion is introduced into the cavity, then this will result in the red spectral components being delayed with respect to the blue components. This results in the compression of the central portion of the pulse in which the SPM and GVD may be balanced. Extremely short pulses have been generated from lasers and OPOs using this technique. When no dispersion compensation is present a self-mode-locked Ti:sapphire laser will typically generate pulses on the picosecond timescale, however the inclusion of a prism pair in the cavity will produce a net

negative intracavity dispersion which will result in the laser producing pulses as short as 10 fs [8]. This demonstrated the importance of these mechanisms in the attainment of ultrashort optical pulses.

2.2.5 Self-focusing

A very important consequence of Kerr effect is the phenomenon known as self-focusing where an intense beam induces a weak positive lens in the optical medium. This effect is understood by considering the phase velocity of the wavefront as it propagates through an optical medium as illustrated in Figure 2.3. The centre of the beam, which is most intense, encounters the highest index of refraction, which causes the centre of the wavefront to be retarded more than the edges, this results in focusing occurring.

In the preceding section the most important aspects of optical pulse propagation in linear and nonlinear media have been discussed. These concepts are paramount in the process of generating ultrashort pulses, in that the combination of the intracavity GVD and SPM are the main factors influencing the production of such pulses.

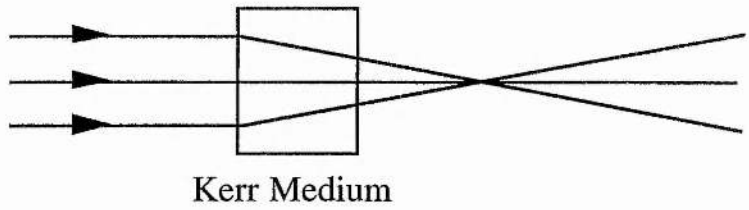

Figure 2.3
Self-focusing of an intense beam due to the optical Kerr effect.

2.3 Measurement of ultrashort optical pulses

When using any ultrashort laser or OPO as a source for experiments it is very important to have accurate temporal and spectral information about the output pulses. In experimental techniques, such as pump probe spectroscopy, it is important that an accurate measurement of the pulse duration can be made, as this duration can have a large bearing on the interpretation of the obtained results. In such experiments it is also not sufficient to simply measure the pulse durations, determination of the frequency bandwidth of the pulse is also required, as if this is too large then features such as, say, an exciton resonance

may not be resolved. Hence accurate temporal and spectral measurement techniques are required.

2.3.1 Temporal measurement

2.3.1.1 Linear Detection

The most convenient method to measure mode-locked laser pulses is direct detection using a photodiode and a fast oscilloscope. Photodiodes which have bandwidths in excess of 100 GHz, which represents a temporal resolution of < 5 ps, have been produced [9]. The resolvable pulse duration is in fact limited by the bandwidth of the oscilloscope being used, which is typically of the order of 0.5 GHz. Although these oscilloscopes have insufficient bandwidth to enable the measurement of pulses of less than 1ns duration, they are however capable of resolving the individual pulses in a mode - locked pulse train. Sampling oscilloscopes have bandwidths as large as 50 GHz, which represents a temporal resolution of 10 ps [10].

2.3.1.2 Second Harmonic Generation Autocorrelation

None of the above methods are capable of measuring pulses of durations of less than ~1 ps, for these pulses it is necessary to use nonlinear correlation techniques. The most commonly used technique is that of second harmonic generation (SHG) autocorrelations [11], [12] and [13]. The pulse to be measured is divided into two equal components. One pulse is delayed with respect to the other using an optical delay line, the two pulses are then recombined in a nonlinear crystal.

Since the second harmonic generation depends quadratically on the input intensity, the second - order autocorrelation function $G_2(\tau)$ of the pulse can be generated by varying the temporal overlap of the two pulses in the crystal using the delay line. The duration of the pulse can then be inferred by measuring the displacement of the delay stage. An unfortunate feature is however, that the autocorrelation function is symmetric, and so information relating to the temporal profile of the pulse is lost. This makes the exact duration of the pulse ambiguous, since it depends on the pulse shape chosen.

There are several methods of obtaining SHG autocorrelations, each depends on the type of phase-matching used in the crystal and whether the two beams are

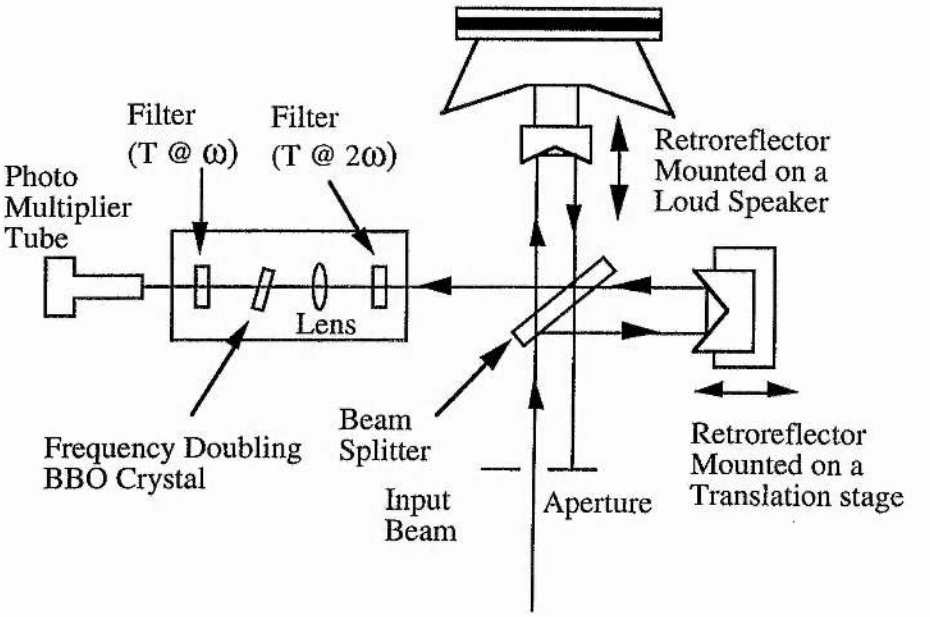

Figure 2.4
Schematic of the Second Harmonic Generation Autocorrelator.

collinear. In early autocorrelators type II phase-matching was used, requiring orthogonally polarised input beams. In this configuration the second harmonic is only generated when the pulses have some degree of temporal overlap in the crystal. It is now more popular to use type I phase-matching, when the two beams entering the crystal are collinear, the autocorrelation function will have a background level. This occurs because each pulse produces SHG, the SHG is however enhanced greatly when the pulses are coincident. Background free autocorrelations can be obtained by using a noncollinear arrangement. The arrangement used in this work is shown in Figure 2.4. The light is input to a delay line formed by a 50/50 beamsplitter and two retroreflectors, one of the retroreflectors is attached to the cone of an 8 inch diameter loudspeaker. The speaker is driven by a rounded sawtooth waveform which enables real time monitoring of the autocorrelation using an oscilloscope [14]. In the other arm of the delay line the corner cube is mounted on a three axis translation stage, so that the two beams input into the correlator can be overlapped. The second harmonic generation section comprises a 200 μm thick BBO crystal, a focusing lens, and two filters. The filters prevent room light or light at the fundamental laser frequency entering the photomultiplier tube (Thorn EMI Model No 9972 KB). For collinear autocorrelation, the second-order intensity autocorrelation function is given by

$$G_2(\tau) = 1 + 2\frac{\int_{-\infty}^{\infty} I(t)I(t-\tau)dt}{\int_{-\infty}^{\infty} I^2(t)dt} \tag{2.16}$$

equation (2.16) where I(t) is the intensity of the pulse and τ is the delay. By inspection of this equation it can be seen that the minimum possible background intensity is one unit (no overlap) and the maximum is three units (complete overlap). The shape and contrast ratio of the autocorrelation signal yields information regarding the quality of the mode-locked pulse train. Three important cases have been modelled, these are presented in Figure 2.5. Figure 2.5 (a) displays the autocorrelation for CW light. The contrast between the maximum intensity and the background level is 3:2. The peak at the centre of the autocorrelation occurs when the two arms of the delay line are exactly matched and is due to the coherent addition of the two fields. When a noise burst is input into the autocorrelator Figure 2.5 (b) is obtained. The broad pulse, which has a contrast ratio of 2:1, relates to the duration of the noise burst and the duration of the coherent spike. For perfectly mode-locked Gaussian pulses the autocorrelation is shown in Figure 2.5 (c). The 3:1 contrast ratio indicates that the entire oscillation bandwidth is phase locked and that there is no inter pulse radiation. The relationship between the pulse duration (τ_p) and measured autocorrelation duration (τ_{ac}) is,

$$\tau_p = \frac{\tau_{ac}}{k} \tag{2.17}$$

where the duration of the autocorrelation function is measured at an intensity of 2 units. The factor k used depends on the assumed pulse shape. The validity of this assumed pulse shape can be verified by measuring the bandwidth of the pulse spectrum and comparing the duration-bandwidth product, with the calculated value for the chosen pulse profile. The above comparison is only valid for pulses that have no frequency chirp. Examples of transform-limited pulse duration bandwidth products $\Delta\tau_p\Delta\nu$ and the factor k for common pulse shapes can be seen below, in Table 2.1. If the detection system used to measure the second harmonic generation has sufficient bandwidth, then it is possible to resolve the fringe pattern which results from the interference of two beams in the nonlinear crystal. In this case the second order interferometric autocorrelation function is given by [14], see equation 2.18.

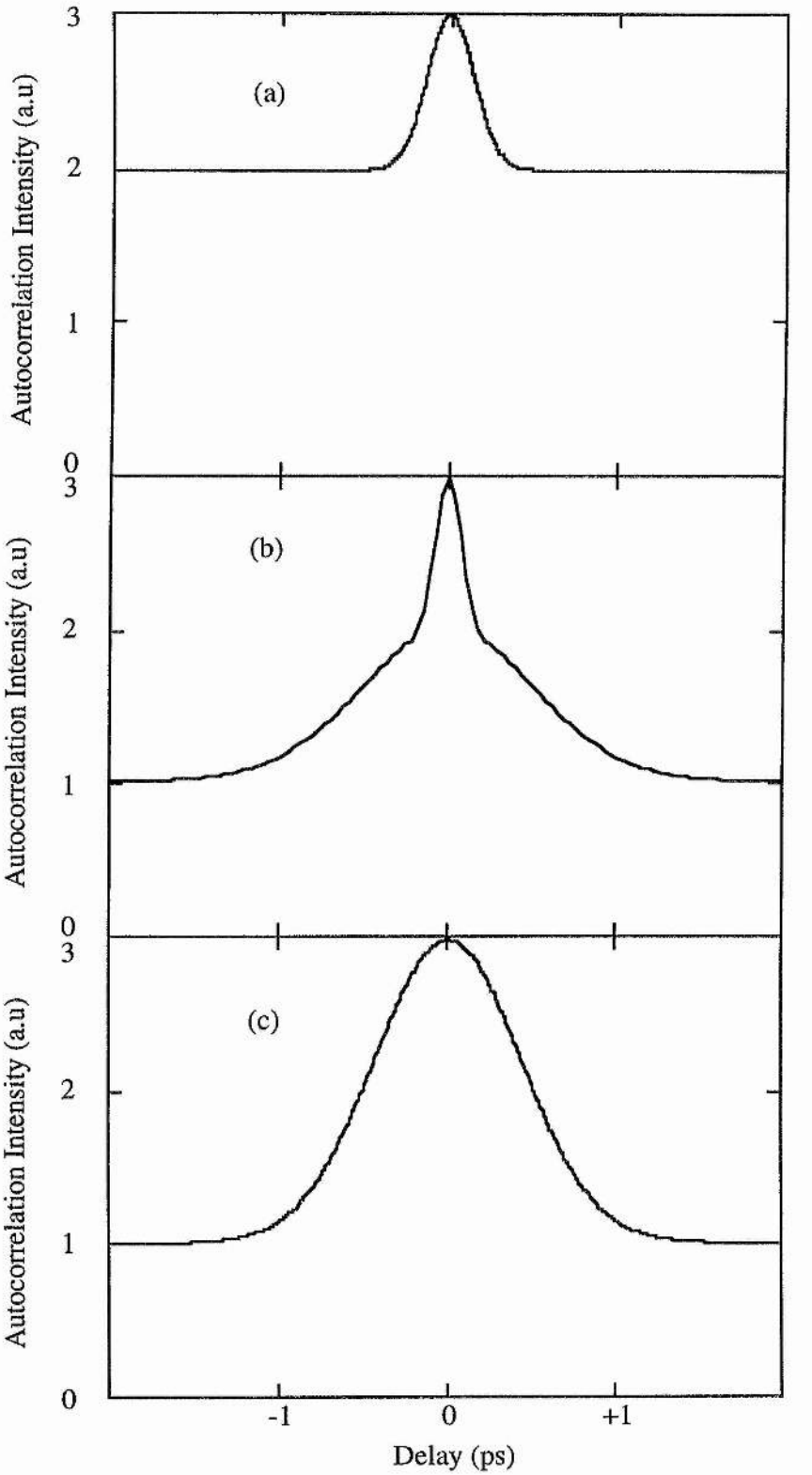

Figure 2.5

Calculated intensity autocorrelation traces for (a) cw radiation, (b) a noise burst, and (c) mode-locked pulses.

Pulse Profile	Intensity I(t)	$\Delta\tau\Delta\nu_p$	k
sech^2	$\operatorname{sech}^2\left(\frac{t}{T}\right)$	0.315	1.543
Gaussian	$\exp\left(-\frac{t^2}{T^2}\right)$	0.441	1.414
single- sided exponential	$\exp\left(-\frac{t}{T}\right)$; $t \geq 0$ 0; $t \leq 0$	0.110	2.00

Table 2.1
Transform-limited duration - bandwidth products and correlation factors for some common pulse shapes.

$$G_2(\tau) = \frac{\int_{-\infty}^{\infty} \left| \left\{ E(t)e^{i(wt+\phi)} + E(t-\tau)e^{i[w(t-\tau)+\phi(t-\tau)]} \right\}^2 \right|^2 dt}{2^4 \int_{-\infty}^{\infty} E^4(t)dt} \qquad (2.18)$$

The autocorrelation function can now be seen to depend quadratically on the electric field, this results in an increase in the contrast ratio to 8:1. The autocorrelation function is now able to resolve individual optical cycles, i.e. is fringe resolved. Using this method it is possible to measure the frequency chirp present on a pulse. This process has been modelled for Gaussian pulses, see Figure 2.6. Figure 2.6 (a) shows a transform-limited pulse, with (b) and (c) showing pulses with increasing linear chirp. The chirp has the effect of reducing the visibility of the fringes, since the wings of the pulse cannot interfere fully. For large degrees of chirp, as in Figure 2.6 (c) then the autocorrelation tends to the intensity autocorrelation case.

2.3.2 Frequency-domain measurements

The temporal measurement of an ultrashort pulse is not sufficient in itself to properly classify the quality of a laser pulse; it is also necessary to measure the optical spectrum. The measurement of the spectral bandwidth can be used in determination of pulse profiles. The value obtained for spectral bandwidth can

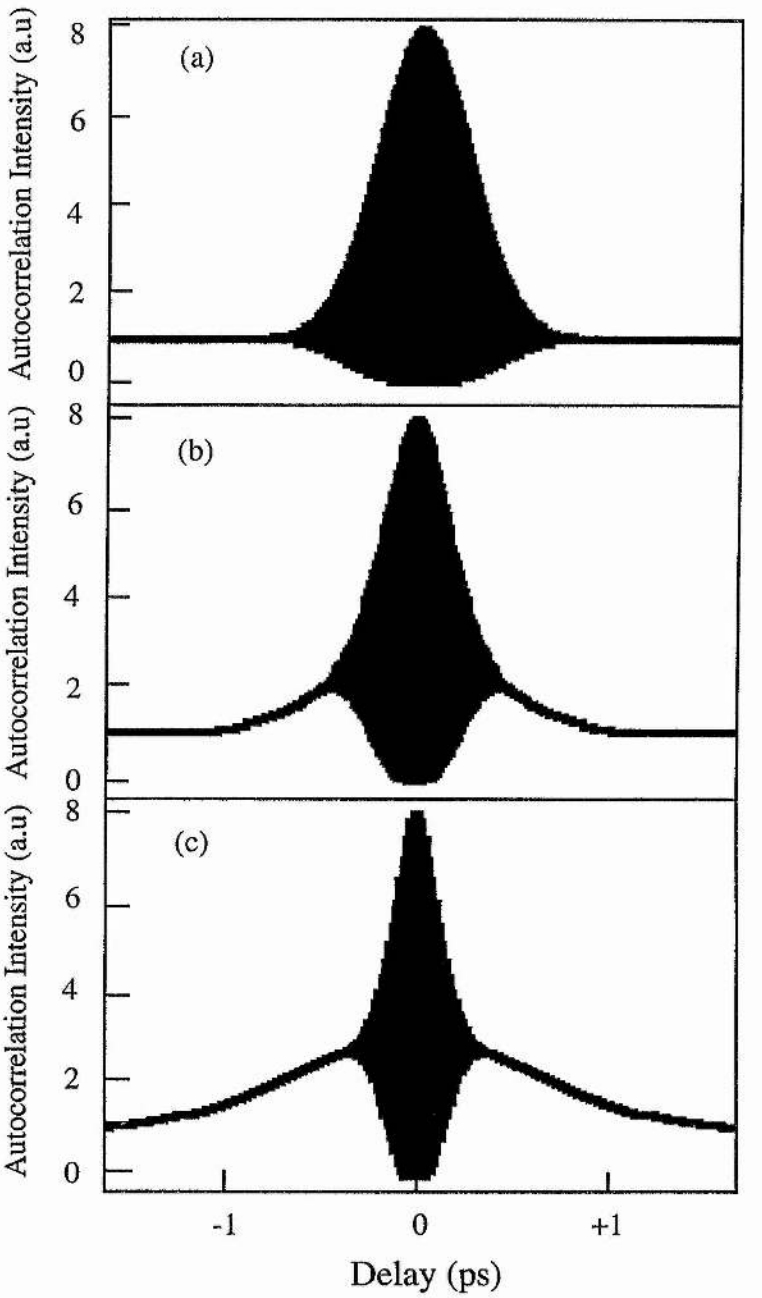

Figure 2.6

Calculated interferometric autocorrelations for Gaussian pulses having: (a) no frequency chirp, (b) a frequency chirp parameter of 1 and (c) a chirp parameter of 3.

then be used to calculate the duration - bandwidth product of the pulse in question.

The spectral characteristics of a mode-locked laser can be determined by measurements at either optical frequencies or radio frequencies corresponding to investigation of the spectral bandwidth of the pulse or examination of the repetition frequency of the laser. Together with pulse duration measurements, the former can give an estimation of the amount of chirp present within each pulse in the mode-locked output. The latter can give details of the phase noise or timing jitter of the mode-locked pulse sequence and provides information about the stability of the laser.

Measurements of the pulse intensity spectra were made using a Rees Instruments R202 Laser Spectrum Analyser, this provides a real time representation of the spectral content of the pulses, which can be displayed directly onto the oscilloscope. The resolution of this instrument was approximately 0.1 nm, which is acceptable to resolve picosecond pulses, as these have bandwidths of the order of ~ 1nm.

2.4 The Ti:sapphire Pump Laser

As discussed previously the performance of any OPO is dependent on the quality of the pump source, in this section a description of the Ti:sapphire pump laser is given.

2.4.1 Ti:sapphire laser configuration

The laser used as the pump source for the picosecond optical parametric oscillators described in the following chapters was a commercial self-mode-locked Ti:sapphire laser (Spectra-Physics, Tsunami) which is configured for picosecond operation. For a description of the Ti:sapphire laser gain medium and the process of self mode-locking, see reference [15].

The main requirement for laser action under continuous-wave (cw) pumping is that the unsaturated round-trip cw gain must be larger than the round-trip loss from all sources. To achieve a sufficient cw gain it is necessary to have a high inversion density coupled with an adequate length of Ti:sapphire material. A high inversion density is achieved by having a high pump intensity as well as a large Ti^{3+} ion concentration. The largest source of losses in the Ti:sapphire laser are from losses in the Ti:sapphire material itself, this loss is proportional to the rod length and varies with the Ti^{3+} concentration, generally increasing as the

Ti^{3+} concentration increases. Other sources of loss are from absorptions in mirror coatings and Fresnel reflections from polished surfaces.

In a Ti:sapphire laser the pump beam must be collinear with the cavity mode over a suitably long length of the laser rod. To achieve a continuous, high inversion density over the entire volume of a rod, which is several millimetres in diameter can be difficult. This problem is solved by using a technique called longitudinal pumping in which the pump light is focused to a narrow line within the rod, the oscillating laser mode is then focussed in a similar manner. The two modes are then overlapped within the same volume. The output beam is then collimated and expanded to normal size. The unused pump beam is dumped through the second cavity focus mirror. The laser has a purge regulator/filter unit connected between an external nitrogen supply and the laser head to remove dust and water vapour and provide clean, dry nitrogen gas to purge the sealed laser head. A chiller keeps the Ti:sapphire rod at a constant temperature for performance stability.

2.4.2 Experimental configuration

Figure 2.7 shows the six-mirror folded cavity the of the Ti:sapphire pump laser. While folding the cavity produces a compact laser, it makes pumping

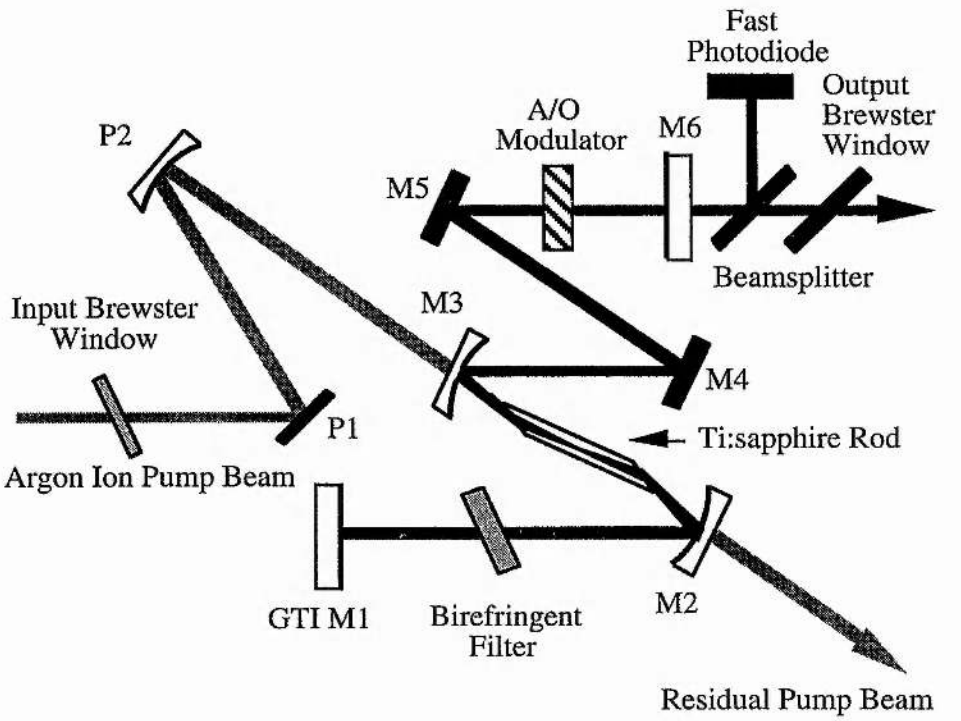

Figure 2.7
Cavity configuration of the self-mode-locked Ti:sapphire laser.

the system more complex. Using a focusing mirror at an angle other than normal incidence creates astigmatism, this can be eliminated by other cavity elements such as a Brewster angled rod. If astigmatism is not eliminated in folded cavity geometries this leads to the creation of output beams that are elliptical and hard to focus. The astigmatism in the output beam can however be virtually removed by carefully choosing the angles of the cavity focus mirrors and the length of rod. Astigmatism will still however exist within the laser rod. The pump beam must therefore also be astigmatic to achieve efficient coupling between the pump and intracavity beam. The use of a concave focusing mirror used at other than normal incidence and at the proper angle can generate astigmatism in the pump beam that will match that of the cavity mode. This result in a laser that will have a high conversion efficiency and a good beam quality.

2.4.3 Experimental Results

2.4.3.1 Tuning and Power Characteristics

If the Ti:sapphire laser is to be used as a pump source for optical parametric oscillators then it must be capable of producing several hundred milliwatts of average output power. The Ti:sapphire laser was pumped by a small-frame spectra physics 2060 argon ion pump laser which can supply 10 W of broadband power. With a pump power of 10 W from the argon ion laser the typical average output power when self-mode-locked was approximately 1.7 W.

To obtain broadband tuning, the Tsunami uses a birefringent filter to tune over its entire wavelength range. The birefringent filter consists of two crystalline quartz plates, which are placed one on top of the other, these are then inserted into the laser cavity at Brewster's angle. The plates are cut parallel to their optical axes and their birefringence causes the linear polarisation of the incident laser beam to become elliptical. As a result only one wavelength will make a complete 180° (or multiple thereof) polarisation flip and remain linearly polarised; all the other wavelengths will remain elliptically polarised. The elliptically polarised wavelengths will suffer loss at each Brewster angle surface within the cavity and will fail to reach lasing threshold.

The Tsunami birefringent filter has a free spectral range of approximately 150 nm. This free spectral range represents the difference between the adjacent eigenwavelengths, which are the wavelengths that remain linearly polarised after passing through the filter. Rotating the filter about an axis normal to the plates changes these eigenwavelengths. Although the broad tuning range of

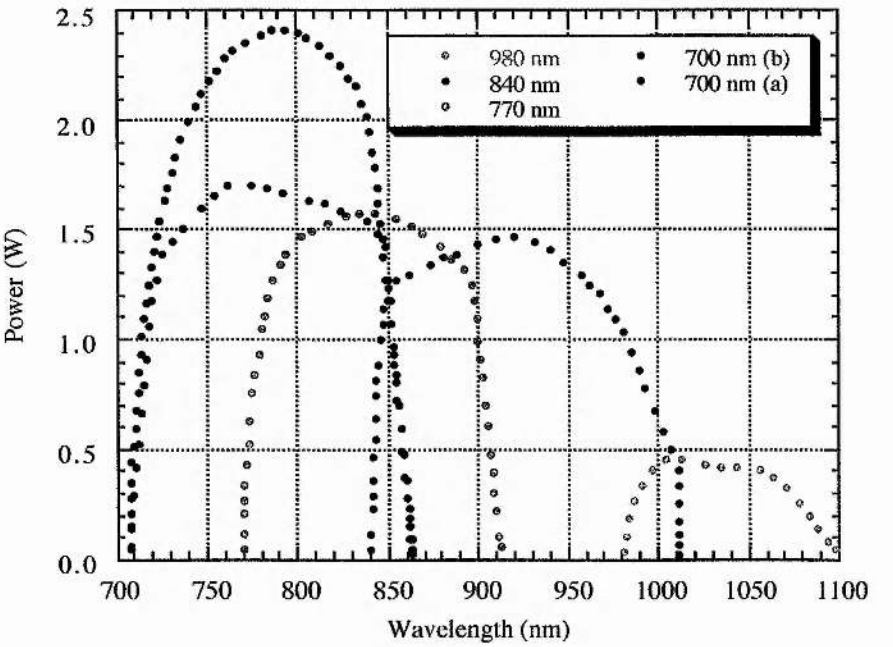

Figure 2.8
Output power and tuning range obtained from the five available Ti:sapphire mirror sets, for a pump power of 10W, from ref [16].

Ti:sapphire overlaps two "orders" of the filter, the narrower wavelength range of the mirror set allows only one order to oscillate at a time. The filter is rotated approximately 10° to select one of the two "orders", namely either 720 to 850 nm or 840 to 1080 nm.

To cover a tuning range of 720 nm to 1080 nm the Tsunami requires three different mirror sets, but five are available. The tuning and output power produced for an argon pump power of 10 W by these mirror sets have been reproduced from [16] and are shown in Figure 2.8. It can be observed that the largest output power is obtained for the 700 nm set (a) with nearly 2.4 W being obtained. However over 1.5 W of power is produced for all mirror sets except the higher wavelength set for which only 500 mW is produced. The mirror set used on the pump laser used in this thesis were the 770 nm set, which can be seen to produce ~1.5 W at the centre of the reflectivity band. However it was possible to obtain in excess of 12 W from the argon ion pump laser used in this work, this resulted in the output power increasing to 2.2 W as shown in Figure 2.9. Measurement of the output power against input power is useful as this can

give an indication of the slope efficiency of the laser, i.e. the rate of energy transfer from the argon to Ti:sapphire laser. Figure 2.10 shows that the Ti:sapphire laser has a threshold of 4 W and a slope efficiency of 28 %. A proportion of the output power was required for diagnostic purposes to monitor the output pulses and a further fraction was lost at steering and isolator optics. These processes led to a reduction of some 200 mW from the laser output, however, the output power was still large enough to make this system ideal for the pumping of the picosecond OPO system.

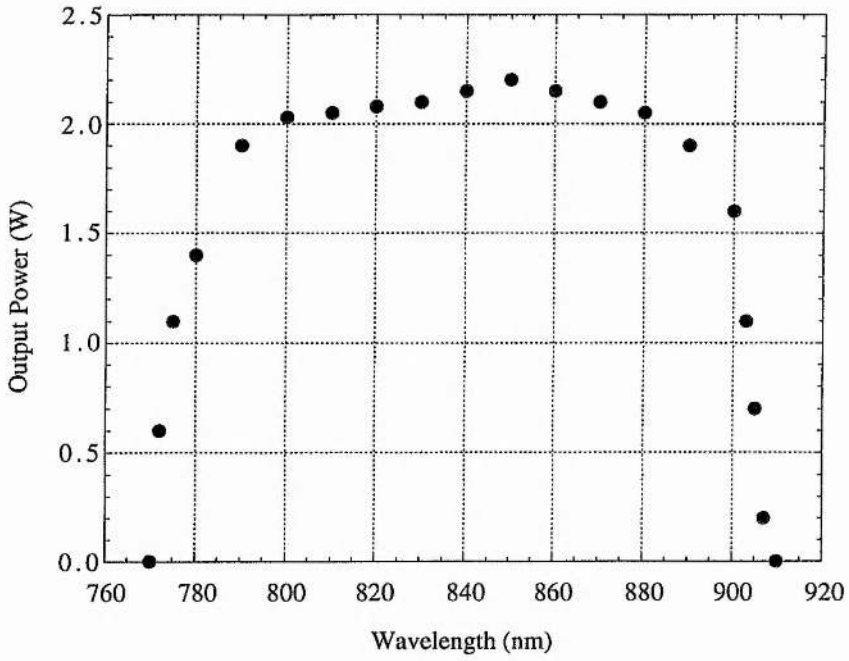

Figure 2.9
Measured output power of the Ti:sapphire laser and tuning from the 770 nm tuning set, for an argon ion laser pump power of 12W.

2.4.3.2 Pulse Durations

Variation of pulse durations is achieved by the use of a device called a Gires-Tournois Interferometer (GTI), this device is similar to a Fabry-Perot interferometer, with an exception being that the first mirror is a partial reflector instead of a high reflector. It has the benefit of being highly reflective over a broad spectral range, yet introduces a frequency-dependent optical phase shift. It also provides an adjustable negative group velocity dispersion (GVD) that can compensate for the positive GVD introduced by the optical components in the laser cavity.

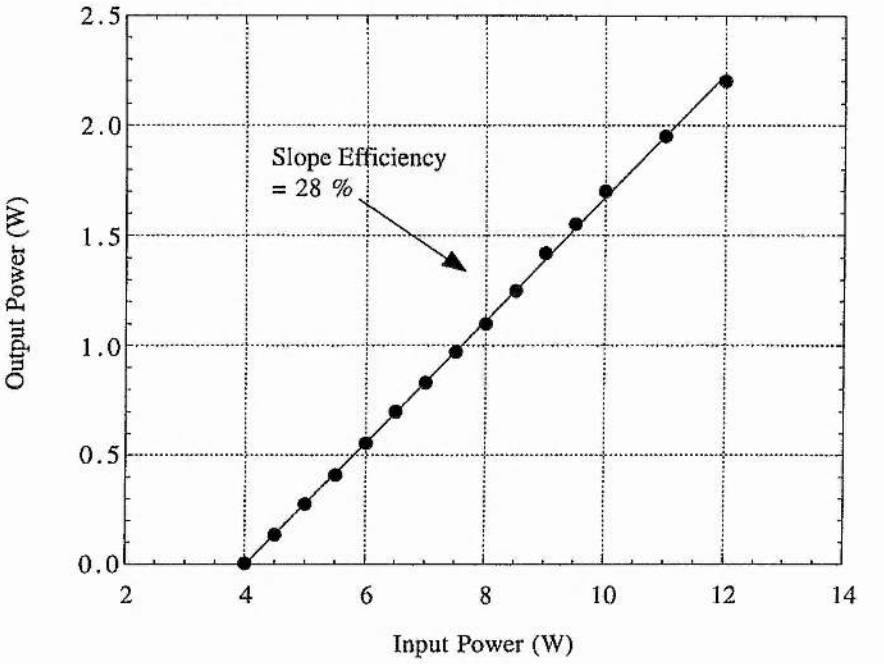

Figure 2.10
Output power against input power for the Ti:sapphire pump laser.

The Tsunami also has a Brewster angled Acousto-optic (A/O) modulator which is driven by a low-power radio frequency (rf) source. This modulator ensures an 81 MHz nominal pulsing action at laser start up. It also prevents the dropouts or shut-downs associated with standard passive mode-locking systems and so allows the laser to operate for extended periods of time. Autocorrelation measurements have been performed on the laser so that the pump pulse durations can be determined across the entire tuning range of the Tsunami. If a sech^2 pulse shape is assumed, then it can be seen from Figure 2.11 that the laser produces pulses of the order of 1.1 ps, these pulses can be extended out to ~ 2.5 ps by simply varying the position of the GTI. This autocorrelation was performed at a wavelength of 800 nm. The optical spectrum can be seen to have no modulation present, which indicates that there is no SPM present. The time bandwidth product of 0.335 indicates that the pulses obtained from this laser are transform-limited. The pulse durations were measured across the entire laser tuning range, with the available mirror set, with the results being depicted in Figure 2.12. It can be observed that the pulse durations remain constant at ~ 1.1 ps. Measurement of the amplitude noise of the pump laser is also a very important consideration as any fluctuations in this laser will be passed onto the

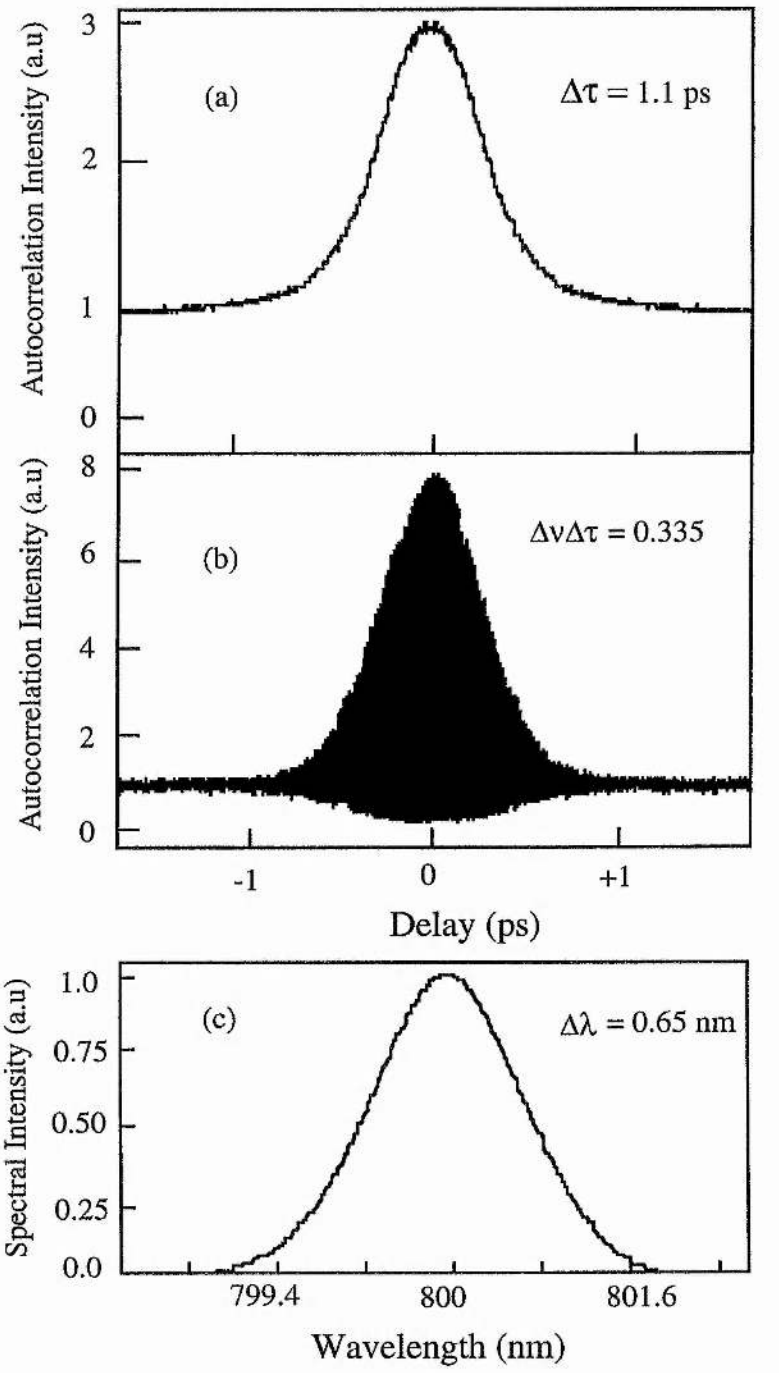

Figure 2.11

(a) Intensity and (b) interferometric autocorrelation, and (c) spectrum of Ti:sapphire output pulses at 800 nm. The pulse duration determined from the intensity autocorrelation is 1.1 ps, with a corresponding time-bandwidth product 0.335.

OPO itself, hence it is of paramount importance that the Ti:sapphire has as low an amplitude fluctuation as possible.

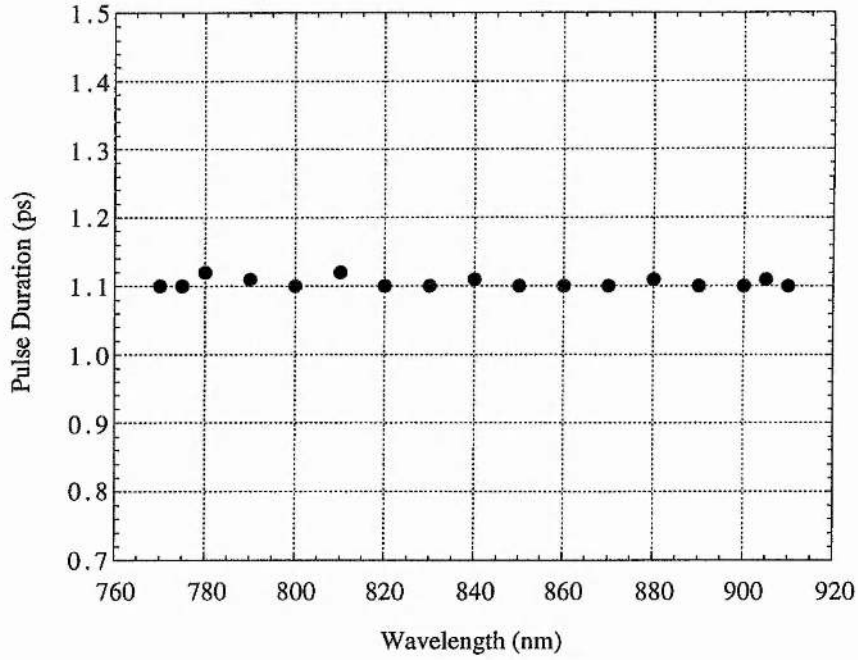

Figure 2.12
Variation of the pump laser pulse durations across its entire tuning range.

2.4.3.3 Amplitude Noise

The amplitude noise on the output of the Ti:sapphire laser was investigated by monitoring the output pulse sequence on an oscilloscope using a fast silicon photodiode. Intensity fluctuations of the order of 1 % were measured from the output of the Ti:sapphire laser, when using a 10 ms timebase on the oscilloscope. An oscillogram showing the output pulse sequence is displayed below in Figure 2.13. Results presented later in Chapter 4 describe a comparison between the amplitude noise present on a picosecond OPO and the intensity fluctuations of the pump laser and so this value is very important.

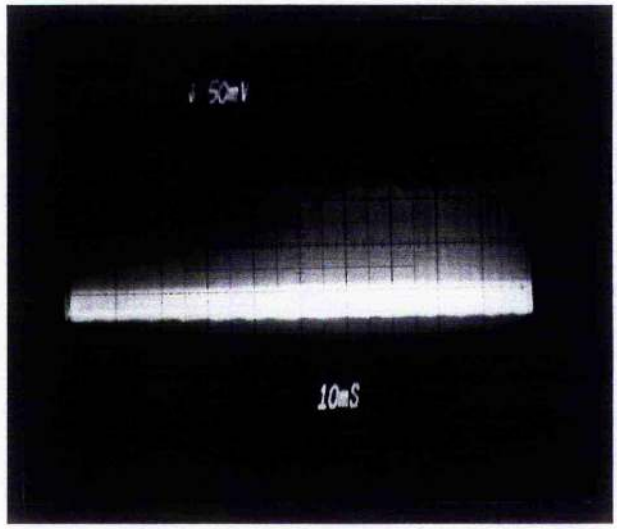

Figure 2.13
Oscillogram showing the amplitude noise (intensity fluctuations) on the output pulse sequence from the self-mode-locked Ti:sapphire laser.

2.5 Conclusions

In this chapter a description of the effects governing the propagation of ultrashort pulses in transparent optical media has been given. Additionally a description of the diagnostics required to characterise the temporal and spectral components of ultrashort laser and OPO pulses has been presented. Finally a detailed description has been presented of the performance of the self-mode-locked Ti:sapphire laser used as a pump source for the optical parametric oscillators described in subsequent chapters. In typical operation the laser has demonstrated an average output power of over 2.2 W. The laser produces transform-limited 1.2 ps pulses across the continuous tuning of the laser of 770 - 910 nm. In Chapter 3 the important features relating to the design of a picosecond optical parametric oscillator will be discussed in detail.

References

1. J. Kuhl and J. Heppner, IEEE J. Quantum Electron. **22**, 182 (1986)

2. A. E. Siegman, in Lasers (University Science Books, California, 1986), Ch. 12

3. R. L Fork, O. E. Martinez, and J. P. Gordon, Opt. Lett. **9**, 150 (1984)

4. G. P. Agrawal, in Nonlinear Fibre Optics (Academic Press, London, 1989)

5. Y. R. Shen, in The Principle of nonlinear Optics (Wiley Interscience, New York, 1984)

6. F. Shinizu, Phys. Rev. Lett. **19**. 1097 (1967)

7. L. F. Mollenauer, R. H. Stolen, and J. P. Gordon, Phys. Rev. Lett **45**, 1095 (1985)

8. C. P. Huang, M. Asali, J. Zhou, D. Garnvey, H. P. Kapteyn, and M. M. Murmane, in *Conference on Lasers and Electro-Optics*, Vol. 11 of 1993 OSA Technical Digest Series (Optical Society of America, Washington, D.C., 1993), paper JWA1

9. D.G. Parker, P. G. Say, A. M. Hansom, and W. Sibbett, Electron Lett **23**, 527 (1987)

10. Tektronix Model No CSA 803 Tektronix Product catalogue 1993 p250

11. J. A. Armstrong, Appl Phys **10**, 16 (1967)

12. H.P. Weber, J Appl. Phys **38**, 2231 (1967)

13. M. Maier, W. Kaiser, and J. Giormaine, Phys Rev. Lett **17**, 275 (1966)

14. K. L. Sala, G. A. Kenney-Wallace, and G. E. Hall, IEEE J. Quantum Electron. **QE-16**, (1990)

15. D. T. Reid, PhD thesis, University of St. Andrews (1994)

16. Tsunami, Mode-locked Ti:sapphire Laser User's Manual, Spectra Physics Lasers, Inc. 1330 Terra Bella Avenue, Mountain View, Ca 94039-7013, U.S.A.

Contents Page

3.1 Introduction

In this chapter a description is given of the process by which a picosecond OPO is conceived and designed. In Chapter 2 a description was given of pulse propagation in nonlinear media. Many of the concepts presented in that section are still relevant for the description of pulse propagation in optical parametric oscillators (OPOs). A very important element in any OPO is the nonlinear crystal. An outline is given as to how the choice of nonlinear crystal is made to meet the tuning and temporal requirements. The Chapter commences with a discussion of the theory relating to the parametric interaction of electromagnetic waves in nonlinear crystals. The Chapter concludes with a discussion of all the other relevant features relating to the design of a picosecond parametric oscillator.

3.2 The optical parametric oscillator

Optical parametric oscillators are devices that have been developed a great deal over the past decade in an attempt to extend the available tuning ranges from conventional pump sources. An optical parametric oscillator is a device that consists of a nonlinear crystal being placed within a resonator, in a similar

manner to a conventional laser, as shown in Figure 3.1. A high power wave at frequency ω_p is passed through the nonlinear material resulting in the generation of two output waves at frequencies ω_s and ω_i , given by,

$$\omega_p = \omega_s + \omega_i \tag{3.1}$$

The high power wave ω_p is conventionally known as the *pump*, with the higher frequency generated wave known as the *signal* and the lower frequency field known as the *idler*. Gain will be experienced at the frequencies ω_s and ω_i through a difference frequency mixing process provided that the phase-matching condition shown below is satisfied,

$$k_p = k_s + k_i \tag{3.2}$$

Where k represents the wavevector in the nonlinear material.

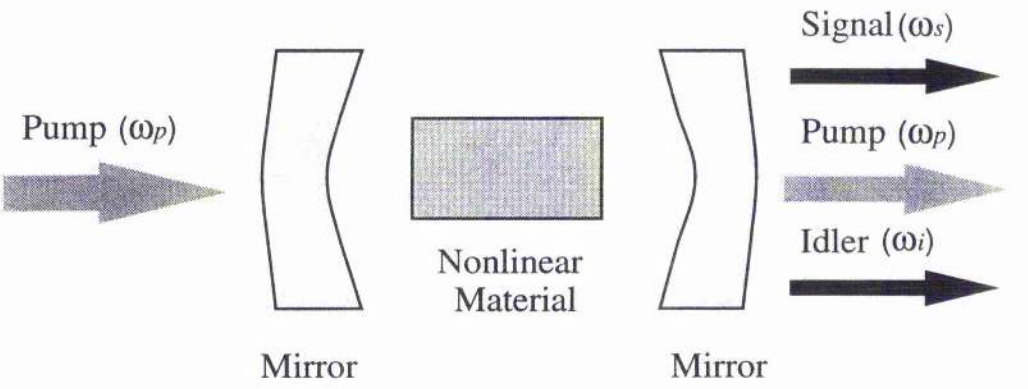

Figure 3.1
Schematic representation of an optical parametric oscillator.

When both the above conditions are satisfied an input pump frequency will result in the generation of a pair of signal and idler frequencies. The magnitude of these frequencies will depend on the value of the pump frequency and the dispersion of the nonlinear medium. The value of the signal and idler frequencies can be changed by a number of methods, although all involve the variation of the refractive indices of the material in the direction of propagation. Changing the pump wavelength results in a change in the generated signal and idler values due to the wavelength dependence of the refractive indices. This is a useful method to extend the limited tunability available from the pump laser. When a fixed wavelength pump source is used then the tuning is achieved by either varying the crystal angle with respect to the pump beam or by changing the crystal temperature. This process therefore allows a laser with little or no

tunability to acquire the capability to access a large section of the optical spectrum.

3.3 Cavity design considerations

This section describes the choices that are available in the design of the OPO resonator. The choice of resonator can effects features such as the threshold of the system and the conversion efficiency of the parametric interaction. These can in turn affect the output power and pulse durations obtainable from the OPO.

3.3.1 OPO cavity considerations

As discussed previously an OPO is in many respects similar to a conventional laser, in this respect the OPO cavity may provide feedback at either at one of the frequencies ω_s and ω_i or both. For the case where only one of the waves is resonated, generally the signal then this is described as a singly-resonant oscillator (SRO). When both ω_s and ω_i are resonated then this is referred to as a doubly-resonant oscillator (DRO).

The threshold condition in a OPO is similar to that in a laser, except in this case oscillation takes place when the single-pass gain experienced by the resonating wave exceeds the round-trip cavity losses. Both types of oscillators have positive and negative features. In the DRO both the signal and idler waves resonate which results in a lower oscillation threshold due to the higher gain available in this system. Problems do however occur in DROs due to the fact that both the signal and idler waves must be resonant simultaneously in the cavity. This results in only certain cavity lengths being suitable to meet the simultaneous resonance condition, which leads to mode-hopping effects that result in poor output stability.

The SRO will have a higher threshold than the DRO but due to the fact that it only requires the resonating of one wavelength component results in it producing a far superior output stability. It is therefore more desirable to operate in the SRO regime, so that a better degree of stability can be produced on the OPO output. This better stability performance outweighs the disadvantage of a much higher operational threshold. For certain applications, such as pump-probe spectroscopy a high degree of output stability is required, this type of operation will only be obtained from the singly-resonant oscillator.

Three pumping schemes exist to meet the high operational threshold of the SRO system. The first approach is use high peak power pulsed laser systems. A

second approach is to use quasi-continuous wave mode-locked operation within the duration of a Q-switched pulse envelope, this approach is however undesirable for operations that require a continuous train of identical pulses, such as in time resolved spectroscopy. The most common method in ultrashort pulse OPOs and the one of choice in all the work described in this thesis is the cw synchronous pumping geometry. In this arrangement the OPO cavity is designed such that the resonant signal wave is synchronous with the cw mode-locked pump laser pulse repetition period. This involves matching the pump laser and OPO laser cavity lengths. In this system the gain of the signal pulse is replenished on each occasion it returns to the nonlinear crystal as it is then met by the following pump pulse. One of the disadvantages of this system is that gain is only produced when a certain degree of overlap between the pump and the signal pulses exists in the nonlinear crystal. This puts a constraint on the choice of crystal material and orientation that can be used in this type of resonator.

3.3.2 Synchronously-pumped cavities

As is the case with a laser a multitude of resonator configurations exist that can be utilised in an OPO. It is necessary to consider the properties of many of these resonator designs so that a decision on the most appropriate for a particular requirement can be made. As discussed in the previous section it is essential to minimise the OPO threshold of the system so that operation many times above threshold can be achieved, for the following reasons.

An important feature in synchronously-pumped OPOs is the requirement to match the cavity lengths of the OPO and the pump laser to an interferometric degree. Any small mismatch between the cavity repetition periods of the pump laser and the OPO results in a reduction in pump and signal pulse overlap, which leads to a drop in efficiency and ultimately to a cessation of operation.

Two configurations of OPO resonator have been considered for the work in this thesis, namely the three-mirror (V) standing-wave cavity and the four-mirror ring cavity, which are shown in Figure 3.2. These cavities are designed such that intracavity mode size of the resonant wave will be of the order of 20 μm. This leads to high intensities being present which produce low threshold operation and results in large conversion efficiencies and high output powers being achieved.

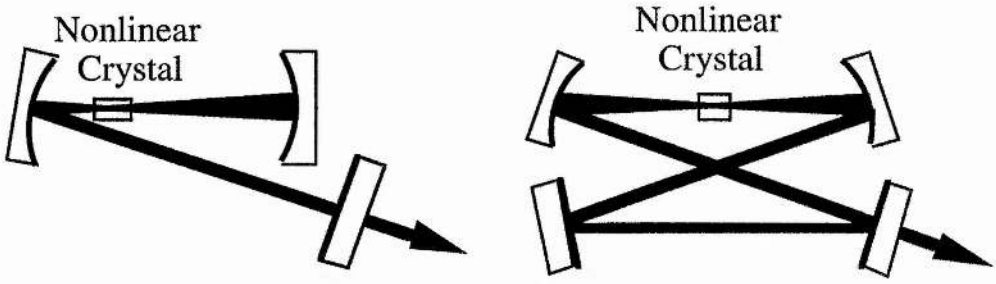

(a): V cavity Arrangement (b): Ring cavity Arrangement

Figure 3.2
Schematic of V and Ring cavities.

Each of the two cavities have advantageous and disadvantageous properties. A major difference between laser and OPO operation is that in an OPO configured for single-pass pumping, as is the case in this work, phase-matching demands lead to the situation that the pulse only experiences gain when travelling in a forward direction through the OPO crystal.

In the V cavity this results in the resonating pulse experiencing a single gain pass of the crystal for four mirror reflections and a passage through four crystal surfaces. The ring cavity on the other hand experiences a single pass gain of the crystal for four mirror reflections and travel through only two OPO crystal surfaces. The ring cavity therefore produces a lower threshold. There is however a downside to this configuration which is that it has a very low alignment tolerance, this can lead to a great deal of added difficulty being introduced for only a small increase in gain. The standing-wave three-mirror V cavity is therefore the cavity of choice in this work.

Two main options exist for cavity loss reduction when concerned with crystal features. These are whether to use a Brewster angled crystal or an anti reflection coating, there are of course pros and cons in respect of each. A Brewster angled crystal is useful if operating with a crystal material that experienced difficulties in coating or if extremely high operating temperatures are being used which may lead to coating damage. If the ellipticity of the output mode is of importance then a Brewster-angled geometry should be chosen as this can provide complete astigmatic compensation, the use of such a crystal can however lead to alignment difficulties. An antireflection-coated crystal used at normal incidence is the preferable choice in this work because it provides easier cavity alignment. Advances in reflection coating techniques have also resulted in excellent quality coatings now being available that can operate readily up to

temperatures of up to and beyond 250 °C. Astigmatic problems can be minimised by keeping the resonator fold angle tight, e.g. angles of 2-3 degrees can easily be achieved.

3.3.3 Threshold predictions in an optical parametric oscillator

When designing any OPO system it is essential that the chosen crystal will provide a threshold that is accessible by the pump laser available. To obtain oscillation in an OPO the single pass gain of the nonlinear crystal must exceed the roundtrip losses of the resonator, in a similar manner to a laser. It is important to minimise the threshold of the OPO as this leads to greater output powers from the system as well as greater stability. Several factors effect the threshold of a device, these include a combination of crystal properties and resonator design. One of the main factors affecting threshold is the correct matching of the pump and cavity mode focusing in the resonator.

Models to predict the pump power threshold expected from an OPO have been devised by a number of authors, for different resonator designs, although all concentrate around the importance of pump focusing on parametric generation. Work has been carried out for singly-resonant [1, 2] and doubly-resonant oscillators [3], with some studies concentrating on both type of system [4, 5]. Most of these studies have however made a number of assumptions and simplifications in the formulation of the models. Boyd and Kleinmann [3] assumed that the confocal parameters of the pump, signal and idler beams were equal to each other, where the confocal parameter of a beam is defined as:

$$b = \frac{2\pi w_o^2}{\lambda} \tag{3.3}$$

where w_o is the radius of the beam waist formed in the crystal.

The analysis of Kreuzer [1], involved the use of only plane waves and did not take into account the Gaussian nature of laser beams. Bjorkholm [4, 5], again used a plane wave assumption with no estimation of the signal and idler beam sizes being made. This model did however use the Gaussian beam size of the pump wave to calculate the pump beam intensity. In the Brosnan and Byer model to estimate OPO threshold power the size of the resonant signal beam size is determined from the pump beam size and not from the characteristics of the optical cavity [2].

The most complete model, to date of this important feature has been performed by Guha, Wu and Falk [6] who derived general expressions for pump intensity thresholds for both singly and doubly resonant systems. The pump power threshold P_{th} for a singly resonant system has been calculated in terms of the pump, signal and idler frequencies and a focusing term h_s, this is shown below in equation (3.4).

$$P_{th} = \frac{\varepsilon_s n_s n_i n_p c^3 (k_s + k_p)}{128 \omega_s \omega_i \chi^2 \pi^2 l h_s k_s k_p} \tag{3.4}$$

ε_s is the cavity roundtrip loss with h_s being a factor which describes how the efficiency of the parametric interaction is affected by focusing. The focusing factor h_s is dependent on many factors, namely the wavelength, crystal length, walkoff angle and the confocal parameters of the resonated and pump beams. l is the crystal length. All factors with dimensions should be expressed in S.I. units, this does however require a conversion for the χ factor as this is generally expressed in esu units, the conversion factor is shown below,

$$\chi(\text{esu units}) = \frac{3 \times 10^4}{2\pi} d_{eff} \quad (\text{SI units}) \tag{3.5}$$

To use this model an estimation of the focusing factor h_s must be made. It was calculated in the model that h_s maximises at ≈ 0.25 for optimum focusing when the confocal parameters of the pump and signal waves are equal. It was also calculated in this model that it is not necessarily the case that the largest values of h_s are obtained when the confocal parameters of the pump and resonant waves are equal. It is in fact possible to produce comparable and indeed in certain situation when $b_s > b_p$ a larger value of h_s when unequal pump and signal confocal parameters are used. This is a positive result as experimentally it is very difficult to achieve a situation in which the pump and signal beams will have equal confocal parameters.

This type of threshold analysis has been performed on the OPOs described in this work, with the results being shown in subsequent chapters. An important consequence of this model is that it can be seen that the threshold power varies inversely with crystal length, this therefore implies that longer crystals should provide lower thresholds, as more gain is accessible.

3.4 Essential crystal properties

When considering an nonlinear crystal as a possible candidate for use in an OPO it is not sufficient to consider only phase-matching conditions. There are several other crystal properties that must be considered, namely optical transparency and optical damage threshold.

3.4.1 Optical transparency

For an OPO to operate optimally in a particular wavelength range it is desirable if as little absorption as possible is present in the crystal, i.e. it is necessary for the nonlinear crystal to have a high degree of transparency at the pump, signal and idler wavelengths. Absorption will lead to reduced system performance and crystal heating, which may result in damage to the crystal. The optical transparency of the nonlinear materials used in this work are as follows. LBO is transparent in the range 160 nm - 2.6 μm [7] and so can be seen to have cutoff frequencies in the near-infrared, KTA on the other hand has an optical transparency of 350 nm - 5.3 μm [8] and so has an extended transparency into the mid-infrared.

3.4.2 Optical damage threshold

It is important when making a choice of nonlinear material that it can withstand the very high intensities produced by pulsed or mode-locked lasers for a prolonged period, i.e. it is no good if a crystal meets all the requirements to make it a good candidate for OPO work if it cannot withstand the incidence of the focused pump pulses for prolonged period without damaging. The damage threshold of a nonlinear crystal is dependent on many factors, with the most important being the wavelength, pulse duration and pulse energy.

Optical damage is in general more of a problem in Q-switched nanosecond pulsed systems in which pulse energies are very high in comparison to the low average powers produced from the high repetition rate lasers used to synchronously pump the OPOs in this work. LBO is characterised by having one of the highest known optical damage thresholds of any nonlinear crystal of > 15 GW/cm^2 [9]. KTA has a very similar chemical structure to KTP and so can be assumed to have a damage threshold similar to the value of > 500 MW/cm^2 [9, 10, 11] reported for KTP. Previous experiments in cw mode-locked picosecond OPOs have reported thresholds of the order of ~100 MW/cm^2 [12],

and so optical damage is not thought to be a major consideration in the systems being constructed in this work.

3.5 The coupled-wave equations

In §3.2 it was stated that an OPO is capable of producing a tunable signal and idler wave from a pump wave. In the following section a discussion is presented on how this process occurs, what governs the generated values of signal and idler as well as the factors that influence the conversion efficiency of this process. A description is given of how to derive a general equation that describes any steady state three wave nonlinear process.

The starting point for any description relating to the interaction of electromagnetic waves and optical media is Maxwell's equations. The parametric process is a three wave interaction, involving the interaction of three travelling waves of different frequencies. For this interaction it is important to determine the response of the optical medium as the three constituents waves propagate through the medium. This response is described by the wave equation in a nonlinear medium. An excellent description of the derivation of the nonlinear wave equation is given by Boyd [13].

3.5.1 The nonlinear wave equation

When a high intensity electric field interacts with an optical material then it is no longer sufficient to describe the induced polarisation of that material in terms of the linear susceptibility as the response of that material may become nonlinear. The polarisation is instead expressed in the series given below,

$$P = \chi_{(1)}\varepsilon_0 E + \chi_{(2)}\varepsilon_0 E^2 + \chi_{(3)}\varepsilon_0 E^3 + \ldots \qquad (3.6)$$

where $\chi_{(1)}$ is the linear susceptibility and $\chi_{(2)}$ and $\chi_{(3)}$ are higher-order nonlinearities in the dielectric response of the material.

Different nonlinear phenomena are associated with different terms in equation 3.6. Pulse propagation effects resulting from $\chi_{(1)}$ and $\chi_{(3)}$ have already been discussed in Chapter 2. The most important factor in this chapter is the $\chi_{(2)}$ susceptibility term with nonlinear processes resulting from this term being referred to as second order effects. These include all three wave interactions such as second harmonic generation, sum/difference frequency mixing and optical parametric oscillation. Nonlinear effects relying on $\chi_{(2)}$ will only be

observed if the material is a non-centrosymmetric media, i.e. lacks inversion symmetry [13].

Maxwell's equations relate to the response of the internal electric field **E** of an optical medium when a driving polarisation **P** is presents. These equations are expressed as

$$\nabla \times E = -\frac{\partial B}{\partial t}, \qquad \text{and} \qquad \nabla \times H = \frac{\partial D}{\partial t} + J \tag{3.7}$$

These expressions are commonly used in conjunction with the following expressions,

$$D = \varepsilon_o E + P \qquad J = \sigma E \qquad B = \mu_o H \tag{3.8}$$

to formulate the standard wave equation,

$$\nabla^2 E - \mu_o \sigma \frac{\partial E}{\partial t} - \mu_o \varepsilon_o \frac{\partial^2 E}{\partial t^2} = \mu_o \frac{\partial^2 P}{\partial t^2} \tag{3.9}$$

3.5.2 Three wave nonlinear interactions

In this section the coupled wave equations are derived for a three wave interaction. If it is assumed that the electric fields are constrained to propagation in one dimension, under these conditions the fields are described by the complex expressions,

$$\mathbf{E}(z,t) = \frac{1}{2}[E(z,\omega)\exp j(\mathbf{k}\cdot\mathbf{z} - \omega t) + E^*(z,\omega)\exp j(\mathbf{k}\cdot\mathbf{z} + \omega t)] \tag{3.10a}$$

$$\mathbf{P}(z,t) = \frac{1}{2}[P(z,\omega)\exp j(\mathbf{k}\cdot\mathbf{z} - \omega t) + P^*(z,\omega)\exp j(\mathbf{k}\cdot\mathbf{z} + \omega t)] \tag{3.10b}$$

using the further assumption of the slow variation of the complex field envelope with distance, in which second order derivatives can be neglected, this leads to the form of the wave equation given below,

$$\frac{\partial \mathbf{E}}{\partial z} + \alpha \mathbf{E} + \frac{1}{c}\frac{\partial \mathbf{E}}{\partial t} = \frac{i\mu_o c\omega}{2n}\mathbf{P} \tag{3.11}$$

where $\alpha = \mu_o \sigma c/2$ is the electric field loss coefficient.

When considering the nonlinear polarisations of three interacting waves, related by $\omega_1 + \omega_2 = \omega_3$, (as is the case for optical parametric oscillation) it can

be shown (using equations 3.10) that the polarisation relating to each frequency component is dependent on the electric field component of the other two frequency components, as shown below:

$$\begin{aligned} P(\omega_1) &= 2\, d_{eff}\, \varepsilon_o\, E(\omega_3)\, E^*(\omega_2) \\ P(\omega_2) &= 2\, d_{eff}\, \varepsilon_o\, E(\omega_3)\, E^*(\omega_1) \\ P(\omega_3) &= 2\, d_{eff}\, \varepsilon_o\, E(\omega_1)\, E(\omega_2) \end{aligned} \tag{3.12}$$

A general equation can then be derived that describes any steady-state three-wave nonlinear interaction by substituting the polarisation expressions into Equation (3.11). The resulting expressions which have been derived by various authors [14-16] are shown below:

$$\frac{dE_1}{dz} + \alpha_1 E_1 = j\kappa_1 E_3 E_2^* e^{j\Delta k \cdot z} \tag{3.13a}$$

$$\frac{dE_2}{dz} + \alpha_2 E_2 = j\kappa_2 E_3 E_1^* e^{j\Delta k \cdot z} \tag{3.13b}$$

$$\frac{dE_3}{dz} + \alpha_3 E_3 = j\kappa_3 E_1 E_2 e^{-j\Delta k \cdot z} \tag{3.13c}$$

where E_1 denotes $E(\omega_1)$ etc and with,

$$\kappa_i = \frac{\omega_i d_{eff} \varepsilon_o}{n_i c}\,, \qquad \alpha_i = \mu_o\, \sigma_i\, c/2\,,$$

$$\omega_3 = \omega_1 + \omega_2\,, \qquad k_3 = k_1 + k_2 + \Delta k\,. \tag{3.14}$$

The coupled wave equations given in equations 3.13 can be used to analyse any second order nonlinear effect. There are two important features of these equations; the first is that they describe the energy transfer between particular frequency components as each wave travels through the crystal. For the case of an OPO they demonstrate that as the pump beam moves through the crystal it will convert to signal and idler radiation until a point that all the energy resides in the signal and idler wavelength components. Progression past this point will result in the commencement of conversion back to the pump wavelength. An important feature of equation (3.13) is that it shows that the conversion efficiency of the three wave processes is governed by the quantity Δk. Maximum conversion will occur when $\Delta k = 0$, with any variation away from this

condition resulting in conversion efficiency being reduced by a factor of sinc ($\Delta kl/2$) where l is the length of the nonlinear medium. The factor Δk represents to what degree the system being considered is phase-matched (see §3.7).

3.6 The effective nonlinear coefficient

When considering a material as a candidate for an OPO it is necessary to ensure that sufficient conversion from the pump to the signal and idler waves will take place. The effective nonlinear coefficient, d_{eff}, which is usually expressed in units of pm/V, is a measure of the degree of coupling between the three fields that a wave of a given polarisation and propagation direction will experience on travelling through a material in the presence of two other intense fields and so governs the degree of energy transfer between the three interacting fields.

When a field is applied to an optical medium the polarisation response in a particular direction will be determined by field components in several directions. The relationship describing this process is given below, see [13]

$$P_i(t) = \sum_{ijk} 2d_{ijk}^{(2)} \varepsilon_o E_j(t) E_k(t) \qquad (3.15)$$

where $d_{ijk}^{(2)}$ is the nonlinear susceptibility tensor.

It is possible to combine the indices j and k into just one, namely l, because the order of multiplication of the independent fields E_j and E_k has no bearing on the value, this results in d_{ijk} being reduced to a 3 x 6 matrix, d_{il} . These indices are generally number from 1 to 6, with the jk reduction to l leading to the simplifications , $11 \rightarrow 1$, $22 \rightarrow 2$, $33 \rightarrow 3$, $23 = 32 \rightarrow 4$, $13 = 31 \rightarrow 5$, and $12 = 21 \rightarrow 6$. The number of independent components of tensor d_{il} can be further reduced to only ten components by applying a procedure known as Kleinman's conjecture which exploits symmetries which exist in most materials away from absorption regions [13, 17],

These simplifications leads to the effective nonlinear coefficient being defined by,

$$P_i = d_{eff} E_j E_k \qquad (3.16)$$

For a material to be a viable choice for an OPO this must be as large a possible. Several description of how to calculate this quantity from first principles have been performed [13, 18].

The effective nonlinear coefficient for the materials used in work, namely LBO and KTA are discussed later in Chapters 4 and 7.

The means of classifying the geometry and nonlinear properties of an optical material has led to confusion in the past due to the use of various reference frames to describe different properties. The four different crystallographic axes used are the piezoelectric axes (XYZ), which define the nonlinear susceptibility tensor, the crystallographic axes (abc), which describe the unit cell, the optical axes (xyz) to describe wave directions inside the crystal and the polar axes (123) where 3 is the spherical-polar axis ($\theta = 0$) and 1 is the azimuthal axis ($\phi = 0$). The (123) frame is equivalent to xyz with 1=x, 2=y and 3=z , for a positive biaxial crystals and 1=y, 2=z and 3=x for negative biaxial crystals. Several authors have produced work on solving this confusion by standardising these axes sets [18, 19].

In the following section the factors effecting the phase-matching characteristics of a particular crystal or orientation are discussed.

3.7 Phase-matching considerations in nonlinear media

As discussed in §3.2 the essential feature of an optical parametric oscillator is its ability to produce extensively tunable signal and idler outputs. This tuning can be achieved by a number of methods, most commonly angle, temperature or pump-tuning. All the methods however rely on changing the refractive indices of the material in the direction of propagation. As discussed previously the parametric process will be most efficient when the phase-mismatch, $\Delta k = 0$.

To achieve a three wave nonlinear process, such as parametric oscillation, it is necessary to satisfy simultaneously the energy conservation equation given by

$$\omega_3 = \omega_1 + \omega_2 \tag{3.17}$$

and the phase-matching condition given by

$$k_3 = k_1 + k_2 + \Delta k. \tag{3.18}$$

Using the fact that $k = \left(\frac{\omega}{c}\right) n$ and assuming $\Delta k = 0$ allows this expression to be expressed in the form

$$n_3\omega_3 = n_1\omega_1 + n_2\omega_2 \tag{3.19}$$

The refractive index is a frequency dependent quantity, this effect is known as dispersion and results in the fact that in general, three waves of different frequencies will propagate in a medium at different phase velocities given by c/n. This would result in a low conversion efficiency occurring for the parametric process being considered. It is possible to compensate for this effect by using the phenomenon known as birefringence which is present in most nonlinear crystals. Birefringence describes the effect that the refractive index in such materials is dependant on the direction of propagation and polarisation through the medium.

It is therefore possible to choose the angle of propagation and polarisation of the three waves such that the birefringence will allow them to travel in phase with each other. Efficient generation and phase-matching can be produced simultaneously because of the situation that in many materials it is possible to couple energy from a wave of one polarisation to a wave of the orthogonal polarisation because of the presence of nonlinear susceptibilities.

When designing an OPO system with specific tuning demands, a phase-matching direction in the chosen crystal must be determined that will satisfy the system requirements. In such a situation it is necessary to be able to calculate the refractive indices associated with a given direction in the crystal.

The materials used in this work are biaxial, i.e. they have three independent refractive indices, with one associated with each of the x, y and z directions. The refractive index encountered by a wave polarised along the arbitrary direction (θ, ϕ), (see Figure 3.3) can be described mathematically by the transcendental equation [20], which is represented in equation (3.20), where i represents the wavelengths 1, 2 or 3.

$$\frac{\sin^2\theta\cos^2\phi}{n_i^{-2}-n_{1_i}^{-2}}+\frac{\sin^2\theta\sin^2\phi}{n_i^{-2}-n_{2_i}^{-2}}+\frac{\cos^2\theta}{n_i^{-2}-n_{3_i}^{-2}}=0 \qquad (3.20)$$

This equation is used in conjunction with equations (3.17) and (3.19) to determine what wavelengths will be phase-matched from a particular combination of pump wavelength and crystal orientation.

The relative polarisations of the three waves in this form of interaction, i.e. $\omega_3 = \omega_1 + \omega_2$ have two distinct forms. When the polarisations of ω_1 and ω_2 are parallel then this is referred to as Type I phase-matching. The case where the

polarisations of ω_1 and ω_2 are orthogonal is referred to as Type II phase-matching.

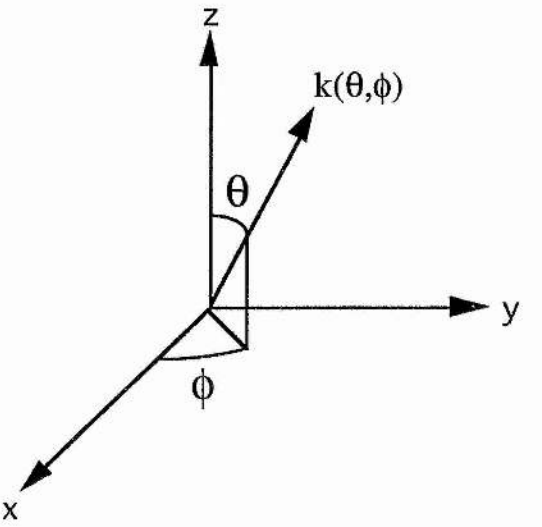

Figure 3.3
Propagation in a biaxial crystal.

3.7.1 Poynting Vector Walkoff in Birefringent Crystals

A further important quantity relating to the conversion efficiency of a nonlinear process in a birefringent medium is the Poynting-vector walkoff. The directions of the electric displacement vector D and the electric field vector E are, in general, not in the same direction in anisotropic media. It follows that the wavevector direction, k, and the energy propagation direction, given by the Poynting vector S=ExH, are also not in the same direction since k is perpendicular to both B and D, see Figure 3.4. The angle between k and S is known as the walkoff angle, this also represents the angle between the electric field vector E and the displacement vector D. In a biaxial crystal, a ray propagating in any direction other than along an optical axis will "walkoff" from the wavevector direction. This effect limits the efficiency of any energy conversion processes by reducing the spatial overlap between the interacting waves [21].

This property is very important in picosecond optical parametric oscillators, as the low peak powers involved in these systems results in the requirement to use longer crystal, this can therefore result in a large 'walkoff' problem. This problem is solved by using a non-critical crystal geometry in which all rays propagate along an optical axis, this phase-matching geometry is used exclusively in this work.

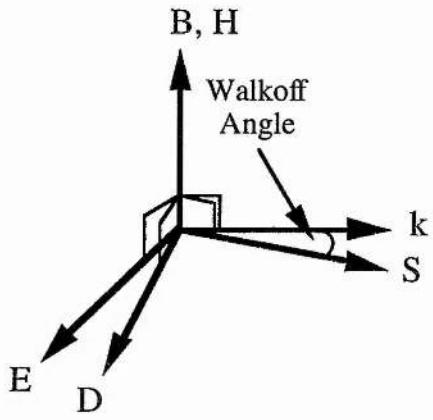

Figure 3.4
The relationship between k and S with respect to E and D, with the walkoff angle indicated.

3.7.2 Temperature-tuning

As discussed above when operating in the picosecond time regime it is necessary to use non-critical phase-matching (NCPM) to avoid walkoff problems. This situation therefore precludes the use of angle-tuning and so another means of tuning must be used. The refractive indices of the material KTA are insensitive to temperature and so the only option available in this situation is to use a pump source that is tunable. The situation for LBO is quite different as the birefringence of this material is strongly temperature dependent. This means that by fixing the pump wavelength at a constant value and varying the temperature of the crystal it is possible to access a large wavelength region without having to resort to angle-tuning and so avoiding the associated walkoff problems.

3.8 The effect of momentum mismatch on parametric gain

If maximum conversion between constituent wavelengths in a nonlinear process is to be achieved then several criteria must be met. Three of these criteria have already been outlined, i.e. those of the need to achieve the ideal phase-matching condition of $\Delta k = 0$. The degree to which energy is coupled between the constituent frequencies depends on the nonlinear susceptibility d_{il} and the need to minimise the effect of walkoff.

A further important feature is the finite spectral and angular bandwidths of the interacting waves, this can result in a degree of imperfect phase-matching

occurring in any process. In the following section these features are described in more detail with respect to the degree to which they effect ideal energy transfer.

3.8.1 Spectral bandwidth and acceptance angles

The spectral bandwidth and acceptance angles are concerned with the degree to which ideal phase-matching can be deviated from, while still producing a defined conversion efficiency [22].

It can be seen from Figure 3.5 that the efficiency of a three wave interaction process depends on the directions and magnitudes of the constituent wavevectors. The phase-mismatch is given by equation (3.21) below,

$$\begin{aligned}\Delta k &= |\mathbf{k}_1 \pm \mathbf{k}_2 - \mathbf{k}_3| \\ &= k_1 \cos\varphi_3 \pm k_2 \cos(\varphi_2 - \varphi_3) - k_3\end{aligned} \tag{3.21}$$

The efficiency of a nonlinear process is dependent upon the mismatch occurring between the wavevectors of the interacting waves according to the power conversion factor $\sin c^2(\frac{\Delta kL}{2})$. These criteria are generally defined to be the degree away from ideal phase-matching that causes the conversion efficiency to drop to $\approx$ 50 % of the peak conversion efficiency that occurs when $\Delta k = 0$, this occurs when the maximum allowable wavevector mismatch has the following value

$$\Delta k = \pm\frac{0.886\pi}{L} \tag{3.22}$$

The spectral bandwidth and the acceptance angle are calculated by expanding the phase-mismatch condition in a power series centred around the exact phase-matching conditions, as shown below.

$$\Delta k = \Delta k_o + \frac{\partial \Delta k}{\partial \Delta X}\Delta X = \pm\frac{0.886\pi}{L} \tag{3.23}$$

There will therefore be a maximum allowable variation away from the ideal case denoted by ΔX, which can represent the internal angle or wavelength in these cases, that can be sustained while $|\Delta k| \leq \frac{0.886\pi}{L}$.

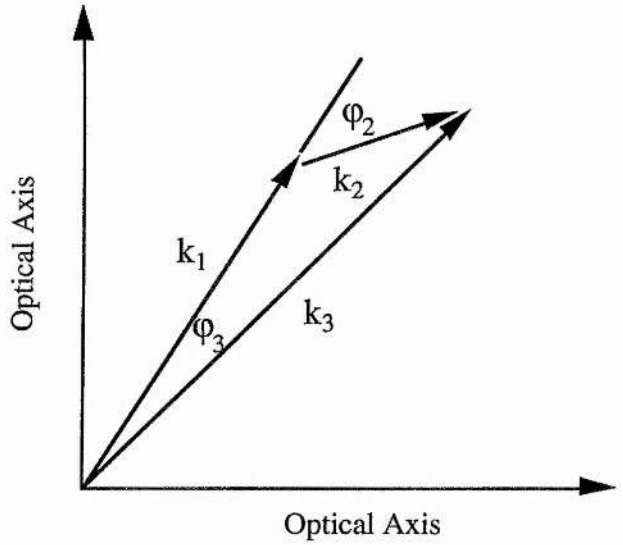

Figure 3.5
Wavevector diagram defining the relative angles between interacting waves.

In certain situations, such as the non-critical phase-matching geometry that is used exclusively in this work the first order term can be small, in such situations it is necessary to expand the power series to the second order term.

The most important consequence of this work is that phase-matching bandwidth has a reciprocal relationship with crystal length. This limits the length of crystal which can be used in the three wave interactions of ultrashort pulses, due to the large bandwidths that must be supported in such pulses to produce transform-limited behaviour.

The acceptance angle is defined as the angle which causes the magnitude of the wavevector mismatch for the parametric generation process to reduce to no less than $\frac{0.886\pi}{L}$. The calculation of crystal acceptance angles is performed in a similar manner to that of the spectral bandwidth, only in this case the parameter that is varied is the crystallographic angles. To define the acceptance angle correctly it is necessary to define two acceptance angles, namely ($\Delta\theta$ and $\Delta\phi$). A second order analysis of this property has again been performed in Reference [22]. As mentioned previously all the work carried out in this thesis used non-critical phase-matching in which all the waves interact collinearly along a principal optical axis. In this situation the first two terms in the power series expansion become zero and so only the quadratic term is relevant, this leads to a large increase in the angular acceptance angles ($\Delta\theta$ or $\Delta\phi$). The spectral and

angular acceptance have been calculated for all the materials used in this work, with the results being presented in subsequent chapters.

3.9 Pulse duration evaluation in synchronously-pumped OPOs

There are many crystal parameters that effect the ultimate temporal and spectral width that can be obtained from a picosecond parametric oscillator, namely, the group velocity walkaway amongst the pump, signal and idler pulses, the group velocity dispersion and the spectral bandwidth. It is important that these properties are investigated before any crystal is considered for use as these effects can increase the threshold and cause output pulse broadening.

3.9.1 Group velocity walkaway

One of the most important crystal properties in an ultrashort OPO is the group velocity walkaway between the pump, signal and idler pulses. This mechanism affects the temporal overlap of the three waves which results in gain reduction and pulse broadening in the OPO. It is therefore imperative that the group velocity walkaway for a particular nonlinear material or crystal orientation is calculated to check that this does not exceed greatly the duration of either signal or pump pulse, so as to maintain as high a conversion efficiency as possible. The group velocity walkaway has been calculated for the materials used in this work, with the results being given in subsequent chapters. The relevance of these results to the maximum useful crystal length is also discussed.

3.9.2 Group velocity dispersion

A further feature that will effect the duration of the resonant signal pulse in the OPO is the group velocity dispersion. This effect will cause an initially transform-limited pulse to broaden in pulse duration due to the fact that different wavelengths components of the pulse will propagate at different group velocities. As discussed in Chapter 2 it is possible to fully compensate for the effects of this dispersion by using an intracavity prism sequence.

3.9.3 Spectral bandwidth

Any nonlinear crystal has a limited phase-matching bandwidth, which if it isn't sufficient to accommodate the spectral component of a pulse will lead to pulse broadening and frequency chirping of the pulse. This can be a problem in femtosecond systems in which pulse bandwidths are of the order of tens of nms. In picosecond systems however, bandwidths are more typically of the order of <

1nm and so this effect is less of a problem. As such crystals of lengths of the order of tens of mms can be used in picosecond systems.

3.9.4 Predictions of pulse durations in ultrafast OPOs

The prediction of the pulse expected from a synchronously-pumped OPO is a complex process as many interacting processes occur simultaneously. There have however been several attempts to achieve this goal. Two notable pieces of work are by Becker et al [23] and Cheung and Liu [24]. The similarities and differences in the results produced from these models will now be discussed.

The analysis presented by Becker et al [23] is the less complete of the two as they consider only the degenerate case of type I phase-matching, which results in the signal and idler pulses being treated identically, which is obviously not the full story.

The analysis presented by Cheung and Liu [24] is more complete as in this procedure the general case of non-degenerate signal and idler wavelengths in a singly-resonant oscillator is solved. Both model are, however, not complete as several important features have been neglected for simplicity, namely the effects of self phase modulation were not taken into account.

Although the models have some differences, some common results were found to occur; in both cases the pump pulse duration was found to limit the width of the signal pulse obtainable. It was also found in both analyses that the signal pulse duration was ultimately determined by the degree of pump depletion taking place. It was found that the intensity dependent parametric gain caused the pump pulses to broaden because it depletes the centre of the pulse preferentially over the wings. This has the knock-on effect that the OPO is actually being pumped by a longer pump pulses, which results in a longer signal pulse being produced. It is therefore found that signal pulses become broader as operation further above threshold is obtained. It is of course not desirable to operate close to threshold as this can lead to device instability and so a compromise position must be achieved. The two models produced different results when an actual prediction of the shortest signal pulses available were made. In the degenerate case Becker et al predicted output pulses as short as 0.25 $\Delta\tau_p$, where $\Delta\tau_p$ represents the pump pulse duration, whereas in the more complete, non-degenerate analysis, Cheung and Liu predicted the signal pulse durations to be restricted to around 0.4 $\Delta\tau_p$. The results of these models are compared with the experimental results in subsequent chapters.

3.10 Conclusions

In this chapter all the relevant features required to design a picosecond optical parametric oscillator have been outlined, including the factors affecting the choice of nonlinear crystal and resonator design. In the subsequent chapters a complete characterisation of several OPOs systems is given, which will demonstrate that these types of devices are capable of producing high output powers across a wide spectral range from the visible to mid-infrared.

References

1. L. B. Kreuzer, Proc. Joint Conference on Laser and Electro-optics p 53 (1969)

2. S. J. Brosnan and R. L. Byer, IEEE J. Quant. Electron. **15**, 415 (1979)

3. G. D. Boyd and D. A. Kleinman, J. Appl. Phys. **39**, 3597 (1968)

4. J. E. Bjorkholm, IEEE J. Quant. Electron. **5**, 293 (1969)

5. J. E. Bjorkholm, IEEE J. Quant. Electron. **7**, 109 (1971)

6. S. Guha, F. Wu, and J. Falk, IEEE J. Quant. Electron. **18**, 907 (1982)

7. Private communication via Photox optical systems P.O. Box 274, No 2, Pullens Lane, Headington, Oxford, OX3 OBJ

8. G. M. Loiacono and R. A. Stolzenberger, Private communication via Crystal Associates, Inc., Waldwick, NJ 07463, U.S.A

9. G. J. Hall, M. Ebrahimzadeh, A. Robertson, G. P. A. Malcolm, and A. I. Ferguson, J. Opt. Soc. Am. B **10**, 2168 (1993)

10. L. J. Bromley, A. Guy, and D. C. Hanna, Opt. Commun. **70**, 350 (1989)

11. D. C. Edelstein, E. S. Wachman, and C. L. Tang, Appl. Phys. Lett. **54**, 1728 (1989)

12. A. Nebel, C. Fallnich, R. Beigang, and R. Wallenstein, J. Opt. Soc. Am. B **10**, 2195 (1993)

13. 'Nonlinear Optics'. Boyd. Academic Press Inc., Boston

14. 'Optical Electronics'. Amnon Yariv. CBS Publishing, New York. p236

15. J. A. Armstrong, N. Bloembergen, J. Ducing, and P. S. Pershan, Phys. Rev. 127, 1918 (1962)

16. R. G. Smith, J. Appl. Phys. 41, 4121 (1970)

17. D. A. Kleinman, Phys. Rev. **126**, 1977 (1962)

18. D. T. Reid, PhD thesis, University of St. Andrews (1994)

19. D. A. Roberts, IEEE J. Quant. Electron. **28**, 2057 (1992)

20. J. Yao, W. Sheng, and W. Shi, J. Opt. Soc. Am. B **9**, 891 (1992)

21. S. Singh in, Handbook of Laser Science and Technology (Ed., M. J. Weber) **3**, Part 1, Section 1.1 (1986)

22. N. P. Barnes and V. J. Corcoran, Appl. Opt. **15**, 696 (1976)

23. M. F. Becker, D. J. Kuizenga, D. W. Phillion, and A. E. Siegman, J. Appl. Phys. **45**, 3996 (1974)

24. E. C. Cheung and J. M. Liu, J. Opt. Soc. Am. B **7**, 1385 (1990)

Contents

4.1 Introduction

In the previous chapter the design criteria demanded for the operation of a synchronously-pumped picosecond optical parametric oscillator were discussed. These criteria are now used to construct a new source of tunable picosecond/sub-picosecond pulses for the near-infrared based on a singly-resonant OPO that uses LiB_3O_5 (LBO) as the nonlinear material. This device is synchronously-pumped by a continuous train of picosecond pulses from a self-mode-locked Ti:sapphire laser. A detailed discussion of the results is presented in this chapter. A discussion of the properties of the material LBO is also given so as to indicate the suitability of this material for picosecond parametric oscillation in the 1-3 μm wavelength region of the optical spectrum. A description of the experimental configuration of the OPO is given with a detailed characterisation of the results being presented. The described device is highly attractive as it is potentially tunable over a continuous wavelength range of 1-2.7 μm with a single LBO crystal, under temperature-tuned non-critical phase-matching. The combination of the Ti:sapphire pump laser and the LBO OPO represents a uniquely versatile source of picosecond/sub-picosecond pulses with extended tunability from 0.68 to 2.7 μm.

4.2 The nonlinear material LiB_3O_5

This section is concerned with the material and optical properties of LiB_3O_5 (LBO) including its crystal structure and mechanical qualities. An outline of the

phase matching properties and the effective nonlinear coefficient are given. The LBO crystals properties are used to indicate the most appropriate choice of crystal orientation for this particular OPO.

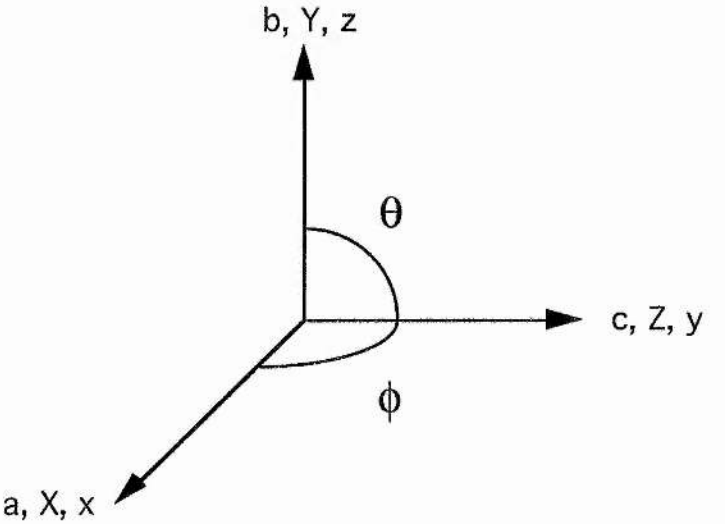

Figure 4.1
The three axis systems (a,b,c), (X,Y,Z) and (x,y,z) and the polar angles θ and ϕ. The angle θ is measured from the z-axis to the x-y plane and the angle ϕ is measured from x to y.

4.2.1 Structural and optical properties of LBO

The nonlinear material, lithium triborate (LBO), was first reported by Chen et al [1] in 1989. The nonlinear material LBO is an orthorhombic crystal. It is optically biaxial and belongs to the point group mm2. Following the crystallographic convention, the crystal diad is called the c axis and the other two axes, which are orthogonal, are called a and b, such that |a| < |b|. The piezoelectric axes X,Y, and Z coincide with the crystallographic axes a, b, and c such that X maps to a, Y to b, and Z to c. The axes of the index ellipsoid x, y, and z, which are defined such that the principle refractive indices are ordered $n_z > n_y > n_x$, map to the crystallographic axes as x to a, y to c and z to b. The orientation of the three co-ordinate sets (a,b,c), (X,Y,Z) and (x,y,z) in LBO are shown in Figure 4.1. The angles shown in the diagram, θ and ϕ, are measured with respect to the (x,y,z) axis set. The angle θ is measured from z to the x-y plane and ϕ is measured from x to y in the x-y plane. The nonlinear coefficients d_{ijk} are determined relative to the (X,Y,Z) axis set. To calculate the effective nonlinear coefficients at a propagation angle, (θ,ϕ), it is necessary to transform the (X,Y,Z) system. Thus the axes (X,Y,Z) map to (x,z,y), as shown in Figure 4.1. The transmission range of LBO extends over 160-2600 nm (see Figure 4.2)

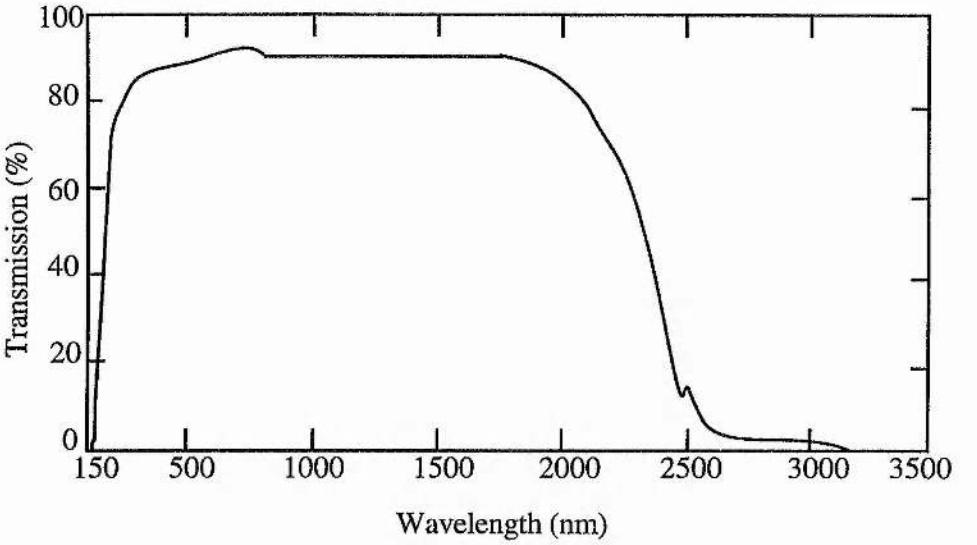

Figure 4.2
Complete LBO Transmission spectrum supplied by Reference [2].

making it ideal for many nonlinear processes such as frequency-doubling and parametric oscillation from ultraviolet through to the near-infrared portion of the optical spectrum. LBO also possesses a damage threshold of 25 GW cm^{-2} for 10 ns pulses which is the highest of all the commonly-known nonlinear crystals [1]. The following section discusses the optimal choice of crystal orientation to maximise the effective nonlinear coefficient in LBO.

4.2.2 Nonlinear Coefficient

LBO has three independent nonlinear coefficients, namely d_{31}, d_{32}, and d_{33}, of which d_{33} is small, ~0.2 pm/V, and may be ignored. Initial measurements for the other two coefficients given by Chen et al [1] were $d_{31(yxx)}$ = -1.1 pm/V and $d_{32(yzz)}$ = 1.46 pm/V at 1.064 μm. More recent measurements [3] obtained values of $d_{31(yxx)}$= 1.15 and $d_{32(yzz)}$ = 1.24 pm/V, again at 1.064 μm.

The maximum coupling is found to occur when one wave is polarised along y and the other two are polarised along z, i.e. propagation along the x-axis. In this case the expression for the d_{eff} is found via the expressions for the x-z and y-z planes.

In the x-z plane

$$d_{eff} = d_{yxx}\cos^2\theta + d_{yzz}\sin^2\theta \qquad (4.1)$$

where θ is the angle between the z-axis and the x-y plane, and in the y-z plane

$$d_{eff} = d_{yxx}\cos\theta \qquad (4.2)$$

For propagation along the x-axis when $\theta = 90°$ in the x-z plane, the nonlinear coefficient $d_{eff} = d_{yzz}$.

4.2.3 Phase-matching

For parametric generation, LBO can be phase-matched in a number of geometries under both type I and type II interaction, with non-vanishing nonlinear coefficients. However due to the nature of the OPO design in a picosecond synchronous system crystal orientations are restricted to non-critical phase-matching (NCPM) and so all further reference to LBO in this chapter will be to a NCPM geometry.

This can be accomplished along the crystal optic axes without the deleterious effects of spatial walkoff. Since LBO possesses smaller nonlinearities than, for example, KTP or BBO, the NCPM property can be exploited to yield comparable parametric gains with the use of longer interaction lengths. The NCPM geometry is also accompanied by large angular acceptance bandwidths so that tightly focused beams can be used without compromising conversion efficiency. These characteristics are particularly important in efficient parametric conversion of relatively low-energy, low-peak-power pump pulses with tightly-focused beams. This is the case with the high-repetition-rate pump pulses available from the picosecond Ti:sapphire laser used in these experiments, where pulse energies of typically 10-20 nJ with peak powers of around 10-20 kW are available in focused beam diameters of ~50 μm (FWHM). In the following section the reasons for the choice of OPO crystal are discussed with the most important crystal properties being modelled.

4.2.4 The OPO Crystal

The choice of LBO as the nonlinear gain medium was governed in the main part by its unique and highly versatile tuning characteristics and tailorable phase-matching properties. In contrast to materials such as, KTP or BBO, LBO is also temperature-tunable, which leads to one of the most attractive properties of LBO for parametric generation applications, which is its exceptionally broad tunability under type I temperature-tuned NCPM along the optical x-axis of the crystal. This unique feature allows efficient and wideband parametric conversion over extended and continuous spectral regions, without recourse to angle-tuning, which often results in a reduction in conversion efficiency and output power and requires adjustment of the OPO resonator. This was the cut of crystal chosen for our experiments for the reasons given above. All further work in this chapter on LBO will relate to this particular crystal cut.

4.2.5 Tuning characteristics

Since LBO was first reported [1], there have been a number of sets of Sellmeier equations published, each providing progressively improved fits to the measured OPO tuning ranges. Several sets of Sellmeier equations that have been reported to date, these are listed in [1, 3, 4, 5 and 6]. Several different reports of the temperature dependence of the LBO Sellmeier equations have also been made [6, 7, 8]. The Sellmeier equations derived by Lin [6] and temperature dependence of the refractive indices reported by Velsko [7] provide the best fit to the experimental results and so are used in theoretical calculations involving LBO.

The phase-matching temperatures for type I parametric generation in x-cut LBO, for a range of pump wavelengths, have been computed, by following the algorithm of Hall et al [9] (see Appendix 1). The calculations were performed by solving the momentum conservation equation for type I propagation along the crystal x-axis, with the pump polarised parallel to the y-axis and the generated waves polarised along the z-axis, that is

$$\frac{\lambda_s}{\lambda_i} - \frac{n_y(\lambda_p,T) - n_z(\lambda_s,T)}{n_z(\lambda_i,T) - n_y(\lambda_p,T)} = 0 \qquad (4.3)$$

where T is the phase-matching temperature. The temperature dependence of refractive indices n_y and n_z was determined by expressing $n_y(\lambda,T)$ and $n_z(\lambda,T)$ in the functional form,

$$n_y(\lambda,T) = n_y(\lambda) + \frac{\partial n_y}{\partial T}(T - T_0) \tag{4.4a}$$

$$n_z(\lambda,T) = n_z(\lambda) + \frac{\partial n_z}{\partial T}(T - T_0) \tag{4.4b}$$

where T_0 is the room temperature and λ is the wavelength in μm. The form of (4.4a) and (4.4b) allows computation of $n_y(\lambda,T)$ and $n_z(\lambda,T)$ from the room-temperature Sellmeier relations for the material [7] and the thermal dependence of refractive indices [7]. Substitution of these parameters into (4.4a) and (4.4b) yields

$$n_y(\lambda_p, T) = n_y(\lambda_p)_{T_0} + (-13.6)10^{-6}(T - T_0) \tag{4.5a}$$

$$n_z(\lambda_s, T) = n_z(\lambda_s)_{T_0} + (-6.3 + 2.1\lambda_s)10^{-6}(T - T_0) \tag{4.5b}$$

$$n_z(\lambda_i, T) = n_z(\lambda_i)_{T_0} + (-6.3 + 2.1\lambda_i)10^{-6}(T - T_0) \tag{4.5c}$$

For a given pump and signal wavelength combination, the energy conservation condition $1/\lambda_i = 1/\lambda_p - 1/\lambda_s$ determines all valid idler wavelengths. These can then be used in equations (4.5) and substituted in (4.4) to determine the phase-matching temperature T by an iterative method.

In Figure 4.3 (a), the calculated parametric tuning curves in type I LBO are depicted as a function of phase-matching temperature, for a range of pump wavelengths between 523.5 nm (frequency-doubled Nd:YLF laser) and 620 nm. It is seen that the phase-matching temperatures for wideband parametric generation steadily decline from above 200°C as the pump wavelengths increases from 523.5 nm. The rate of decline of the phase-matching temperature with pump wavelength in this region (around –2.5°C/nm) would imply that phase-matched interaction is not attainable at Ti:sapphire wavelengths or at best possible only at cryogenic temperatures. Interestingly, however, the decline in the phase-matching temperature is halted at around 550 nm, with the tuning curve remaining essentially stationary for pump wavelengths between ~550 nm and ~650 nm. This can be seen from the overlapping tuning curves in Figure 4.3 (a) corresponding to two pump wavelengths, 575 nm and 620 nm, in this region. Beyond ~650 nm, the decline in the phase-matching temperature undergoes a reversal so that a steady rise in the temperature is encountered with increasing wavelengths. This is shown in Figure 4.3 (b) where temperature phase-matching curves are plotted for a range of Ti:sapphire pump wavelengths between 700 and

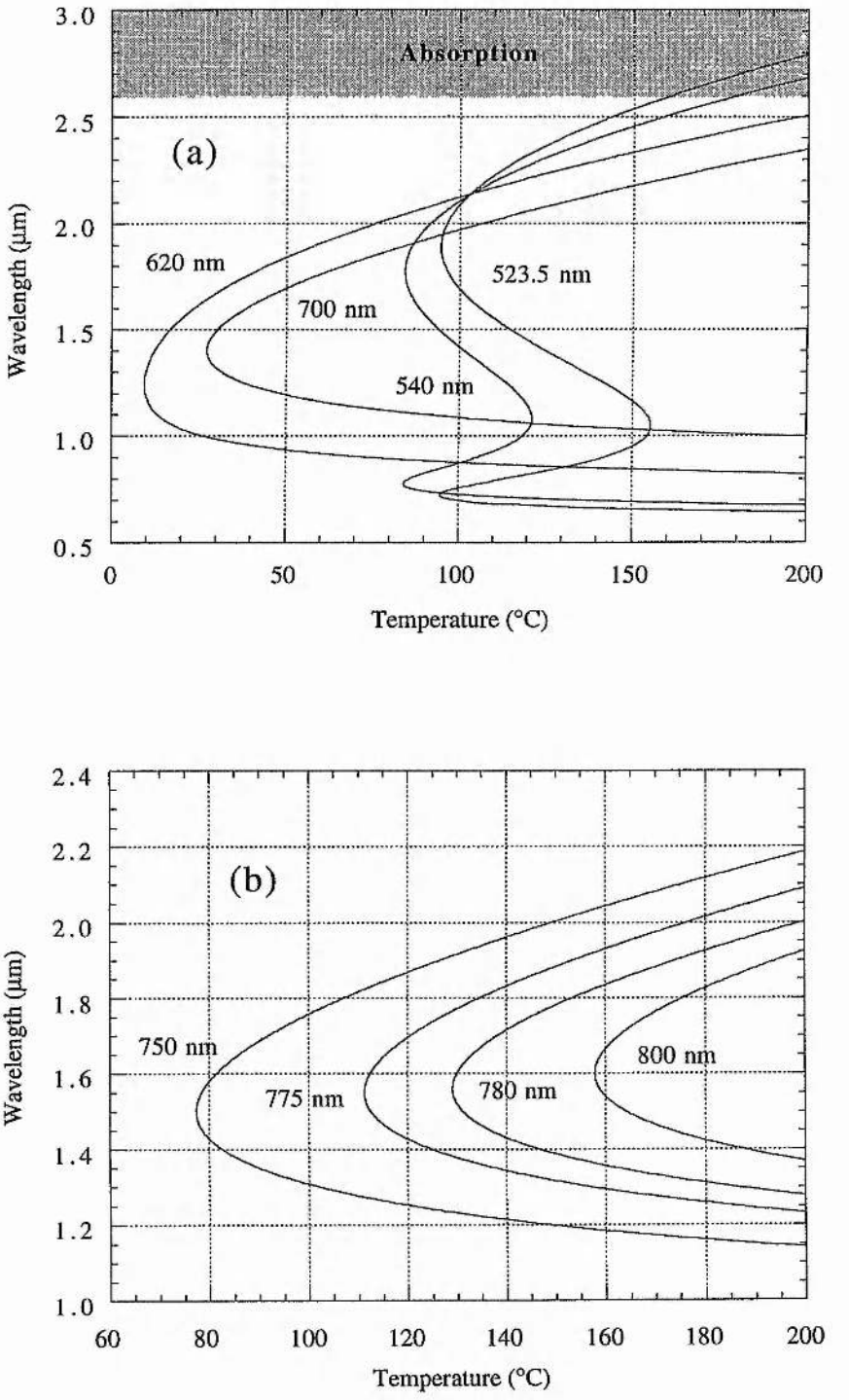

Figure 4.3

Calculated temperature-tuning range for parametric generation in type I non-critically phase-matched LBO (θ=90°, ϕ=0°) for (a) pump wavelengths between 523.5 nm and 620 nm and (b) between 750 nm and 800 nm.

800 nm. As can be seen from Figure 4.3 (b), Ti:sapphire-pumped parametric generation in type I LBO is possible at similar temperatures to those with frequency-doubled Nd:YAG or Nd:YLF pumping. This unique retracing behaviour in phase-matching is a consequence of the change in the birefringence of LBO at around 650 nm [6] and was first observed in second harmonic generation experiments by Lin et al [10]. The effect is also manifested in a different form by double-peaked parametric tuning curves where two distinct signal/idler pairs are simultaneously generated at a given phase-matching temperature (see Figure 4.3 (a)). This has been observed in parametric generation experiments in the crystal by a number of investigators. [6, 11, 12, 13]

4.3 Parametric generation conversion-efficiency properties

When considering parametric generation it cannot be assumed that the phase-mismatch condition Δk, is zero. This is due to the fact that laser pulses have finite bandwidths. It is therefore of interest to see the extent to which the pump beam can differ from the ideal case yet still provide gain at the signal and idler wavelengths.

The acceptance angle and spectral bandwidth are very important crystal features as these relate to the ultimate conversion efficiency that can be obtained from the pump to the signal and idler wavelengths. These two parameters limit the usable crystal length for a given pump beam divergence and linewidth. Exceeding these values leads to gain reduction or back conversion to the pump wavelength.

4.3.1 Acceptance angle

The variation away from the ideal phase-matching case of $\Delta k = 0$, due to finite laser linewidths and beam divergences, is important because it effects the amount of gain produced at the signal and idler wavelengths.

The acceptance angle was calculated for type 1 NCPM in LBO. For NCPM the acceptance angle must be defined more fully [14]. To calculate the angular acceptance the phase mismatch condition $\Delta k = k_p - k_s - k_i$ is expanded about $\phi = \phi_{pm}$ and $\theta = \theta_{pm}$, where ϕ_{pm} and θ_{pm} are the exact phase-matching angles in the x-y (ϕ) and x-z (θ) planes, respectively

$$\Delta k(\alpha) = \Delta k_{\alpha=\alpha_{pm}} + \frac{d\Delta k}{d\alpha}_{\alpha=\alpha_{pm}} \Delta\alpha + \frac{1}{2}\frac{d^2\Delta k}{d\alpha^2}_{\alpha=\alpha_{pm}} (\Delta\alpha)^2 \qquad (4.6)$$

Where $\alpha = \phi,\theta$ and $\alpha_{pm} = \phi_{pm},\theta_{pm}$.

For NCPM the first two terms in the expansion Δk and $\frac{d\Delta k}{d\alpha}$ are equal to zero, so that only the quadratic term is relevant. The acceptance angle is defined as the half angle in which the parametric gain is reduced by a factor of 2.

This is the case for the ($sinc^2$) function $\dfrac{\sin^2\left(\frac{\Delta kL}{2}\right)}{\left(\frac{\Delta kL}{2}\right)^2}$

when $$\Delta k = \frac{0.886\pi}{L} \tag{4.7}$$

Inclusion of the angular components of the refractive indices gives the values for $\Delta k(\phi,\theta)$. This expression is then differentiated with respect to ϕ and θ to give values for the required derivatives, these are then substituted into (4.6) to give Δk, this is then equated to equation (4.7). In the geometry being considered the appropriate angles are $\phi = 0$ and $\theta = \pi/2$, substituting these values leads to the following equations for Δk in the ϕ and θ planes.

$$\Delta k(\phi) = \left[\frac{\left(n_{x,\lambda p}\right)^3}{\lambda_p}\left[\frac{1}{n^2_{x,\lambda_p}} + \frac{1}{n^2_{y,\lambda_p}}\right]\right](\Delta\phi)^2 = a(\phi)(\Delta\phi)^2 \tag{4.8a}$$

$$\Delta k(\theta) = \left[\frac{\left(n_{z,\lambda_s}\right)^3}{\lambda_s}\left[\frac{1}{n^2_{z,\lambda_s}} + \frac{1}{n^2_{x,\lambda_s}}\right] + \frac{\left(n_{z,\lambda i}\right)^3}{\lambda_i}\left[\frac{1}{n^2_{z,\lambda_i}} + \frac{1}{n^2_{x,\lambda_i}}\right]\right](\Delta\theta)^2 \tag{4.8b}$$

$$= a(\theta)(\Delta\theta)^2$$

Equating (4.7) with (4.8) leads to the following solutions in the principal planes

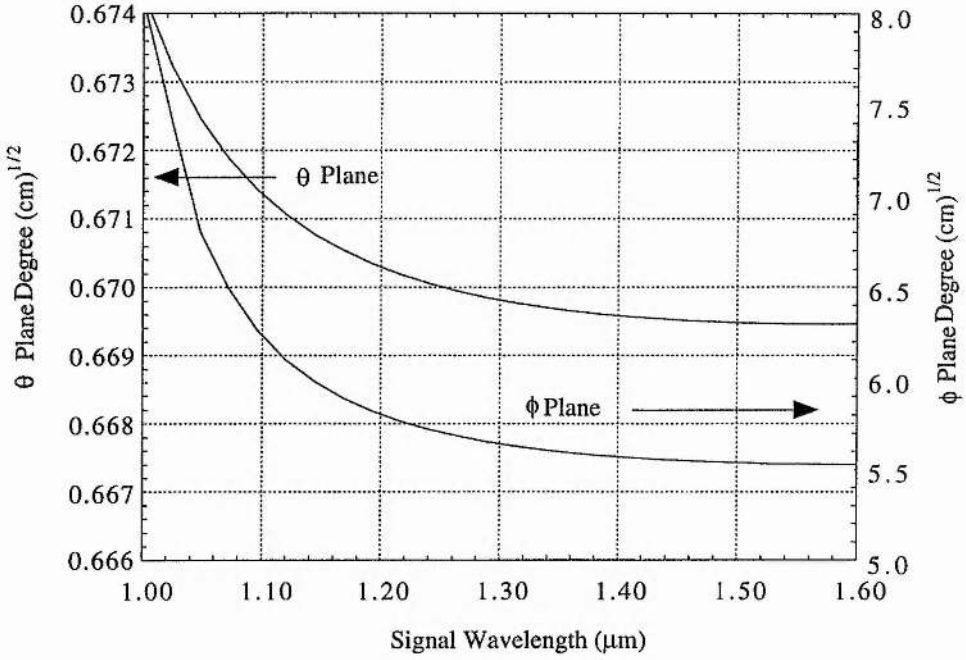

Figure 4.4
The calculated acceptance angles in the φ and θ direction in temperature-tuned LBO for non-critical propagation along the optical x-axis ($n_x<n_y<n_z$).

φ direction

$$\sqrt{L}\Delta\phi = \sqrt{\frac{0.886\times 2\pi}{a(\phi)}} \tag{4.9a}$$

θ direction.

$$\sqrt{L}\Delta\theta = \sqrt{\frac{0.886\times 2\pi}{a(\theta)}} \tag{4.9b}$$

These results are plotted above in Figure 4.4

The NCPM allows the use of tightly focused beams because of the large angular acceptance angle in this geometry compared with critical configurations.

In critical phase matching a similar method is used, only in this case the linear term $\frac{d\Delta k}{d\theta}$ of the phase matching expansion is non-zero, so the second derivative of Δk is neglected. For an alternative discussion of acceptance angle see [15].

4.3.2 Spectral acceptance bandwidth

The spectral acceptance bandwidth for phase-matching is also an important crystal parameter that needs to be considered. This quantity is particularly relevant in parametric generation of ultrashort pulses where large spectral widths are involved. The acceptance bandwidth can affect both the efficiency of parametric conversion and the signal and idler pulse durations. If the acceptance bandwidth is too small, the crystal can not accommodate the available spectral content of the pump and parametric pulses. This leads to gain-narrowing by lowering the gain available to the wings of the pulse so that the overall parametric gain is reduced, thus resulting in an increase in oscillation threshold. The spectral filtering of the parametric pulses can also limit the minimum attainable signal and idler pulse durations in an OPO if bandwidth generation due to self phase modulation (SPM) is not significant. The spectral acceptance bandwidth of LBO has been calculated by considering the phase-mismatch broadening relative to the pump spectrum (i.e. $\partial\Delta k / \partial\lambda_p$) and defining the bandwidth as $\Delta kL = 0.886\pi$. This leads to the following expression for the acceptance bandwidth, where L is the crystal length.

$$\Delta\lambda_p . L = \lambda_p^2 \left[\left(n_p - n_i \right) + \lambda_i \frac{dn_i}{d\lambda_i} - \lambda_p \frac{dn_p}{d\lambda_p} \right]^{-1} \tag{4.10}$$

Evaluation of this relation for type I NCPM in LBO yields the plot shown in Figure 4.5, where the variation in the pump acceptance bandwidth of LBO is shown as a function of signal wavelength. The bandwidth values are in the range 2-9 nm.cm across the available tuning range. The spectral bandwidth corresponding to a transform-limited 1 ps pulse at 800 nm is around 0.7 nm ($sech^2$ pulse shape assumed). Hence, for 1 ps pump pulses gain reduction due to spectral acceptance limitations in LBO is not significant even for crystals up to 50 mm or longer. On the other hand, with 100 fs pulses crystals as long as 10 mm may be used without serious degradation in efficiency.

4.4 Modelling of temporal effects

In the context of ultrashort-pulse parametric generation, there are a number of important temporal effects that also need to be taken into account when designing a OPO. These crystal properties are important in that a proposed crystal must satisfy all these requirement before it may be considered as a suitable OPO crystal. Lack of suitability in any of these areas may lead to an

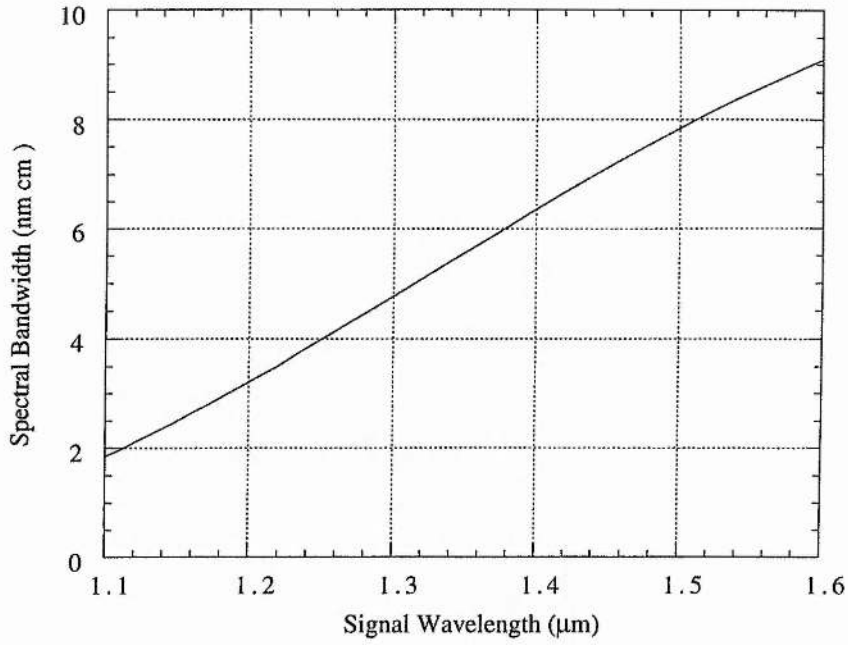

Figure 4.5
The calculated spectral acceptance bandwidth in temperature-tuned LBO (θ=90°, ϕ=0°). The pump wavelength is 800 nm.

OPO threshold that is above the available pump power. These important temporal features shall be discussed and modelled below.

4.4.1 Group velocity walkaway

A particularly important parameter is temporal walkaway between the pump, signal and idler which determines the degree of temporal overlap between the interacting pulses. Because of the absence of gain outside the temporal window of the pump pulse, a large temporal walkaway can result in significant reductions in parametric gain and can also lead to pulse broadening. This can limit the useful length of nonlinear crystal over which efficient interaction can occur. The effects of temporal walkaway can be estimated by evaluating the differences in the inverse group velocity between the pump, signal, and idler pulses, namely

$$\Delta v_g^{-1} = v_{g1}^{-1} - v_{g2}^{-1}. \tag{4.11}$$

where the group velocity is given by

$$v_g = \frac{c}{n - \lambda\left(\frac{\partial n}{\partial \lambda}\right)} \tag{4.12}$$

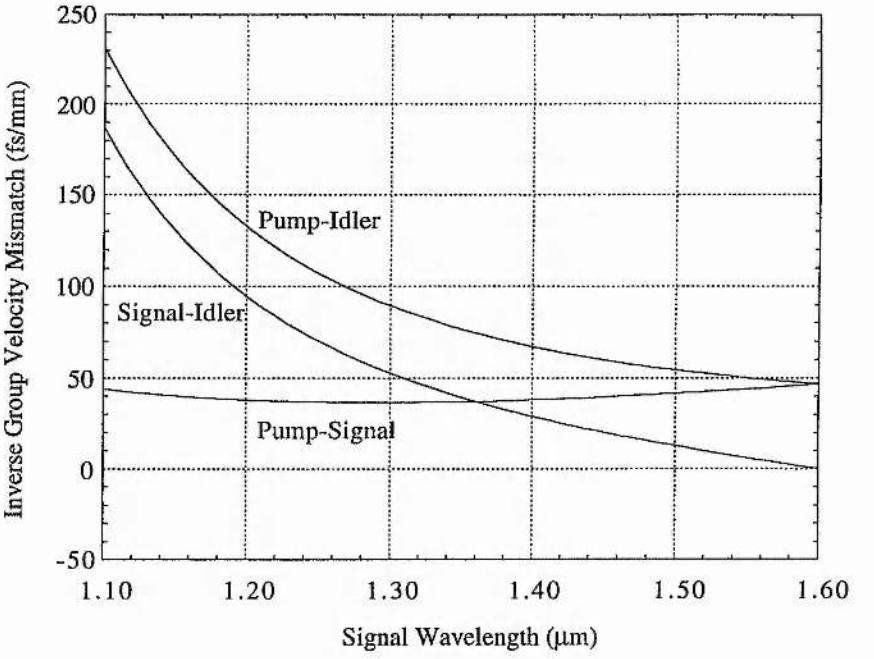

Figure 4.6

The variation in the inverse group velocity mismatch, Δv_g^{-1}, between the pump, signal and idler across the tuning range of temperature-tuned LBO (θ=90°, ϕ=0°). The pump wavelength is 800 nm.

The result of these calculations can be seen in Figure 4.6 where the magnitude of the inverse group velocity mismatch, Δv_g^{-1}, between the pump, signal, and idler in temperature-tuned LBO is plotted as a function of the signal wavelength. The pump wavelength is 800 nm. The calculations are based on the Sellmeier equations of Lin et al [6] and the temperature dependent refractive indices of Velsko et al [7]. It is seen that the temporal walkaway between the resonated signal and pump is limited to about 40-45 fs/mm across the tuning range with the corresponding signal/idler and pump/idler walkaway amounting to 0-180 fs/mm and 45-230 fs/mm, respectively. The walkaway between the pump and resonated signal has a first-order effect on OPO oscillation threshold and conversion efficiency [16] and is thus the most important parameter in determining the maximum useful interaction length.

4.4.2 Crystal length calculations

It is possible to calculate the maximum useful crystal lengths. To restrict the broadening in pulse length to less than 10%, the maximum temporal dispersion between the pump and the signal wave pulses as defined by [14] as,

$$\Delta\tau = L\left(v_p^{-1} - v_s^{-1}\right) \tag{4.13}$$

should be less than half the pump pulse width. Where v_p and v_s represent the pump and signal wave group velocities. This means that the maximum permissible crystal length is given by

$$L = \frac{\tau_p}{2\left(v_p^{-1} - v_s^{-1}\right)} \tag{4.14}$$

where τ_p is the pulse duration (FWHM). If a crystal longer than this is used then this will lead to a reduction in gain in the system as little or no interaction will take place between the pump, signal and idler pulses. This calculation was carried out for a 1 ps pulse, the results can be seen in Figure 4.7. The 40-45 fs/mm pump/signal walkaway implies that the maximum crystal length permissible that can be used without serious degradation in parametric gain or significant pulse broadening varies between ~22 and 27 mms across the tuning range of the OPO . With 100 fs pump pulses, interaction lengths of up to 3 mm are available. We may, therefore, conclude that temporal walkaway in LBO is not a limiting factor in the attainment of sufficiently high parametric gains with the use of long interaction lengths. A crystal length must be chosen that is satisfactory at all signal wavelengths, i.e. walkaway must be minimal across the entire tuning range of the device. However production techniques and cost also place a restriction on crystal length to be used. The maximum crystal length available at the time of this work was ~20 mm, the actual crystal used in the experiment shall be discussed in a later section.

4.4.3 Group velocity dispersion

In addition to group velocity walkaway, a second important temporal effect is group velocity dispersion (GVD). GVD leads to a linear chirp and an increase in pulse duration. For example, the pulse length τ of a Fourier transform-limited Gaussian pulse shape after propagation through a path length z inside a crystal is given by,

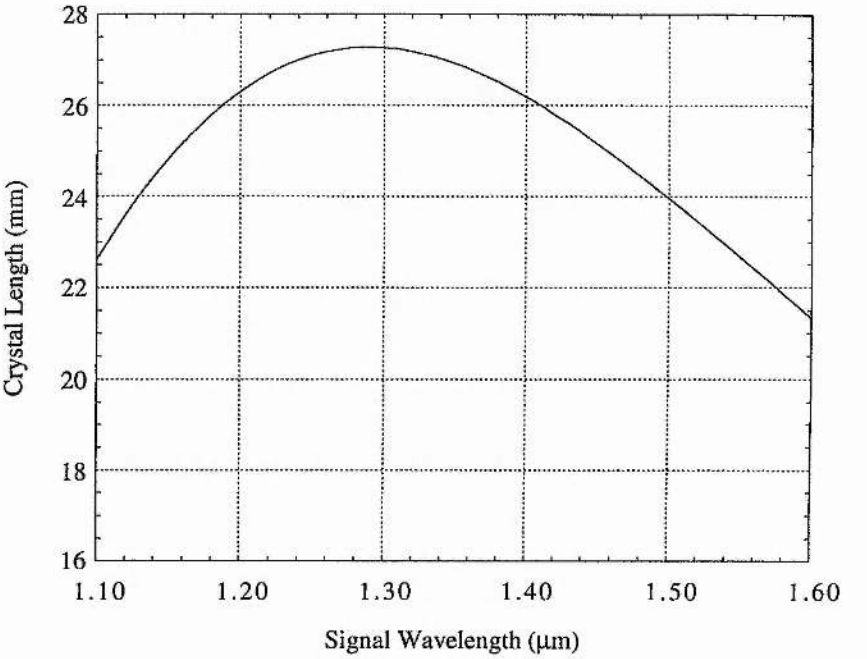

Figure 4.7
Variation in the maximum useful crystal length across the tuning range of temperature-tuned LBO (θ=90°, ϕ=0°). The pump wavelength is 800 nm. The pump pulse duration is 1 ps.

$$\tau^2(z) = \left(1 + \frac{z}{z_d}\right)^2 \tau_o^{\,2} \tag{4.15}$$

where

$$z_d = \frac{\tau_o^2}{4\ln(2)\beta''} \tag{4.16}$$

and

$$\beta'' = \frac{\partial^2 k}{\partial \omega^2} = \frac{\lambda^3}{2\pi c^2}\frac{\partial^2 n}{\partial \lambda^2} \tag{4.17}$$

where z_d is the dispersion distance. After the pulse has travelled a path length of z_d, the pulse length has increased by a factor of $\sqrt{2}$. The parameter τ_o denotes the pulse duration of the pulse before it enters the crystal, k is the wave vector, and c is the vacuum speed of light.

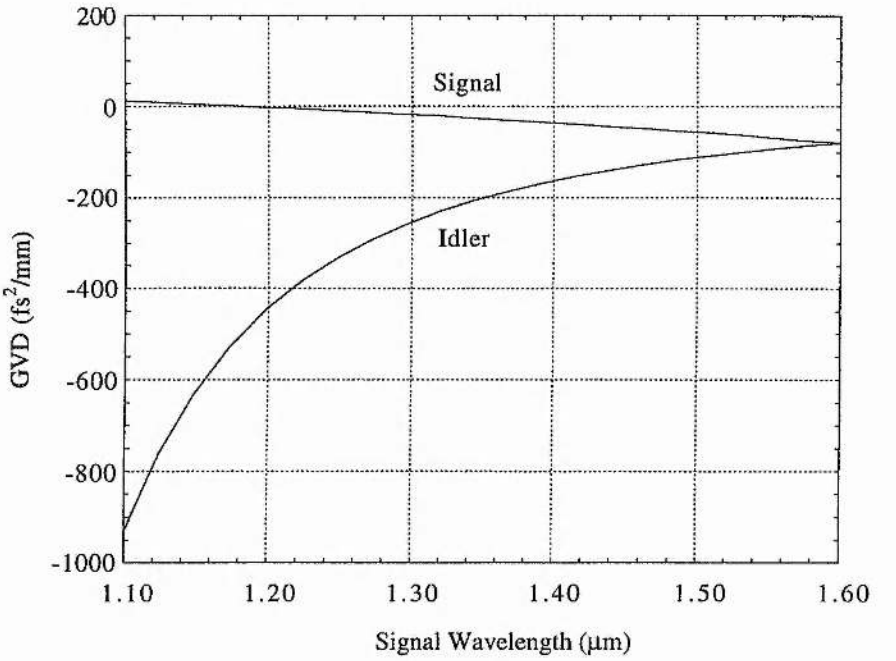

Figure 4.8
The variation in group velocity dispersion in temperature-tuned LBO (θ=90°, ϕ=0°). The pump wavelength is 800 nm.

In Figure 4.8, the variation in the signal and idler GVD in LBO is shown across the tuning range of the OPO. The pump wavelength is 800 nm. The GVD values were calculated by evaluating the dispersion parameter β''. It is seen from the plot that signal GVD in LBO remains small ($0 < \beta'' < 50$ fs²/mm) and close to zero across the entire available tuning range. It is also interesting to note that the transition from the positive to the negative GVD occurs at ~1.2 μm. This implies that for signal wavelengths beyond this value, transform-limited pulses may be attainable without the need for intracavity dispersion compensation. This characteristic makes LBO particularly attractive for use in ultrashort pulse OPOs. Therefore, as with spatial walkoff and temporal walkaway, dispersion broadening in type I temperature-tuned LBO is generally not a limiting factor in the attainment of transform-limited output pulses, particularly for signal wavelengths longer than ~1.2 μm. For signal wavelengths below this value, pulse broadening may result from the effects of positive GVD. Dispersion broadening generally becomes more significant with shorter pump pulse durations and longer interaction lengths.

Therefore it can be concluded that the above considerations indicate that despite its smaller nonlinearities compared to KTP, BBO, and some other nonlinear materials, LBO is a highly attractive crystal for parametric generation of ultrashort pulses. Its non-critical phase-matching, small temporal walkaway, low dispersion, and wide acceptance bandwidths allow the use of long interaction lengths with minimal degradation in OPO performance. Combined with its wideband tuning capability, these characteristics make LBO an excellent choice of material for use in picosecond and femtosecond OPOs. A summary of the crystal properties of LBO is given in Table 4.1 below. The properties of other commonly used OPOs crystals are shown for comparison purposes. The values quoted for KTP, KTA and RTA relate to the crystal geometry of type II NCPM along the x-axis with the pump and signal being polarised along the y-axis and the idler being polarised along the z-axis. This geometry was chosen for comparison purposes as it is commonly used in ultrashort pulse OPOs.

Nonlinear Material	Transmission	d_{eff} coefficient (pm/V)	Spectral Bandwidth (nm.cm)	Acceptance Angle $(cm)^{1/2}$(Deg)	GVW (fs/mm) (p-s)	GVD (signal) (fs^2/mm)	(Ref)
LBO	160 nm - 2.6 μm	1.24	5.0	0.670(θ) 6.5(ϕ)	40	- 40	[17]
KTP	350 nm - 4.5 μm	3.60	5.1	4(θ) 12(ϕ)	100	100	[14] [18]
KTA	350 nm - 5.2 μm	3.23	2.5	6(θ) 18(ϕ)	90	85 -	[17]
RTA	350 nm - 5.3 μm	4.10	4.2	5(θ) 14(ϕ)	130	75	[14]

Table 4.1

Comparison of the crystal properties of LBO with other popular OPO crystals.

The values quoted are for signal wavelengths of around 1.2 μm, so a that a fair comparison can be made with the LBO values. It can be observed that LBO has a smaller d_{eff} than all the other materials, however it can also be seen that LBO has a smaller GVW so longer crystals can be used to overcome this negative feature. LBO can be seen to have far more favourable GVD conditions, in that the GVD is small and negative. The values of spectral bandwidths and acceptance angles for all the materials are such that no reduction in efficiency would be expected. The following section describes the experimental configuration of the OPO.

4.5 Optical parametric oscillator

4.5.1 The picosecond LBO OPO

A schematic of the Ti:sapphire-pumped picosecond LBO OPO is shown in Figure 4.9. The OPO is configured in a standing-wave, folded cavity formed by two concave reflectors and a plane mirror through which the output signal is collected. The resonator fold angle is kept to <3° to minimise astigmatism in the

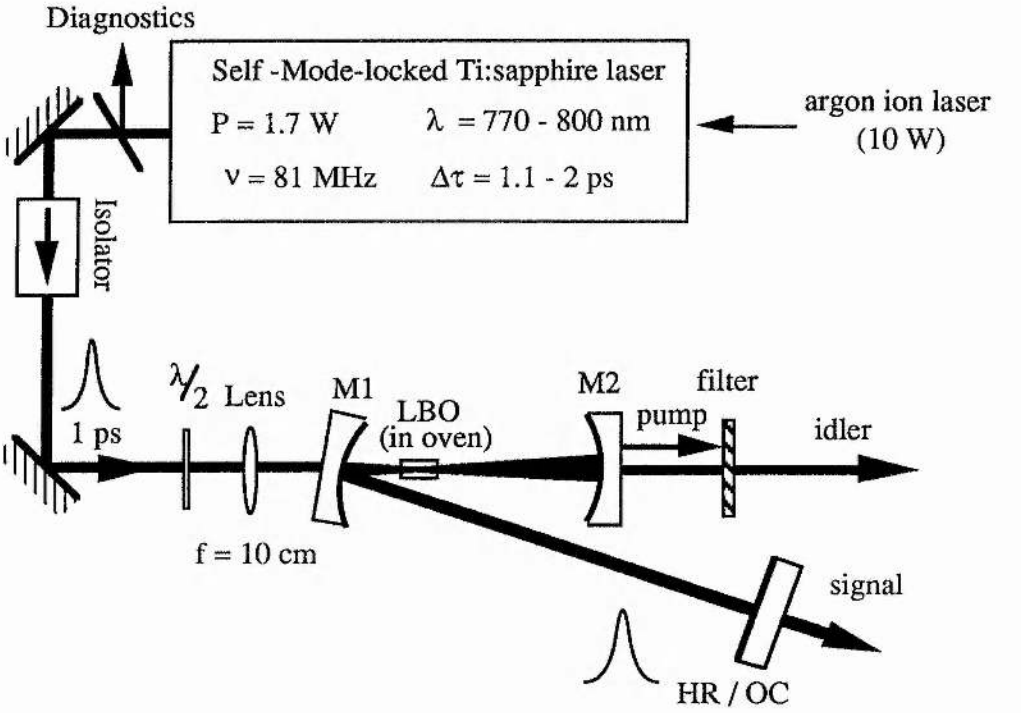

Figure 4.9
Schematic of the Ti:sapphire-pumped LBO OPO. The mirrors M_1 and M_2 have radii of curvature r=20 cm. λ/2 is a half-wave plate.

cavity. The oscillator is singly-resonant and the pump is single-pass. The short-wavelength portion of the tuning curve was resonated because of the smaller group velocity walkaway (GVW) between the pump and signal in this configuration (see Figure 4.6).

Resonating this wave also has the advantage of a larger tuning range for a given mirror set. The mirrors are all highly reflecting (R>99.7%) for signal wavelengths centred at 1.4 μm and have high transmission (T>95%) over the range 0.75-1.1 μm. The back surfaces of the mirrors are also antireflection-coated at the centre wavelength of 800 nm. The concave mirrors have a radius

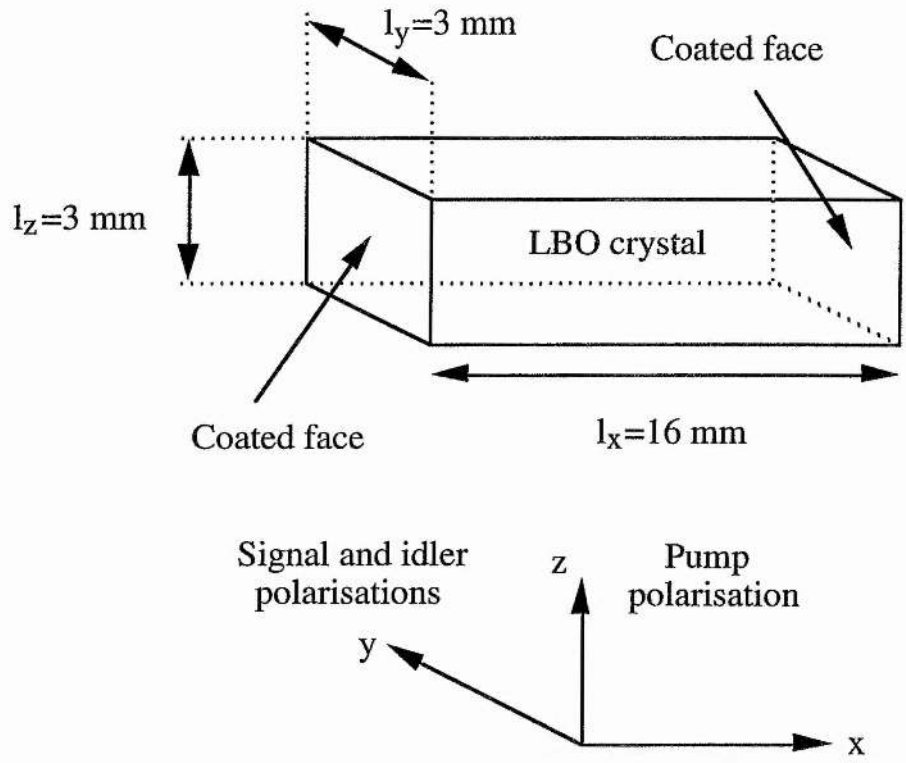

Figure 4.10

Schematic representation of the LBO crystal, cut for propagation along the x-axis, to satisfy type I non-critical phase-matching.

of curvature r=20 cm, resulting in a signal waist radius of 39 μm at the centre of the stability region. This arrangement represents a suitable compromise between the optimum signal focusing condition [13] and the resonator stability range. The LBO crystal was supplied by PHOTOX optical systems [2]. The crystal was 16 mm in length and 3 mm x 3 mm in aperture. It was cut for non-critical type I temperature phase-matching along the x-axis (θ=90°, ϕ=0°). The end faces of the crystal are antireflection-coated at 1.4 μm and the measured overall single-pass transmission loss of the crystal and coatings at 800 nm is ~2.5% (see Figure 4.10). The phase-matching temperature can be adjusted with an accuracy of better than ± 0.1°C by using an insulated oven and a precision temperature controller (Eurotherm Model no 818P/TC/RTRI). This temperature controller uses a thermocouple to monitor the crystal temperature and a feedback system to adjust the current sufficiently to heat or reduce the temperature of the crystal. The temperature controller is connected to a Mica band heater which performs the actual heating process, this was supplied by [19]. A schematic of the insulating oven can be seen in Figure 4.11. (a) represents the front view, (b)

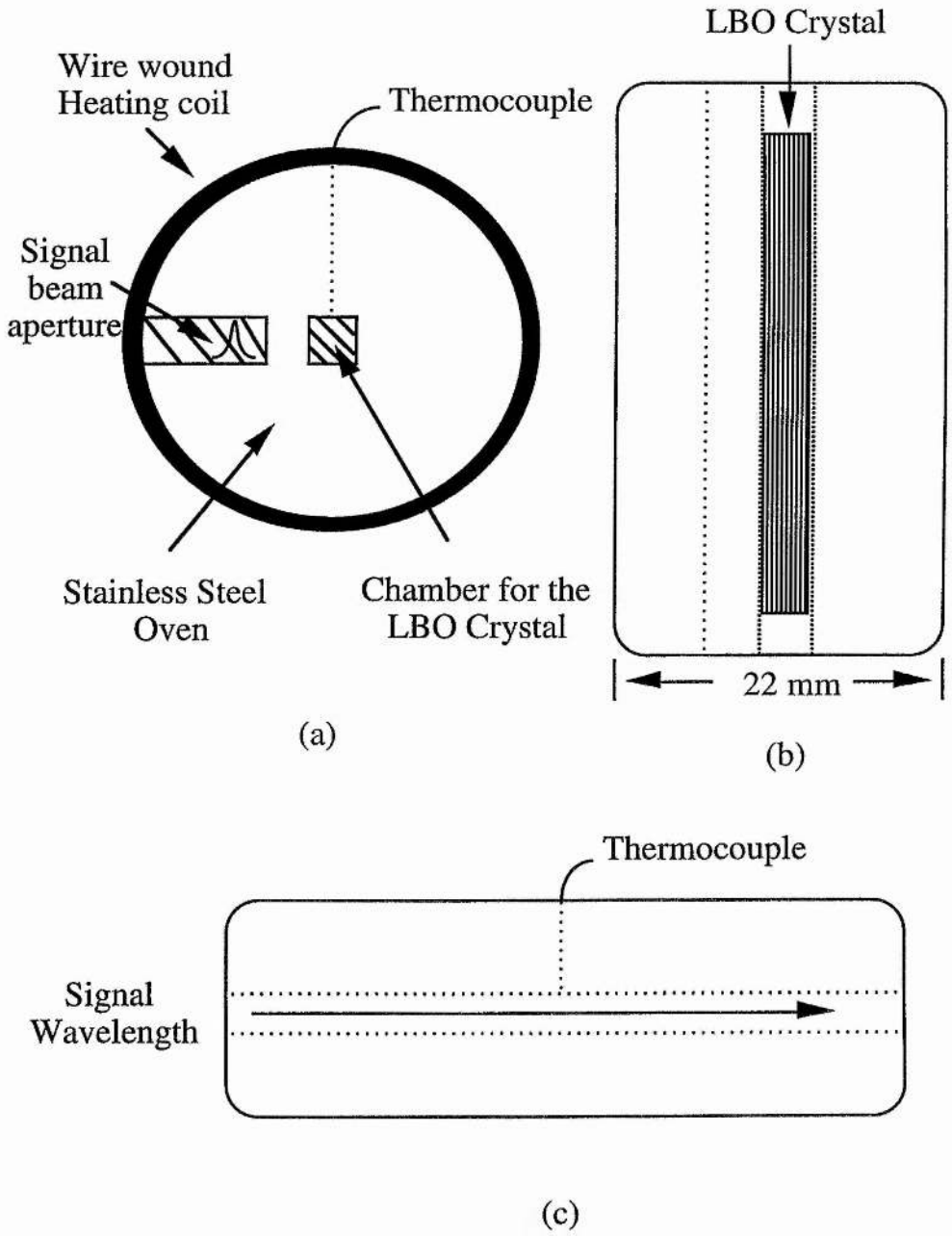

Figure 4.11
Schematic of the LBO OPO insulated Oven.

represents the top view and (c) represents the side view. The inner section is made from stainless steel, with a wire wound heating section encapsulating this, with the whole arrangement being surrounded with a section made from a material called Torlon. This material has a very low coefficient of thermal conductivity, i.e. it has very good heat insulating properties. The oven consists of a main chamber in which the crystal is placed as well as a secondary gap through which the resonant signal beam passes as it reflects from mirror M1 to

the plain mirror. This oven was found to produce a constant temperature across the entire length of the crystal, a temperature gradient would be very undesirable as this would lead to different parts of the crystal phase-matching at

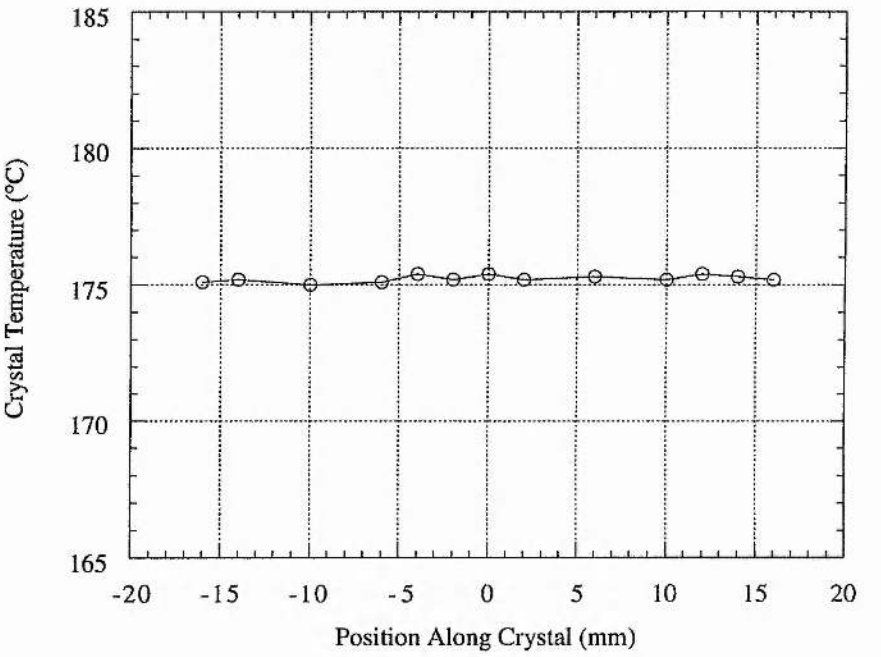

Figure 4.12
Representation of the temperature gradient along the LBO crystal.

different wavelengths. A representation of the temperature gradient across the crystal length is given in Figure 4.12 in which it can be seen that for an oven temperature of 175°C the temperature along the length of the crystal varies by less than 1°C and is therefore a minimal effect. These measurements were taken by placing the thermocouple at various positions along the length of the oven.

The pump laser is a commercial self-mode-locked Ti:sapphire laser (Spectra-Physics, Tsunami) which was configured for picosecond operation. It delivered a maximum average output of 1.7 W for 10 W of argon ion pump power. The duration of the pump pulses deduced from autocorrelation measurements was typically 1.1-2 ps (assuming $sech^2$ pulse profile) and the pulse repetition rate was 81 MHz. With the available mirror set, the laser could be tuned from 770 to 900 nm. For a more detailed description of the pump laser see Chapter 2. The pump beam was focused through the input concave mirror to a spot radius of ~25 μm inside the crystal, using a plano-convex lens of 10 cm focal length. Since the OPO was collinearly pumped, an optical isolator (Model No IO-5-NIR-HP),

which was supplied by OFR [20], was used between the two cavities to avoid back reflections into the Ti:sapphire laser. A half-wave plate was also used to yield a pump polarisation along the *y*-axis of the crystal. The total pump power reduction from the Ti:sapphire to the OPO was around 400 mW in this system and is accounted for by reflection losses due to transmission optics and power loss to diagnostics. Therefore, a maximum of 1.3 W was available for pumping the oscillator.

4.6 Results and discussion

The OPO cavity was aligned simply by monitoring the residual back reflections of the pump from the crystal end faces and the cavity mirrors. Oscillation occurs when the OPO is brought into synchronism with the pump through fine cavity length adjustments. Interestingly, the LBO crystal also generates a weak visible signal in the blue when the pump polarisation is along the crystal *z*-axis. This radiation which is generated as a result of non-phase-matched, single-pass second harmonic generation of the pump may also be used as an alternative pilot light for the alignment of the resonator.

4.6.1 Tuning characteristics

Wavelength measurements were performed by using a Rees Instruments laser wavelength monitor. In Figure 4.13 the measured tuning range of the LBO OPO is shown as a function of phase-matching temperature, for a range of Ti:sapphire pump wavelengths from 775 to 800 nm. The solid curves represent the calculated tuning range. With the available mirrors set, a total signal coverage from 1.374 to 1.530 μm and idler coverage from 1.676 to 1.828 μm was obtained over a temperature range of 117.1°-193.3°C. The range of phase-matching temperatures varies with the pump wavelength, and shifts to lower temperatures for shorter Ti:sapphire wavelengths. For this reason, the use of pump wavelengths above 800nm was avoided in order to prevent possible degradation to the crystal coatings, however, no signs of damage to the crystal or the coatings at temperatures as high as 230°C were observed. The discrepancy between the experimental and theoretical tuning range is accounted for, in part, by the uncertainties in the Sellmeier coefficients of LBO and, in part, by the variations in output wavelength caused by small excursions in the OPO resonator length in the absence of active stabilisation. Signal wavelength tuning over typically 20 nm was observed by adjusting the resonator length across the 30 μm synchronous range of the OPO, with longer cavity lengths resulting in a shift in the signal wavelength to shorter wavelengths. This was to be expected, given

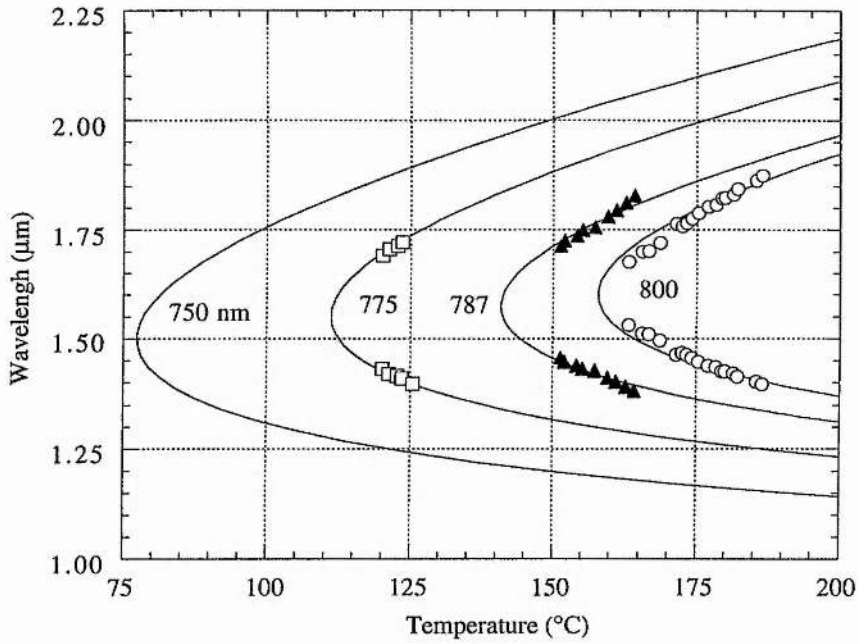

Figure 4.13
Temperature and pump wavelength tuning range of the LBO OPO with type I non-critical phase-matching along the x-axis (θ=90°, ϕ=0°). The output from the OPO is indicated by the experimental data and the solid curves represent the predicted tuning range. The calculations are based on the Sellmeier equations for LBO [6] and the temperature-dependent refractive index data for the material [7].

that the slower group velocities are associated with the longer wavelengths in the anomalous dispersion region. This cavity length tuning which has also been observed in other OPO's is a useful mechanism for fine-tuning the output wavelengths. The observed tuning range is at present limited by reflectivity of the available mirror set. With additional mirrors, continuous tuning over the range 1-2.7 µm will be readily attainable by tuning the pump wavelength down to about 700 nm. The use of shorter pump wavelengths also has the benefit of lower phase-matching temperatures for a given signal and idler wavelength range.

4.6.2 Sum frequency mixing

It is also interesting to note that in addition to the signal and idler beams, the picosecond LBO OPO also generates tunable output in the visible spectrum. This phenomenon which has also been observed in Ti:sapphire-pumped femtosecond OPO's based on KTP [21, 22], is a result of non-phase-matched sum frequency mixing between the resonated signal and the single-pass pump. Figure 4.14 shows the tuning range of this radiation for three pump wavelengths, namely 775, 787 and 800 nm. Since this radiation exits the OPO cavity in the

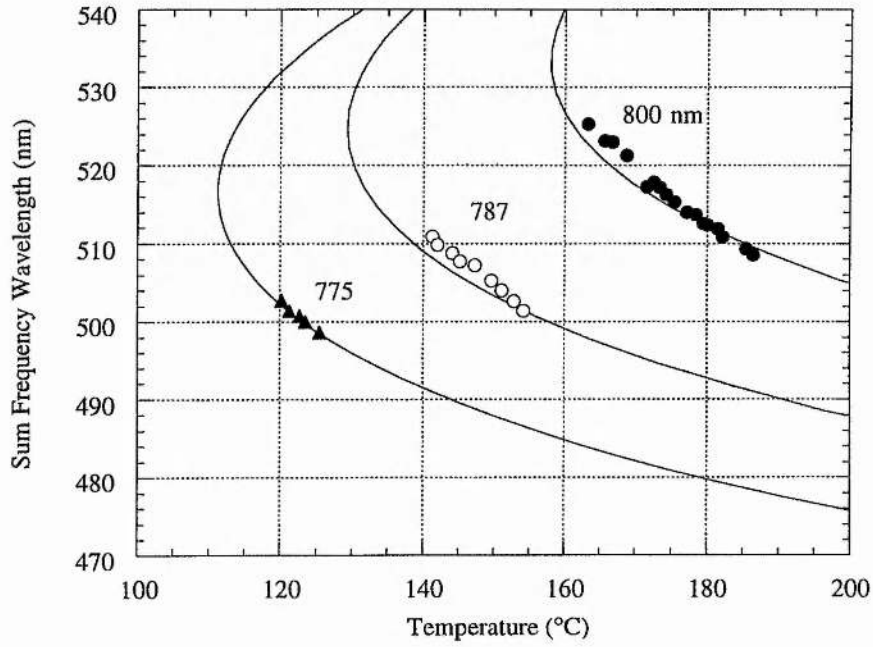

Figure 4.14
Sum frequency mixing between the signal and pump pulses in the Temperature and pump wavelength tuning range of the LBO OPO.

same direction as the pump and idler beams, it can be used as a visual aid for optimisation of the resonator. The polarisation direction of the sum frequency light is the same as the pump (parallel to y-axis) and perpendicular to that of the signal. Over a wavelength range of 498-528 nm in the green up to 2 mW of visible output was measured.

4.6.3 Threshold

The operation of the OPO close to threshold is generally undesirable as this can lead to system instability and can have a "knock on" effect on the stability of such properties as pulse durations and output power, and so therefore it is desirable to try and have a situation in that one is as far above threshold as possible. It was shown in Chapter 3 that it is possible to calculate the expected threshold, this information is then used in conjunction with the available pump laser power to try and maximise the degree to which the system operates above threshold. The average pump power threshold for the picosecond OPO is shown in Figure 4.15 and is found to be typically 900 mW at the input to the nonlinear crystal. This corresponds to a threshold pulse energy of ~ 11 nJ and a peak power density of ~ 290 MW/cm^2 inside the crystal. The threshold predicted from the model devised by Guha, Wu, and Falk [23], see Chapter 3, is also shown in Figure 4.15. It can be seen that a reasonable agreement between the

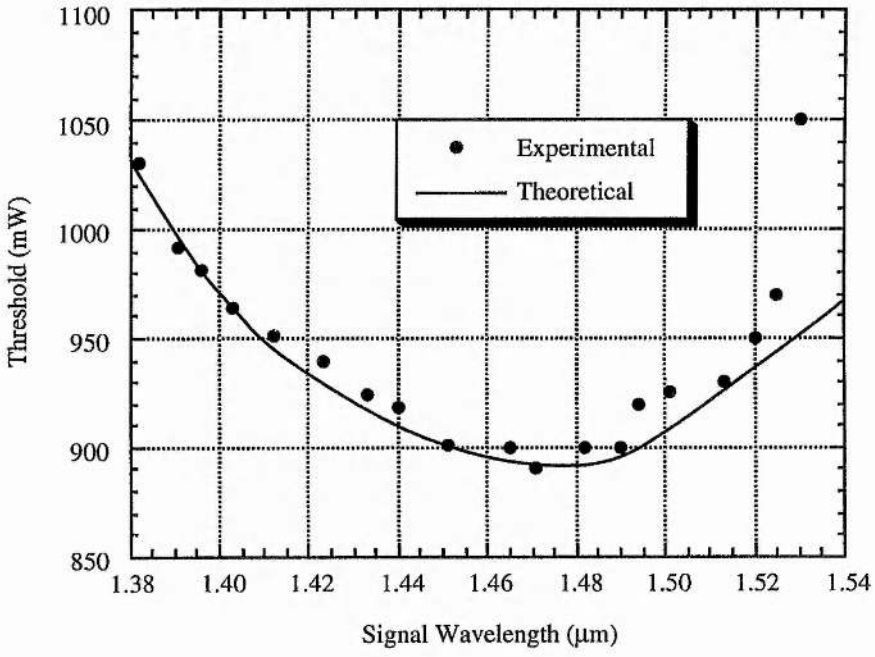

Figure 4.15
The variation in the average pump power threshold across the tuning range of LBO OPO.

theoretical and experimental results is obtained, discrepancies arise from uncertainties such as the exact reflectivities of the cavity mirrors and crystal AR coatings. The inclusion of the known uncertainties of the parameters used in this calculation lead to an estimation of the error in the results produced by the model

to be less than 5%. The threshold could be reduced by improvements in such features as mode-matching as well as the use of optimum mirror coatings.

4.6.4 Pump Depletion

It is important to know how much of the pump energy is converted into the signal and idler energies, this property is known as the pump depletion, i.e. it is the amount of pump energy depleted into the signal and idler energies. This therefore represents the efficiency of parametric conversion from pump to signal and idler. This measurement is performed by placing a power meter behind cavity mirror M2. Readings were taken when the OPO was oscillating and when it was not, this was achieved by simply blocking and unblocking the cavity. This resulted in the situation that when the cavity was blocked then all the pump power (incorporating cavity losses) was incident on the power meter, and when the cavity was oscillating then the difference in power was the power being converted into signal and idler energy. This allowed the pump depletion to be calculated. It is defined as,

$$\text{Pump} - \text{Depletion} = \frac{E_u - E_d}{E_u} \tag{4.18}$$

where E_u is the undepleted pump and E_d is the depleted pump. Since the pump beam travels along the same path in both cases, all the linear losses due to reflection, absorption and scattering in the crystal and mirrors may be ignored. The resulting pump depletions across the tuning range of the OPO are shown in Figure 4.16. It can be seen that the depletion varies between ~15 and 20 %, this data was recorded for a pump power of 1.2 W which is 1.3 times threshold. The variation in the depletion across the tuning range could be due to several factors such as crystal AR coating and mirror reflectivity variation, which will result in variations in the OPO threshold. The variation in pump depletion as a function of pump power above threshold was also measured, (see Figure 4.17), and can be seen to increase linearly with increasing pump power. This observation is consistent with previous reports [24]. The peak value of 20 % is achieved at 1.3 times threshold.

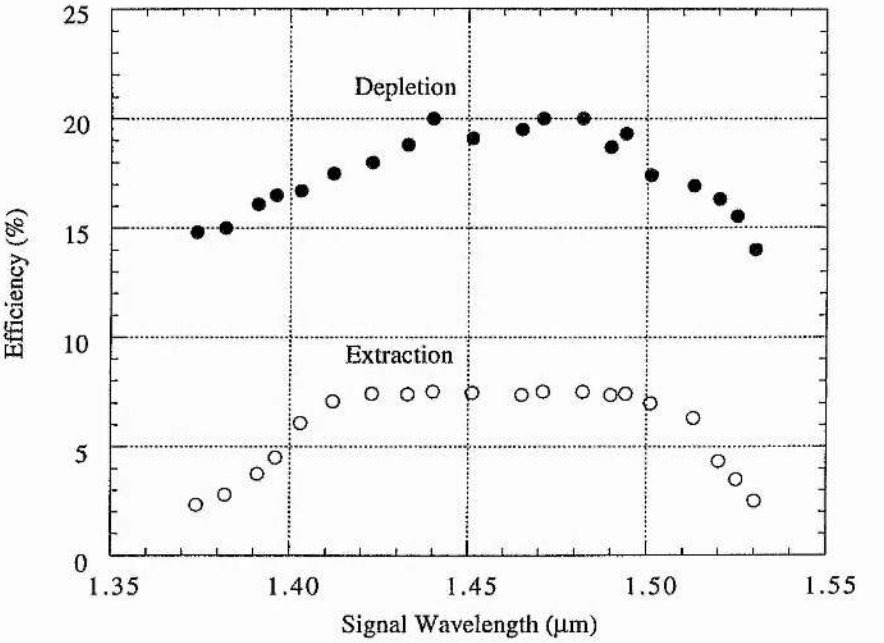

Figure 4.16
Depletion and extraction of the LBO OPO as a function of signal wavelength.

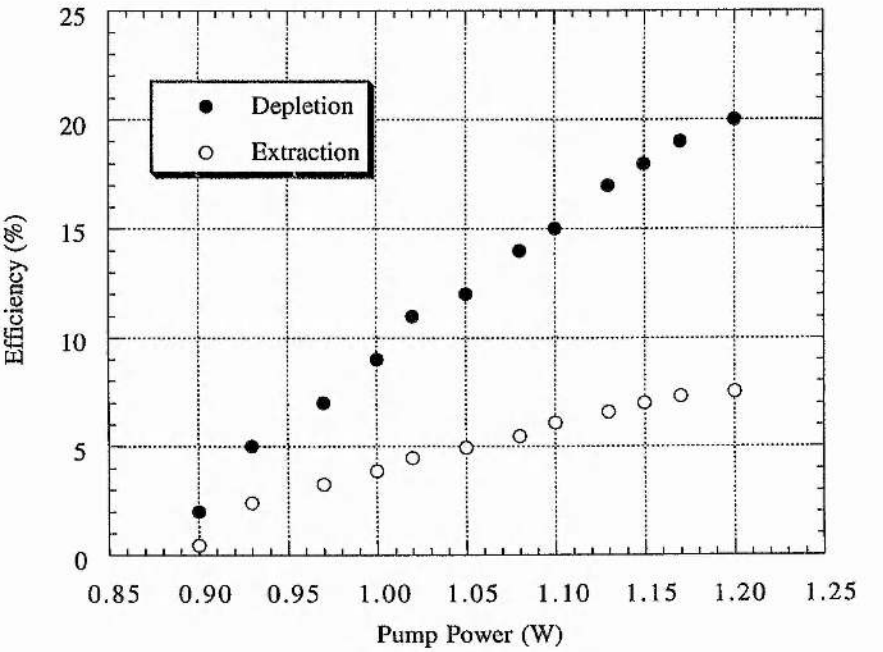

Figure 4.17
Depletion and extraction of the LBO OPO as a function of pumping intensity. The signal wavelength is 1.45 μm.

4.6.5 Output power and efficiency

With highly reflecting mirrors, up to 10 mW of output is available in the signal beam from each arm of the resonator, for 1.2 W of input pump power. In the absence of an optimised output coupler, a plane high reflector with its reflection band centred at 1.6 μm is used as the output coupling mirror. Over the signal wavelength range of 1.44-1.48 μm where the transmission of this mirror is 0.5-1.5%, 50 mW of signal power can routinely be extracted through the mirror. The single-pass power in the idler beam is typically 40 mW, representing a total combined output of 90 mW for 1.2 W of pump, (see Figure 4.18). This corresponds to an external efficiency of around 7.5% at 1.3 times threshold, (see Figure 4.16). At this level the pump depletion is 20% as in Figure 4.17, representing about 13% loss of generated parametric power. This loss is

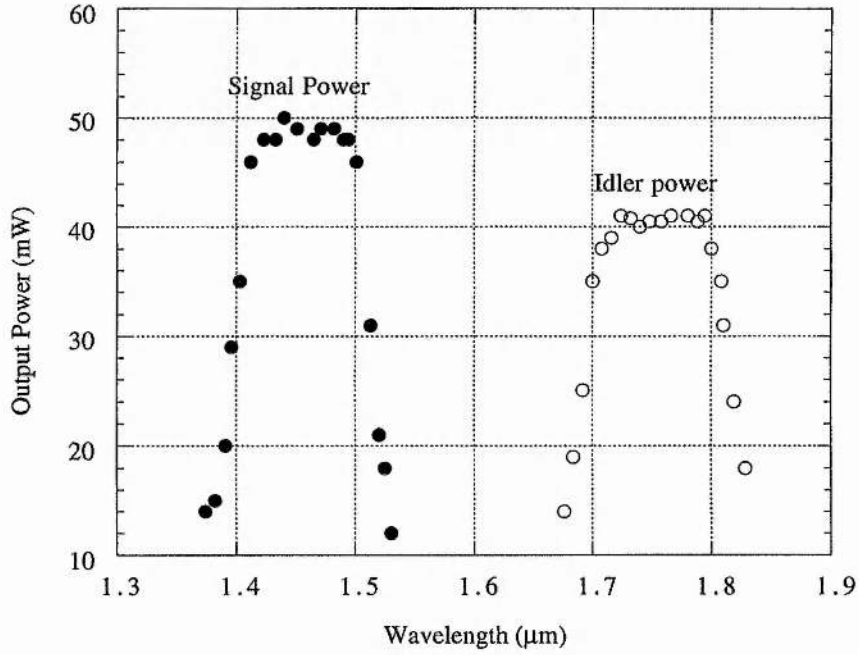

Figure 4.18
The average output power of the LBO OPO as a function of wavelength.

attributed to the intracavity parasitic losses, signal leakage through the resonator high reflectors, and residual mirror reflectivity or substrate absorption at the idler wavelength. These properties can also be investigated in terms of power-in power-out relations. Figure 4.19 demonstrated the variation in total, signal and idler power as a function of pump power (and hence times above threshold). It can be seen that the total power reaches a maximum value of 90 mW at 1.2 W of

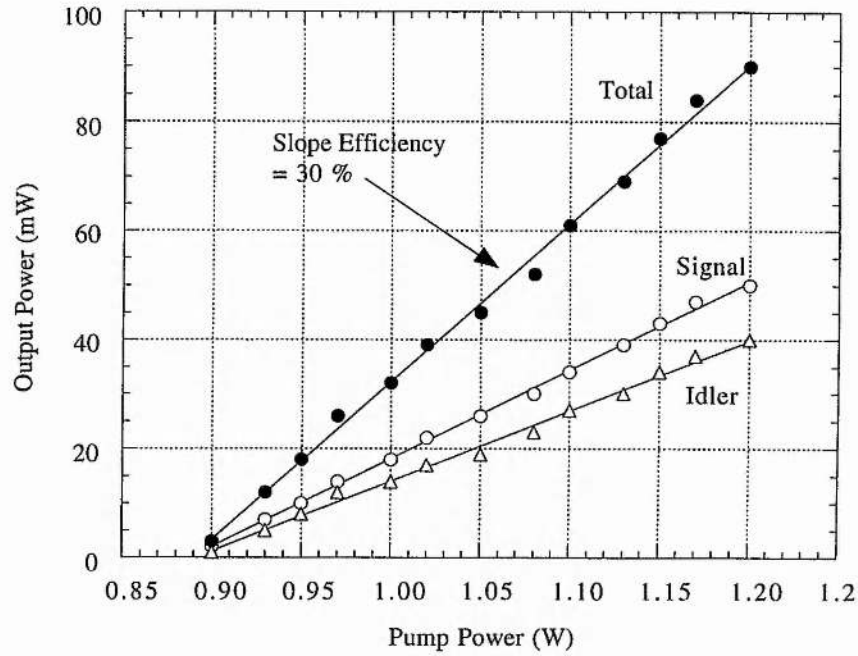

Figure 4.19
The average output power of LBO OPO as a function of pumping intensity. The signal wavelength is 1.45 μm.

pump power, with a pump threshold of 900 mW. This represents a slope efficiency of 30 %. The slope efficiency is simply the gradient of the power output against power input plot, this value indicates the percentage of pump power converted into useful extracted power. These values of output power could be improved by the choice of an optimum output coupler.

4.6.6 Temporal characteristics

The temporal characteristics of the signal pulses from the LBO OPO were determined from autocorrelation measurements. In Figure 4.20 (a)-(c), typical intensity and interferometric autocorrelation and the corresponding spectrum of the signal pulses at a wavelength of 1.41 μm are shown. The data was recorded at minimum cavity length mismatch and at 1.2 times above oscillation threshold, for input pump pulses of 1.8 ps duration. The pulse duration determined from the intensity autocorrelation is 720 fs (sech^2 pulse profile assumed) and the shape of the interferometric autocorrelation is indicative of chirp-free pulses. The signal spectrum has a spectral width of 3 nm, giving a time-bandwidth product of 0.328. Therefore, these pulses are essentially transform-limited. It is

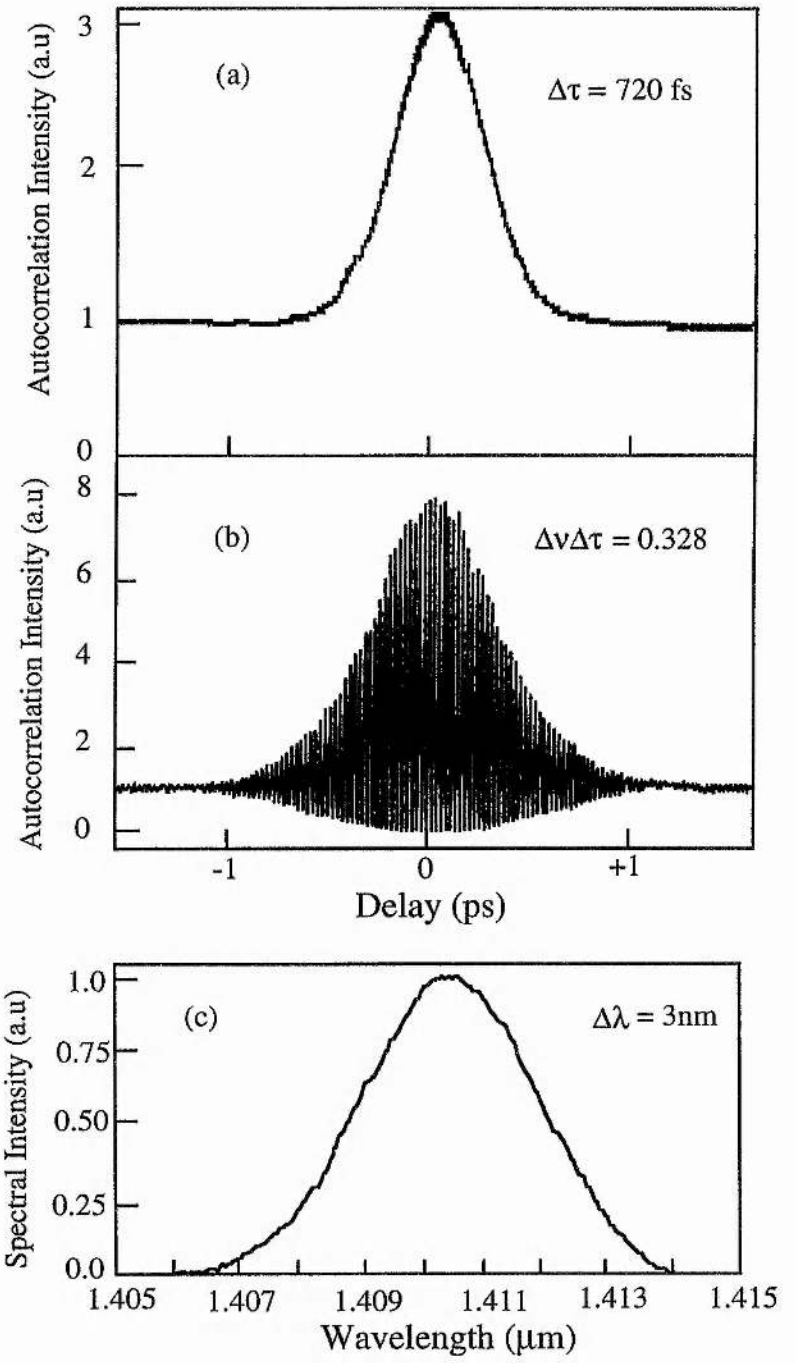

Figure 4.20

(a) Intensity and (b) interferometric autocorrelation, and (c) the corresponding spectrum of signal pulses at 1.41 μm, recorded at 1.2 times pump threshold. The pulse width determined from the intensity autocorrelation is 720 fs, with a time-bandwidth product $\Delta\nu\Delta\tau$=0.328. The input pump pulse duration is 1.8 ps.

interesting to note that unlike femtosecond OPO's, the signal spectrum is not modulated and has a smooth profile [22], indicating the absence of self-phase-modulation (SPM) here. This is to be expected because of the smaller nonlinearity of LBO, lower intracavity intensities associated with the picosecond signal pulses, and operation in the regime where the pump is not significantly depleted. The pulse length reduction from the pump to the signal is also consistent with the theoretical analysis of Cheung and Liu [25] and Becker et al [26] in the limit of small pump depletion and in the absence of significant pulse broadening due to the combined effects GVD, GVW, and SPM. However, little

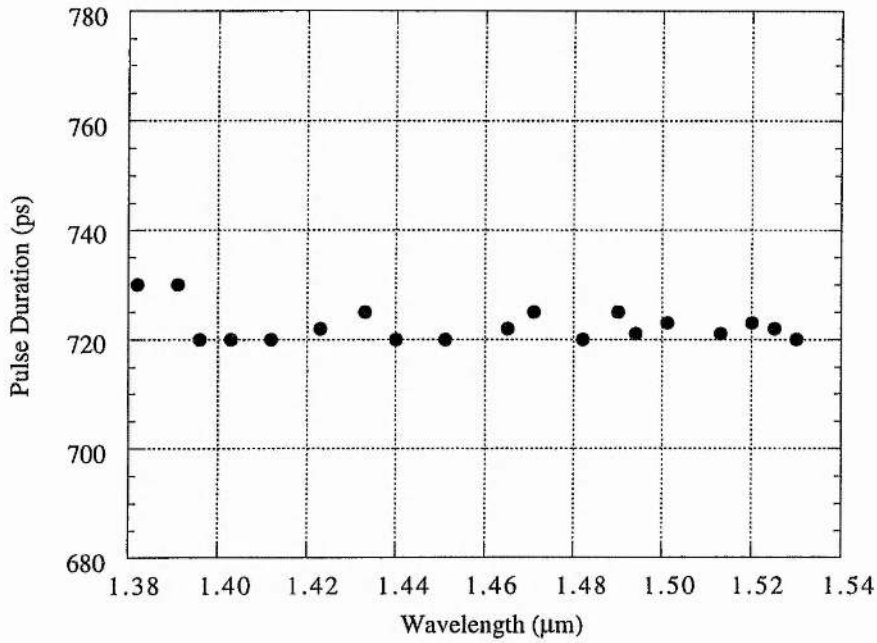

Figure 4.21
Variation of the signal pulse duration across the tuning range of the LBO OPO.

variation is observed in the pulse duration across the signal tuning range, (see Figure 4.21). The minor variations may be accounted for by the small differences in the mirror reflectivities resulting in changes in the pump threshold or by small fluctuations in the OPO cavity length. However, we observe that the signal pulses remain essentially chirp-free and transform-limited across the tuning range, without any requirement for dispersion compensation in the cavity.

4.7 Conclusion

In this chapter a new source of tunable picosecond/sub-picosecond near-infrared pulses based on a LBO OPO which is pumped by a self-mode-locked Ti:sapphire laser has been described. The system produces transform-limited signal pulses with durations of ~720 fs at a repetition rate of 81 MHz. Total average output powers of up to 90 mW over the signal and idler tuning ranges of 1.374-1.530 μm and 1.676-1.828 μm have been generated at 1.3 times the 900 mW threshold. The overall performance of the oscillator can be significantly enhanced through optimisation of output coupling and reductions in oscillation threshold to allow pumping further above threshold. This can be achieved by, for example, additional refinements to mode-matching, improvements to the transmission optics, or by double-passing the pump. Because of the small temporal walk-off and large spectral acceptance bandwidths of LBO, the use of longer crystals is also expected to readily result in major reductions in threshold, with the consequent increase in output power and efficiency. The reductions in oscillation threshold should also enable the generation of longer output pulses with durations of the order of 1-2 ps. In addition to the broad tuning potential of the device, the multi-parameter tuning capability that is available through the tunability of the pump and the phase-matching temperature allows access to a particular combination of wavelengths. This is highly desirable for many applications in pump-probe spectroscopy or wavelength division multiplexing. Although this device proved to be highly tunable with moderate output power levels it suffered from poor stability, which would have rendered it very difficult to use as a source for experiments and so improved stability had to be achieved. In the next chapter the performance of this system is improved by using a new LBO crystal of length 30 mm in contrast to the 16 mm long crystal used in this chapter. This longer crystal became available as crystal production techniques have improved since the date of the work performed in this chapter. This length is closer to the optimal length of crystal which was calculated previously in this chapter and so should lead to greater output powers as well as improved device stability.

References

1. C. Chen, Y. Wu, A. Jiang, B. Wu, G. You, R. Li, and S. Lin, J. Opt. Soc. Am. B **6**, 616 (1989)

2. Photox optical systems P.O. Box 274, No 2, Pullens Lane, Headington, Oxford, OX3 OBJ

3. J. L. Montgomery and K. Kato, Opt. Commun. **80**,159 (1990)

4. B. Wu, N. Chen, C. Chen, D. Deng, and Z. Xu, Opt. Lett. **14**, 1080 (1989)

5. F. Hanson and D. Dick, Opt. Lett. **16**, 205 (1991)

6. S. Lin, J. Y. Huang, J. Ling, C. Chen, and Y. R. Shen, Appl. Phys. Lett. **59**, 2805 (1991)

7. S. P. Velsko, M. Webb, L. Davis, and C. Huang, IEEE J. Quantum Electron. **27**, 2182 (1991)

8. Y. Tang, Y. Cui, and M. H. Dunn, J. Opt. Soc. Am. B **12**, 638 (1995)

9. G. J. Hall, M. Ebrahimzadeh, A. Robertson, G. P. A. Malcolm, and A. I. Ferguson, J. Opt. Soc. Am. B **10**, 2168 (1993)

10. S. Lin, B. Wu, F. Xie, and C. Chen, Appl. Phys. Lett. **59**, 1541 (1991)

11. M. Ebrahimzadeh, G. J. Hall, and A. I. Ferguson, Opt. Lett. **17**, 652 (1992)

12. H. Zhou, J. Zhang, T. Chen, C. Chen, and Y. R. Shen, Appl. Phys. Lett. **62**, 1457 (1993)

13. A. Robertson, G. P. A. Malcolm, M. Ebrahimzadeh, and A. I. Ferguson, in Conference on Lasers and Electro-Optics, Vol. 12 of 1992 OSA Technical Digest Series (Optical Society of America, Washington, D.C., 1992), paper CPD15

14. A. Nebel, C. Fallnich, R. Beigang, and R. Wallenstein, J. Opt. Soc. Am. B **10**, 2195 (1993)

15. N. P. Barnes and V. J. Corcoran, Appl Optics, **15**, no 3, 696 (1976)

16. E. C. Cheung and J. M. Liu, J. Opt. Soc. Am. B **7**, 1385 (1990)

17. S. French, PhD thesis, University of St. Andrews (1996)

18. D. T. Reid, PhD thesis, University of St. Andrews (1994)

19. Bray Chromalox, Unit 71, Portmanmoor Road Industrial Estate, East Moors, Cardiff, CF2 2YY, Wales

20. Optics for Research, Box 82, Caldwell, New Jersey, 07006, U.S.A.

21. W. S. Pelouch, P. E. Powers, and C. L. Tang, Opt. Lett. **17**, 1070 (1992)

22. J. M. Dudley, D. T. Reid, M. Ebrahimzadeh, and W. Sibbett, Opt. Commun. **104**, 419 (1994)

23. S. Guha, F. Wu, and J. Falk, IEEE J. Quantum Electron. **QE-18**, 907 (1982)

24. See, for example, Special Issue on Optical Parametric Amplification and Oscillation, J. Opt. Soc. Amer. B **10**, 2151-2239 (1993)

25. E. C. Cheung and J. M. Liu, J. Opt. Soc. Am. B **7**, 1385 (1990)

26. M. F. Becker, D. J. Kuizenga, D. W. Phillion, and A. E. Siegman, J. Appl. Phys. **45**, 3996 (1974)

Contents

5.1 Introduction

In Chapter 4, a characterisation of a picosecond optical parametric oscillator (OPO), which used temperature-tuned LBO as the nonlinear material, was presented. By using a 16 mm long crystal cut for type I NCPM, 720 fs output pulses were generated at 90 mW average power over a signal wavelength range of 1.374-1.530 μm and an idler wavelength range of 1.676-1.828 μm. This system was based on a 16 mm long LBO crystal, because at the time of this work production techniques restricted crystal lengths to < 20 mm, although this was shorter than the optimum crystal length that could have been used. In Chapter 4, it was predicted that because of the desirable properties of LBO including small temporal walkaway and minimal spatial walkoff, power scaling and improved overall performance of the OPO could be brought about with the use of longer crystals. The work in this chapter describes the configuration and full characterisation of an efficient, high-power, and widely tunable Ti:sapphire-pumped picosecond OPO based on a 30 mm-long LBO crystal. Detailed results are presented describing the signal and idler output pulses and highlighting the increased tunability and output powers.

5.2 LBO OPO based on a 30 mm long crystal

The OPO described here uses a picosecond Ti:sapphire pump laser in combination with temperature-tuned LBO to provide output pulses with durations of 1-2 ps. Output powers of up to 690 mW have been generated for 2.0 W of pump power. Also demonstrated is transform-limited performance over the 1.2-2.2 μm spectral range without the need for intracavity dispersion

compensation. The OPO is tunable over a continuous wavelength range from 1.160 to 2.185 μm and the potential tuning range of the device is from 1 to 2.4 μm, with a single crystal. The combination of the Ti:sapphire laser and LBO OPO thus provides a highly versatile source of picosecond pulses with extended tunability from around 700 nm to 2.4 μm.

5.2.1 Experimental configuration

The configuration of the Ti:sapphire-pumped picosecond LBO OPO is depicted in Figure 5.1. The pump source was again a commercial self-mode-locked Ti:sapphire laser (Spectra-Physics, Tsunami) which was configured for picosecond operation. It delivered a maximum average output of 2.2 W for 12 W of argon ion pump. The duration of the pump pulses deduced from

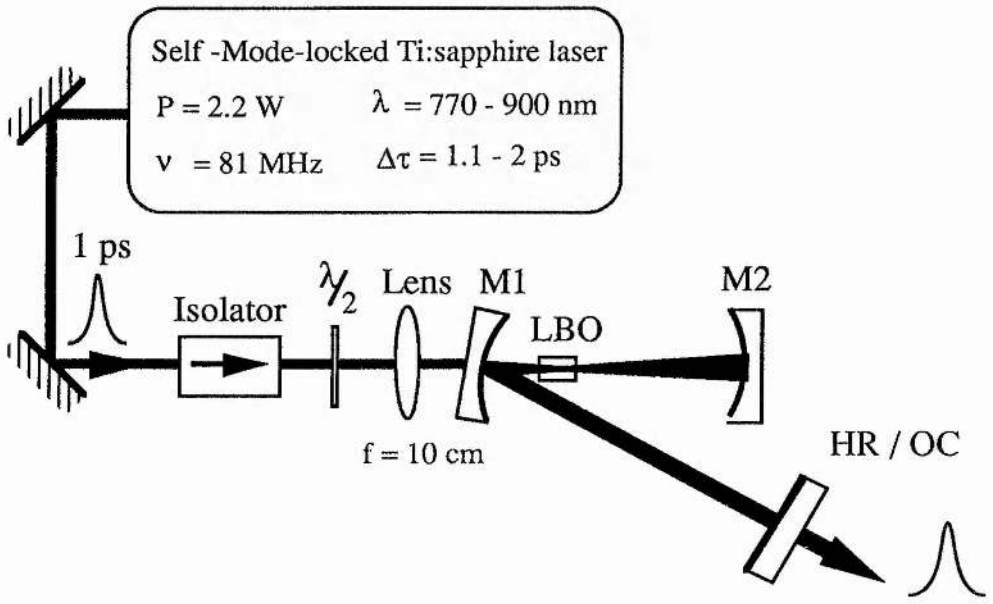

Figure 5.1
Schematic of the Ti:sapphire-pumped LBO OPO. The mirrors M_1 and M_2 have radii of curvature r=20 cm. λ/2 is a half-wave plate. HR/OC, high reflector or output coupler.

autocorrelation measurements were typically 1.1-2.0 ps (assuming $sech^2$ pulse shape) and the pulse repetition frequency was 81 MHz. With the available mirror set, the laser could be tuned from 770 to 900 nm. The OPO experimental setup was identical to that of the 16 mm long crystal case, with identical mirror coatings and curvatures being used. The LBO crystal used in this system was 30 mm in length and 3 mm x 3 mm in aperture and was supplied by [1]. The crystal was cut for non-critical type I phase-matching along the *x*-axis (θ=90°, ϕ=0°) and the end-faces were antireflection-coated at 1.4 μm.

5.3 Results and discussion

The alignment of the OPO resonator is achieved in a similar manner as in the 16 mm long crystal case in which the residual back reflections of the pump from the crystal end-faces and the cavity mirrors are monitored. Oscillation occurs when the OPO is brought into synchronism with the pump through fine cavity length adjustments. Again, a weak visible signal in the blue is generated when the pump polarisation is along the crystal z-axis. This radiation which is generated as a result of non-phase-matched, single-pass second harmonic generation of the pump may also be used as an alternative visual guide for the initial alignment of the resonator and optimisation of pump focusing.

5.3.1 Tuning characteristics

In Figure 5.2 the experimental tuning range of LBO OPO is shown as a function of phase-matching temperature, for a range of Ti:sapphire pump wavelengths between 770 and 800 nm. With the 1.4 μm mirror set, a signal tuning range from 1.290 to 1.534 μm and idler range from 1.610 to 1.973 μm was accessed by varying the pump wavelength or crystal temperature. As can be seen from the plots, the total signal and idler tuning range provides nearly continuous coverage over 1.290-1.973 μm with the single mirror set, except for small gaps near degeneracy. Operation in these regions is, in any case, undesirable due to doubly-resonant oscillation. Doubly-resonant operation can lead to device instability, due to mode-hopping. With the use of a second mirror set with high reflectivity (R>99.7%) centred at 1.18 μm, it was possible to extend the signal tuning range down to 1.160 μm and the corresponding idler range up to 2.260 μm by tuning the pump wavelength down to 770 nm. Therefore, the combination of the two mirror sets provides continuous tuning from 1.160 to 2.260 μm. The demonstrated tuning range was limited by the shortest available pump wavelength and can be further extended to cover 1-2.4 μm by tuning the Ti:sapphire laser down to about 700 nm. This would require a different mirror set for the Ti:sapphire laser than those currently available in the laboratory. The use of shorter pump wavelengths also has the advantage of lower phase-matching temperatures for a given tuning range. However, operation of the OPO is extremely robust even at temperatures as high as 230°C. Indeed, no degradation has been observed in the performance of the OPO or damage

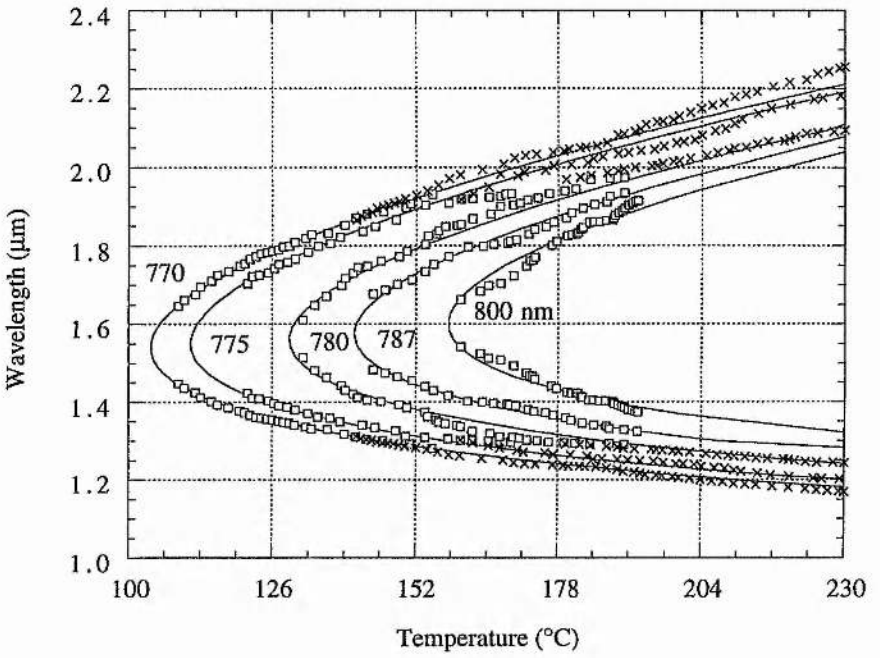

Figure 5.2
Temperature and pump wavelength tuning range of the Ti:sapphire-pumped LBO OPO. The output from the oscillator is indicated by the experimental data and the solid curves represent the predicted tuning range. The different symbols correspond to the two sets of mirrors used; open squares: 1.4 μm mirrors, crosses: 1.18 μm mirrors.

to the LBO crystal and its coatings despite sustained day-to-day operation over several months.

The comparison of the experimental data in Figure 5.2 with the predicted tuning curves calculated from [2, 3] indicates good overall agreement. However, the small discrepancies may be accounted for by uncertainties in the dispersion data for LBO or by the possible variations in output wavelength caused by small excursions in the OPO resonator length in the absence of active stabilisation.

5.3.2 Non-phased-matched processes

The intracavity peak intensity of the LBO OPO is very large, i.e. of the order of 1 GW/cm^2. This level of intensity makes it possible to directly generate observable sequences of pulses in the visible via non-phase-matched processes that would normally be too inefficient to be observed through parametric oscillation. A total of seven non-phase-matched interactions have been observed

in addition to the production of the signal and idler pulse sequences and these are listed in Table 5.1. This data was recorded for a pump wavelength of 800 nm, with a corresponding signal and idler pair of 1.4 μm and 1.87 μm.

Wavelength (nm)	*Description of Nonlinear Interaction*	*Average Intracavity Power*
466	$\omega = \omega_s + \omega_s + \omega_s$	< 1 mW
400	$\omega = \omega_p + \omega_p$	1 mW
509	$\omega = \omega_s + \omega_p$	100 mW
700	$\omega = \omega_s + \omega_s$	10 mW
560	$\omega = \omega_i + \omega_p$	< 1mW
1398	$\omega = \omega_p - \omega_i$	5 W
1867	$\omega = \omega_p - \omega_s$	20 mW

Table 5.1
Nonlinear interactions and corresponding average intracavity powers in the LBO OPO.

The dominant processes involve sum frequency mixing between the single-pass signal and the pump light to generate blue light at 509 nm and single-pass frequency-doubling of the pump light producing a wavelength of 400 nm. The other processes observed are the second and third harmonic generation of the signal which generate pulses at 509 nm and 466 nm, respectively, and sum frequency mixing between the single-pass idler and the pump light that produces light at 560 nm. The spectral bandwidths of the light generated at 509 nm and 560 nm are sufficient to support pulses of sub psec duration. The addition of a second intracavity nonlinear crystal cut for efficient sum frequency mixing or second harmonic generation would therefore provide picosecond pulses with tunability in the visible. The spectrum included as Figure 5.3 shows the frequency-doubled signal at 700 nm. The 0.53 nm bandwidth of the output at 700 nm is consistent with pulses of 1.0 ps duration if they are assumed to be transform-limited with a sech^2 intensity profile but autocorrelation measurements would be necessary to confirm the exact pulse duration.

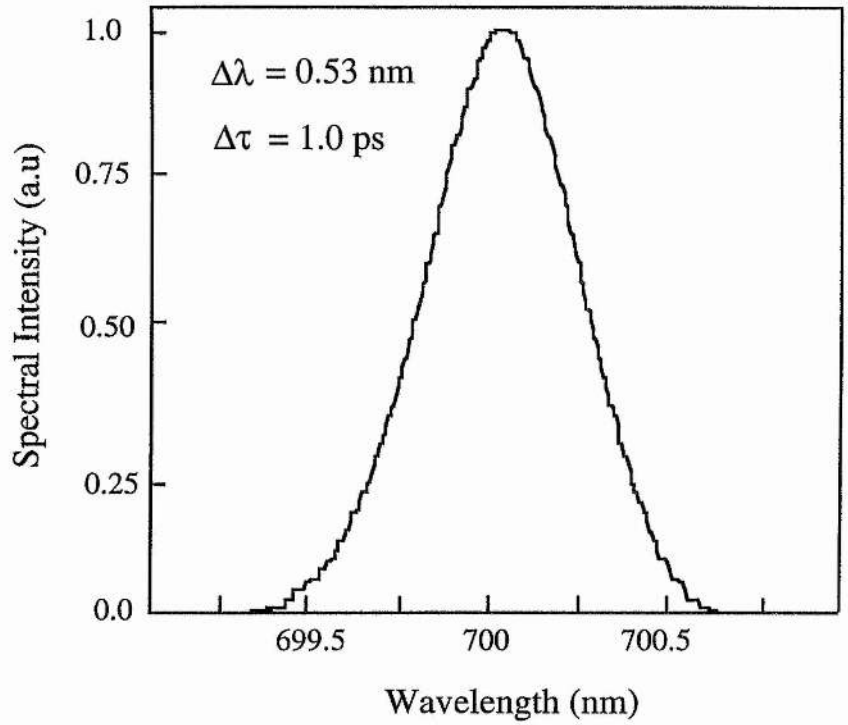

Figure 5.3
Spectrum of the frequency-doubled signal centred at 700 nm.

5.3.3 Sum frequency mixing

As discussed in the previous section, as well as the signal and idler beams, our OPO also generates tunable output in the visible spectrum. This phenomenon which has also been observed in femtosecond oscillators based on KTP [4, 5, 6], is a result of non-phase-matched sum frequency mixing (SFM) between the resonated signal and the single-pass pump. This process is by far the strongest of all the processes discussed in the section above and has some very interesting features, and so will be discussed in more detail. Since this radiation exits the OPO cavity in the same forward direction as the pump and idler beams, it can be used as a visual aid for optimisation of the resonator. The polarisation direction of the sum frequency light is the same as the pump (parallel to *y*-axis) and perpendicular to that of the signal. In Figure 5.4 it can be seen that this process is widely tunable from 472-528 nm in the blue-green portion of the optical spectrum. This process produces up to 2 mW of visible output over the entire tuning range of 472-528 nm. Interestingly, however, at a pump wavelength of 780 nm, the SFM process between the pump and signal becomes phase-matched over a temperature range of 134.9-142.5°C which corresponds to a wavelength range of 511.6-500.1 nm. This results in intense SFM generation in the green, with up to 25 mW being produced, (see Figure 5.5) although the output can

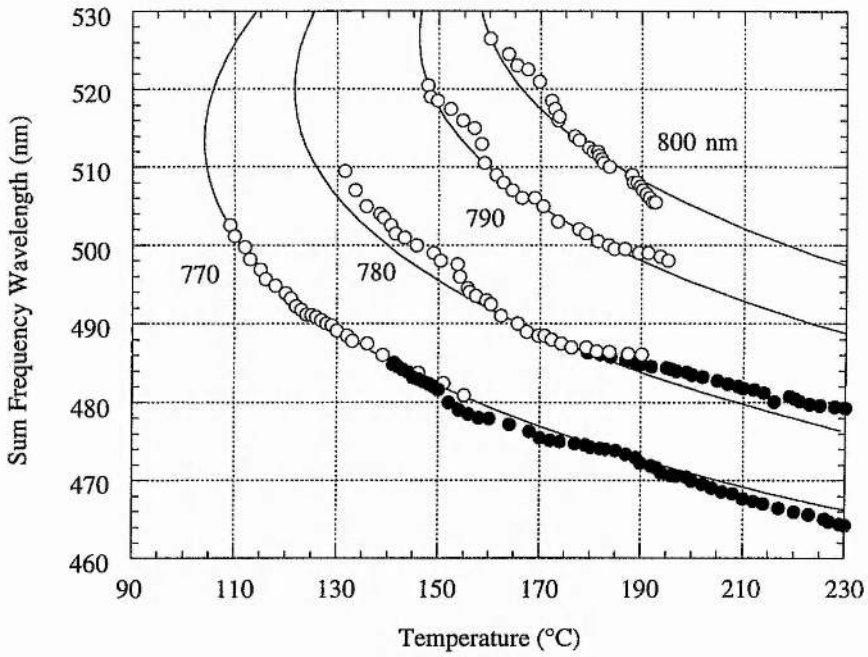

Figure 5.4
Visible SFM tuning as a function of Ti:sapphire pump wavelength. The solid lines represent the theoretical curves derived from the Sellmeier equations of Reference 2 and the temperature dependence of the refractive indices given in Reference 3. The different symbols correspond to the two sets of mirrors used open circles: 1.4 μm mirrors, closed circles 1.18 μm mirrors.

become unstable due to the depletion of the intracavity signal. In this process there is a competition between the signal and the SFM light. This is due to the fact that for the SFM process to exist there must be sufficient signal energy available to combine with the pump pulses. However, the process of SFM causes the OPO to be depleted of signal radiation. Hence, the SFM process effectively competes with the process that creates it. Tuning the cavity to different synchronous lengths results in the signal wavelength tuning, which in turn leads to better or worse SFM phase-matching conditions. This makes it possible to surpress the SFM process by simply tuning the cavity length to maximise the parametric generation process. An autocorrelation and spectrum of SFM pulses at 506 nm is depicted in Figure 5.6, and the pulses can be seen to have a spectral width of 0.28 nm, with a duration of 1.02 ps. This corresponds to a time-bandwidth product of 0.335 and indicates that the pulses are transform-limited. Also, the absence of modulation is present on the spectrum indicating that no SPM is present.

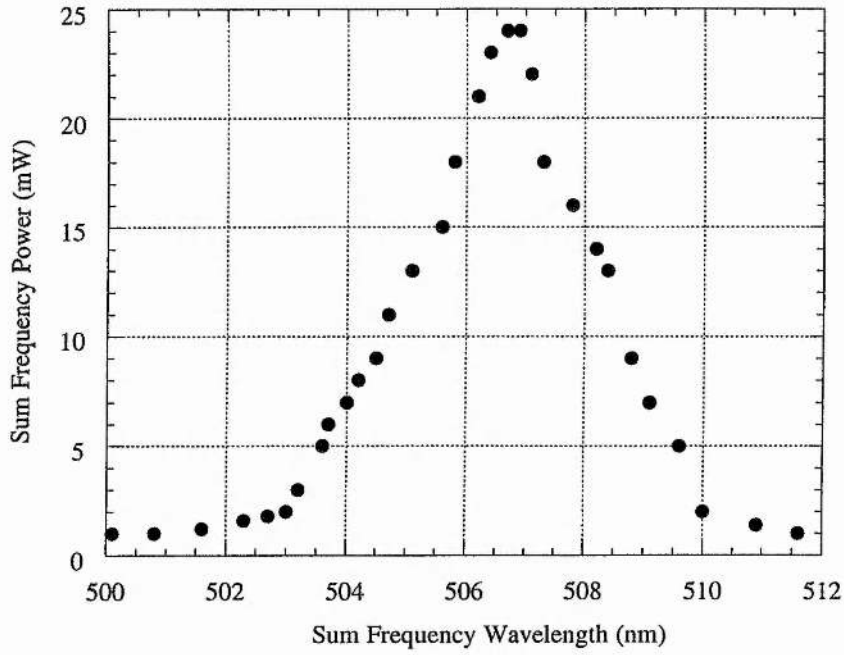

Figure 5.5
SFM power as a function of SFM wavelength for a pump wavelength of 780 nm.

In Figure 5.7 the phase-matched SFM process between the signal and pump can be seen, as a very intense green light. This photograph shows the light as it passes down the cavity and out through the back curved mirror.

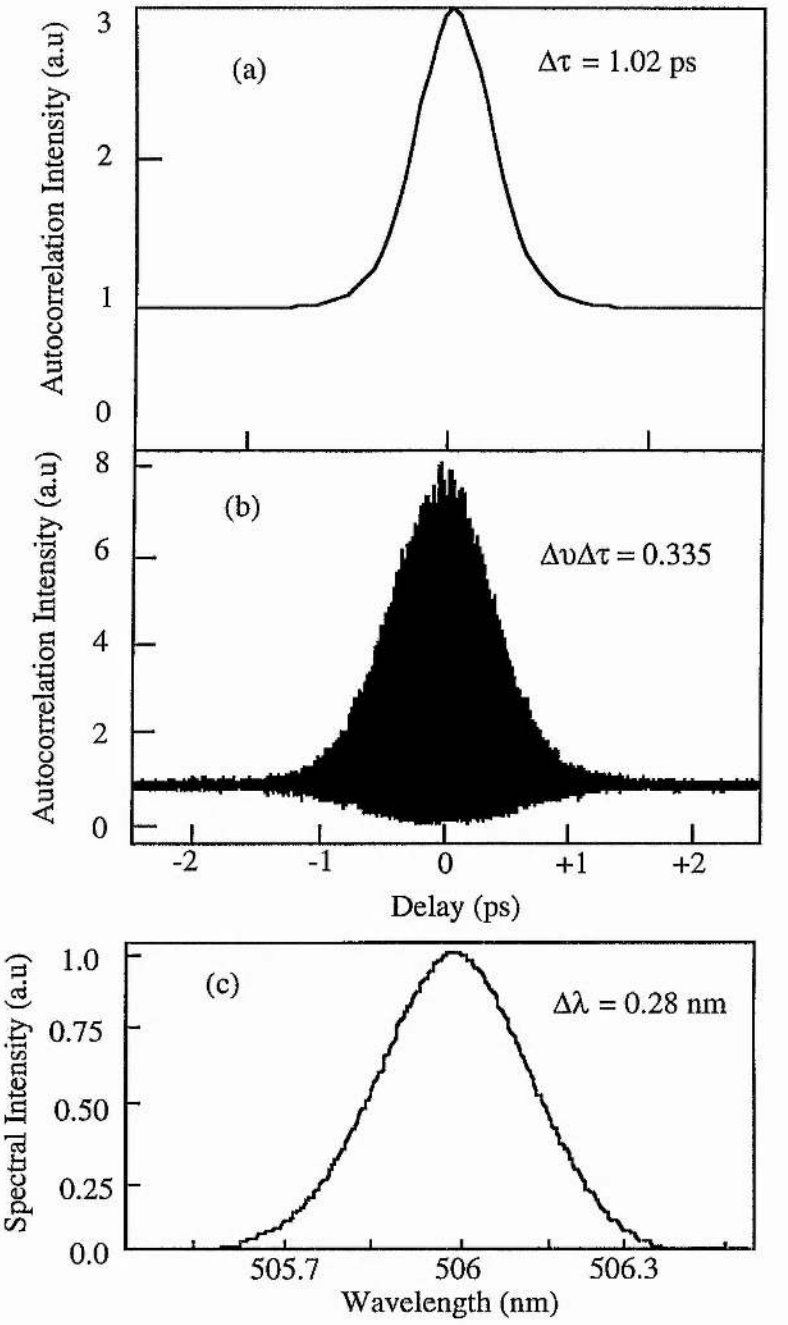

Figure 5.6

(a) Intensity and (b) interferometric autocorrelation, and (c) the corresponding spectrum of the sum frequency mixing pulses at 506 nm. The pulse width determined from the intensity autocorrelation is 1.02 ps, with a time-bandwidth product $\Delta\nu\Delta\tau = 0.335$.

Figure 5.7
Sum-frequency mixing along the length of the crystal oven of the picosecond LBO OPO. The green light was generated by pump-signal sum-frequency-mixing.

5.3.4 Threshold

With 1.2 ps input pump pulses and configured with all highly reflecting mirrors, the average pump power threshold for the OPO was about 350 mW at the centre of the mirror reflectivity band (see Figure 5.8). Therefore, the threshold pump pulse energy was 4 nJ, corresponding to a peak power of 3.6 kW, and peak intensity of 120 MW/cm^2 inside the LBO crystal. Oscillation could be maintained across the entire signal tuning range for average pump powers below 550 mW. At the extreme of the reflectivity band of the 1.4 μm mirrors,

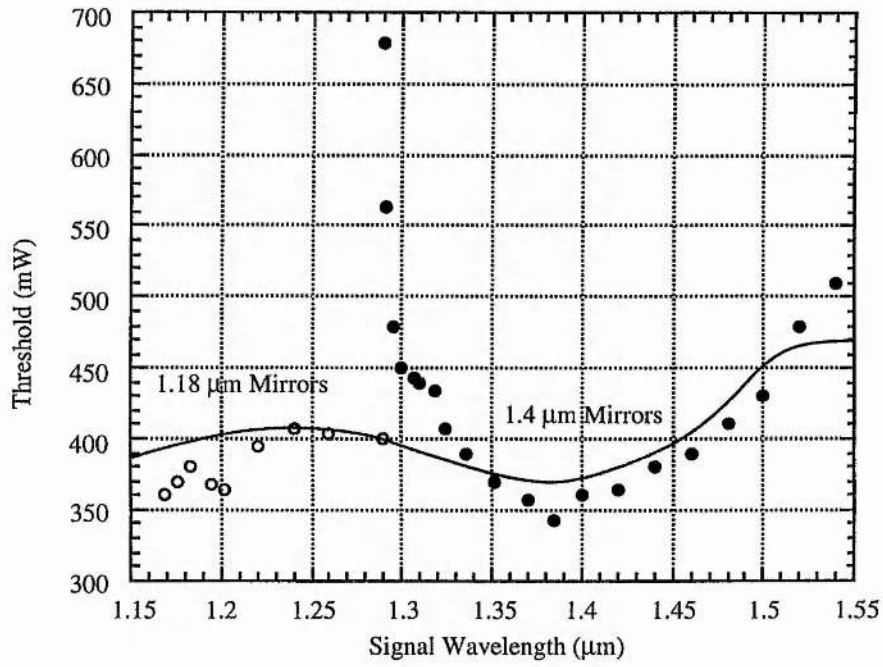

Figure 5.8
Variation in the average pump-power threshold across the tuning range of the LBO OPO.

the threshold increased above 650 mW, but lower thresholds below 450 mW were available in this region with the 1.2 μm mirror set. With both mirror sets oscillation could be maintained for an output coupling loss of up to 12%. The increase in threshold with output coupling was found to be negligible, indicating that output coupling was not the dominant loss mechanism here. A prediction of the threshold has again been made by using the model of Guha, Wu, and Falk [7], using a h_s factor of 0.2, this again produced a good fit to the experimental data, as seen in Figure 5.8. If the exact mirror transmission were known across the entire tuning range then the model could be fitted more accurately to the experimental results. The threshold could be reduced further by the use of an optimum mirror set. Another approach may be to double pass the pump beam.

The reduction in threshold from the previous system was substantial and allows measurements to be made with pump powers many times above the threshold value.

5.3.5 Pump Depletion

As mentioned in Chapter 4 maximisation of the pump depletion is very important as this leads to the ultimate amount of power available form the OPO. In the previous system the pump depletion varied from about 15 to 20 %, this is relatively low and should be able to be improved substantially. The pump depletion is calculated using equation 4.18. The resulting pump depletions across the tuning range of the OPO are shown in Figure 5.9. It can be seen that the depletion has now risen substantially, reaching a maximum of 52% at a

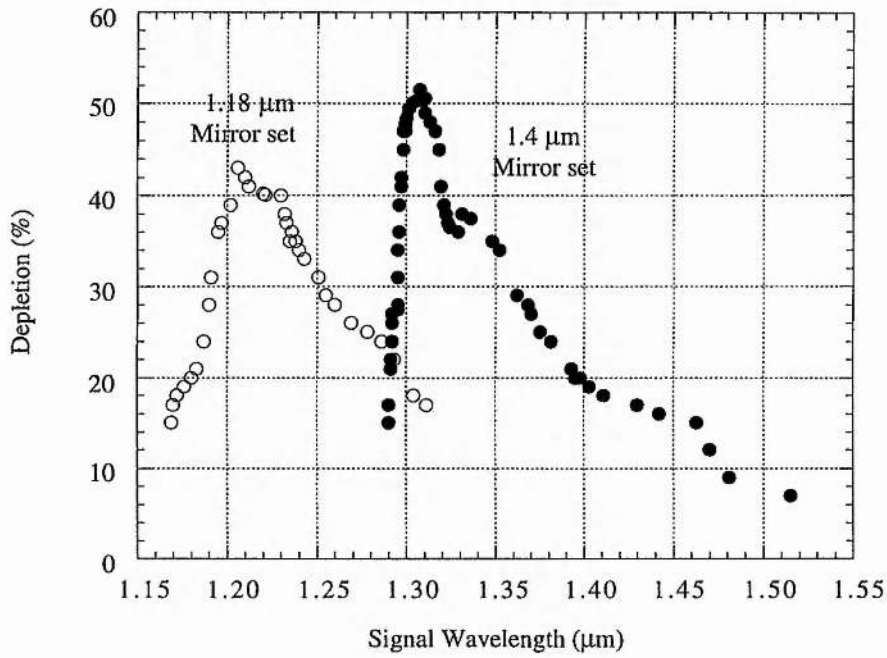

Figure 5.9
Pump depletion of the LBO OPO as a function of signal wavelength.

signal wavelength of 1.31 μm. The maximum values of depletion occur, as would be expected, at the centre of the mirror reflectivities where the highest intracavity powers are achieved. For the most part, the depletion remains in the range 20-50 %, with reductions down to 10 % at the extremes of the mirror reflectivities resulting from a reduction in intracavity power. However, the depletion of this system is considerably improved from that of the previous LBO device using a 16 mm long crystal.

5.3.6 Output coupling

In the ideal situation the external extraction of the OPO energy should mirror that of the depletion. However, this is unlikely to occur as to some extent there will always be spurious losses in the OPO cavity due to Fresnel reflection from crystal and mirror faces and absorption in the mirror substrates, etc. The mirror coatings used in this device are designed to maximise the reflectivity of the resonated wave, in this instance the lower wavelength signal branch. At the non-resonant wavelength the mirrors should be as close to 100 % transmitting as possible, so that all this energy is coupled out of the cavity. This will of course not occur, due to the fact that the substrate of the mirrors invariably produce

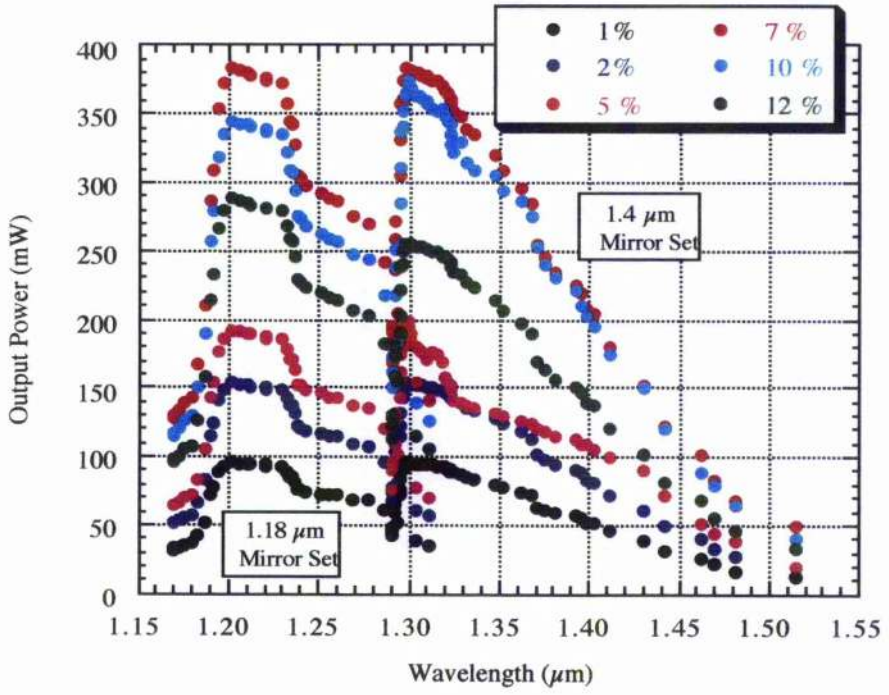

Figure 5.10
Variation in the average extracted output signal power as a function of output coupler transmission in the LBO OPO for 2 W of pump power.

some degree of absorption at the non-resonating wavelengths as well as at the resonant signal wavelengths. The correct choice of output coupler can have a profound effect on the amount of energy extracted from the cavity. In this section the signal output power from the OPO is detailed for several different values of output coupling. The results presented in Figure 5.10 represent the signal output powers, measured for output coupler transmissions of, 1 %, 2 %, 5 %, 7 %, 10 % and 12 %. It can be observed in Figure 5.10 that the maximum

output power value of 390 mW occurs for the 7 % output coupler. The 10 % and 12 % cases lead to 'overcoupling', in which too high an output coupling results in a large reduction in the intracavity power, ultimately leading to a reduction in output power. This effect results in the maximum powers reducing to 370 and 260 mW for the 10 % and 12 % cases respectively. On the other hand, for the 1 %, 2 % and 5 % cases 'undercoupling' takes place, in this case the lack of output power is due to the fact that the power is unable to 'escape' from the cavity due to a lack of transmission in the output couplers and instead converts to idler output power. This process results in the maximum powers reducing to 100, 150 and 190 mW for the 1 %, 2 % and 5 % values, respectively. The 7% output coupler, therefore, represents the best value of transmission to match the gain and loss of the OPO cavity and leads ultimately to the best values of output power. All further work in this chapter has been performed with the 7% output coupler unless otherwise stated.

5.3.7 Output power and efficiency

As discussed earlier the optimum performance of the OPO was achieved with 7% output coupling at 1.32 μm, where a total average output power of 690 mW was achieved, with this power being split into a signal power of 390 mW and a single-pass idler power of 300 mW. These values, which were generated for 2 W of pump power, can be observed in Figure 5.11. At 5 times threshold the total output power of 690 mW represents an extraction efficiency of 34.5%, with the pump depletion reaching 52%. There is also found to be no evidence of saturation, which implies that significantly higher output powers and conversion efficiencies will be available with higher pump powers, longer crystals, or improvements in mode-matching. It should be noted that while the maximum total output power from the OPO corresponded to an output coupling of 7%, the power in the single-pass idler beam could be as high as 350 mW when the output coupler was replaced by a high reflector. This is simply due to the fact that the lack of output coupling results in an increase in intracavity power, which in turn results in a increase in signal and idler power, but the signal can not of course exit the cavity. In this case, however, the signal power collected through the end mirror dropped to ~100 mW. In the absence of optimised output coupling for all signal wavelengths, the maximum output power of 690 mW could not be maintained across the entire tuning range (see Figure 5.12). However, the OPO could routinely deliver total output powers in excess of 300 mW over most of the available tuning range. This results in the total extraction of the system remaining in the range ~15-35 % across the majority of the tuning range (see

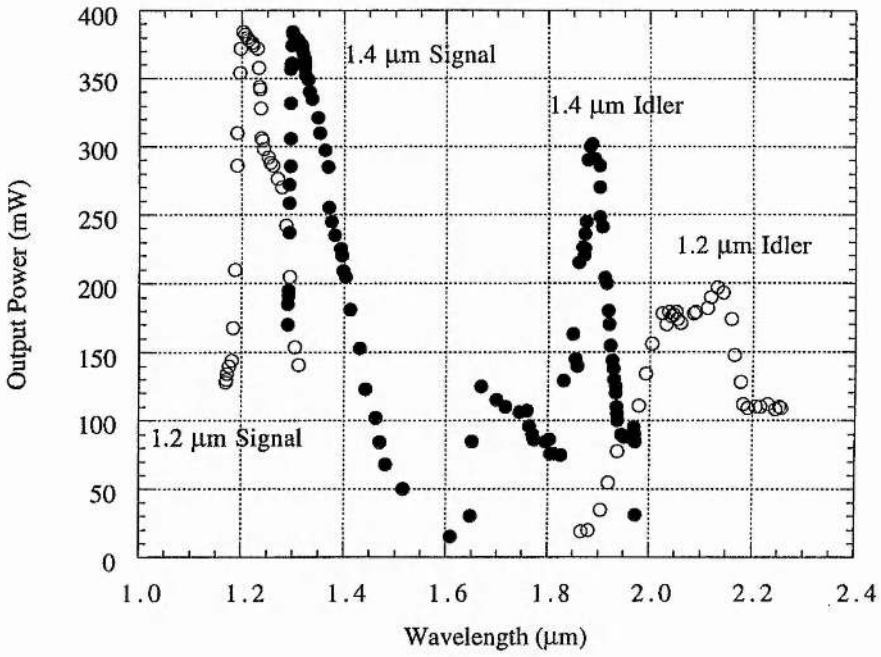

Figure 5.11
The average signal and idler output powers of the LBO OPO as a function of wavelength, for a pump power of 2 W.

Figure 5.12). If output coupler coatings could be obtained that produce the optimum transmission across the entire tuning range of the OPO then it is not unrealistic to assume that extraction efficiencies of the order of 40 % could be obtained over the entire tuning range. It is also useful to consider the variation of output power of the OPO as a function of pump power so that an indication of slope efficiency can be made. It can be observed in Figure 5.13 that the slope efficiency of this system is 45 % and so represents a substantial increase from the value of 30 % obtained from the oscillator using the 16 mm long crystal. The depletion and extraction is a very important property of the OPO, the extraction values will of course follow the values of the output powers. The depletion, on the other hand, relates to the conversion efficiency of the parametric generation process, which involves the conversion of the pump pulse. For low pump powers, i.e. just over threshold only the central portion of the

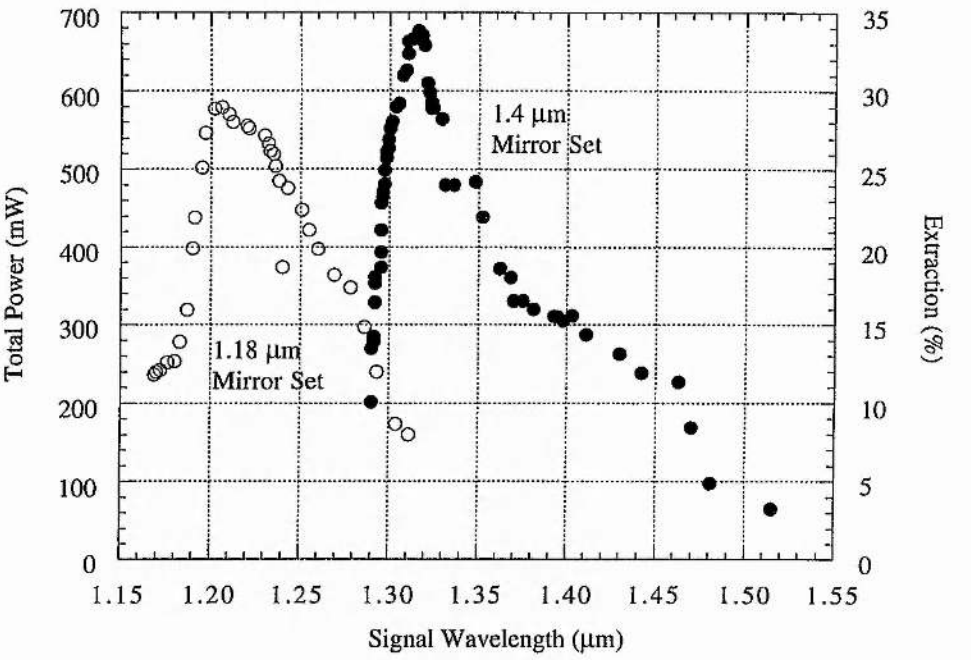

Figure 5.12

The total average output power of the LBO OPO as a function of wavelength.

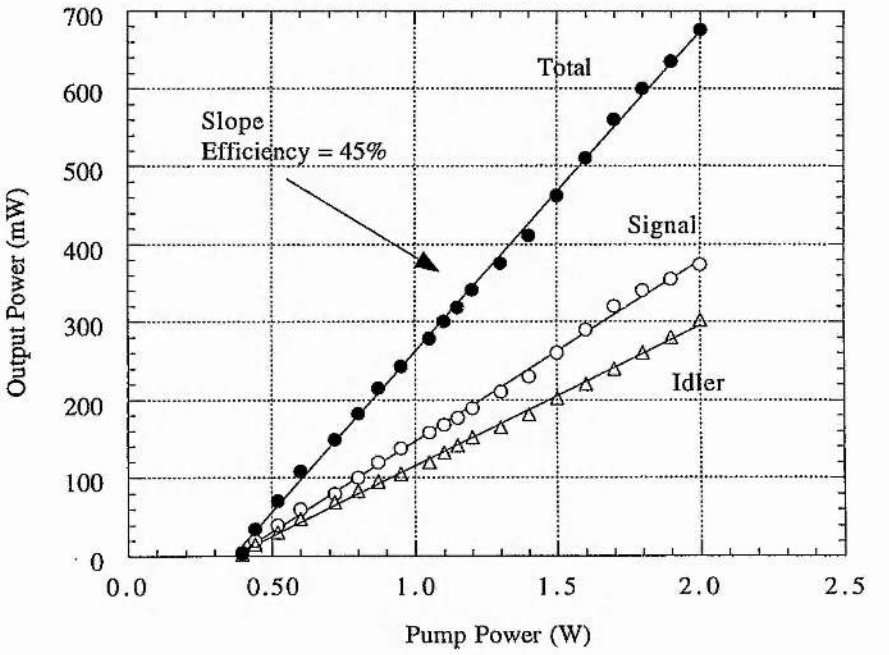

Figure 5.13

Output power as a function of input power, for a signal wavelength of 1.32 μm.

pump pulse will be converted to signal and idler, which will lead to small conversion efficiencies. However, as the pump power is increased to many times above threshold a larger percentage of the pump pulse will be converted. Ultimately the depletion will begin to saturate as all the pump pulses are converted, with further increases in pump power resulting in a smaller increase in total converted power. This effect is shown in Figure 5.14.

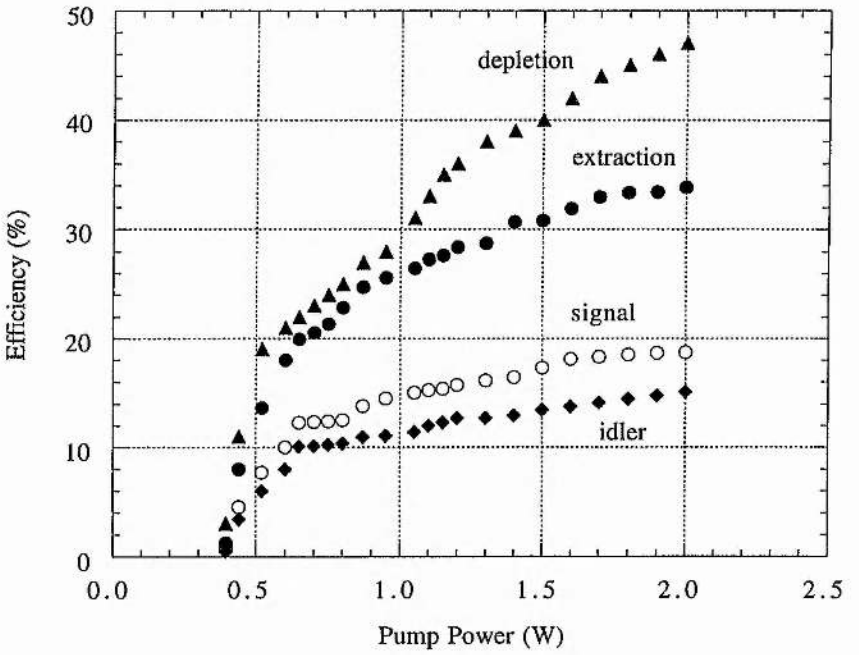

Figure 5.14
Depletion and extraction of the LBO OPO as a function of input power, for a signal wavelength of 1.32 μm.

5.3.8 Amplitude noise measurements

It would be expected that the amplitude noise on the output of the LBO parametric oscillator would be greater than that of the pump laser, due to the nonlinear conversion process that takes place from the laser to the OPO. Figure 5.15 shows the oscillograms obtained from both the pump laser and the OPO. It can be seen that for the Ti:sapphire pump laser the amplitude fluctuations are typically less than 1 % and for the OPO around 3 %. These values agree well with the theoretical and experimental work carried out by [8, 9]. Amplitude fluctuations are caused by various sources; a large number of these are from the laboratory enviroment such as temperature fluctuations and air currents, another

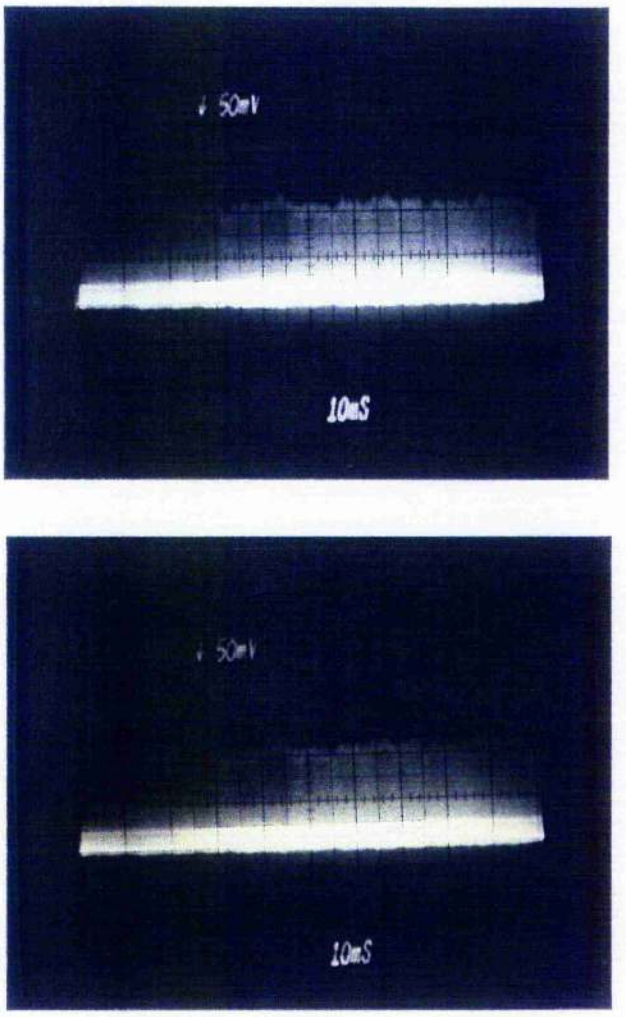

Figure 5.15
Oscillograms showing the amplitude noise (intensity fluctuations) of the self-mode-locked Ti:sapphire pump laser (a), the OPO (b). The timebase is 10 ms/division in each case.

source is from the argon laser used to pump the Ti:sapphire laser. The picosecond LBO OPO is, however, a very stable device and can operate over large periods of time with only small cavity variations required to sustain operation over an entire day.

5.3.9 Temporal characteristics

As mentioned in Chapter 4 an important effect limiting minimum attainable pulse durations is the group velocity dispersion (GVD), the variation in the signal and idler GVD in LBO is shown in Chapter 4 and reference [10]. It is found that the signal GVD in LBO remains small ($0 < \beta'' < 50$ fs^2/mm) and close

to zero across the entire available tuning range. It is also interesting to note that the transition from the positive to the negative GVD occurs at ~1.2 μm. This implies that for signal wavelengths beyond this value, transform-limited pulses may be attainable without the need for intracavity dispersion compensation. Therefore, dispersion broadening in type I temperature-tuned LBO is generally not a limiting factor in the attainment of transform-limited output pulses, particularly for signal wavelengths longer than ~1.2 μm. For signal wavelengths below this value pulse broadening may result from the effects of positive GVD.

The temporal characteristics of the signal pulses were determined from autocorrelation measurements. Figure 5.16 (a)-(c) represent typical intensity and interferometric autocorrelations and the corresponding spectrum of the signal pulses at a wavelength of 1.42 μm. The data was recorded at minimum cavity length mismatch and at 5 times above oscillation threshold, with input pump pulses measuring 1.2 ps. The pulse duration (FWHM) deduced from the intensity autocorrelation is 1.1 ps ($sech^2$ pulse profile assumed) with the shape of the interferometric autocorrelations being indicative of chirp-free pulses. The spectrum has a smooth profile with a spectral width of 2 nm, giving a time-bandwidth product of ~0.325. Therefore, these pulses are essentially transform-limited. It is interesting to note that there is no evidence of self phase modulation (SPM) in the signal spectrum in Figure 5.16 (c). The absence of spectral modulation may be attributed to the balance between GVD and SPM in the negative GVD regime. The variation of signal pulse duration with pump depletion was also studied by recording autocorrelation data for a range of input pump powers from 350 mW to the maximum available 2 W (see Figure 5.17). The signal pulse length increases from about 400 fs at ~1.15 times threshold to 1.1 ps when pumping at 2 times above threshold, thereafter no increase in signal pulse duration is observed as saturation is reached. This behaviour is consistent with the theoretical predictions of Becker et al [11] and of Cheung and Liu [12], where the change in the curvature of the pump pulse due to depletion is suggested to be responsible for pulse broadening. The process may, however, be more simply viewed as an increase in the signal gain further above the loss level with increasing pump power, as in a conventional laser. This has the effect of enhancing gain towards the wings of the pulse, thus resulting in an increase in pulse width. However, it is interesting to note that the shortest signal pulse duration of 400 fs measured in this experiment is somewhat lower than the minimum attainable pulse width of 480 fs (~0.4 times the pump pulse width) predicted by theory. Although this model does not include the effects of GVD or SPM which, in the negative dispersive regime, will tend to shorten the pulses.

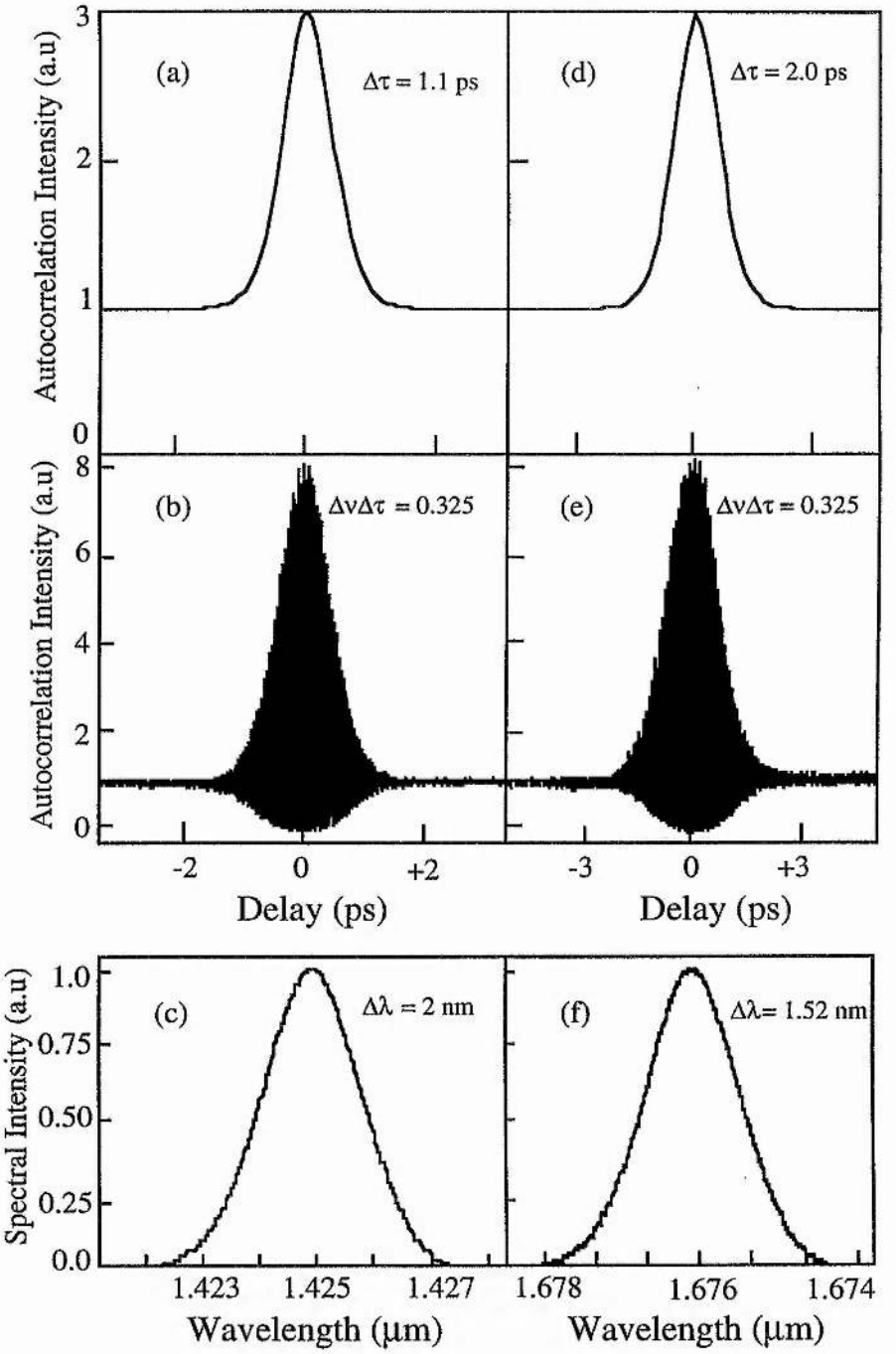

Figure 5.16

(a) Intensity and (b) interferometric autocorrelation, and (c) the corresponding spectrum of the signal pulses at 1.425 μm. The pulse width determined from the intensity autocorrelation is 1.1 ps, with a time-bandwidth product $\Delta\nu\Delta\tau = 0.325$. (d) Intensity and (e) interferometric autocorrelation, and (f) the corresponding spectrum of the idler pulses at 1.676 μm. The pulse width is 2.0 ps, with a time-bandwidth product $\Delta\nu\Delta\tau = 0.325$.

The duration of the idler pulses were also determined by direct autocorrelation measurements. Representative autocorrelation data and the spectrum of the idler pulse recorded at a wavelength of 1.67 μm are shown in Figure 5.16 (d)-(f). The data were obtained under the same pumping conditions as for the signal (5 times threshold) and with 1.2 ps input pump pulses. The intensity autocorrelation trace implies an idler pulse width of 2 ps ($sech^2$ pulse shape assumed) and the time-bandwidth product suggests that the idler pulses are also close to the transform-limit. This is supported by the shape of the

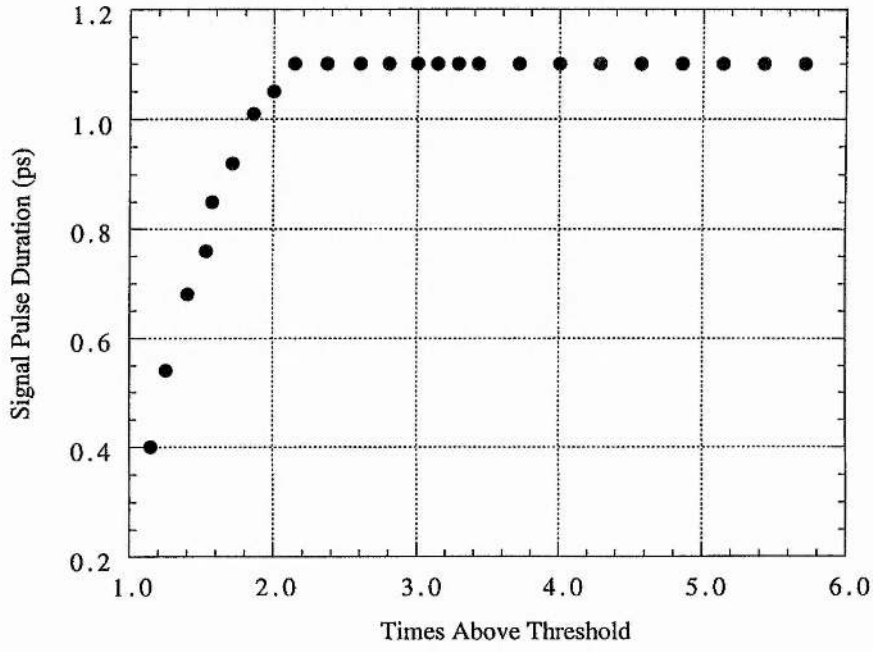

Figure 5.17
Dependence of the signal pulse duration on pumping intensity. The signal wavelength is 1.37 μm.

interferometric autocorrelation which indicates the absence of chirp on these pulses. The variation in signal and idler pulse length across the tuning range of the OPO was also verified and this is shown in Figure 5.18. As expected, in the negative GVD regime above ~1.2 μm, the signal pulse durations remain essentially constant at 1-1.2 ps. The small variations in pulse length may be attributed to the small differences in mirror reflectivities resulting in changes in pump threshold or by small fluctuations in resonator length in the absence of active stabilisation. However, in this region the pulses remain chirp-free and transform-limited. In the positive GVD regime, on the other hand, the signal pulses become increasingly chirped, with pulse durations increasing to 1.8 ps at

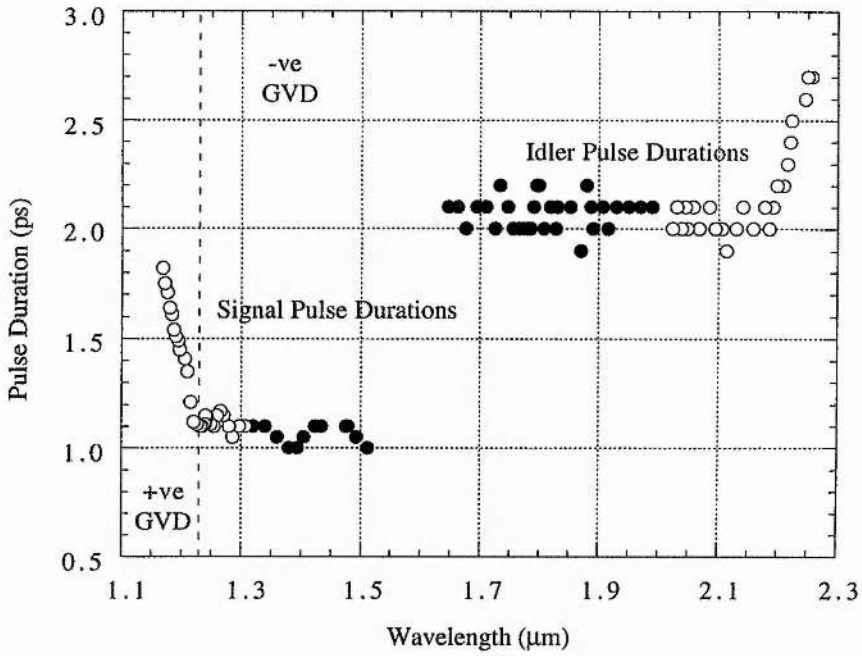

Figure 5.18

The variation in the signal and idler pulse width across the tuning range of LBO OPO. The dashed line represents the approximate transition from the positive to the negative GVD region.

1.17 μm. The idler pulses undergo a corresponding increase in duration up to 2.7 ps, as shown in Figure 5.18, but unlike the signal pulses, they are observed to remain chirp-free, with a time-bandwidth product close to the transform limit ($\Delta\nu\Delta\tau$~0.33). This result is similar to the previous observations in a femtosecond OPOs based on KTA where the non-resonant idler pulses were found to remain close to the transform limit even when the signal pulses were chirped [13]. In Figure 5.19 (a)-(c), a typical autocorrelation of the signal in the positive GVD regime is shown. The modulation in the wings of the interferometric autocorrelation is clearly indicative of a chirp content and the time-bandwidth product of 0.777 is more than twice the transform limit. The dip at the centre of the signal spectrum may be due to the effect of SPM, but the modulation is not as strong as that observed in femtosecond oscillators. This may be due to the lower intracavity intensities of the picosecond signal pulses (typically < 3 GW/cm^2), but may also imply a small nonlinear index in LBO, particularly given the 30 mm crystal length used here. Therefore, to produce transform-limited ~1 ps across the entire tuning range of the system dispersion compensation must be added to the cavity (see section 5.4). In Figure 5.19 (d)-

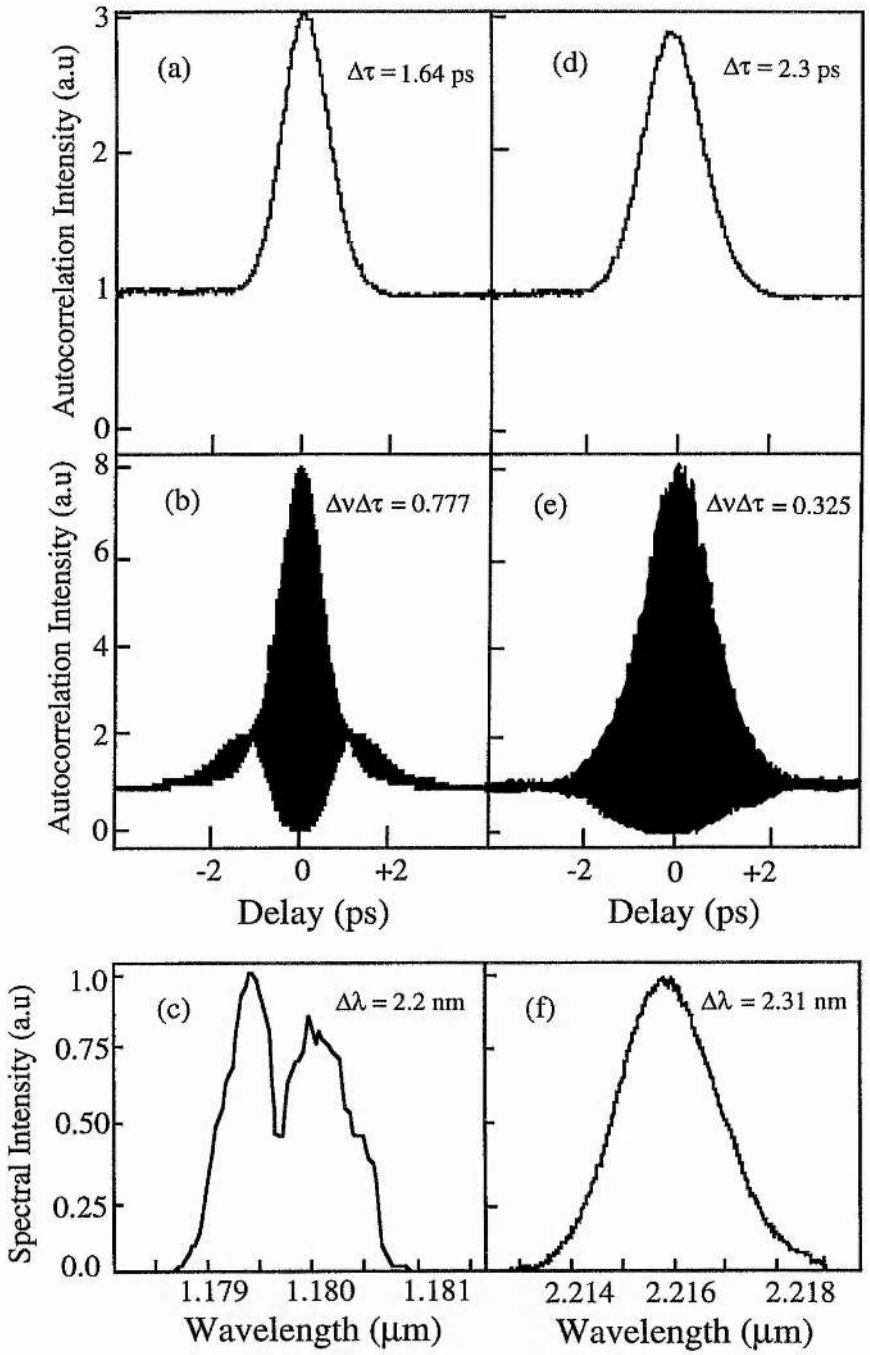

Figure 5.19

(a) Intensity and (b) interferometric autocorrelation, and (c) the corresponding spectrum of the signal in the region of positive GVD at 1.18 μm. The pulse width is 1.64 ps, the time-bandwidth product is $\Delta\nu\Delta\tau = 0.777$. (d) Intensity and (e) interferometric autocorrelation, and (f) spectrum of the corresponding idler in the region of positive GVD at 1.18 μm. The pulse width is 2.3 ps, the time-bandwidth product is $\Delta\nu\Delta\tau = 0.325$

(f) a typical autocorrelation of the idler in the positive GVD regime is shown. This can be seen to be transform-limited, as would be expected from its non-resonant nature. A model has been devised to emulate the SPM effects found to occur in this system below 1.2 μm. This model can be used as a tool to make an estimation of the value of the nonlinear refractive index n_2.

5.3.10 Self phase modulation

The interferometric autocorrelation profile in Figure 5.19 (b) together with spectral component given in 5.19 (c) indicates that, below signal wavelength values of 1.2 μm and in the absence of any dispersion compensation, pulses produced by the OPO are chirped. This chirp is thought to be primarily due to self phase modulation (SPM) occurring in the highly focused region within the LBO crystal. This results from a phase shift induced by the intensity-dependent refractive index (n_2) of the material. The pulse broadening observed is produced from the combined effects of SPM and group velocity dispersion (GVD) of the signal pulse as it makes multiple passes of the OPO cavity. Similar effects have already been reported by several groups [14, 15]. Dudley et al [16] presented a simple model to estimate the consequences of SPM for the OPO in terms of both pulse and spectral broadening. For a full description of this model see [16]. If the model is tested using the intracavity intensity of 1 $GWcm^{-2}$ present in the LBO crystal and taking the n_2 for LBO to be 3.4×10^{-16} cm^2 W^{-1} [17], then it produces a good match to the experimental results observed.

5.3.11 Cross-correlation measurements

It is often desirable to have several independent tunable wavelengths, either for pump-probe spectroscopy or for frequency mixing. In such a case, the degree of synchronism between the pulses at each wavelength is of paramount importance because it directly affects the time resolution achievable in the experiment. If the OPO is to be used as a source for such experiments then the output pulses must be synchronised. This is especially important if one wavelength is used as the pump, say the signal and the other, the idler is used as the probe. In some situations it may be desirable to pump with the Ti:sapphire laser and probe with one of the OPO wavelengths. By measuring the cross correlation of the various combinations of laser and OPO wavelengths it is possible to determine the degree to which these wavelengths are synchronised.

When calculating the relative timing jitter of two pulses (τ_j), a type of pulse profile has to assumed as is the case in autocorrelation measurements. If the

pulses are assumed to be Gaussian then the cross correlation width (τ_{cc}) may be calculated using equation (5.1),

$$\tau_{cc} = \sqrt{\tau_{\lambda_1}^2 + \tau_{\lambda_2}^2 + \tau_j^2} \tag{5.1}$$

where $\tau_{\lambda_{1,2}}$ represents the pulse durations of the two individual pulses being cross correlated, whether this is the Ti:sapphire laser or the signal or idler pulses. However, in our experiments we will assume $sech^2$ intensity profiles throughout, as with all the previous results presented in this thesis. For $sech^2$ pulses the cross correlation width may be written as the approximation [18]

$$\tau_{cc} = \left(\tau_{\lambda_1}^{1.615} + \tau_{\lambda_2}^{1.615} + \tau_j^{1.615}\right)^{0.619} \tag{5.2}$$

Therefore, the timing jitter is measured by autocorrelating the individual pulses and then cross correlating the desired pulses and substituting these values into equation (5.2) to produce the required value of jitter. The experimental configuration of the cross correlator is shown in Figure 5.20.

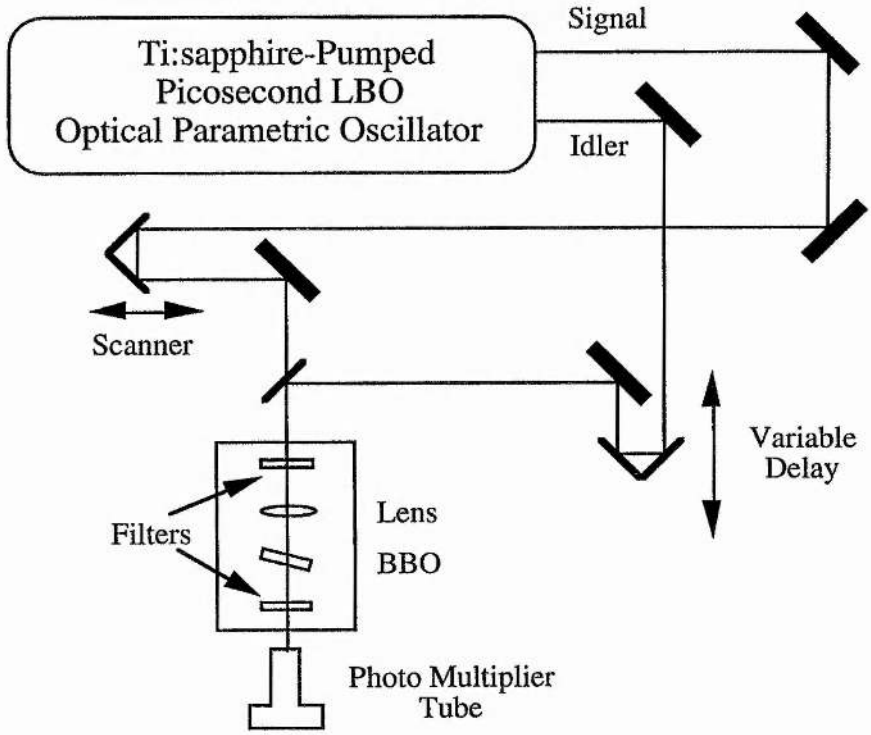

Figure 5.20
Schematic of the experimental apparatus used to perform cross-correlation measurements on the Ti:sapphire-pumped LBO OPO.

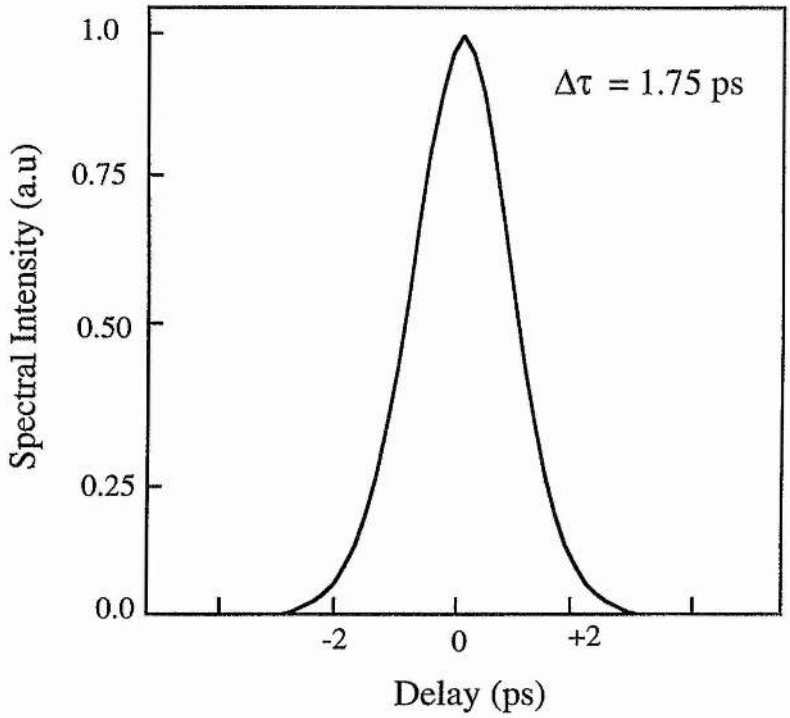

Figure 5.21

Cross-correlation between the mode-locked Ti:sapphire laser and the OPO signal at 800 nm and 1.4 μm, respectively. The individual pulse durations were 1.2 and 1.05 ps for the Ti:sapphire laser and OPO signal, respectively.

To get an approximate measure of the jitter between the three wavelength components in the Ti:sapphire-pumped OPO, cross correlations measurements were performed between the three pulse trains. The measurements between the pump and signal and the signal and idler were made using type II sum frequency mixing (SFM) in BBO. The corner cube scanned at a rate of ~20 Hz to provide a variable delay. The cross correlation results were obtained over an average of ~1000 scans and hence the measurements were valid over the frequency range > 0.02 Hz. The cross correlation between the pump and idler was made using type I SFM in the same BBO crystal. In Figure 5.21 a typical cross correlation between the pump and signal is presented. For this measurement the individual pulse durations at 800 nm and 1.4 μm were measured as 1.2 ps for the Ti:sapphire and 1.05 ps for the OPO signal. This yielded a cross correlation width of 1.75 ps, assuming a $sech^2$ pulse profile. Cross correlation measurements of the signal and idler were also carried out, with the results being presented in Figure 5.22. This was performed for the 1.05 ps signal at 1.4 μm and the 2.1 ps idler at 1.87 μm, with the cross correlation being measured to be

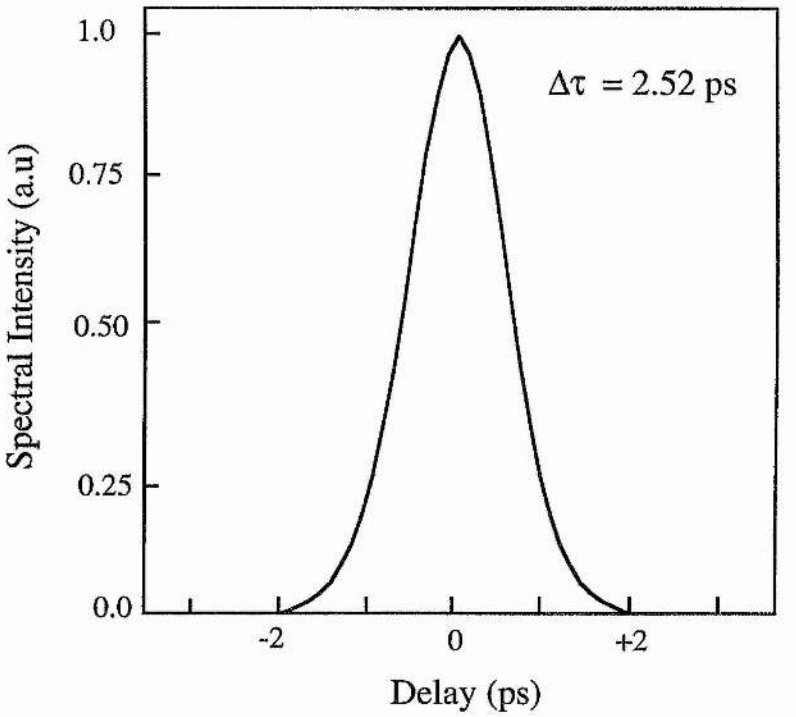

Figure 5.22
Cross-correlation between the OPO signal at 1.4 μm and the idler at 1.87 μm. The individual pulse durations for the OPO were 1.05 ps for the signal 2.1 ps for the idler.

2.52 ps. Finally the pump and idler were cross correlated for the 1.2 ps pump at 800 nm and the 2.1 ps idler at 1.87 μm, this measurement produced a cross correlation width of 2.62 ps, and is shown in Figure 5.23. Applying these values to equation 5.2 yielded values for the jitter of ~50 fs for the pump and signal, 55 fs for the signal and idler and 50 fs for the pump and idler. Therefore, the jitter was only a fraction of the individual pulse durations in all cases and with the cross correlation width being approximately equal to the longest pulse duration. Hence, the achievable resolution is limited primarily by the pulse durations rather than the jitter. The Ti:sapphire-pumped OPO should therefore be an excellent source for time-resolved spectroscopy measurements.

5.3.12 Detuning characteristics

The signal tuning was found to vary by as much as 30 nm by adjusting the resonator length across the synchronous range of the OPO (see Figure 5.24 (a)). The wavelength tuning occurs because the cavity length detuning introduces a loss mechanism at the signal wavelength by reducing the synchronism between the pump and signal pulses. To maintain synchronism and optimise gain, the

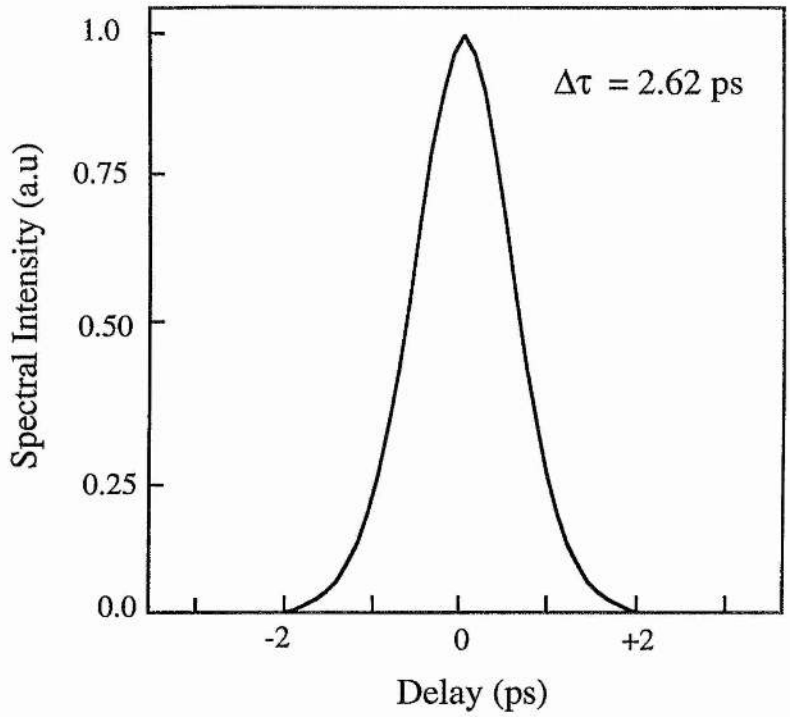

Figure 5.23

Cross-correlation between the mode-locked Ti:sapphire laser and the OPO idler at 800 nm and 1.87 μm, respectively. The individual pulse durations were 1.2 and 2.1 ps for the Ti:sapphire laser and OPO idler, respectively.

signal shifts to a more favourable wavelength with a group velocity that satisfies a constant round-trip time. This cavity length tuning which was first observed by Edelstein et al [19] in a femtosecond OPO is a useful mechanism for fine-tuning the output wavelength. However, the shift in signal wavelength from the centre of the synchronous range is accompanied by a drop in output power. For this OPO, a detuning range of 30 μm (FWHM) was observed when pumping at around 1.5 times threshold. At higher pump powers longer detuning ranges will be available because of the increase in the signal pulse duration with pump depletion and higher instantaneous gains. It is interesting to note that the asymmetric shape of the detuning curve in Figure 5.24 (b) is nearly identical to that of Chung and Siegman [20] and similar to that observed by McCarthy and Hanna [21]. This asymmetry is consistent with the theoretical predictions of Cheung and Liu [12] for a singly-resonant OPO. The exact nature of cavity length tuning depends on the net intracavity GVD. In this OPO, an increase in the cavity length results in a shift in the signal to shorter wavelengths. This is to be expected, given that the slower group velocities are associated with the longer wavelengths in the anomalous dispersion region. It is also important to note that

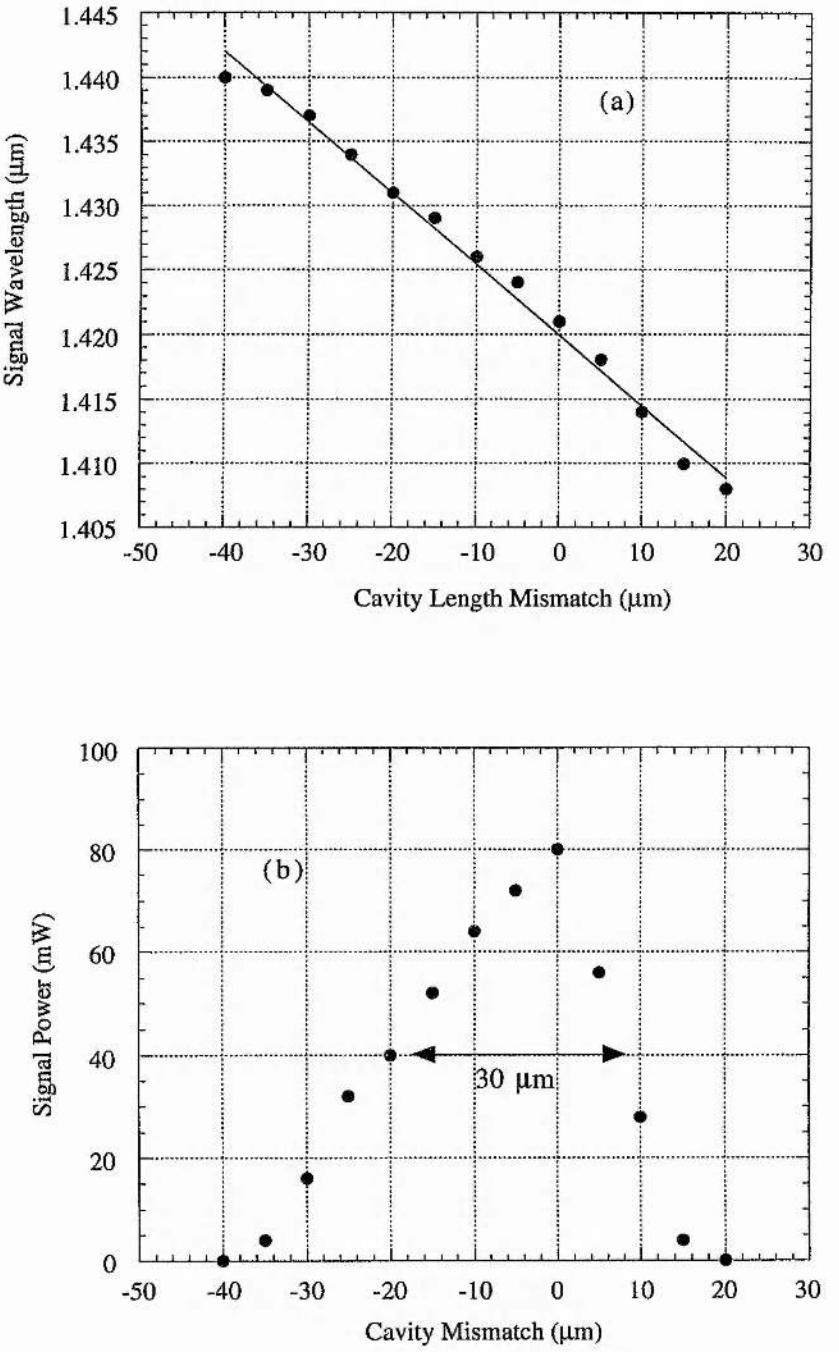

Figure 5.24

(a) The signal wavelength detuning and (b) cavity synchronous range in LBO OPO. The straight line in (a) represent the best fit to the experimental data. The FWHM synchronous range of the cavity in (b) is 30 μm.

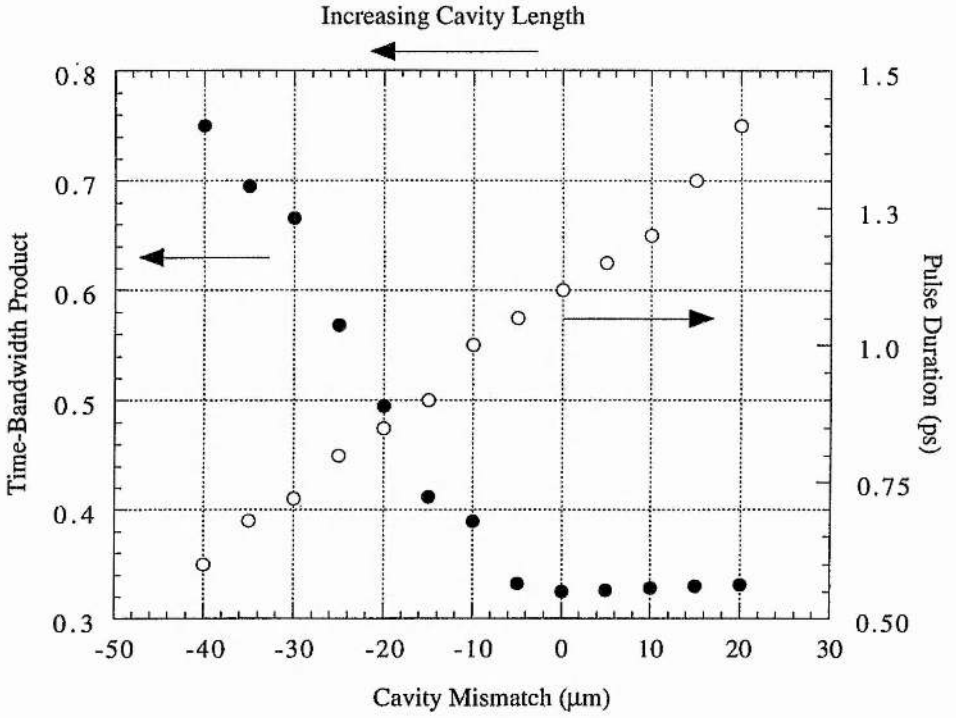

Figure 5.25
Signal pulse duration and bandwidth product variation as a function of cavity length detuning.

the signal wavelength shift of 30 nm in the OPO is much larger than of other picosecond systems based on KTP [22] and is in fact similar to that observed in femtosecond oscillators [4, 5, 6, 22-27]. The effect of cavity length detuning on pulse duration and shape has also been investigated. From Figure 5.25 it can be seen that detuning to shorter cavity lengths resulted in a gradual pulse broadening, with the pulses remaining transform-limited. By contrast, detuning to longer cavity lengths resulted in a large reduction in the signal pulse duration, with the pulses becoming increasingly chirped. This effect can be seen in Figure 5.26 in which lengthening the cavity by 30 μm from the optimum cavity mismatch reduced the signal pulse duration from 1.1 to 0.72 ps and increased the bandwidth product from 0.334 to 0.654. This effect is consistent with a similar previous measurement conducted by McCarthy and Hanna [21].

As discussed previously, to achieve transform-limited performance across the entire tuning range of the OPO it is essential to use dispersion compensation in the cavity, to produce a net negative GVD at signal wavelengths below 1.2 μm. In the following section the results of this procedure shall be presented.

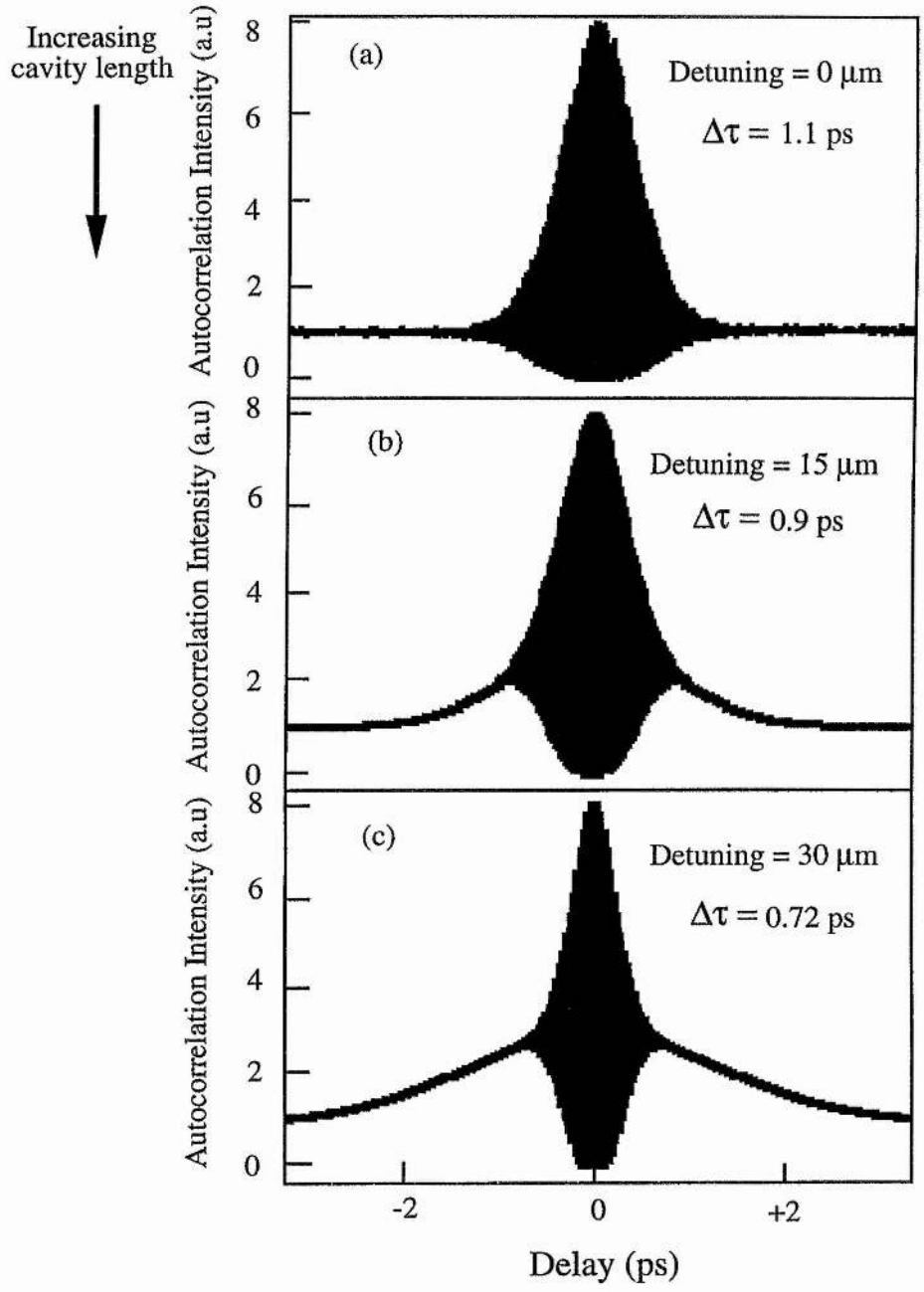

Figure 5.26
Signal autocorrelations as a function of cavity length detuning to longer than optimum values.

5.4 Dispersion compensated LBO OPO

5.4.1 Introduction

An important feature affecting pulse durations from the OPO is the group velocity dispersion (GVD) in the crystal. Excessive amounts of GVD can result in the broadening of pulses to durations greater than the transform limit by inducing a linear chirp across the pulse. The effect can be exacerbated by the presence of SPM and becomes increasingly important with shorter pulse durations and longer crystal lengths.

5.4.2 Theory of dispersion compensation

The magnitude of GVD can be calculated by evaluating the dispersion parameter β", where

$$\beta'' = \frac{\partial^2 k}{\partial \lambda^2} = \frac{\lambda^3}{2\pi c^2}\frac{\partial^2 n}{\partial \lambda^2} \tag{5.3}$$

Evaluation of β" for temperature-tuned LBO yields signal GVD in the range $0 < \beta'' < 80$ fs²/mm, with the corresponding values for the idler GVD ranging from $100 < \beta'' < 1000$ fs²/mm [28]. Interestingly, the signal GVD also remains small and close to zero across the GVD tuning range of the LBO OPO, with the transition from the positive to the negative occurring near 1.2 μm. This implies that for signal wavelengths longer than 1.2 μm, dispersion broadening i s generally not a limiting factor in the attainment of transform-limited pulses. However, for signal wavelengths below 1.2 μm, pulse broadening can result from the effects of positive GVD, as was confirmed by previous experimental findings (Figures 5.18, 5.19). To extend the transform-limited performance of the LBO OPO to signal wavelengths below 1.2 μm, dispersion compensation must therefore be implemented.

To compensate the pulse chirping in the OPO, a pair of highly dispersive SF14 prisms were inserted into the cavity (see Figure 5.28). If the OPO is operated as a ring cavity, a four prism sequence is required as shown in Figure 5.27. In a linear arrangement, as was used for all the OPOs described in this thesis, only two prisms are required as an end mirror can be placed in the plane of symmetry indicated by SS'. The theory pertaining to prism dispersion compensation was first proposed by Fork et al [29, 30], who noted that a double

pass through a prism pair gives a second derivative of the phase with respect to frequency of

$$D_{2P} = \frac{d^2\phi_p}{d\omega^2} = \frac{\lambda^3}{2\pi c^2}\frac{d^2P}{d\lambda^2} \tag{5.4}$$

with the derivative of the optical path with respect to the wavelength given by [31]

$$\begin{aligned}\frac{d^2P}{d\lambda^2} &= 4\left[\frac{d^2n}{d\lambda^2} + \left(2n - \frac{1}{n^3}\right)\left(\frac{dn}{d\lambda}\right)^2\right] d\tan\frac{\alpha}{2} \\ &-8\left(\frac{dn}{d\lambda}\right)^2\left(l + d\tan\frac{\alpha}{2}\tan\frac{\varepsilon}{2}\right)\end{aligned} \tag{5.5}$$

where n is the SF14 index of refraction at wavelength λ, α is the prism apex separation angle, ε is the deviation angle, d is the prism insertion (i.e. the distance from the resonated beam in the prism to the prism apex), and l is the separation of the prism apices when $d = 0$. The deviation angle can be calculated if the n and α values are known by using the fact that at the minimum of deviation the angle of incidence corresponds to the Brewster angle. Approximations lead to a simplified relation of

$$\frac{d^2P}{d\lambda^2} = 4l\left\{\left[\frac{d^2n}{d\lambda^2} + \left(2n - \frac{1}{n^3}\right)\left(\frac{dn}{d\lambda}\right)^2\right]\sin\varepsilon - 2\left(\frac{dn}{d\lambda}\right)^2\cos\varepsilon\right\} \tag{5.6}$$

For a given distance l and an insertion d, the overall negative GVD introduced can be calculated with the relations given above and the Sellmeier equations for SF14 glass [32]. Initial calculations neglect nonlinear effects such as SPM. The minimum negative GVD produced by the prisms must at minimum negate the positive GVD arising from the LBO material dispersion. For a single pass through an LBO crystal with l_c = 30 mm, the positive GVD can be calculated from

$$D_{2c} = \frac{d^2\phi_c}{d\omega^2} = \frac{\lambda^3 l_c}{2\pi c^2}\frac{d^2n}{d\lambda^2} \tag{5.7}$$

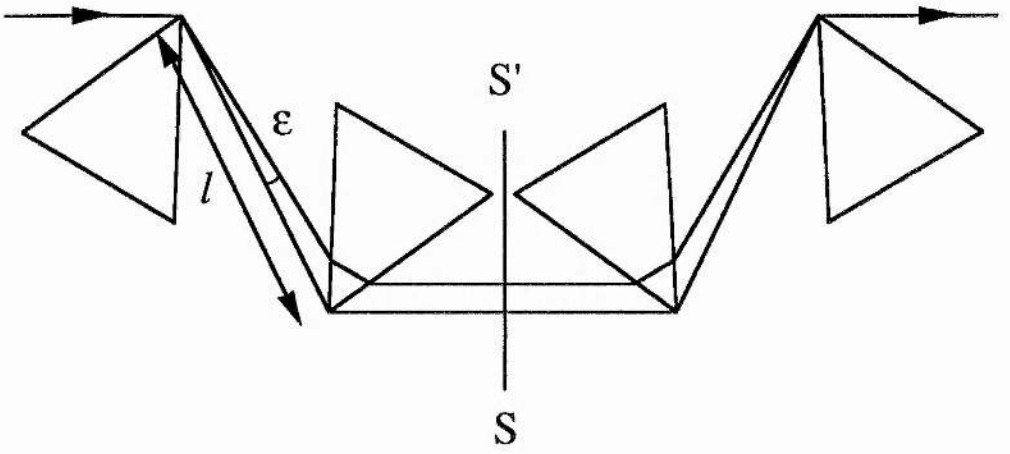

Figure 5.27
Dispersion compensation Fork prism sequence, taken from reference [29].

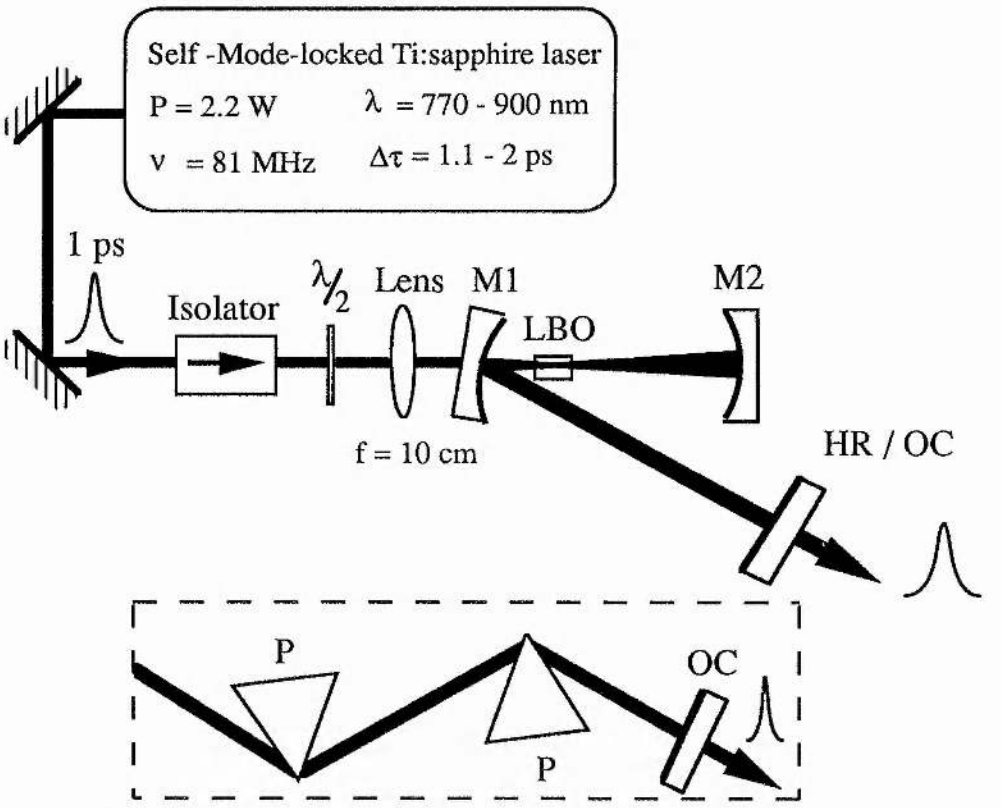

Figure 5.28
Schematic of the Ti:sapphire-pumped LBO OPO with dispersion compensation. The mirrors M_1 and M_2 have radii of curvature r=20 cm. λ/2 is a half-wave plate. HR/OC, high reflector or output coupler.

Using the Sellmeier equations for LBO given by Lin et al [2], a quadratic phase distortion was estimated for the ordinary wave at 1.2 μm of D_{2c} = +115 fs^2/pass in the nonlinear crystal (D_{2c} = +230 fs^2/round trip). For a fixed prism separation, l = 40 cm, the round trip prism insertion to compensate the linear

GVD in the LBO crystal was calculated to be d = 8 mm. This separation was such that the entire positive GVD branch of the OPO could be compensated by simply varying the amount of glass in the cavity with no requirement to alter the prism separation, which would lead to increased system complexity and would be undesirable.

The technique used to insert the prism pair in the cavity was similar to that described by Dudley et al [6]. With the OPO initially oscillating without prisms, the apex of the first prism is inserted slightly into the optical path of the resonated wave, refracting a small amount of signal light but still maintaining parametric oscillation on the undeviated path. The refracted beam is then used to align the second prism and the rear plane mirror. Then, the first prism is inserted further into the optical path to refract all the signal beam. The rear mirror is translated forward to compensate the increased amount of glass introduced into the optical path by the first prism. The OPO oscillates when the cavity is again brought into synchronism.

The optimum prism insertion was found to be equal to d = 4 mm with the prism apex separation l = 40 cm. According to the previous calculations, the corresponding quadratic phase shift was D_{2p} = -125 fs^2, which indicates that the prism pair compensated not only for the linear dispersion of the LBO crystal but also for the nonlinear effects, such as SPM. The experimental configuration of the dispersion compensated cavity is depicted in Figure 5.28, all aspects are identical to the previous case except for the insertion of the prisms. In the following section the results obtained from the dispersion compensated OPO are presented.

5.4.3 Pulse durations

Figure 5.29 shows the variation of the signal pulse durations as the amount of glass is changed in the cavity. The amount of intracavity glass can be converted to an equivalent value of GVD expressed in units of fs^2. In this Figure the variation of the amount of insertion of the SF14 glass into the OPO cavity has the effect of increasing or decreasing the amount of negative GVD contributed by the prism sequence to the cavity. The combined GVD of the cavity elements and crystal as well as the prism sequence result in a variation of the signal pulse duration. It can therefore be observed that by simply adjusting the glass contained in the cavity a variation of pulse duration from 1.9 to 1.1 ps can be obtained. For a glass insertion of 8 mm the minimum signal pulse duration of

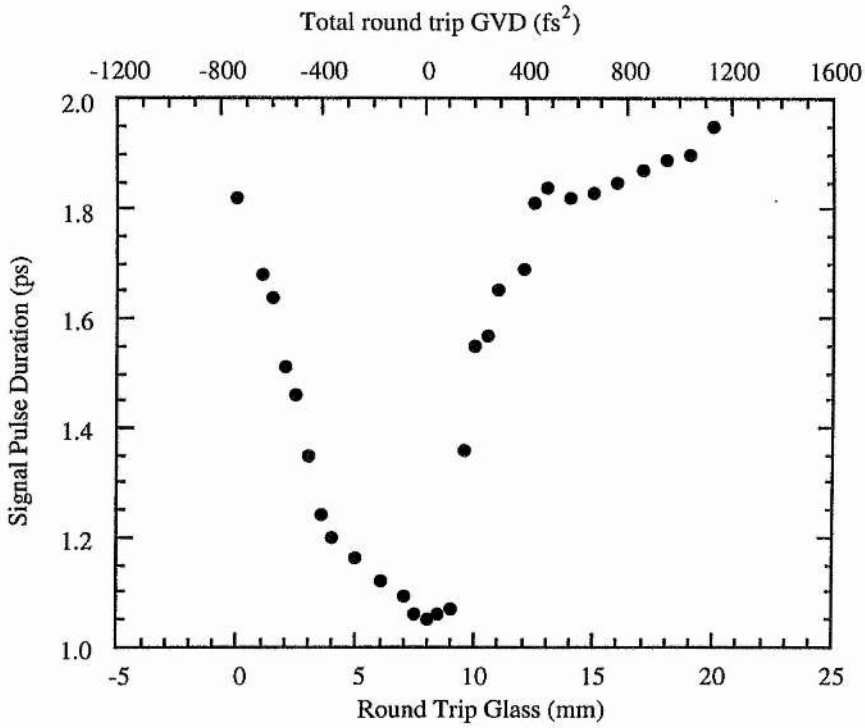

Figure 5.29
Variation in signal pulse duration as a function of insertion of intracavity SF14 glass and round trip GVD.

1.1 ps is observed. The insertion of more glass into the cavity results in an increase to 1.9 ps for 20 mm of glass, due to the fact that there is now too large a net positive GVD in the cavity. By the same argument less than 7 mm of glass results in a net negative GVD, again giving rise to an increased pulse duration. The rise in pulse duration on the negative GVD side is far sharper than for the positive GVD case. These results are similar to those observed in previous studies of mode-locked lasers [33, 34] and are in agreement with theoretical predictions for behaviour in lasers where SPM and GVD co-operate to determine the pulse evolution [26].

The full effect of the dispersion compensation on the signal and idler pulses can be seen in Figures 5.30(d)-(f) and 5.31(d)-(f), where it can be seen that the signal pulse has now become transform-limited with a pulse duration of 1.05 ps. In contrast, the idler pulse is largely unaffected by the prism sequence, as would be expected due to its non-resonant nature. This is further confirmed in Figure 5.32 in which the variation of idler pulse duration is measured as a function of inserted SF14 glass, and hence variation in the complete cavity GVD, it can be observed that the idler pulse duration increases from 2.7 ps for no glass to 2.85 ps for 20 mm of glass, representing an increase of only 5 %. The variation in

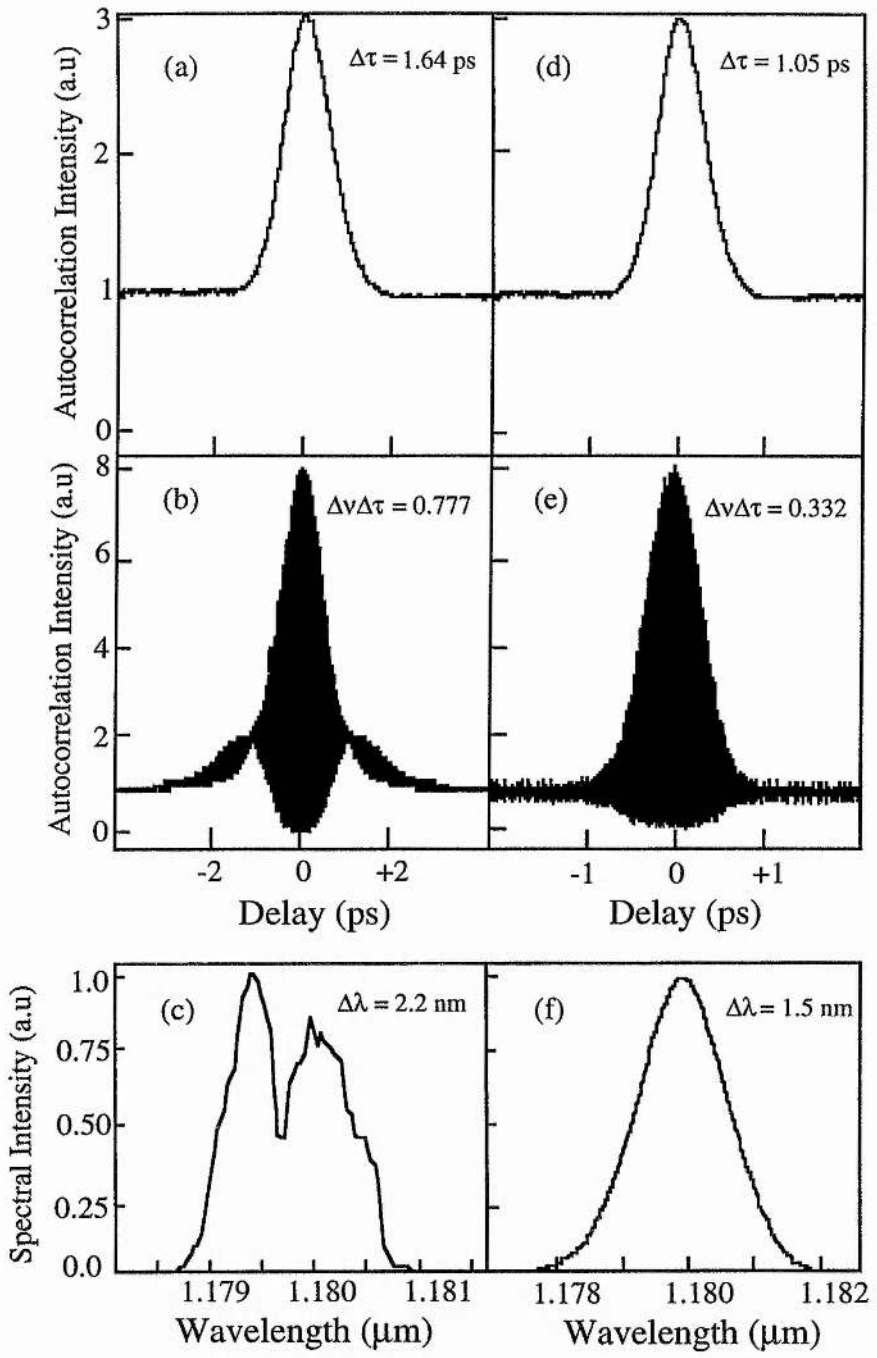

Figure 5.30

(a,d) Intensity and (b,e) interferometric autocorrelation, and (c,f) the corresponding spectrum of the uncompensated and dispersion compensated signal in the region of positive GVD at 1.18 μm. The uncompensated pulse width is 1.64 ps, the time-bandwidth product is $\Delta\nu\Delta\tau$ = 0.777 and the dispersion compensated pulse width is 1.05 ps, with a time-bandwidth product is $\Delta\nu\Delta\tau$ = 0.332.

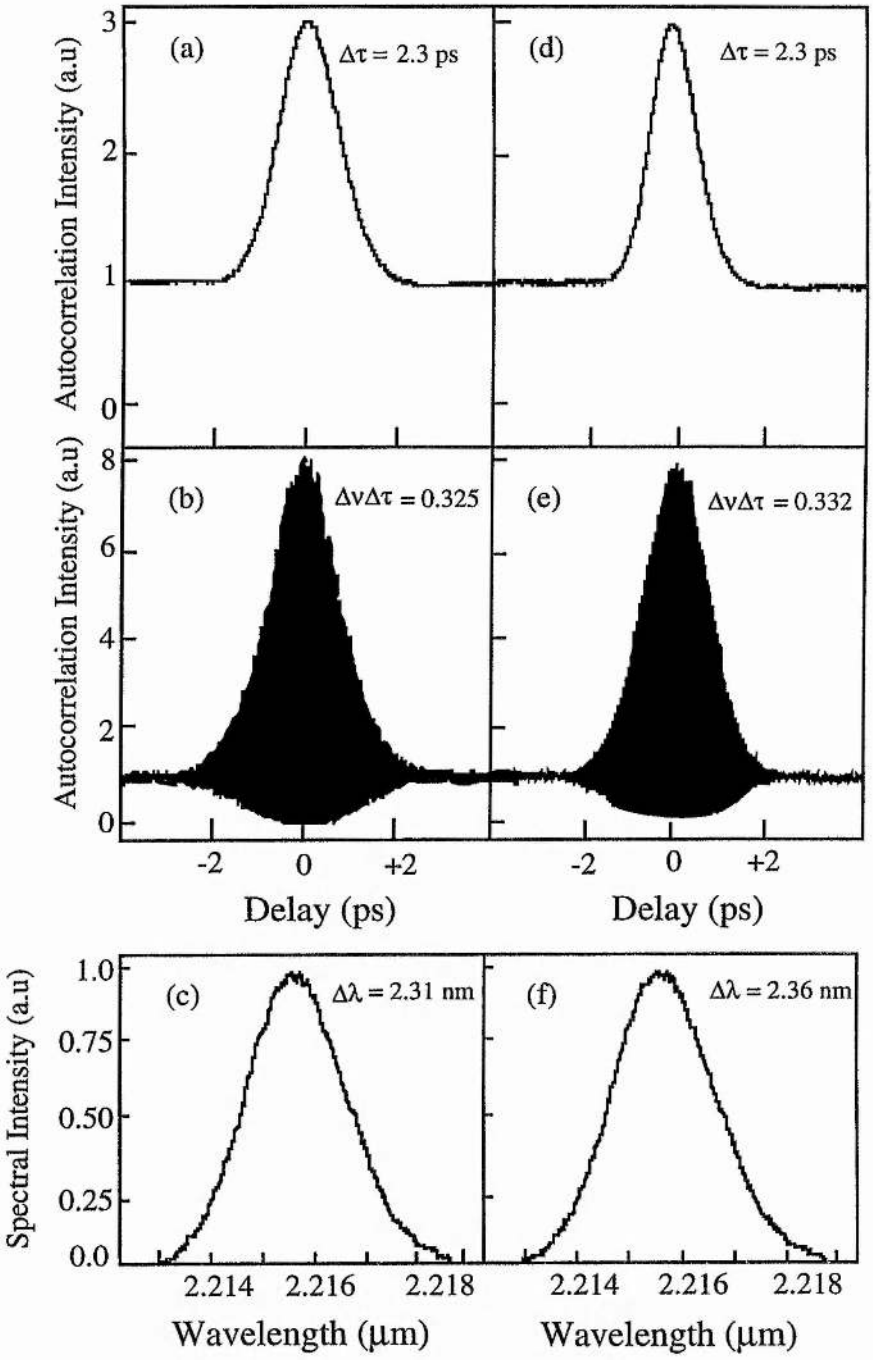

Figure 5.31

(a,d) Intensity and (b,e) interferometric autocorrelation, and (c,f) the corresponding spectrum of the uncompensated and dispersion compensated idler in the region of positive GVD. The uncompensated pulse width is 2.3 ps, the time-bandwidth product is $\Delta\nu\Delta\tau = 0.325$ and the dispersion compensated pulse width is 2.3 ps, with a time-bandwidth product is $\Delta\nu\Delta\tau = 0.332$.

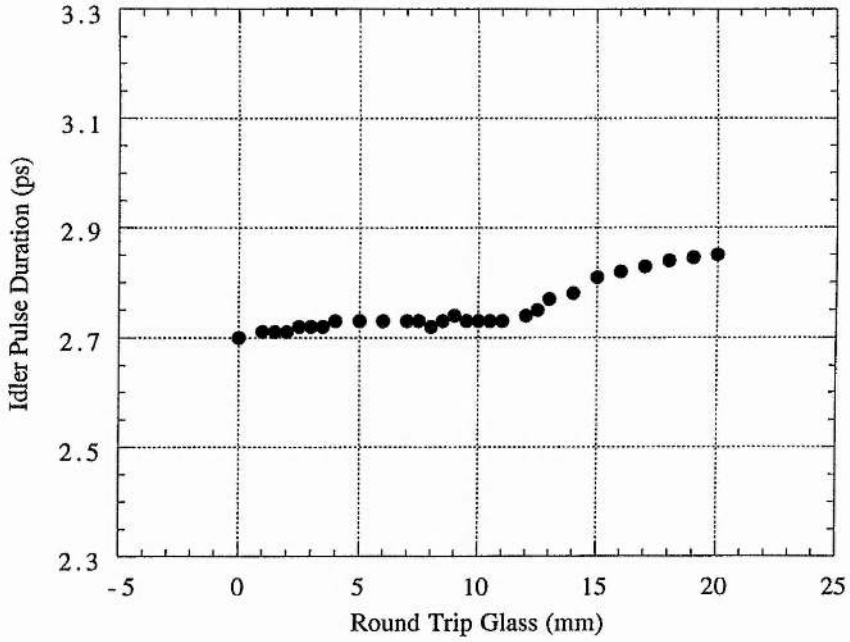

Figure 5.32
Variation in idler pulse duration as a function of insertion of intracavity SF14 glass.

pulse durations across the section of the tuning range covering the transition from negative to positive GVD of the dispersion compensated OPO can be observed in Figures 5.33 (a)-(b). In (a) it can be observed that with the addition of the prism sequence the signal pulse durations remain essentially constant at ~ 1.05 ps, whereas previously they rose from 1.1 to 1.8 ps. In (b) it can be observed that the idler pulse durations increase from 2.0 to 2.7 ps from 2.19 to 2.26 μm irrespective of whether the prism sequence is present. The addition of the prisms to the cavity have been shown to have been successful in correcting the undesirable effect of increasing signal pulse durations due to a net positive GVD. However the prism sequence may have additional negative features, such as increased threshold or a reduction of output power from the OPO. These additional features are investigated fully in the following sections.

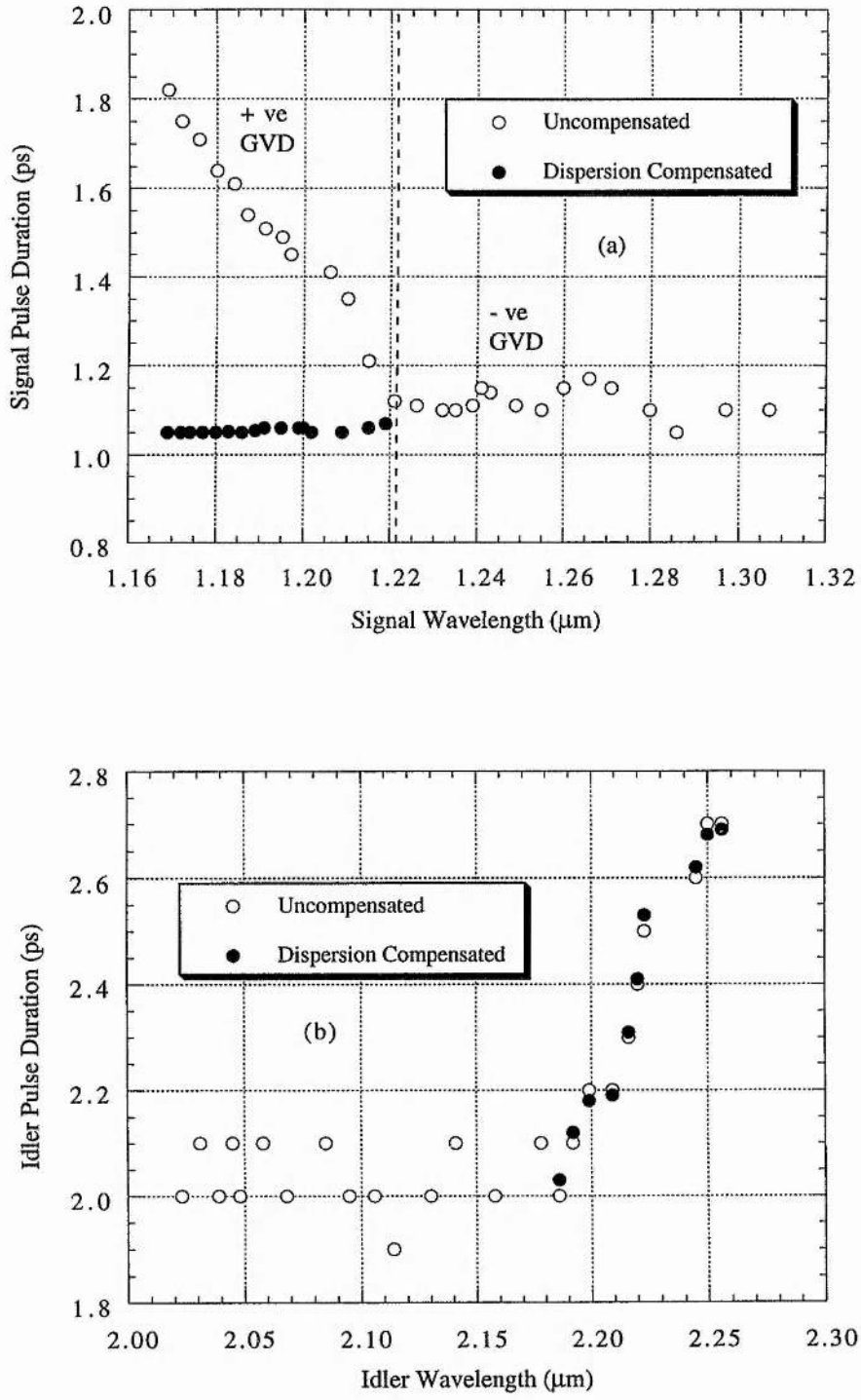

Figure 5.33

The variation in the signal (a) and idler (b) pulse width across the tuning range of LBO OPO. The dashed line represents the approximate transition from the positive to the negative GVD region.

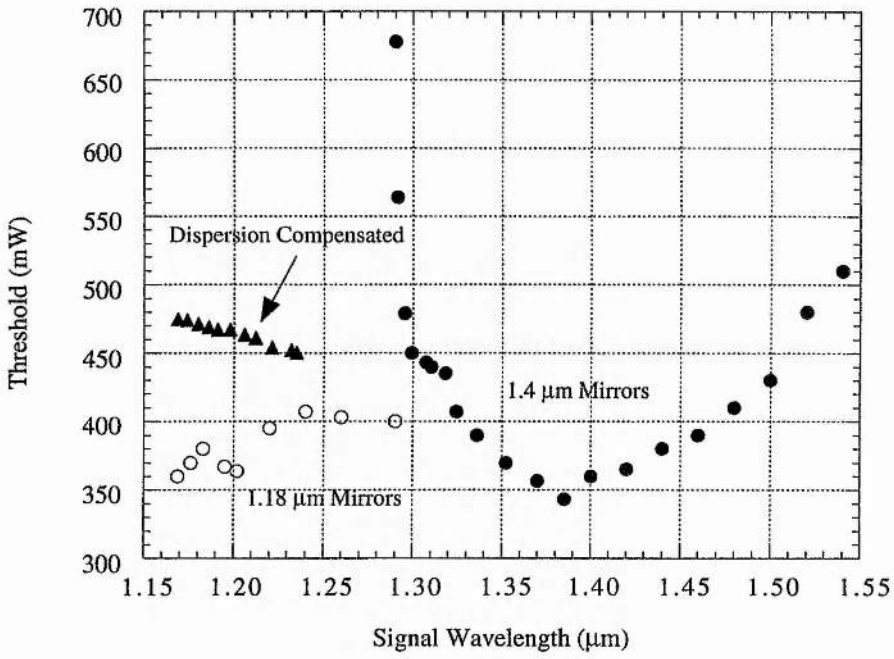

Figure 5.34
Variation in the average pump-power threshold across the tuning range of the LBO OPO.

5.4.4 Threshold

Although the addition of the dispersion compensation measures are essential, if transform-limited performance is to be achieved across the entire tuning range of the OPO, it would be unacceptable if this increased performance resulted in a very large increase in the threshold of the system, as this could lead to device instability. The effect of the prism sequence on threshold is shown in Figure 5.34 in which it can be observed that the threshold increases from ~350 to 450 mW in the positive GVD regime when the prisms are present, representing an approximate increase of 25 %. This increase could be due to several factors, one being that, the addition of dispersion compensation results in reduced temporal overlap between pump and the signal pulse in the OPO. Another factor may be that imperfections in the cut of the LBO crystal rotate the polarisation of the signal wave and, consequently, increase loss at each of the eight Brewster surfaces encountered by the pulse during one cavity roundtrip. This moderate increase in not problematic as it occurs over only a very small section of the tuning range. However, it should still be possible to reduce this increased

threshold by further work in optimising the prism orientations and positions, hence making it an even less significant increase.

5.4.5 Output power

The output power of the dispersion compensated OPO can be seen in Figure 5.35. The addition of the prisms produces a 90 mW reduction in output power,

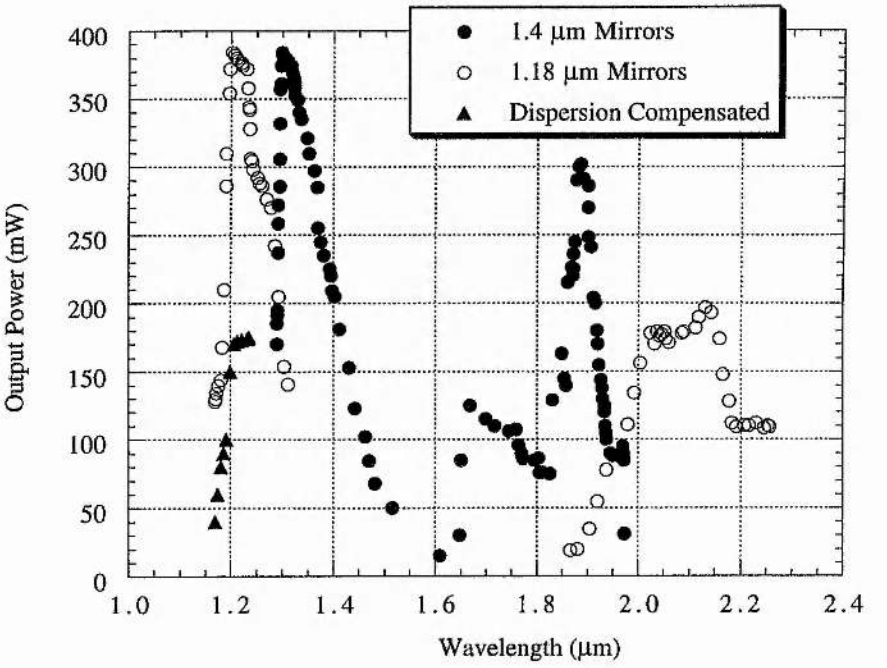

Figure 5.35
The average output power of the LBO OPO as a function of wavelength, for a pump power of 2 W.

again this loss is relatively small and might be reduced by further optimisation of the prism alignment. Optimisation of mirror reflectivities should also allow the maintenance of high output power across the entire available tuning range.

5.5 System Improvements

Although the 30 mm LBO system is a very robust system producing excellent quality, highly tunable pulses, several design amendments may improve its performance still further. The most important improvements are discussed below.

5.5.1 Ring cavity

In an OPO, the parametric gain is present only in the direction in which the pump pulses are travelling. The second pass through the crystal causes only loss, and thus a ring cavity will have lower threshold and higher efficiency. The linear cavity was used in this device because it is easier to align and has a larger stability region. A cavity configuration for a ring cavity is shown below in Figure 5.36, the ring cavity also has advantages in frequency-doubled systems (See chapter 6).

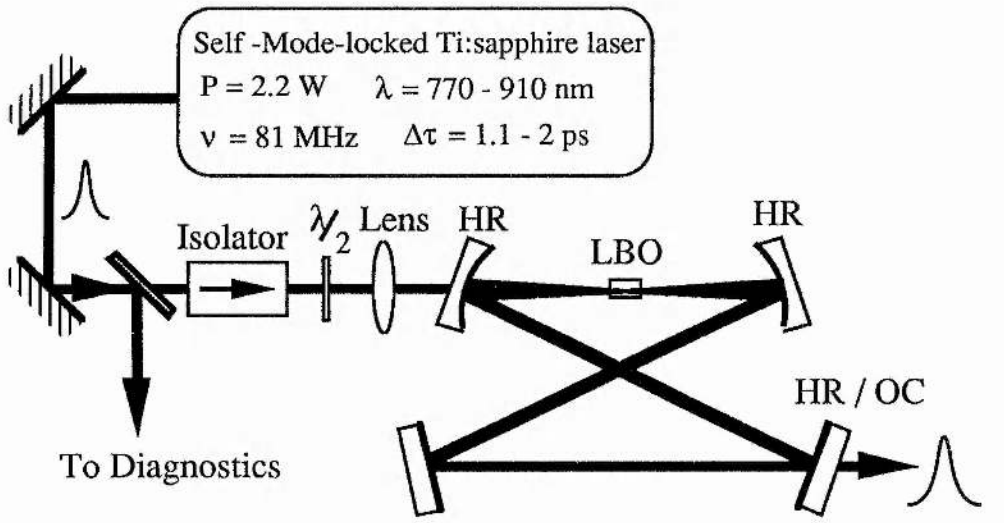

Figure 5.36
The experimental configuration for the LBO OPO in a ring cavity.

5.5.2 Cavity Loss Reduction

The amount of loss encountered by the signal and pump pulses in the OPO cavity are of paramount importance in the operation of the device, as these processes govern ultimately the threshold and output power produced from the device. The LBO crystal used in this experiment was antireflection coated to reduce Fresnel losses in the pump and signal beams. The coatings used proved to be excellent,

with no problems encountered up to the highest operational temperature of 230 °C. However, if operation to more extreme temperatures (lower signal wavelengths) was required, then difficulties may start to arise in the depositing of these AR coatings on the surface of the LBO crystal. Problems can arise due to the fact that the thermal expansion coefficients are different in the 3 directions, which can result in coatings falling off. This problem can be solved by the use of a Brewster cut crystal, which as there is no coating has very little difficulty in being operated at very high temperatures. The disadvantage of using a Brewster cut crystal is that alignment becomes more difficult than that of the plain face conditions.

5.5.3 Air currents and absorption

A design feature already implemented to produce better device stability against such features as air current movement due to air conditioning is the enclosing of the OPO in a perspex case. This case was designed to allow easy access to the

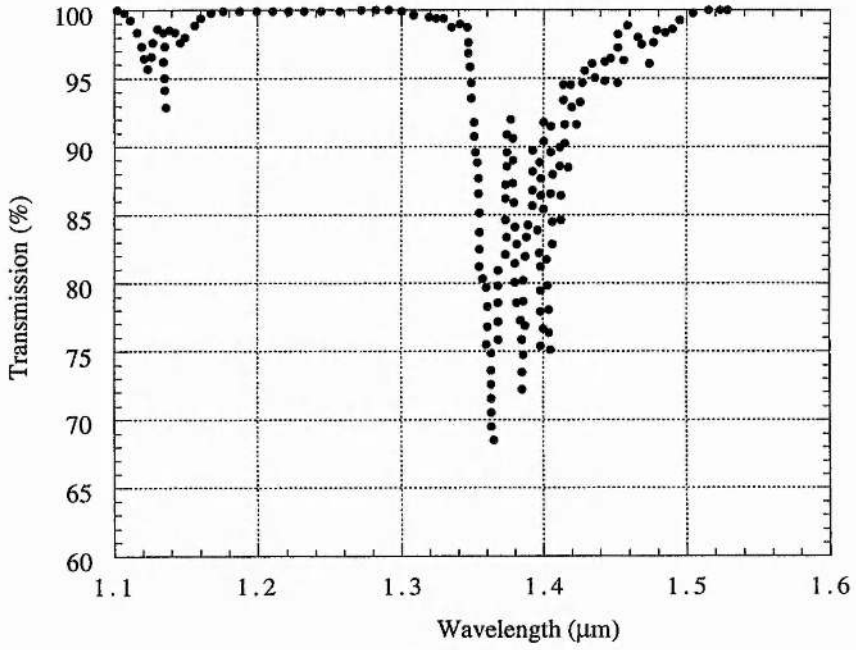

Figure 5.37
Absorption spectrum of 4 m of air as a function of wavelength [35].

system so that optimum operation could be maintained as well as sealing the cavity from external perturbations. This box typically reduced the amplitude noise by ~ 1%. Further refinement of the box design could lead to the solving of a further problem. Water vapour within the cavity leads to losses in the cavity at

wavelengths around 1.38 μm. These losses are due to a series of narrow absorption lines whose maximum can approach 30 % [35], as shown in Figure 5.37. To improve the tuning and power output throughout this region it would be necessary to seal and purge the cavity with dry nitrogen [35].

5.5.4 OPO Stabilisation.

The operation of the OPO over a period of several minutes is very stable. It was, however, observed that over many hours the cavity length drifted, hence causing instability in the output. This can be attributed to temperature induced shifts in the optical bench and optical components, as well as excessive air currents. If results were required to be taken over periods of hours, with the OPO remaining at optimal operation then an active length stabiliser would have to be implemented.

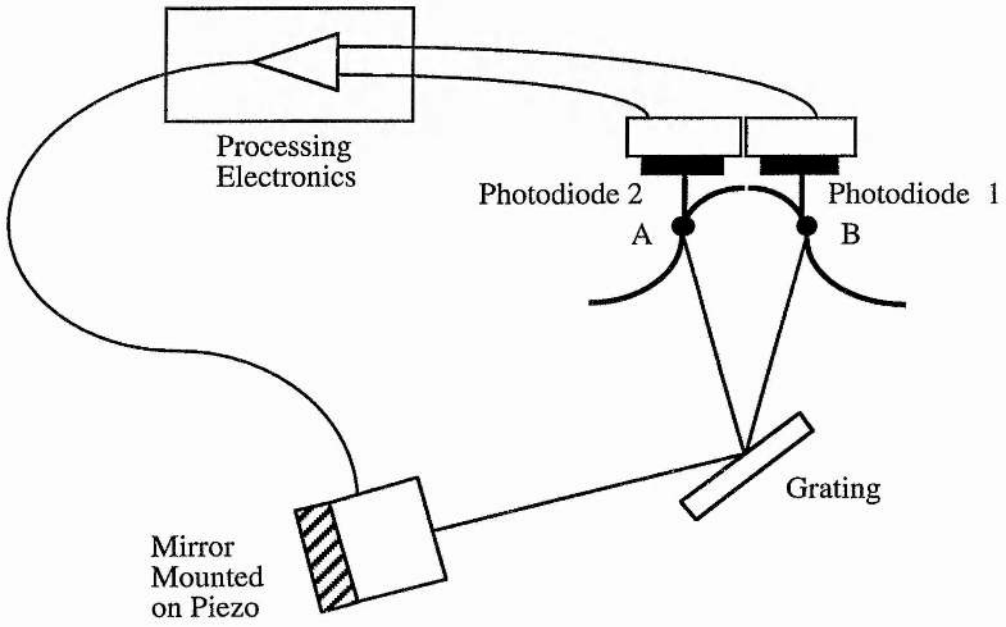

Figure 5.38
Arrangement for detecting error signal for active cavity length stabiliser.

This involves the detection of an error signal which indicates the error in cavity length. This signal is fed through an operational amplifier, which then drives a PZT in the proper direction to correct the length error. The error signal should be a monotonic function of cavity length, and the optimum operating point should not be the peak. The best error signal comes from the OPO length tuning. This was first used by Chesnoy and Fini [36] to stabilise a synchronously-pumped femtosecond laser. The arrangement can be seen in Figure 5.38. A leakage beam is sent to a diffraction grating, and two apertured photodiodes are

put in the dispersed spectrum, so as to sample points A and B, on either side of the spectral peak. Since the spectrum shifts monotonically with changes in cavity length, either A or B provides a suitable error signal. The difference signal A - B allows cancellation of intensity fluctuations and additionally produces a larger error signal for a given spectral shift. An electronic stabiliser unit must be built to process the error signal and provide a drive voltage for the PZT, for more details see [37] and [38].

5.5.5 1.5 μm mirror set.

One of the disappointing features of the OPO performance is the dip in output power encountered at around 1.5 μm. The main reason for this is that at present the system is operated with 1.18 μm and a 1.4 μm mirror sets, which of course produce optimal performance around the central coating wavelengths only. In order to produce better output power performance around 1.5 μm it is proposed that a 1.5 μm coated mirror set is used, this is currently being implemented. This will allow greater output powers around the very important communication window of 1.55 μm. Initial measurements with this mirror set demonstrate that the OPO can produce ~100 mW of output power at 1.55 μm [39].

5.6 Conclusions

In this chapter a new Ti:sapphire-pumped OPO based on the material LBO has been demonstrated. The LBO system has been shown to be a powerful and versatile source of high-repetition-rate picosecond pulses for the near-infrared. It can provide transform-limited 1.1 ps signal and 2.1 ps idler pulses over a wavelength range from 1.2 to 2.2 μm, without the requirement for dispersion compensation in the cavity. Transform-limited signal and idler pulses beyond these limits are also readily attainable with intracavity dispersion compensation, with little resulting degradation in performance. The tuning range of the LBO OPO is continuous except close to wavelength degeneracy and the total wavelength coverage extends from 1.160 to 2.185 μm, with a single LBO crystal. This spectral range is at present limited by the tunability of the pump laser and could be further extended to cover the range 1-2.4 μm with a new Ti:sapphire mirror set. Up to 690 mW of output power has been generated for 2 W of input pump power at 5 times threshold. For this output power a depletion of 52 % was achieved with a corresponding external extraction efficiency of 34.5 %. Successful dispersion compensation of the Ti:sapphire-pumped LBO OPO has been achieved so that it can now provide transform-limited 1.1 ps signal and

2.1 ps idler pulses over the entire wavelength range from 1.160 to 2.185 μm. The addition of dispersion compensation resulted in a small increase in the threshold from 350 mW to 450 mW and a small reduction in output power of ~ 90 mW. However these may be reduced by further optimisation of the prism orientations. Despite the requirement for cavity length synchronism, the LBO OPO is a remarkably robust and stable source, capable of routine day-to-day operation without the need for re-alignment of the resonator. In the absence of cavity length stabilisation, oscillation can be maintained for extended periods of several hours at a time without re-adjustments of cavity length. The continuous wavelength coverage of LBO OPO with a single crystal is not available to similar Ti:sapphire-pumped picosecond OPOs and its output power capability, high efficiency and transform-limited performance is unmatched by most solid-state-pump-based systems. As such, the LBO OPO represents a highly versatile, yet simple and cost-effective source of picosecond near-infrared pulses which will be useful as a source for many applications.

References

1. Photox optical systems P.O. Box 274, No 2, Pullens Lane, Headington, Oxford, OX3 OBJ

2. S. Lin, J. Y. Huang, J. Ling, C. Chen, and Y. R. Shen, Appl. Phys. Lett. **59**, 2805 (1991)

3. S. P. Velsko, M. Webb, L. Davis, and C. Huang, IEEE J. Quantum Electron. **27**, 2182 (1991)

4. W. S. Pelouch, P. E. Powers, and C. L. Tang, Opt. Lett. **17**, 1070 (1992)

5. P. E. Powers, S. Ramakrishna, C. L. Tang, and L. K. Cheng, Opt. Lett. **18**, 1171 (1993)

6. J. M. Dudley, D. T. Reid, M. Ebrahimzadeh, and W. Sibbett, Opt. Commun. **104**, 419 (1994)

7. S. Guha, F. Wu, and J. Falk, IEEE J. Quantum Electron. **QE-18**, 907 (1982)

8. H. Avramopoulos, P. M. W. French, G. H. C. New, M. M. Opalinska, J. R. Taylor, and J. A. R. Williams, Opt. Commun. **76**, 229 (1990)

9. W. L. Nighan, T. Gong, and P. M. Fauchet, IEEE J, Quant. Electron. **25**, 2476 (1989)

10. M. Ebrahimzadeh, S. French, W. Sibbett, and A. Miller, Appl. Phys B. **60**, 443 (1995)

11. M. F. Becker, D. J. Kuizenga, D. W. Phillion, and A. E. Siegman, J. Appl. Phys. **45**, 3996 (1974)

12. E. C. Cheung and J. M. Liu, J. Opt. Soc. Am. B **7**, 1385 (1990)

13. P. E. Powers, S. Ramakrishna, C. L. Tang, and L. K. Cheng, Opt. Lett. **18**, 1171 (1993)

14. Q. Fu, G. Mak, and H. M. Van Driel, Opt. Lett. **17**, 1006 (1992)

15. W. S. Pelouch, P. E. Powers, and C. L. Tang, Opt. Lett. **17**, 1070 (1992)

16. J. M. Dudley, D. T. Reid, M. Ebrahimzadeh, and W. Sibbett, Opt. Commun. **104**, 419 (1994)

17. S. D. Butterworth, S. Girard, and D. C. Hanna, J. Opt. Soc. Am. B **12**, 2158 (1995)

18. A. P. Baronavski, H. D. Ladouceur, and J. K. Shaw, IEEE J. Quant. Electron. **29**, 580 (1993)

19. D. C. Edelstein, E. S. Wachman, and C. L. Tang, Appl. Phys. Lett. **54**, 1728 (1989)

20. J. Chung and A. E. Siegman, J. Opt. Soc. Am. B **10**, 2201 (1993)

21. M. J. McCarthy and D. C. Hanna, J. Opt. Soc. Am. B **10**, 2180 (1993)

22. 19. D. C. Edelstein, E. S. Wachman, and C. L. Tang, Appl. Phys. Lett. **54**, 1728 (1989)

23. G. Mak, Q. Fu, and H. M. van Driel, Appl. Phys. Lett. **60**, 542 (1992)

24. Q. Fu, G. Mak, and H. M. van Driel, Opt. Lett. **17**, 1006 (1992)

25. J. D. Kafka, M. L. Watts, and J. W. Pieterse, in *Conference on Lasers and Electro-Optics*, Vol. 11 of 1993 OSA Technical Digest Series (Optical Society of America, Washington, D.C., 1993), paper CPD32

26. T. J. Driscoll, G. M. Gale, and F. Hache, Opt. Commun. **110**, 638 (1994)

27. D. T. Reid, M. Ebrahimzadeh, and W. Sibbett, Opt. Lett. **20**, 55 (1995)

28. M. Ebrahimzadeh, S. French, and A. Miller, J. Opt. Soc. Am. B **12**, 2180 (1995)

29. R. L. Fork, O. E. Martinez, and J. P. Gordon, Opt Lett. **9**, 150 (1984)

30. R. L. Fork, C. H. Brito-Cruz, P. C. Becker, and C. V. Shank, Opt Lett. **12**, 483 (1987)

31. Z. Zhang and T. Yagi, Appl. Phys. Lett. **63**, 2993 (1993)

32. Optical glass, Schott Glass Technologies, Inc. catalog

33. A. Finch, G. Chen, W. Sleat, and W. Sibbett, J. Mod. Opt. **35**, 345 (1988)

34. H. Avramopoulos, P. M. W. French, G. H. C. New, M. M. Opalinska, J. R. Taylor, and A.R. Williams, Opt. Commun. **76**, 229 (1990)

35. J. D. Kafka, M. L. Watts, and J. W. Pieterse, J. Opt. Soc. Am. B **12**, 2147 (1995)

36. J. Chesnoy and L. Fini, Opt Lett. **11**, 635 (1986)

37. E. S. Wachman, D. C. Edelstein, and C. L. Tang, Opt Lett. **15**, 136 (1989)

38. D. C. Edelstein, PhD Thesis, Cornell University, 151 (1991)

39. G. T. Kennedy, J. T. Hyland, M. Ebrahmizadeh, and A. Miller (Private communication)

Contents

6.1 Introduction

Many applications in the field of ultrashort spectroscopy require pulses in the visible wavelength region. Up to now, only synchronously-pumped or passively mode-locked dye lasers were used for high-repetition rate picosecond and femtosecond applications in the visible [1]. These systems have many disadvantages because of the necessity to use different dye/pump laser configurations with only limited tuning being available. On the other hand, the red spectral range is of increasing importance, for example, for research on quaternary alloys such as AlGaInP.

Recently, Ti:sapphire-laser-pumped optical parametric oscillators (OPOs) have proved ideal in meeting the need for ultrafast light sources tunable from the visible to the mid-infrared. The device described in Chapter 5 covers the wavelength range 1.150 to 2.260 μm with the signal branch from 1.150 to 1.560 μm. If these signal wavelengths of the LBO OPO are frequency-doubled, as shown in Figure 6.1, this will access the wavelength range 575 to 780 nm. This visible region is extremely important as it lies between the fundamental and second harmonic of the Ti:sapphire laser. The first demonstration of the frequency-doubling of an ultrashort-pulse OPO was performed by Ellingson and Tang [4]. This system used a critically phase-matched BBO crystal inside the

ring cavity of a x-z plane critically phase-matched femtosecond KTP OPO, this system yielded conversion efficiencies of 2.1 %. Recently, Reid et al [5] demonstrated intracavity doubling of a femtosecond RTA OPO, again BBO was used as the doubling medium, this system produced tunable 60 fs pulses in the range 620-660 nm, with powers as high as 170 mW. In this chapter three schemes are described which produce tunable picosecond pulses in the visible wavelength region.

The first approach involves the direct single-pass extracavity frequency-doubling of the LBO OPO to provide high-repetition-rate picosecond pulses in the visible at tens of milliwatts of average power. This technique has also been recently used in a KTP OPO to provide 500 fs pulses tunable in the visible [6]. Using type I and II temperature-tuned non-critically phase-matched LBO, efficient single-pass frequency-doubling of the signal into the red wavelength

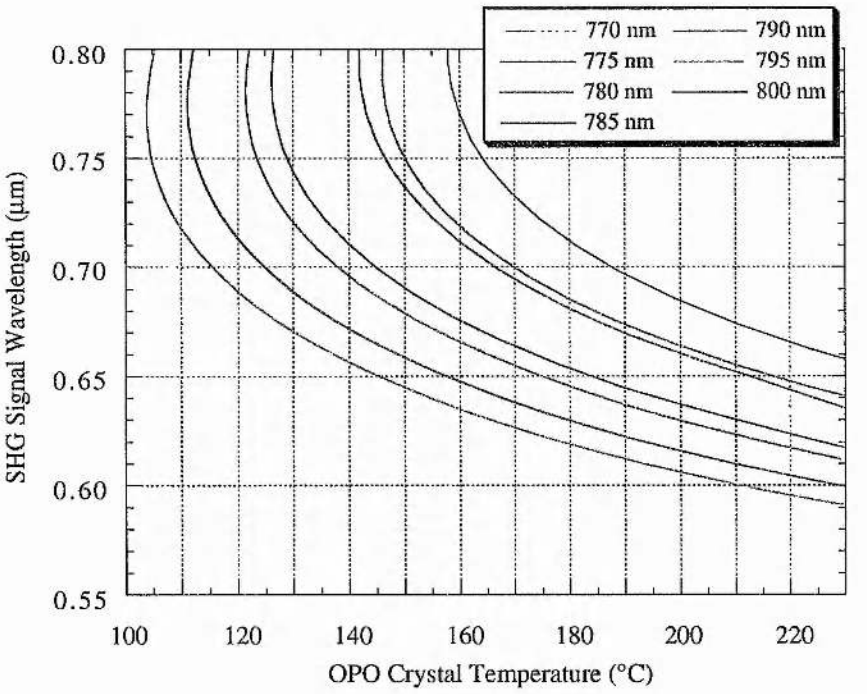

Figure 6.1
Theoretical temperature and pump wavelength tuning range of the frequency-doubled Ti:sapphire-pumped LBO OPO. Using the Sellmeier equations of [2] and the temperature dependence of [3].

region has been achieved. The second approach involves the development of the first Ti:sapphire-pumped intracavity-frequency-doubled picosecond OPO. This system which is based entirely on LBO, uses type I and type II temperature-

tuned NCPM in the material to provide efficient frequency-doubling of the signal pulses into an extended wavelength region in the visible spectrum. The third approach is similar to the second system, with the advantage that it is based solely on type I frequency-doubling, this does however lead to added device complexity.

The operation and configuration of all three approaches to produce tunable visible picosecond pulses will be detailed in this chapter. The suitability of LBO as a frequency-doubling crystal in ultrashort OPOs and lasers will be outlined. The full characterisation of all the devices operated with and without dispersion compensation will also be discussed in detail.

6.2 The LBO frequency-doubling crystal

The choice of LBO as the second harmonic generation (SHG) crystal was governed in the main part by its NCPM capability across the entire signal range of the OPO LBO. For second harmonic generation, LBO can be phase-matched in a number of geometries under both type I and II interaction, with non-vanishing nonlinear coefficients. In particular, NCPM can be accomplished along the crystal optic axes without the deleterious effects of spatial walkoff. In these devices two non-critically cut LBO crystals were used to achieve SHG across the entire tuning range of the signal branch of the OPO; an x-cut crystal was used for type I and z-cut crystal was used for type II (see Figure 6.2). The requirement for the use of two crystals will be discussed later. The NCPM geometry is also accompanied by large angular acceptance bandwidths (see section 6.3) so that tightly focused beams can be used without compromising conversion efficiency. These characteristics are particularly important in efficient SHG conversion of relatively low-energy, low-peak-power pump pulses with tightly focused beams. This is the case with the high-repetition-rate pump pulses available from the picosecond Ti:sapphire laser used in these experiments, where pulse energies of typically 10-20 nJ with peak powers of around 10-20 kW are available in focused beam diameters of ~50 μm (FWHM). In contrast to KTP or BBO, LBO is also temperature-tunable. This feature avoids the need for angle-tuning which often results in a reduction in conversion efficiency and output power and requires re-alignment of the OPO resonator. This is particularly useful in high-repetition-rate picosecond OPOs where, unlike femtosecond oscillators, angle-tuning is generally precluded by the effects of spatial walkoff because of longer interaction lengths, lower peak powers and tightly focused beams.

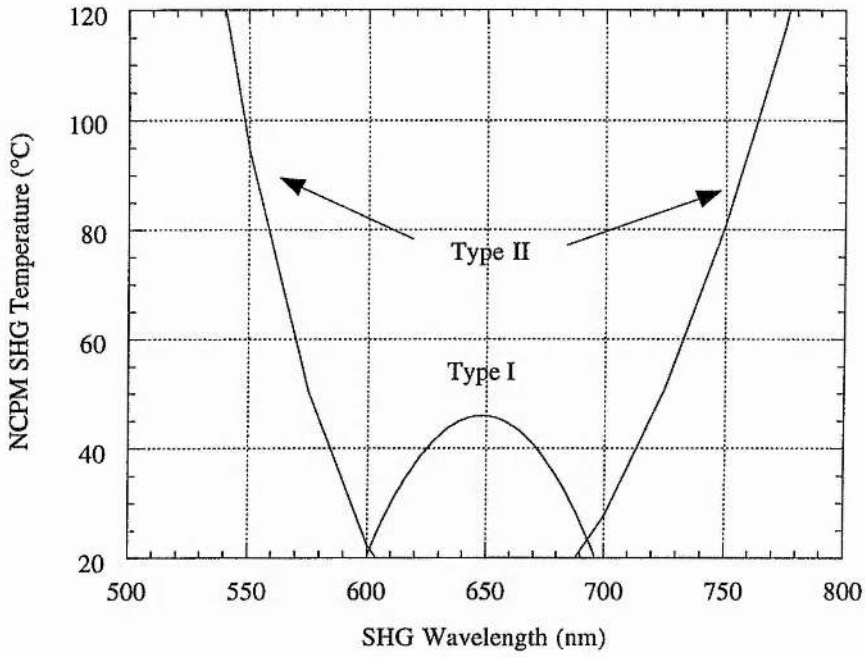

Figure 6.2
Theoretical frequency-doubling crystal temperatures required to double the wavelength tuning range of the Ti:sapphire-pumped LBO OPO. Using the Sellmeier equations of [2] and the temperature dependence of [3].

6.3 Frequency-doubling conversion efficiency properties

As discussed in chapters 3 and 4 when considering parametric generation it cannot be assumed that the phase-mismatch condition Δk, is zero. This is due to the fact that laser pulses have finite bandwidths. It is therefore of interest to see the extent to which the pump beam can differ from the ideal case yet still provide efficient frequency-doubling.

The acceptance angle and spectral bandwidth are very important crystal features as these relate to the ultimate conversion efficiency that can be obtained from the frequency-doubling process. These two parameters limit the usable crystal length for a given fundamental beam divergence and linewidth.

6.3.1 Acceptance angle

The acceptance angle was calculated for type I NCPM frequency-doubling in LBO by using the same method as that outlined in Chapter 4. The result of these calculations are shown in Figure 6.3, the values of between 3.5-6 Degrees

$(cm)^{1/2}$ are comparable with the values obtained for type I parametric generation in NCPM LBO and so this large value of acceptance angle should present no problems governing the usable length of frequency-doubling crystal.

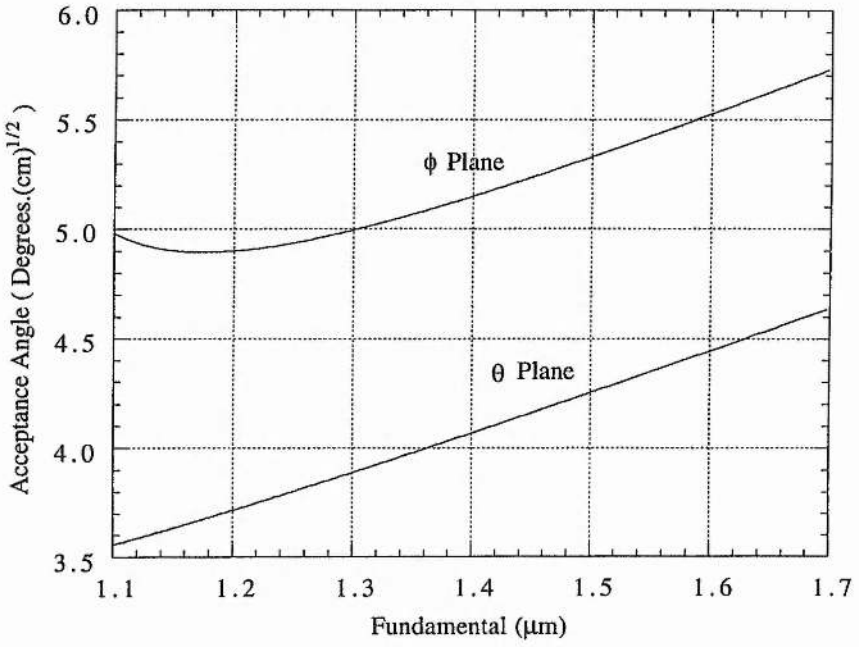

Figure 6.3
The calculated frequency-doubling acceptance angles in the ϕ and θ direction in temperature-tuned LBO for type I non-critical propagation along the optical x-axis ($n_x<n_y<n_z$).

6.3.2 Spectral acceptance bandwidth

The spectral acceptance bandwidth for phase-matching is also an important crystal parameter that needs to be considered. This quantity is particularly relevant in SHG of ultrashort pulses where large spectral widths are involved. The acceptance bandwidth can effect both the efficiency of conversion and the SHG pulse duration. If the acceptance bandwidth is too small, the crystal can not accommodate the available spectral content of the SHG pulses. The SHG acceptance bandwidth of LBO for both type I and II SHG has been calculated. By using the same method as that described in Chapter 4 the full-width acceptance bandwidth for the fundamental wave in a collinear SHG interaction can be derived. When the fundamental radiation has a frequency of ω_1 and the frequency-doubled light ω_2, then the wavevector mismatch will be

$$\Delta k = 2k_1 - k_2 \tag{6.1}$$

The full-width acceptance bandwidth ($-\pi/l < \Delta k < \pi/l$) for a crystal of length l is then calculated using a Taylor-series expansion for $\partial\Delta k/\partial\lambda_1$, and can be written as,

$$\Delta\lambda = \frac{2\pi}{l}\left(\frac{4\pi}{l}\frac{\partial n_1}{\partial\lambda_1} - \frac{2\pi}{l}\frac{\partial n_2}{\partial\lambda_2}\right) \tag{6.2}$$

Evaluation of this quantity yielded in type I, values in the range 7-11 nm.cm across the available tuning range (see Figure 6.4). In type II, the quantity rises from 5 nm.cm to become asymptotic at 1.3 μm, where values of several hundred nm.cm are obtained. This implies that the pulse duration of the frequency-doubled light should not be limited by the crystal bandwidth.

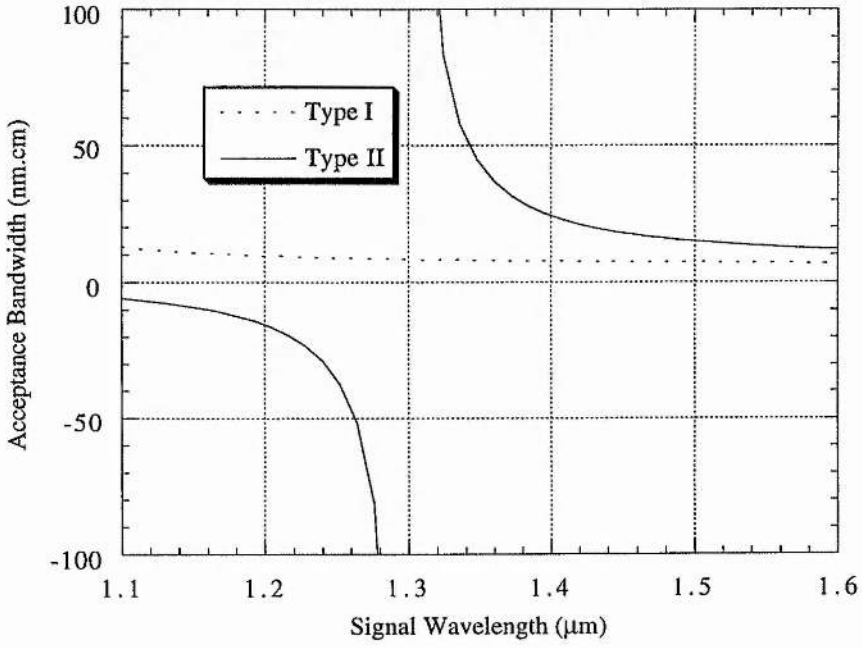

Figure 6.4
The calculated spectral acceptance bandwidth in temperature-tuned frequency-doubling LBO (ϕ=0°, θ=90°).

6.4 Modelling of temporal characteristics

In the context of ultrashort-pulse SHG, there are a number of important temporal effects that also need to be taken into account. These effects have been calculated using the same methods as those discussed in Chapter 4.

6.4.1 Group velocity walkaway

A particularly important parameter is temporal walkaway between the fundamental and second harmonic which determines the degree of temporal overlap between the interacting pulses. Because of the absence of gain outside the temporal window of the fundamental signal pulse, a large temporal walkaway can result in significant reductions in conversion to second harmonic and can also lead to pulse broadening. This can limit the useful length of

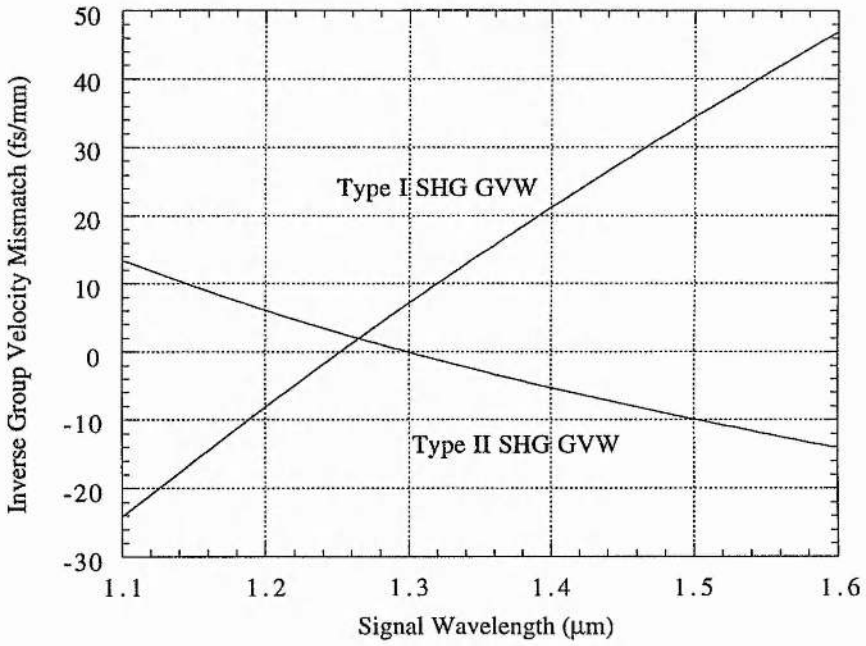

Figure 6.5
Variation in the inverse group velocity mismatch, Δv_g^{-1} between the signal and SHG signal across the tuning range of the LBO (θ=90°, ϕ=0°) OPO.

nonlinear crystal over which efficient interaction can occur. The effects of temporal walkaway can be estimated by evaluating the differences in the inverse group velocity between the fundamental and second harmonic. The result of these calculations in both type I and type II SHG are shown in Figure 6.5 where the magnitude of the inverse group velocity mismatch between the fundamental

and second harmonic in temperature-tuned LBO is plotted as a function of the signal wavelength. The calculations are based on the Sellmeier equations of Lin et al [2] and the temperature-dependent refractive indices of Velsko et al [3]. It is seen that the temporal walkaway between the fundamental and second harmonic in type I (II) is limited to about 20-40 (10-15) fs/mm across the tuning range. The walkaway between the fundamental and second harmonic has a first-order effect on the SHG conversion efficiency [7] and is thus the most important parameter in determining the maximum useful interaction length.

6.4.2 Crystal length calculations

The 20-40 (10-15) fs/mm walkaway in type I (II) implies that with pump pulses of 1 ps duration, LBO crystal lengths up to 50 (20) mm can be used without

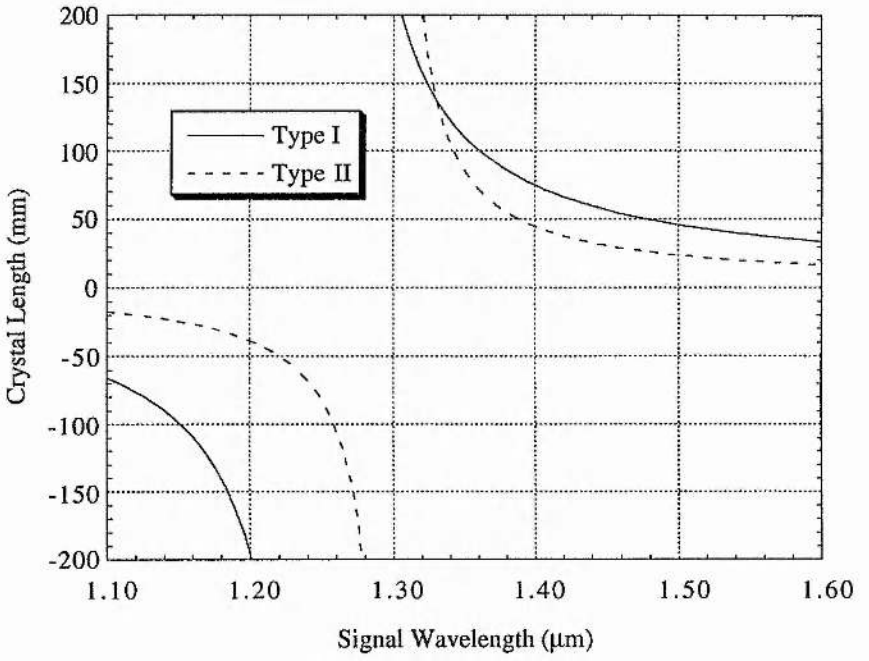

Figure 6.6
Maximum permissible LBO crystal lengths to perform frequency-doubling in the LBO (θ=90°, ϕ=0°) OPO.

serious reduction in SHG efficiency or significant pulse broadening (see Figure 6.6). Therefore, it may be concluded that temporal walkaway in LBO is not a limiting factor in the attainment of (sufficiently) high SHG efficiency.

6.4.3 Group velocity disperison

In addition to group velocity walkaway, a second important temporal effect is group velocity dispersion (GVD). In Figure 6.7, the variation in the signal and frequency-doubled signal GVD in LBO is shown for the polarisation direction that each takes in the frequency-doubling crystal. The GVD values were calculated by evaluating the dispersion parameter β'' where

$$\beta'' = \frac{\partial^2 k}{\partial \omega^2} = \frac{\lambda^3}{2\pi c^2}\frac{\partial^2 n}{\partial \lambda^2} \tag{6.3}$$

It is seen from the plot that for type I the SHG GVD is positive across the entire tuning range, taking the values ($45 < \beta'' < 80$ fs²/mm), with the type I signal GVD being as discussed in the previous chapter. For the type II process, the GVD remains small ($0 < \beta'' < 5$ fs²/mm) and close to zero across the entire

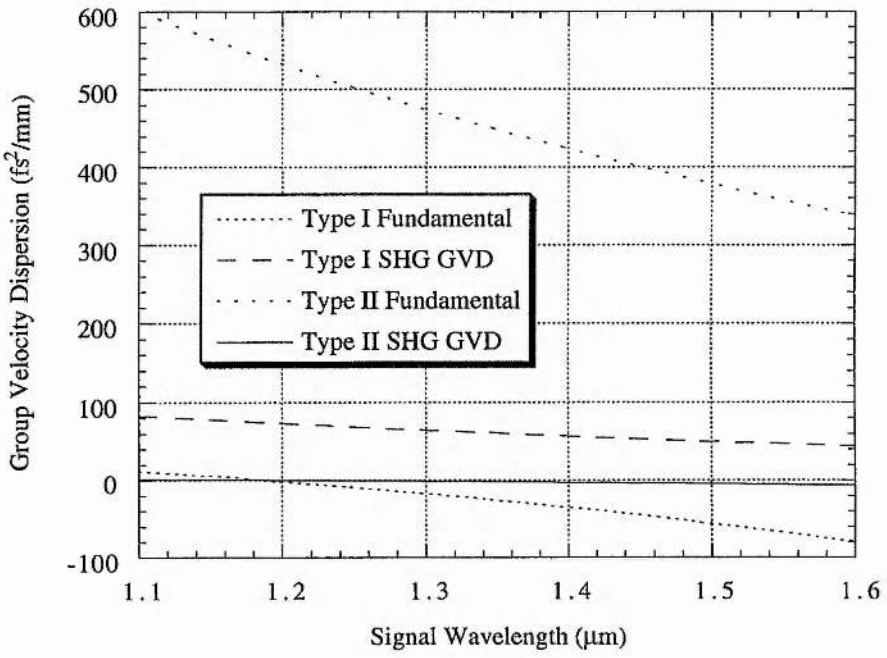

Figure 6.7
The variation in group velocity dispersion in LBO for type I and II frequency-doubling in two different crystal orientations.

available tuning range. The type II fundamental GVD is, however, large ($340 < \beta'' < 600$ fs²/mm). It is, of course, desirable to operate at all times in the negative GVD regime, however it is only the type I SHG signal that is significantly positive. This implies that transform-limited pulses will be

attainable without the need for intracavity dispersion compensation for the three cases where the GVD is small or negative. The situation where the GVD is large and positive will however not necessarily lead to any pulse broadening from the fundamental to the frequency-doubled pulse. This characteristic makes LBO particularly attractive for the use as a doubling crystal in picosecond OPOs.

6.5 Externally-doubled LBO OPO

In this section results are presented for the direct single-pass extracavity frequency-doubling of the LBO OPO to provide high-repetition-rate picosecond pulses in the visible.

6.5.1 Experimental configuration

The OPO experimental configuration is as described in the previous chapter. For second harmonic generation the signal wave was directed into the LBO crystal by using two plane high reflecting mirrors similar to the OPO output mirror, see Figure 6.8. The two non-critically cut LBO crystals both had the end-faces antireflection-coated at 1.4 μm. A combination of two crystals was required to cover the signal wavelength range, and so keep the phase matching temperatures in the range of 20-50 °C. Type I SHG is the most desirable, but around 1.3 μm the NCPM temperature drops to ~0°C, and so this would have required the use of peltier cooling and condensation prevention measures such as enclosing the crystal in a nitrogen purge case, and so for practical simplicity it was decided to use a combination of type I and type II. Both crystals were 16 mm in length with 3 x 3 mm aperture. The signal was focused into the LBO crystal with the use of a 50 mm focal length lens for optimal mode-matching, with a similar lens being used to collimate the SHG output beam.

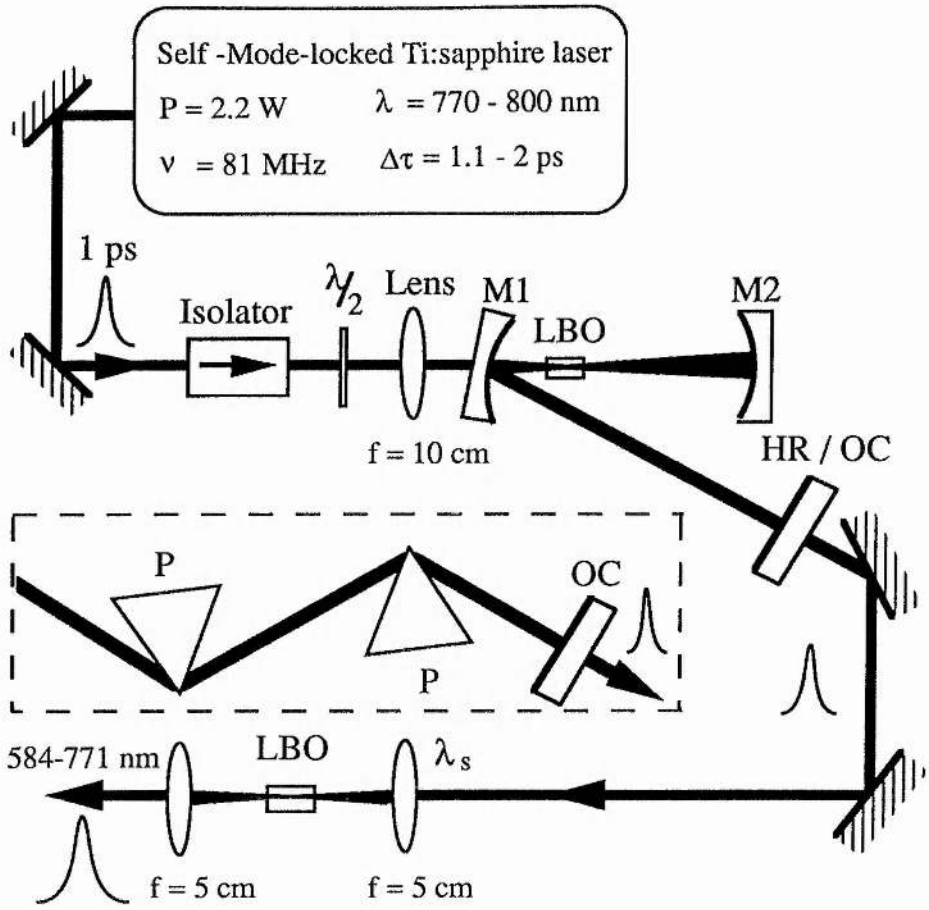

Figure 6.8
Schematic of the extracavity frequency-doubled Ti:sapphire-pumped LBO OPO. The mirrors M_1 and M_2 have radii of curvature r=-20 cm. λ/2 is a half-wave plate.

6.5.2 Results and discussion

6.5.2.1 Tuning characteristics

In Figure 6.9 the experimental tuning range of frequency-doubled LBO OPO is shown as a function of phase-matching temperature. With the 1.4 μm mirror set, a SHG tuning range from 640 to 771 nm was accessed by varying the pump wavelength or crystal temperature. With the use of a second mirror set with high reflectivity (R>99.7%) centred at 1.18 μm, it was possible to extend the tuning range down to 584.5 nm. Therefore, the combination of the two mirror sets provides continuous tuning from 584.5 to 771 nm. This tuning could easily be further extended if a second mirror set was obtained for the pump laser. This

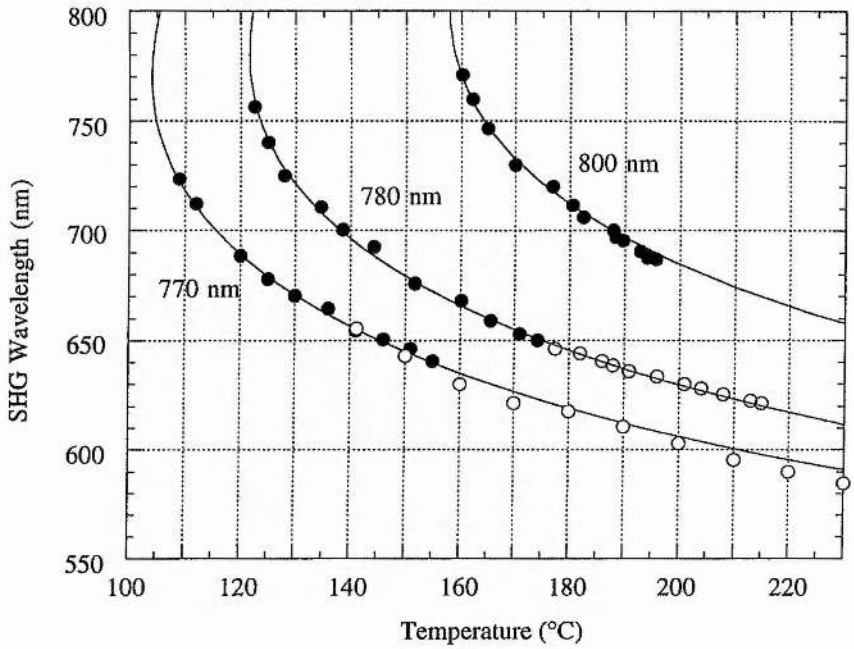

Figure 6.9
Temperature and pump wavelength tuning range of the doubled Ti:sapphire-pumped LBO OPO. The output from the oscillator is indicated by the experimental data and the solid curves represent the predicted tuning range.

tuning range is also shown in Figure 6.10, only in this instance it is expressed as a function of SHG phase-matching temperature to give an indication of the required frequency-doubling phase-matching temperatures required and also whether type I or type II SHG was used. In both cases the comparison of the experimental data with the predicted tuning curves calculated from [2, 3] indicates good overall agreement. In Figure 6.11 the variation of SHG intensity as a function of frequency-doubling crystal temperature is shown. This indicates the extent of the temperature acceptance bandwidth available when using LBO in a temperature-tuned NCPM geometry as a doubling crystal. This particular Figure is for type I SHG at 1.4 μm. The FWHM at this wavelength was measured to be ~6°C which agrees well with the calculated theoretical value of 6.4°C, a similar procedure was carried out for type II SHG, which also yielded a good match between experiment and theory.

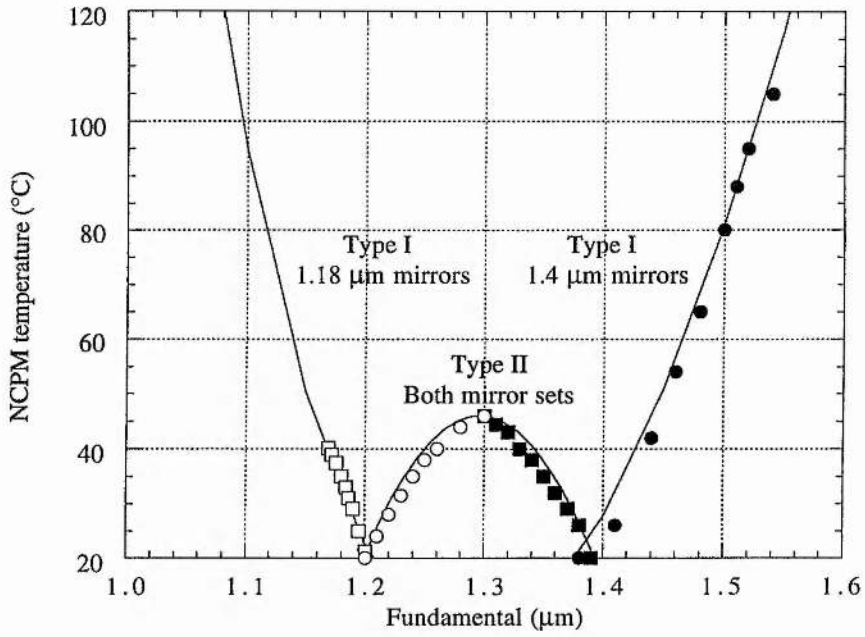

Figure 6.10
Frequency-doubling temperature required to produce the visible range of the externally-frequency-doubled LBO OPO; closed symbols: 1.4 μm mirror set, open symbols: 1.18 μm mirror set.

6.5.2.2 Output power

Figure 6.12 shows the average SHG output power of the frequency-doubled OPO across the SHG tuning range. For 2.0 W of Ti:sapphire pump power, SHG powers as high as 68 mW at 645 nm have been achieved, with powers of over 37 mW being generated over the entire tuning range of 584.5 - 771 nm. The total SHG power of 68 mW, for a signal power of 390 mW represents a conversion efficiency of 18%, from signal to SHG and conversions of ~20 % and greater were achieved across most of the tuning range. Improvements in mode-matching and fine-tuning of the system, such as AR coating the focusing lenses should lead to further increases in the second harmonic power.

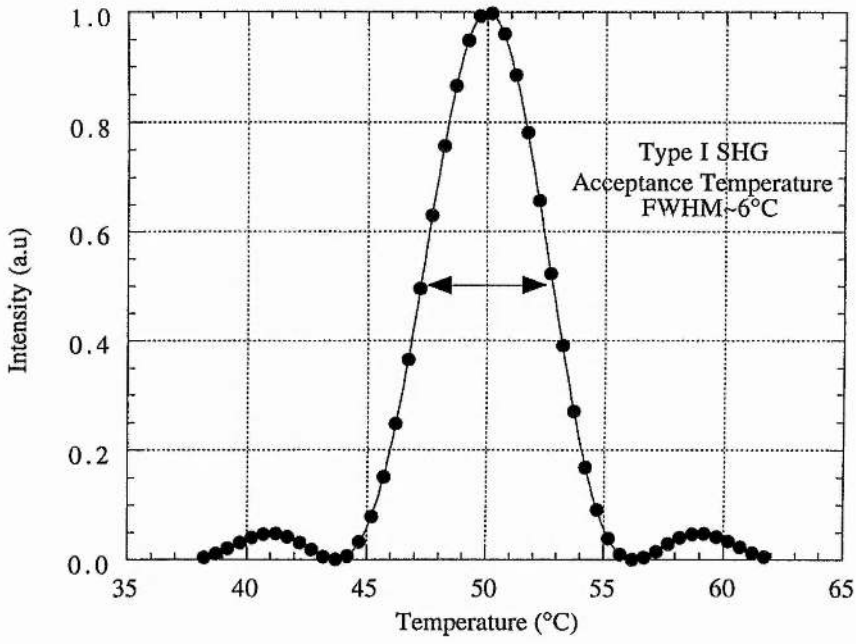

Figure 6.11
Variation of second harmonic power normalised as a function of temperature. The experimental data is represented by the closed circles, the theoretical temperature bandwidth is represented by the solid lines. This represents type I SHG, the fundamental wavelength is 1.4 μm. The crystal length is 16 mm.

6.5.2.3 Temporal characteristics

The temporal characteristics of the SHG pulses were determined from autocorrelation measurements. Figure 6.13 presents the SHG pulse durations across the tuning range and it can be observed that the pulse durations follow the same pattern as those of the OPO itself. No pulse broadening is, however, produced by the additional process of doubling the signal pulses, with the SHG pulses having durations in the range 840-880 fs.

Doubling in the negative GVD regime resulted in the pulses being chirp-free and transform-limited across the entire range. In the positive GVD regime, the doubled signal pulses become increasingly chirped, as was the case with the OPO itself, with pulse durations increasing to 1.4 ps at 584 nm. In Figure 6.14 (a)-(c), a typical autocorrelation of the SHG pulse in the positive GVD regime is shown. The modulation in the wings of the interferometric autocorrelation clearly indicates the presence of chirp and the time-bandwidth product is 1.538.

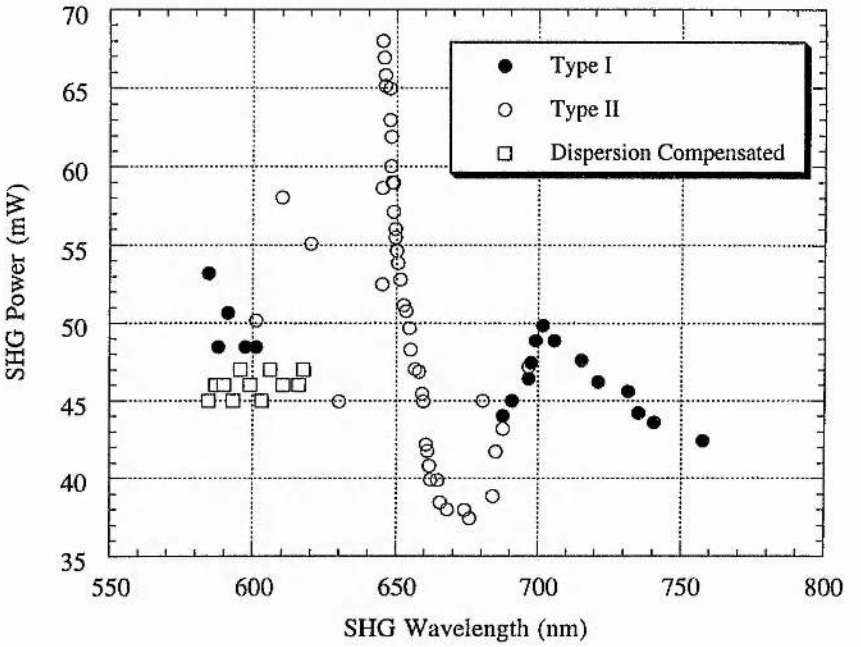

Figure 6.12
The SHG output power from the extracavity frequency-doubled LBO OPO.

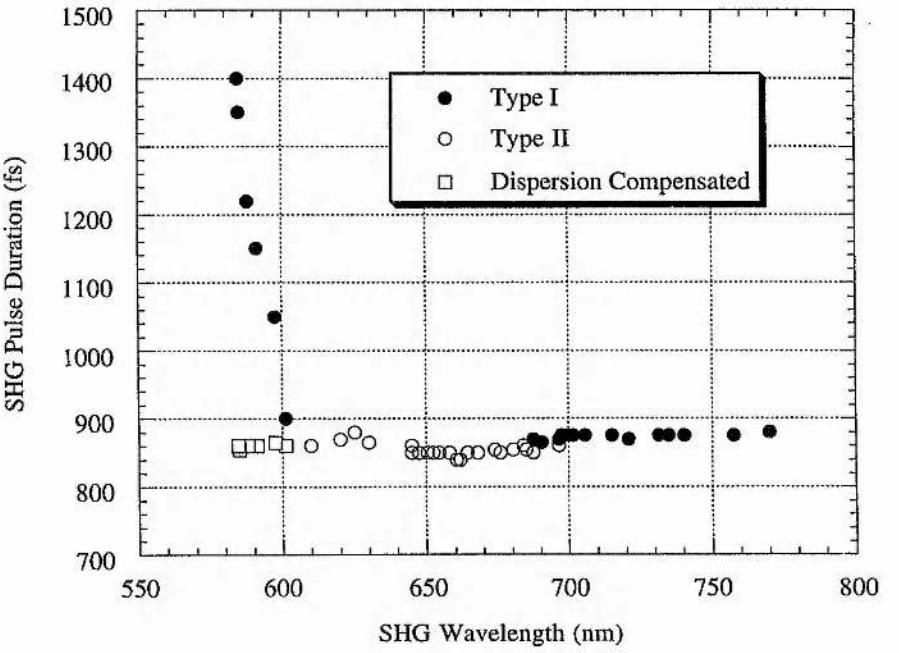

Figure 6.13
SHG signal pulse duration variation across the tuning range of the SHG LBO OPO.

The dip at the centre of the spectrum may be due to the effect of SPM. In Figure 6.14 (d)-(f), a typical autocorrelation of the SHG pulse at the same wavelength is depicted, only in this case the OPO was dispersion compensated before the pulse was frequency-doubled. The output can now be seen to be transform-limited with no evidence of SPM on the spectrum. The pulse duration then reduced to 855 fs.

6.5.2.4 Conclusion

In this section results have been presented that demonstrate wavelength generation in the visible by external single-pass frequency-doubling of the LBO OPO to provide picosecond pulses in the 584-771 nm range. Conversion efficiencies in excess of 20 % have been demonstrated, with output powers in excess of 65 mW being measured, when utilising a combination of type I and type II temperature-tuned NCPM in LBO. The pulse width of the second harmonic was in the region of 840-880 fs. These pulses had bandwidths of the order of ~ 1 nm which will allow time-resolved experiments to be carried out which require such a spectral and temporal resolution.

The combination of the Ti:sapphire pump laser tuning range of 770-910 nm along with its second harmonic of 385-455 nm and the second harmonic of the OPO of 585 - 771 nm and the output of the OPO itself of 1.150 -2.260 μm provides an almost continuous tuning capability from 385 nm to 2.260 μm. The addition of a second Ti:sapphire mirror set would allow the remaining gaps to be filled.

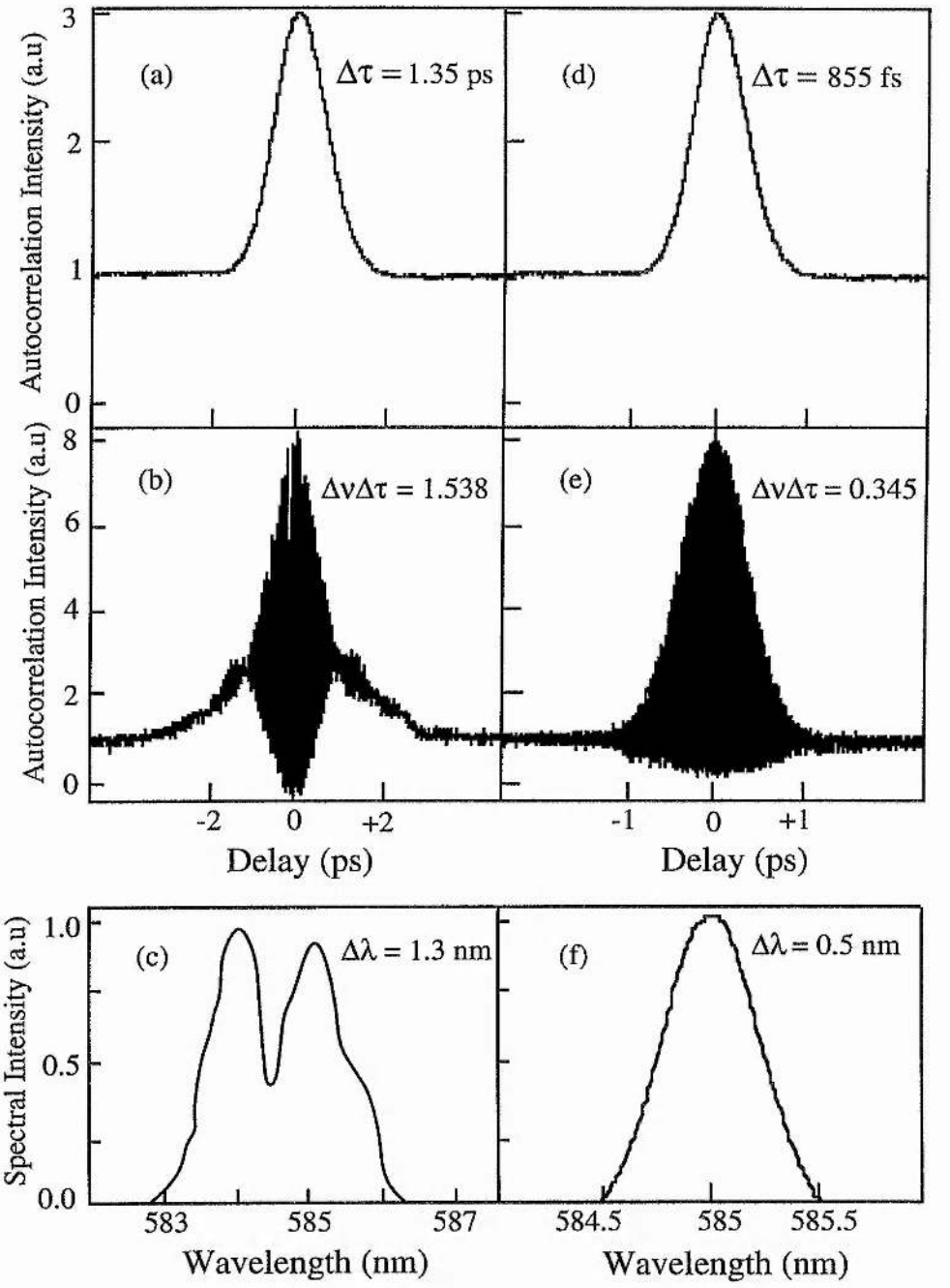

Figure 6.14

Intensity (a, d) and interferometric (b, e) autocorrelation, and the corresponding spectrum (c, f) of the uncompensated and dispersion compensated SHG signal in the region of positive signal GVD at 585 nm. The uncompensated pulse width determined from the intensity autocorrelation is 1.35 ps, and the time-bandwidth product is $\Delta\nu\Delta\tau$ = 1.538. The dispersion compensated pulse width determined from the intensity autocorrelation is 855 fs, and the time-bandwidth product is $\Delta\nu\Delta\tau$ = 0.345.

6.6 Internally-doubled LBO OPO

In the last section results were presented which demonstrate that single-pass frequency-doubling of the OPO produces efficient conversion into the visible. This system also has the benefit that it is easy to switch between the signal and visible pulses very quickly. However, if higher visible power is required then it is advantageous to use intracavity doubling. This process is more complex than the extracavity case and utilises the large intracavity powers available within the OPO cavity to achieve substantially higher conversion efficiencies into the visible and therefore higher output powers.

An intracavity-frequency-doubled picosecond OPO based solely on LBO is described in the following section. Efficient single-pass, frequency-doubling of the signal into the red can be achieved by using temperature-tuned NCPM in LBO, with two different crystal geometries being required to frequency-double the entire signal branch. For both arrangements each LBO crystal was situated at a second intracavity focus.

6.6.1 Experimental configuration

The pump source for the frequency-doubled picosecond LBO OPO was a commercial self-mode-locked Ti:sapphire laser (Spectra-Physics, Tsunami) which was configured for picosecond operation. See Chapter 4 for a detailed description of this laser. The intracavity frequency-doubling was performed in two 16 mm-long LBO crystals located at the second intracavity focus of a standing-wave five-mirror resonator similar to that of Reid et al [8] and is shown in Figure 6.15. The singly-resonant OPO cavity comprised a plane mirror, two r = -200 mm curved mirrors forming the primary focus in the OPO crystal and two r = -100 mm mirrors that formed the secondary focus in the doubling crystal. The type I doubling crystal was cut in an identical geometry to the 30 mm-long LBO used as the OPO crystal. Both these crystals were cut for non-critical propagation along the x-axis (ϕ=0°, θ=90°). The type II doubling crystal was cut for non-critical propagation along the z-axis (ϕ=0°, θ=0°). All crystals had AR-coated end faces centred at 1.4 μm. The frequency-doubling was performed using a combination of type I and type II phase-matching with temperature-tuning. Because of the limitations imposed by the design of the oven, in order to provide continuous coverage in the visible it was necessary to use two crystals with type I and type II phase-matching so as to maintain the SHG process above room temperature. A more suitable oven design based on Peltier cooling (discussed later) will allow frequency-doubling across the available tuning range

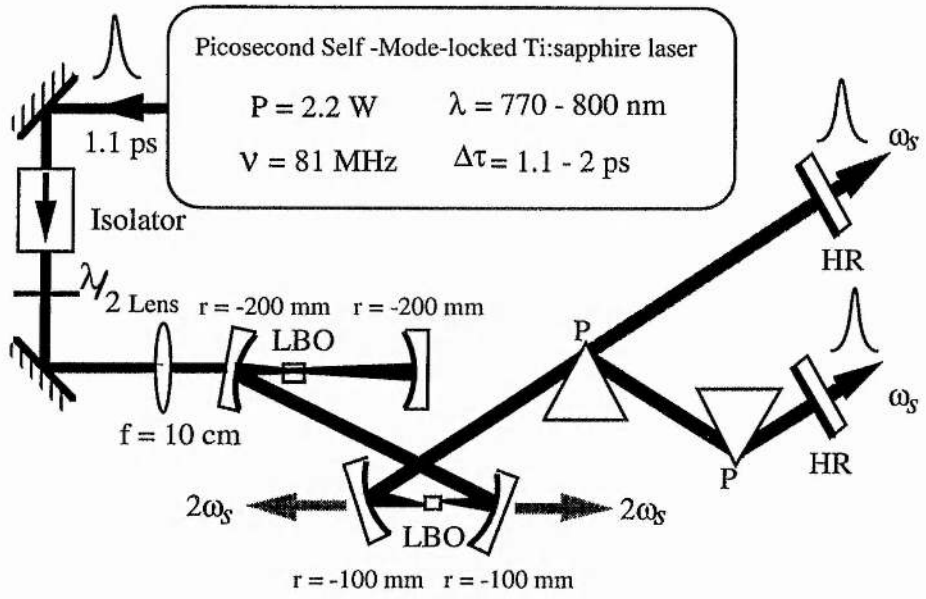

Figure 6.15
Schematic of the frequency-doubled picosecond Ti:sapphire-pumped LBO OPO, with the cavity parameters displayed.

with a single crystal cut for type I phase-matching. To access the demonstrated visible range, two sets of OPO mirrors were used with highly reflecting (R>99.7%) dielectric coatings centred at 1180 and 1400 nm. Both mirror sets also had high transmission (T>95%) centred at 800 nm. The parametric oscillator was initially aligned without the doubling crystal present and, after external orientation, the LBO crystal was inserted into the OPO cavity.

6.6.2 Experimental results

6.6.2.1 Tuning characteristics

In Figure 6.16 the experimental tuning range of frequency-doubled LBO OPO is shown as a function of phase-matching temperature. By using a combination of pump and temperature-tuning, the second harmonic output tuned from 584 to 771 nm, for Ti:sapphire pump wavelengths covering 770-800 nm and OPO crystal temperatures from 110 to 230 °C. The corresponding SHG phase-matching temperatures which were in the range 20 to 120 °C are shown in Figure 6.17. This figure also indicates the extent to which the visible tuning range is split up between the two mirror sets used and between type I and type II frequency-doubling. The solid curves represent the predicted tuning range derived from the Sellmeier equations of Reference 2 and the temperature-dependence of the refractive indices given in Reference 3. It can be observed

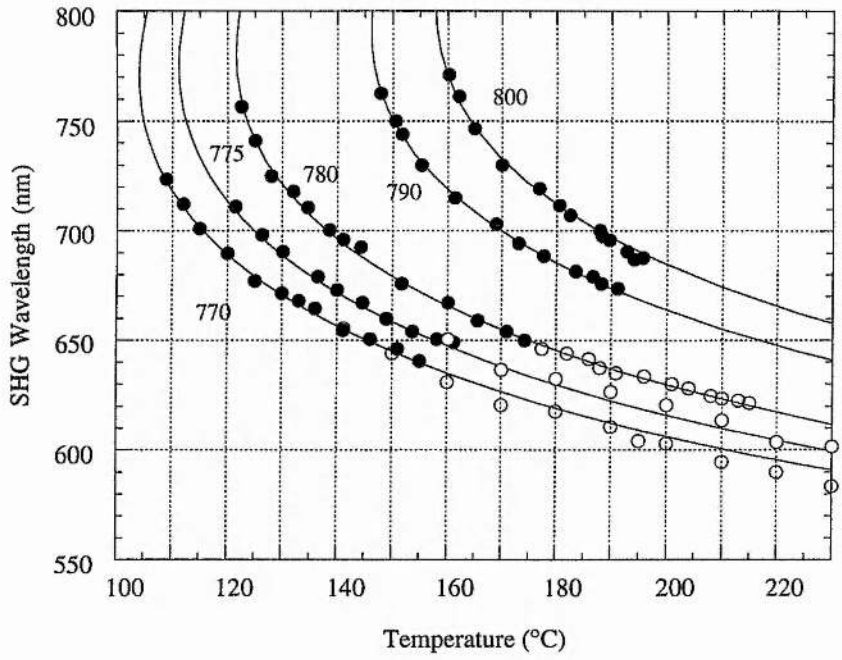

Figure 6.16
Visible range of the internally frequency-doubled LBO OPO; closed circles: 1.4 μm mirror set, open circles: 1.18 μm mirror set, for Ti:sapphire pump wavelengths from 770-800nm.

that there is very little extension to the tuning range accessed by the extracavity case. This implies that the main restriction to the tuning was the OPO mirror reflectivites and not other losses in the cavity. The tuning could also be extended if a complementary Ti:sapphire laser mirror set was available in the laboratory. The visible range of the OPO can potentially be extended to wavelengths as short as 500 nm by using a mirror set for the Ti:sapphire laser with high reflectivity from 700-850 nm.

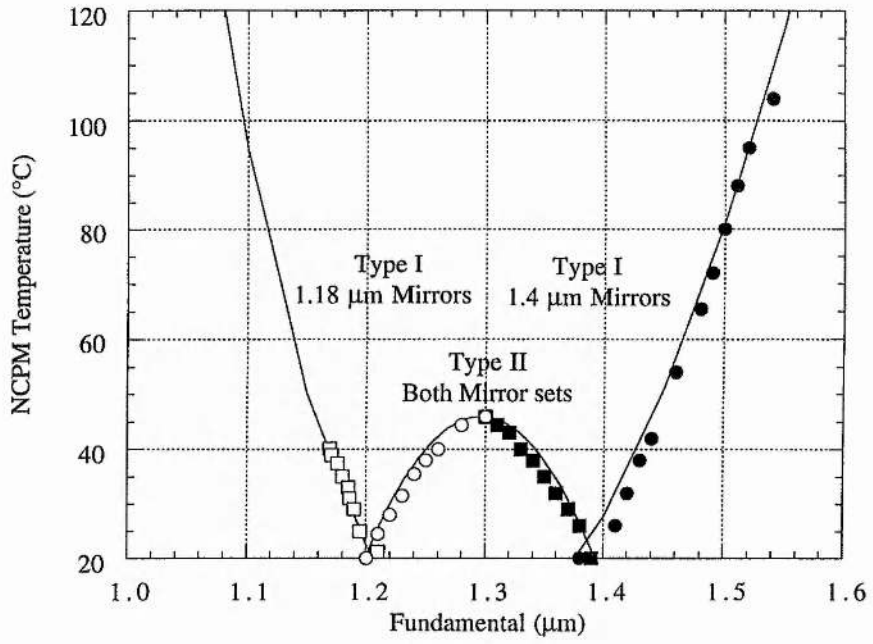

Figure 6.17
Frequency-doubling temperature required to produce the visible range of the frequency-doubled LBO OPO; closed symbols: 1.4 μm mirror set, open symbols: 1.18 μm mirror set.

6.6.2.2 Threshold

With 1.1 ps input pump pulses and configured with all highly reflecting mirrors, the average pump power threshold for the OPO was about 700 mW at the centre of the mirror reflectivity band (see Figure 6.18). The threshold pump pulse energy was therefore 8.5 nJ, corresponding to a peak power of 7.8 kW, and peak intensity of 720 MW/cm^2 inside the LBO crystal. Oscillation could be maintained across the entire signal tuning range for average pump powers below 950 mW. At the extreme of the reflectivity band of the 1.4 μm mirrors, the threshold increased above 850 mW but lower thresholds were available in this region using the 1.2 μm mirror set. With both mirror sets oscillation was maintained for an output coupling loss of up to 8%. To maximise frequency-doubled output it was desirable to operate with all highly reflecting mirrors. The increase in threshold with mirror output coupling was found to be negligible, indicating that mirror output coupling is not the dominant loss mechanism here. A prediction of the threshold has again been made by using the model of Guha, Wu, and Falk [9], this again produces a good fit to the experimental data, as seen

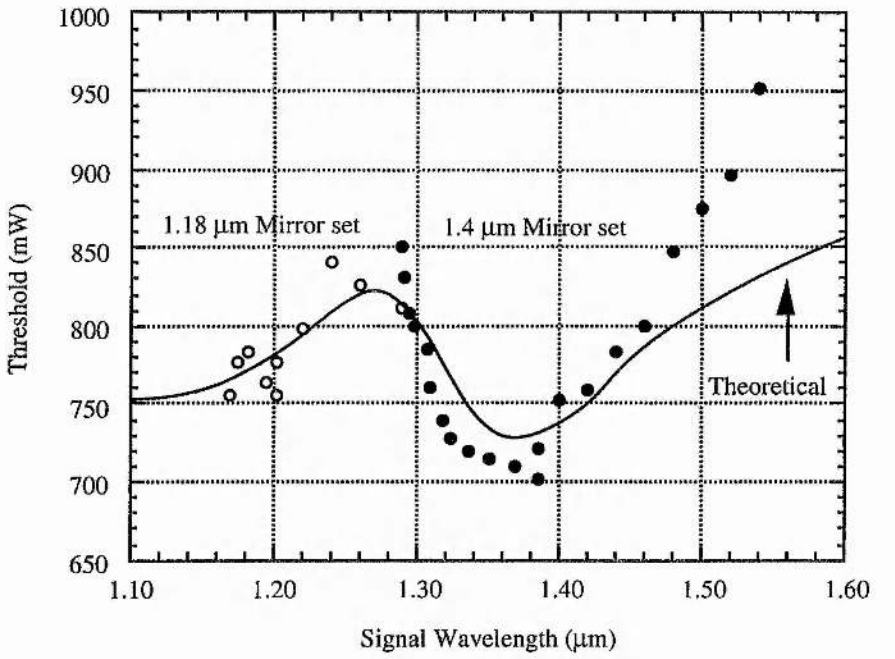

Figure 6.18
Variation in the average pump-power threshold across the tuning range of the intracavity frequency-doubled LBO OPO. With the theoretical threshold indicated by the solid line.

in Figure 6.18. The deviation between the model and the experimental results is due to uncertainties in the value of the AR coating with wavelength across the entire tuning range of the system. If the exact mirror transmission were know across the entire tuning range then the model could be fitted more accurately to the whole tuning range.

6.6.2.3 Output power and efficiency

The frequency-doubled output was coupled out from the cavity in two diverging beams each containing approximately 25 % of the total power through the r = -100mm HR mirrors (T = 50 % @ 650 nm). Fresnel reflections at the surface of the frequency-doubling LBO (~15 %) and transmission loss (~35 %) at two other HR mirrors accounted for the remaining light. If a dual band mirror coating centred at the signal wavelength and with $T > 90$ % at the second harmonic was used then it would be possible to couple the majority of the output into only two beams. The output beams were collimated using a 10 cm focal length lens.

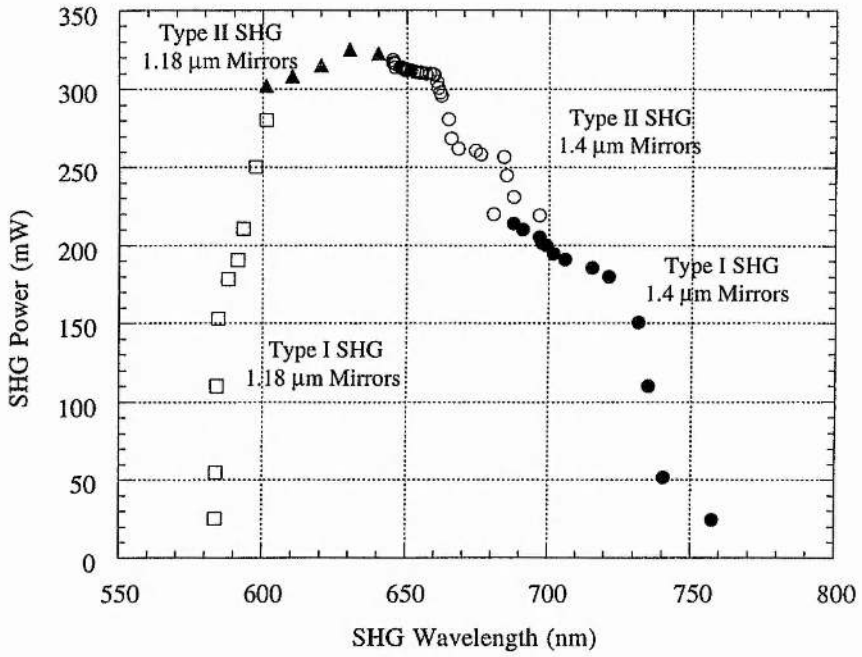

Figure 6.19
Variation of frequency-doubled signal power as a function of wavelength for a pump power of 2 W.

The variation in the second harmonic output power across the visible range of the oscillator is shown in Figure 6.19. The data was obtained for 2 W of pump power at the input to the OPO crystal, with a cavity configured with all highly reflecting mirrors at the signal wavelength. This configuration corresponded to the maximum extraction of visible output and a minimum pump power threshold of 700 mW. It can be seen from Figure 6.19 that as much as 320 mW of output power was extracted in the second harmonic, with the power remaining above 150 mW almost over the entire visible tuning range. This represents a conversion efficiency from the pump to the second harmonic of between 7.5 % and 16 %.

The net conversion efficiency from the pump to frequency-doubled signal is depicted in Figure 6.20 and remains over 5% for effectively all the available tuning range. These values do not account for the residual reflectivity of the OPO mirrors in the visible, which was as high as 50 %. Optimisation of the reflectivity of these mirrors would result in better extraction of the total generated second harmonic power, leading to further increases in useable output power and efficiency.

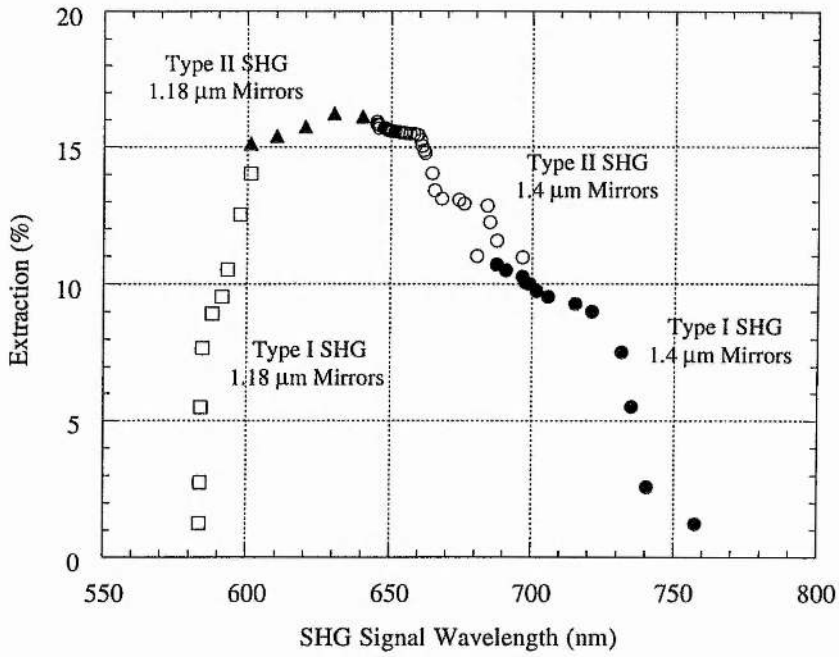

Figure 6.20
Variation of frequency-doubled signal power extraction as a function of wavelength for a pump power of 2 W.

The high reflector was replaced with a 2.5 % signal output coupler and enabled an estimation of the single-pass conversion efficiency to be made. With 2 W of pump power the previous value of 320 mW reduced to 210 mW through the output coupler at 1.26 μm with a fundamental power of 80 mW being measured. This corresponded to a single-pass conversion efficiency from the fundamental to the second harmonic of 3.3 %, when the intracavity power of 3.2 W is considered. This value is higher than those measured previously in two femtosecond intracavity-doubled systems based on KTP and RTA [10].

The visible output powers obtained from this system was indeed very substantial as shown above. To illustrate this point a photograph, which is displayed in Figure 6.21, was taken which demonstrates the amount of power obtained in the red wavelength region.

In Figure 6.22 the variation of SHG power as a function of frequency-doubling crystal temperature is shown, i.e. this indicates the extent of the temperature acceptance bandwidth available when using LBO in a temperature-tuned NCPM geometry as a doubling crystal. This particular Figure is for type I

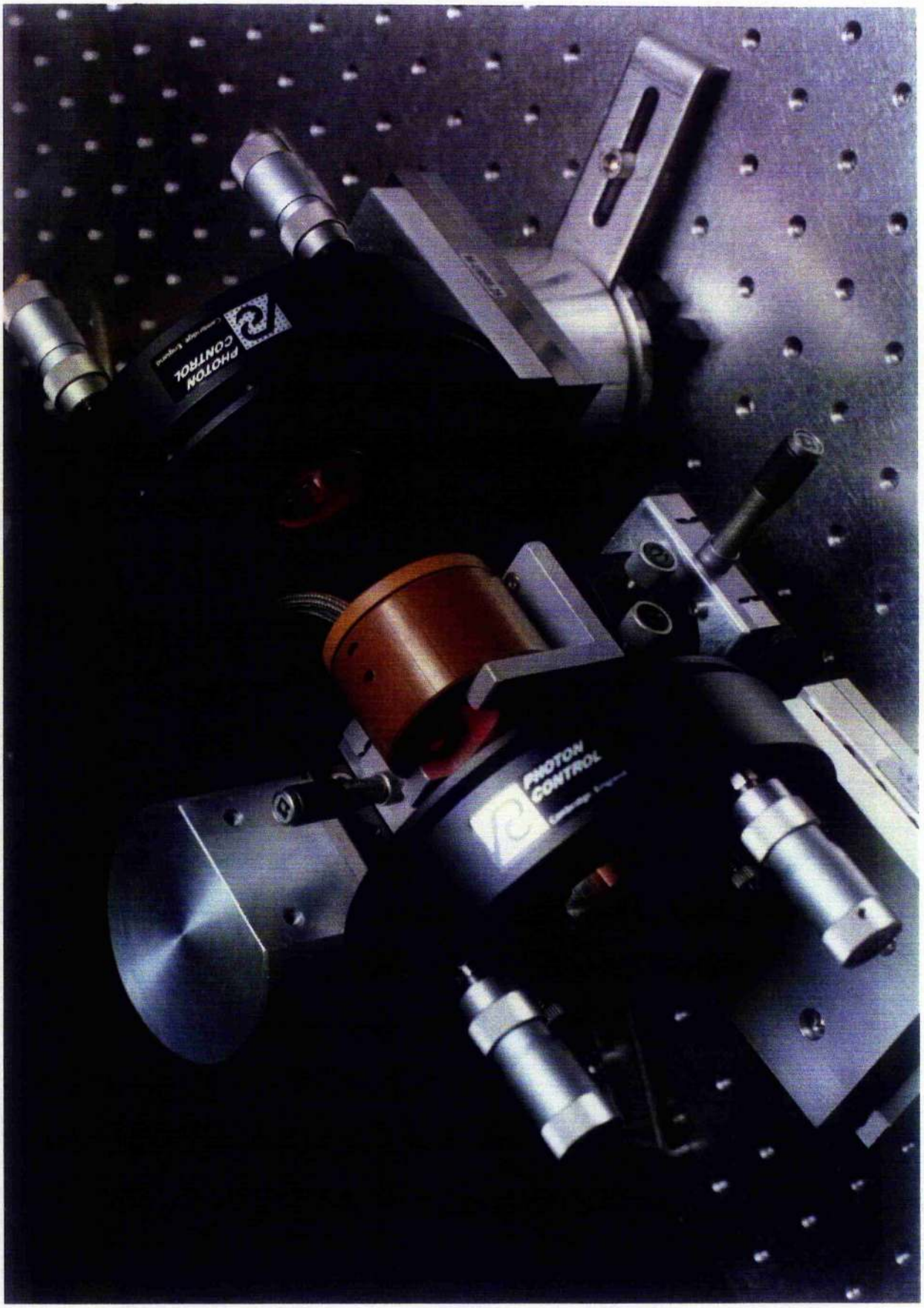

Figure 6.21
The intracavity-doubled LBO OPO in operation, at a wavelength of 600 nm.

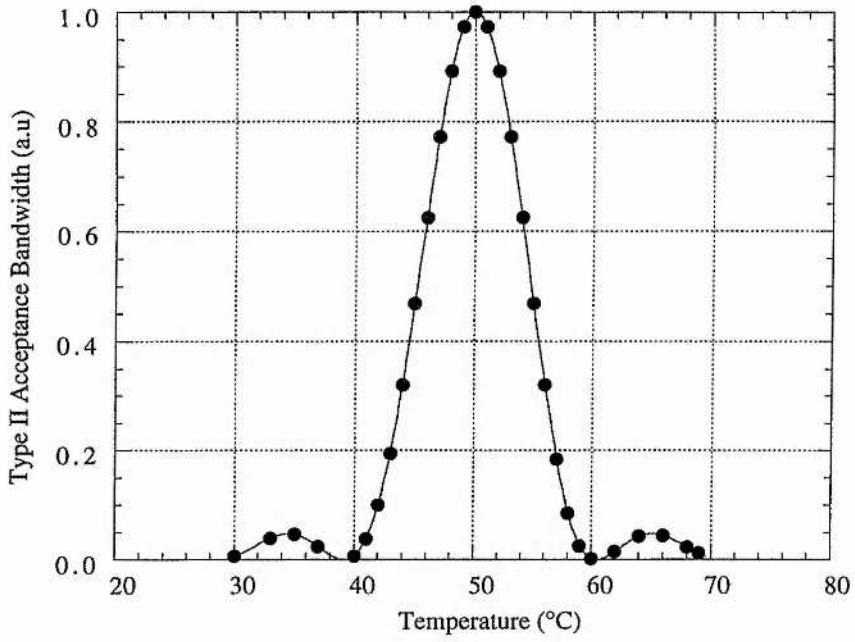

Figure 6.22
Variation of second harmonic power as a function of temperature, the experimental data is represented by the closed circles, the theoretical temperature bandwidth is represented by the solid lines. This represents type I SHG, the fundamental wavelength is 1.4 μm.

SHG at 1.4 μm. The FWHM at this wavelength was measured to be ~6°C, which agrees well with the calculated theoretical value of 6.4°C. A similar procedure was carried out for Type II SHG, which also yielded a good match between experiment and theory.

6.6.2.4 Temporal characteristics

A 2.5 % signal output coupler was used to replace the high reflector to allow the measurement of the fundamental signal pulse duration. One of the high-power beams was used as the input to an autocorrelator constructed using a 4 mm-thick crystal of BBO and a UV visible photomultiplier tube.

The temporal characteristics of the SHG pulses were similarily determined from autocorrelation measurements. Figure 6.23 shows a typical intensity and interferometric autocorrelation, and the corresponding spectrum of the frequency-doubled signal pulses at a wavelength of 675 nm. The pulse duration

deduced from the intensity autocorrelation is 840 fs (assuming a $sech^2$ pulse profile) for a pump pulse of 1.1 ps. The shape of the interferometric autocorrelation is indicative of chirp-free pulses. The spectrum has a smooth profile with a spectral width of 0.53 nm and a time-bandwidth product of 0.339. These pulses are therefore essentially transform-limited. When the SHG signal below 1.2 μm is considered it is found that the pulses have become chirped. Figure 6.24 (a)-(c) represents the frequency-doubled signal output in this dispersion region. It can be observed from the spectrum that extensive SPM exists in this case, this causes the pulse duration to rise to 1.28 ps with the corresponding time-bandwidth product now being 1.432. Figure 6.25 illustrates the frequency-doubled pulse durations across the entire tuning range and demonstrates that the pulse durations remain constant at approximately 850 fs in the negative GVD regime, with them rising substantially in the frequency-doubled positive GVD regime below 600 nm. Therefore to produce transform-limited operation across the entire tuning range dispersion compensation measures must be implemented. The SHG pulse duration is determined mainly by the nonlinear pulse shortening, because of the small temporal walkoff in LBO. Since the nonlinear gain remains constant across the tuning range, there is little change in the SHG pulse duration with wavelength.

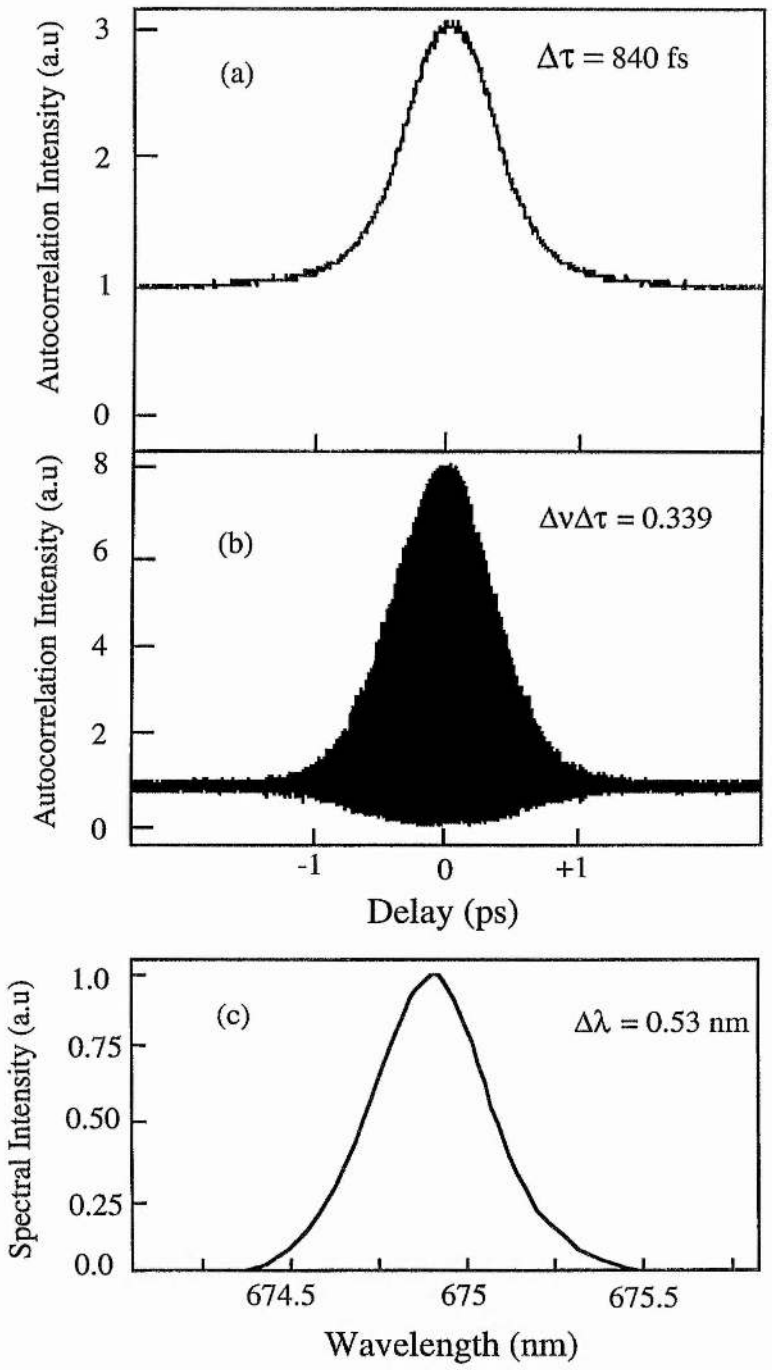

Figure 6.23

(a) Intensity and (b) interferometric autocorrelation, and (c) spectrum of frequency-doubled signal pulses at 675 nm. The pulse duration determined from the intensity autocorrelation is 840 fs, with a corresponding time-bandwidth product of 0.339.

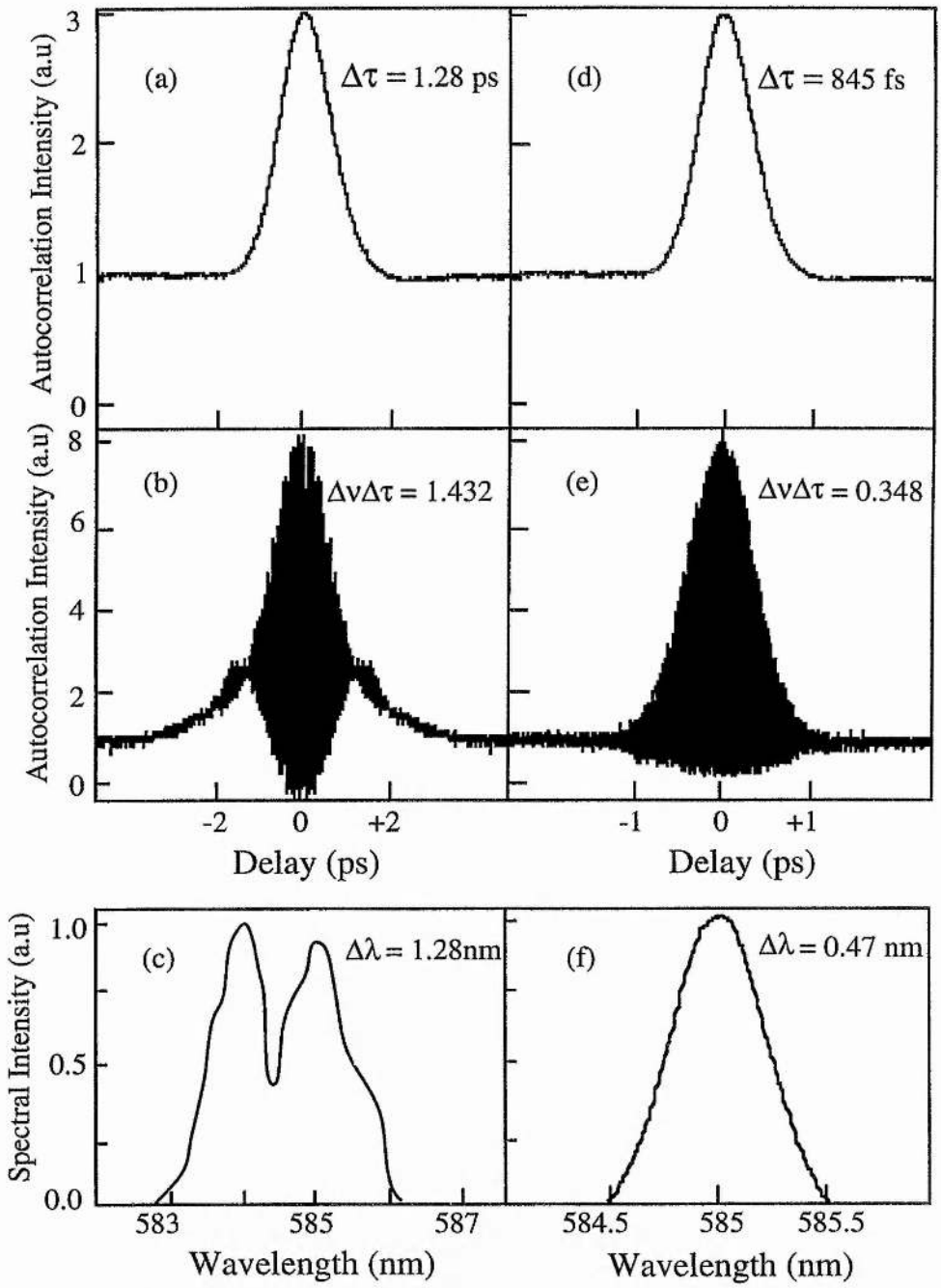

Figure 6.24

Intensity (a, d) and interferometric (b, e) autocorrelation, and the corresponding spectrum (c, f) of the uncompensated and dispersion compensated SHG signal in the region of positive signal GVD at 585 nm. The uncompensated pulse width determined from the intensity autocorrelation is 1.28 ps, and the time-bandwidth product is $\Delta\nu\Delta\tau$ = 1.432. The dispersion compensated pulse width determined from the intensity autocorrelation is 845 fs, and the time-bandwidth product is $\Delta\nu\Delta\tau$ = 0.348.

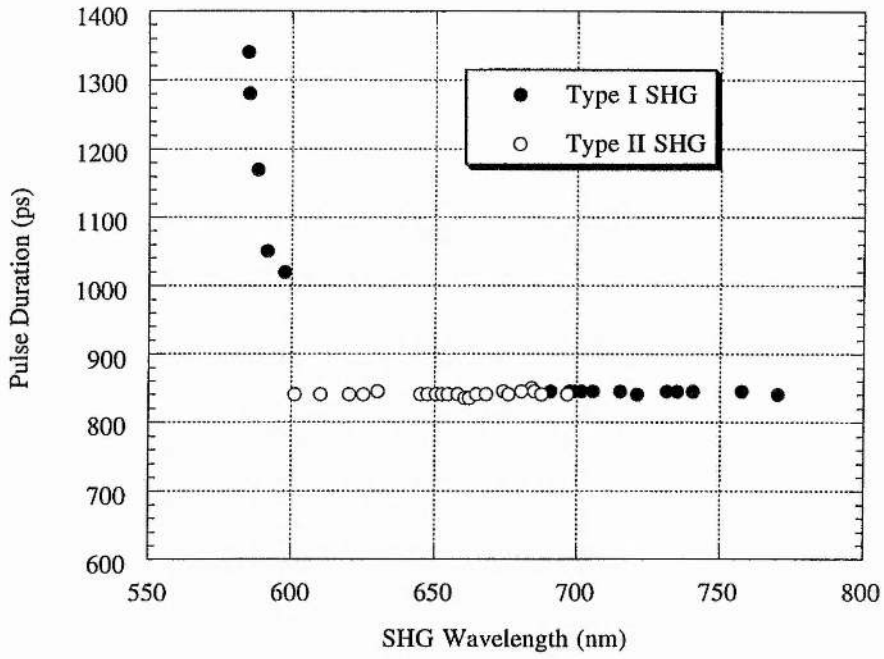

Figure 6.25
SHG signal pulse duration variation across the tuning range of the SHG LBO OPO.

6.6.2.5 Cross Correlation

Cross correlations were performed using the same method as previous. The results indicating that little or no timing jitter existed on the frequency-doubled pulses, as was the case for the OPO itself.

6.6.3 Dispersion compensation

The intracavity-doubled OPO was operated with and without a dispersion compensating prism sequence. As discussed previously, in the negative group velocity dispersion (GVD) regime, the visible pulses were chirp-free and transform-limited across the entire range of 600-771 nm without the need for dispersion compensation. In the positive GVD regime, the doubled signal pulses became increasingly chirped, as did the fundamental pulses themselves (see Chapter 5 § 5.3.9), with pulse durations increasing to 1.4 ps at 584 nm, as shown in Figure 6.25. Intracavity dispersion compensation was therefore necessary for operation below signal wavelengths of 1.2 μm, corresponding to the positive GVD regime in LBO [11]. This was achieved by the insertion of a pair of SF14

glass prisms (apex separation, 40 cm) into the OPO cavity, as shown in Figure 6.15. The pulse depicted in Figure 6.24 can now be seen in its uncompensated and dispersion compensated condition. It can be observed that the spectrum is now smooth with no sign of the SPM present as in the uncompensated case, with the pulse duration now falling to 845 fs, with bandwidth product becoming near transform-limited at 0.346. The dispersion compensation resulted in the generation of transform-limited second harmonic pulses of duration 840-880 fs across the entire tuning range of 584-771 nm, as shown in Figure 6.26. The inclusion of the SF14 prism sequence does however lead to an increase in the threshold and a reduction in output power of the system and the OPO must be monitored to check that these degrading effects are not to great.

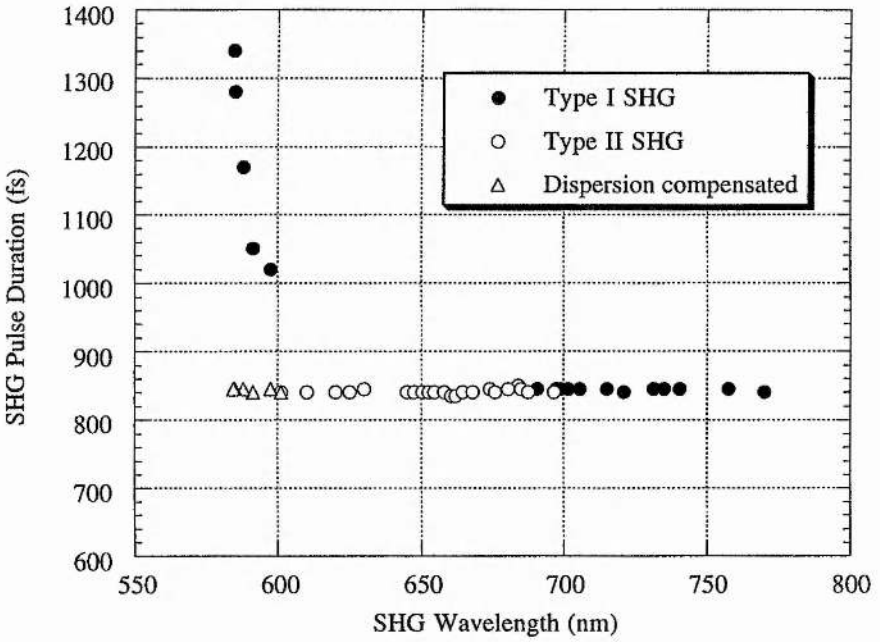

Figure 6.26
SHG signal pulse duration variation across the tuning range of the SHG LBO OPO.

6.6.3.1 Threshold

The addition of the dispersion compensation procedures are essential, if transform-limited performance is to be achieved across the entire tuning range of the OPO. It would however be unacceptable if this increased performance resulted in a very large increase in the threshold of the system, as this could lead to device instability. The effect on threshold of incorporating the prism

sequence is shown in Figure 6.27 in which it can be observed that the threshold increases from ~750 to 800 mW in the positive GVD regime when the prisms are present, representing a small increase of only 7 %. This is therefore not a problem, especially as it occurs over only a small section of the tuning range. However, it should still be possible to reduce the threshold by further work in optimising the prism orientations and positions.

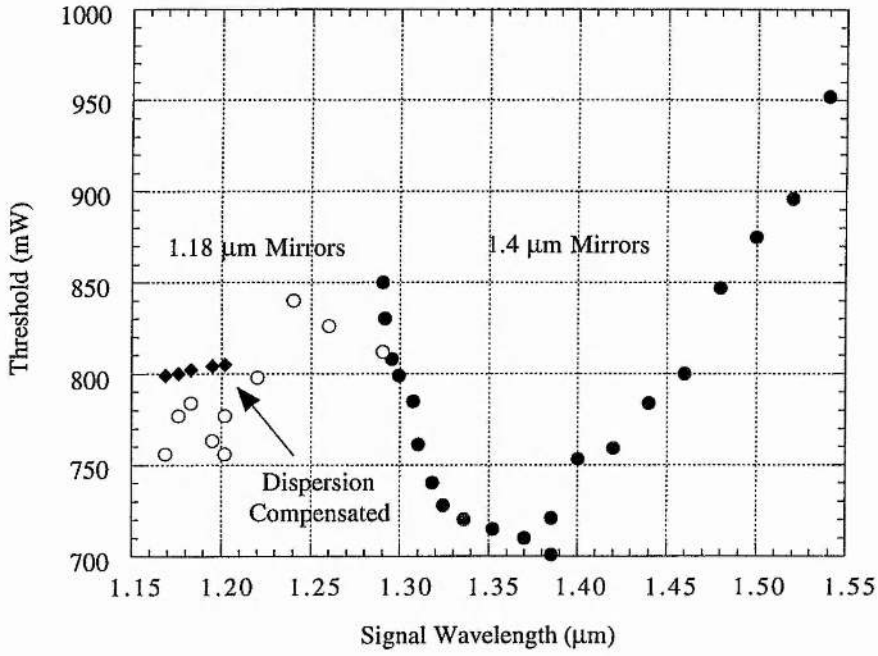

Figure 6.27
The average threshold of the intracavity frequency-doubled LBO OPO as a function of signal wavelength.

6.6.3.2 Output power

The output power of the dispersion compensated OPO can be seen in Figure 6.28. The addition of the prisms can be seen to produce a reduction in output power of less than 10 mW, which is essentially negligible.

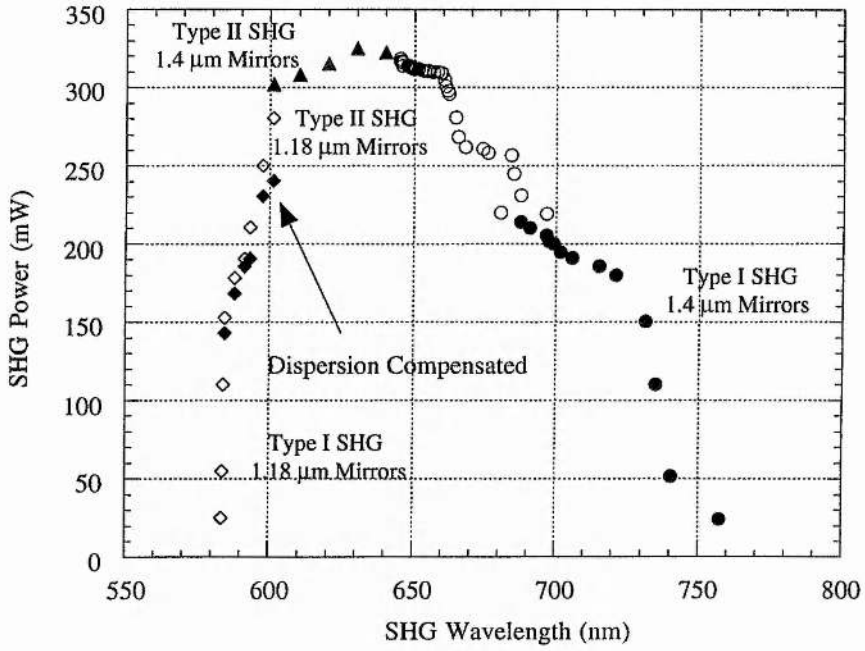

Figure 6.28
The average output power of the LBO OPO as a function of wavelength, for a pump power of 2 W.

6.6.4 Internally-doubled LBO OPO using only Type I SHG

6.6.4.1 Introduction

In the previous sections, it was stated that a combination of two doubling crystals was required to frequency double the OPO whilst keeping the doubling process below 20 °C and maintaining technical simplicity. By the use of a cool air circulation system some progress has been made towards the use of only one doubling crystal, namely type I SHG in an x-cut LBO crystal. This system allowed the crystal to be cooled to ~10°C which when combined with the large frequency-doubling temperature bandwidth of LBO, will allow frequency-doubling of almost the entire OPO tuning range using only this crystal.

6.6.4.2 Experimental configuration

The experimental configuration of this setup was identical to the previous internally-doubled system, with the only difference being in this instance that cold air from an air cooling unit was passed across the faces of the crystal to

facilitate cooling below room temperature, with heating being achieved as in the previous case. The type I doubling crystal was cut in an identical geometry to the 30 mm-long LBO used as the OPO crystal. Both these crystals were cut for non-critical propagation along the x-axis (ϕ=0°, θ=90°).

6.6.4.3 Experimental results

Tuning characteristics

In Figure 6.29 the experimental tuning range of frequency-doubled LBO OPO is shown as a function of phase-matching temperature. By using a combination of pump and/or temperature-tuning, the second harmonic output tuned from 584 to 771 nm, for Ti:sapphire pump wavelengths covering 770-800 nm and OPO

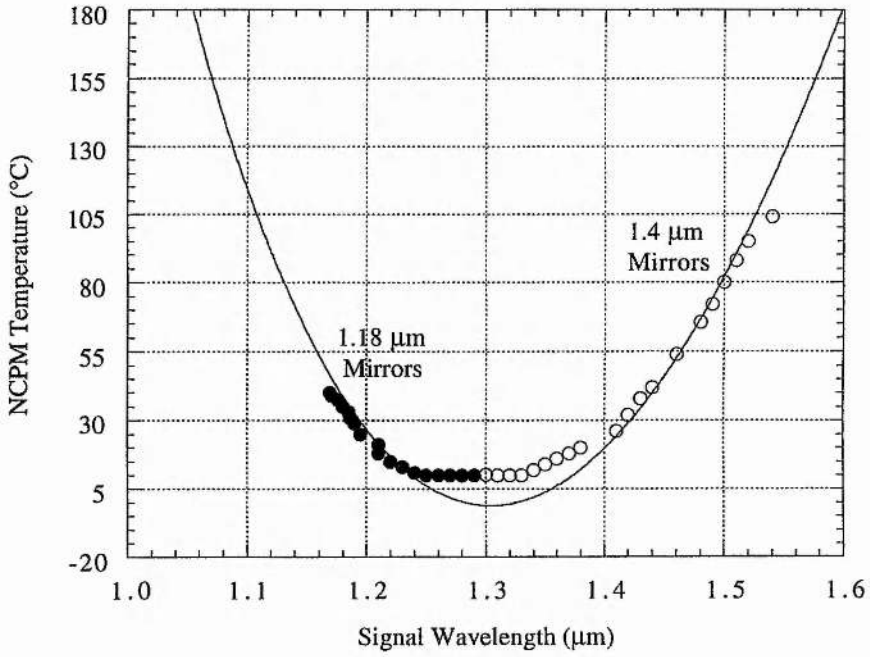

Figure 6.29
Visible range of the frequency-doubled LBO OPO; closed circles: 1.4 μm mirror set, open circles: 1.18 μm mirror set.

crystal temperature from 110 to 230 °C, as in the previous two crystal frequency-doubling case. The corresponding SHG phase-matching temperatures were in the range 10 to 105 °C. The solid curves represent the predicted tuning range derived from the Sellmeier equations of Reference [2] and the temperature-dependence of the refractive indices given in Reference [3]. The discrepancy between the theoretical and experimental results is due to the fact that tuning

below 10 °C is not possible with the current cooling system, so around 1.3 μm the SHG is achieved at the extremes of the frequency-doubling acceptance bandwidth. This may result in a reduction in output power around a signal wavelength of 1.3 μm.

Threshold

With the cavity configures using only high reflector mirrors, the average pump power threshold for the OPO in this type I only doubling configuration was similar to the previous case. Oscillation could be maintained across the entire tuning range for average pump powers below 950 mW (see Figure 6.30).

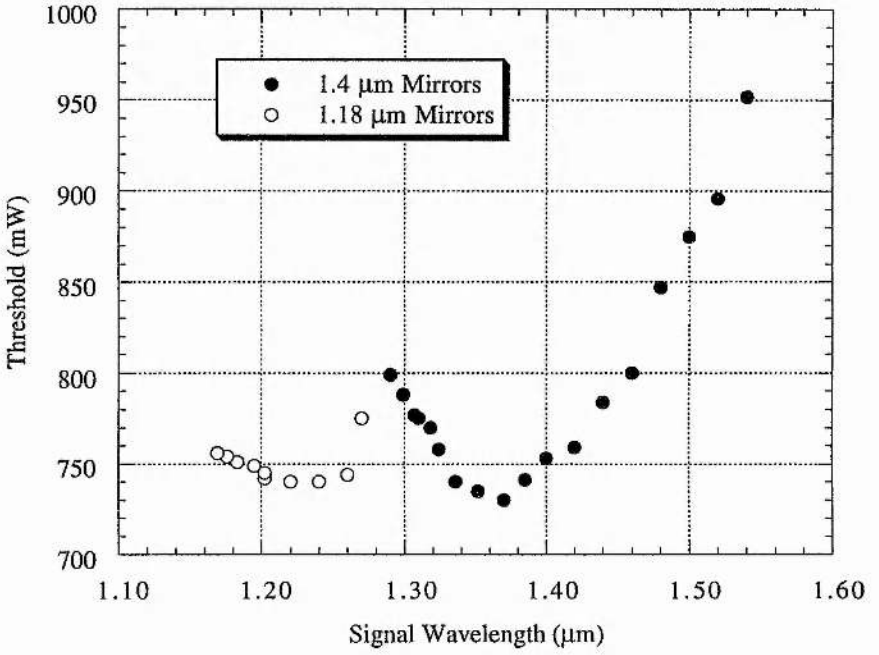

Figure 6.30
Variation in the average pump-power threshold across the tuning range of the intracavity frequency-doubled LBO OPO.

Output power and efficiency

As discussed in the previous section the use of only type I frequency-doubling in LBO around 1.3 μm could not access the entire wavelength tuning range properly unless a Peltier cooling system was used. Although it would be possible to frequency double without active cooling, the process would not be on the centre of the characteristic sinc^2-function typical of temperature-tuning. This will result in a loss of second harmonic generation, which will in turn lead to a reduction in the second harmonic output power across the visible range of the oscillator. This is shown in Figure 6.31 which shows that a dip now exists at 650 nm, an effect not observed in the previous case. The drop in power was as much as 70 mW at 650 nm. Therefore, as expected, the lack of proper crystal cooling resulted in a substantial reduction of power. This drop in output power resulted in the conversion efficiency from the pump to the second harmonic at 650 nm falling from 16% to 12%.

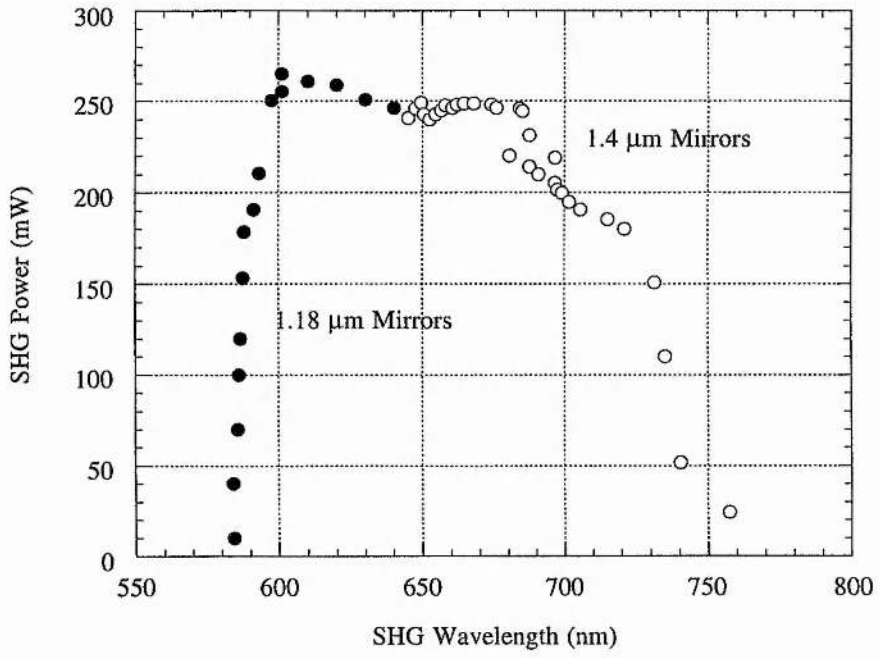

Figure 6.31
The average output power of the LBO OPO as a function of wavelength, for a pump power of 2 W. Type I phase-matching used across the tuning range.

Amplitude noise measurements

In all three different methods for producing visible radiation, device stability was such that each system required no alignment on a day-to-day basis except for minor cavity length adjustment. Furthermore, when aligned correctly, oscillation persists for several hours at a time without any form of active stabilisation. The amplitude noise present on the outputs of all three parametric oscillator configurations and the pump laser were compared and typical oscillograms are shown in Figure 6.32. Intensity fluctuations on the Ti:sapphire

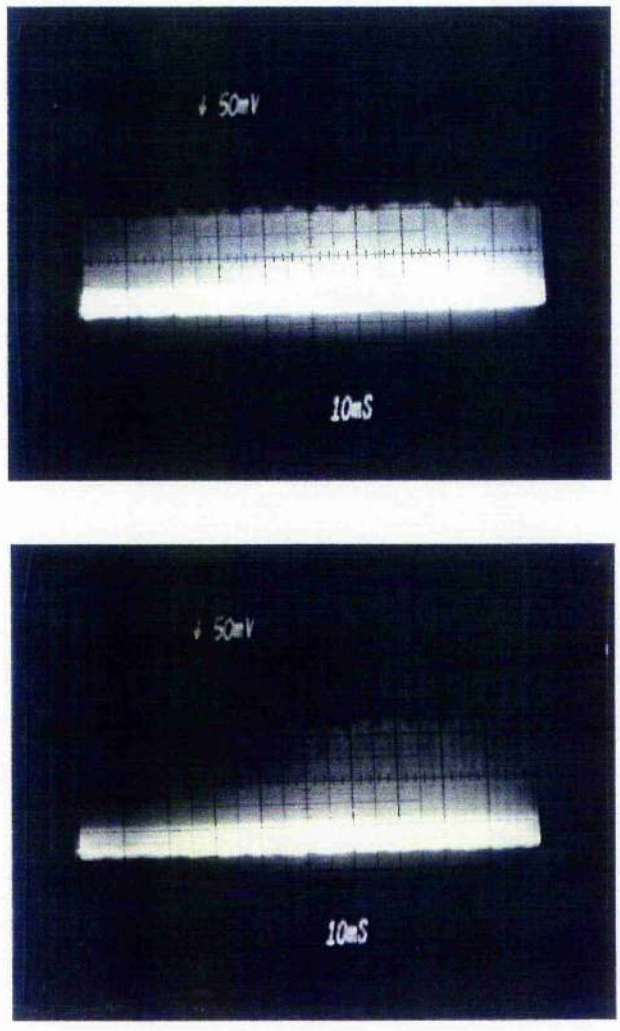

(a)

(b)

Figure 6.32

Oscillograms showing the amplitude noise (intensity fluctuations) of the self-mode-locked Ti:sapphire pump laser (a), and the internally frequency-doubled OPO (b). The timebase is 10 ms/division in each case.

pump laser were typically less than 1 %, with the frequency-doubled OPO, exhibiting amplitude fluctuations of around 4 %. This relatively low value is to be expected as the effects of SPM and GVD in the OPO are minimal.

Temporal characteristics

The temporal characteristics of the SHG pulses were determined from autocorrelation measurements. Using only type I phase-matching the intracavity-doubled OPO was operated with and without a dispersion compensating prism sequence. The pulse duration data obtained was very similar to that obtained in the previous internal doubling case and so no further discussion of the pulse durations are required.

6.7 System improvements

As mentioned in Chapter 5 the use of a ring cavity shown in Figure 6.33 would be advantageous for the intracavity doubled LBO OPO. Using a unidirectional configuration generates visible pulses in only one direction, which would lead to an improvement from the current case in which two output beams are produced. Again the major drawback to this cavity is that it can be a good degree harder to align and operate.

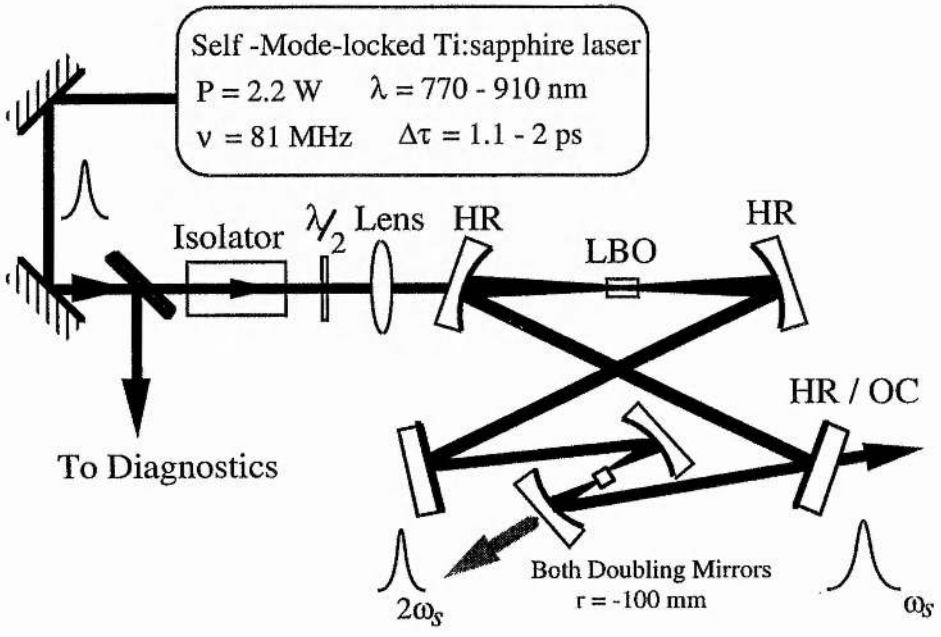

Figure 6.33
The experimental configuration for the intracavity frequency-doubled LBO OPO in a ring cavity.

6.8 Future work

The above method of using just one frequency-doubling crystal is a very effective system with the only drawback at present being the dip in power incurred at around 1.3 μm. This problem can be solved by the use of a more sophisticated cooling system involving a Peltier cooler. To this end, a frequency-doubling system using only one doubling crystal has been designed that uses a water cooled Peltier heater (Model no SP 1848-03 AC) supplied by Marlow Industries Europe Ltd [12]. This cooler is capable of heating and cooling between the temperature range -10 to 120 °C, which easily covers the required frequency-doubling temperature range. The Peltier cooler is operated using an advanced temperature controller (Model No SE 5000-01) also supplied Marlow Industries Europe Ltd [12]. These refinements are currently being implemented.

6.9 Conclusion

In conclusion, a further new source of tunable high-repetition-rate picosecond pulses for the visible has been demonstrated, which is based on an internally-doubled, Ti:sapphire-pumped OPO that uses temperature-tuned LBO both as the OPO and SHG crystal. Oscillation has been obtained for an input pump power of 700 mW with output powers in excess of 320 mW being generated representing conversion efficiencies of as much as 16 %. The system is continuously tunable from 584 to 771 nm and provides transform-limited visible pulses with durations of 840-880 fs across the available range. The combination of the Ti:sapphire tuning range (770-910 nm), its second harmonic (385-455 nm), the frequency-doubled OPO (585-771 nm), and the output of the OPO itself (1.150-2.260 μm) provides an almost continuous tuning capability from 385 nm to 2.260 μm. The use of an optimised mirror set for the Ti:sapphire laser will allow the remaining gaps to be filled. Few systems are capable of such wide tunability, high output power and transform-limited performance. The only slight negative property of this system is the fact that two doubling crystals have to be used. The internally-doubled, Ti:sapphire-pumped OPO that uses temperature-tuned LBO has also been operated with just one x-cut LBO frequency-doubling crystal. Oscillation threshold has increased to 730 mW. With the total output powers falling 250 mW, this represents a reduction in conversion efficiencies from 16 to 12 %. The system is continuously tunable from 584 to 771 nm and can provide transform-limited visible pulses with

durations of 840-880 fs across the available range as in the two crystal doubling case.

References

1. R. L. Fork, B. I. Greene, and C. V. Shank, Appl. Phys. Lett. **38**, 671 (1981)

2. S. Lin, J. Y. Huang, J. Ling, C. Chen, and Y. R. Shen, Appl. Phys. Lett. **59**, 2805 (1991)

3. S. P. Velsko, M. Webb, L. Davis, and C. Huang, IEEE J. Quantum Electron. **27**, 2182 (1991)

4. R. J. Ellingson and C. L. Tang, Opt. Lett. **17**, 343 (1992)

5. D. T. Reid, M. Ebrahimzadeh, and W. Sibbett, J. Opt. Soc. Am. B **12**, 1157 (1995)

6. A. Nebel, H. Frost, R. Beigang, and R. Wallenstein, Appl. Phys B. **60**, 453 (1995)

7. E. C. Cheung and J. M. Liu, J. Opt. Soc. Am. B **7**, 1385 (1990)

8. D. T. Reid, M. Ebrahimzadeh, and W. Sibbett, J. Opt. Soc. Am. B **12**, 1157 (1995)

9. S. Guha, F. Wu, and J. Falk, IEEE J. Quantum Electron. **QE-18**, 907 (1982)

10. R. J. Ellingson and C. L. Tang, Opt. Lett. **18**, 438 (1993)

11. M. Ebrahimzadeh, S. French, and A. Miller, J. Opt. Soc. Am. B **12**, 2180 (1995)

12. Marlow Industries Europe Ltd, 7 Laura House, Jengers Mead, Billingshurt, West Sussex RH-14 9NZ, U.K.

Contents

7.1 Introduction

The work described in Chapters 4, 5, and 6 has concentrated on the development of sources that produce picosecond pulses that are tunable from 580 nm to 2.2 μm. The generation of tunable ultrashort pulses in the near- to mid-infrared is also of considerable interest for many applications in time-resolved spectroscopy. Many applications such as the investigation of intraband transitions in quantum wells require tunable pulses in the 3-5 μm spectral region. The optical parametric oscillator (OPO) represents a highly effective technique for the generation of such radiation. There have previously been two reports on Ti:sapphire-pumped OPOs operating in the picosecond time domain. By using KTP as the nonlinear crystal, Nebel et al reported a device with a tunable range of 1.052-1.214 μm (signal) and 2.286-2.871 μm (idler) [1], while Ebrahimzadeh et al recently demonstrated an OPO based on temperature-tuned LBO [2]. This system, which was described in detail in Chapters 4 and 5, was pumped by a picosecond Ti:sapphire laser and produced tunable 1.1 ps pulses over the wavelength range 1.18 μm to 2.25 μm. Although both these materials have proved to be excellent for the generation of tunable picosecond pulses in the near-infrared, they do not represent the optimal choice of crystal for wavelengths

beyond ~2.5 μm, primarily because of material absorption. Hence LBO cannot be used to achieve efficient parametric generation beyond 2.5 μm.

7.2 The Arsenate Isomorphs of KTP

In LBO the transmission cut off occurs at around 2.6 μm and so operation beyond this wavelength is not possible. On the other hand, KTP does have the advantage that its transparency region extends to ~4.5 μm, but suffers from transparency dips at ~2.4 μm and so making operation in this region difficult. To achieve efficient parametric generation beyond 2.5 μm one must utilise a different nonlinear material.

KTP is just one member of the isomorphic family of nonlinear optical materials with the generic composition $MTiOXO_4$ where M is K, Rb, Tl, NH_4 or Cs, and X is P or As. Some of these other materials have more advantageous nonlinear optical characteristics than KTP, such as a larger d_{eff}. In particular, the material $KTiOAsO_4$ (KTA) has recently become available as an alternative to KTP, and offers improved performance for specific applications. KTA is similar to KTP, but with one important difference. As discussed previously, KTP has a strong absorption band near λ= 3.5 μm due to the orthophosphate overtone. KTA has no significant absorptions below λ= 3.7 μm, with the potential for tuning to wavelengths in mid infra-red spectral region that are inaccessible with KTP.

Various OPOs have been demonstrated using the arsenate isomorphs of KTP, namely $KTiOAsO_4$ (KTA) [3, 4], $CsTiOAsO_4$ (CTA) [5], $RbTiOPO_4$ (RTP) [6] and $RbTiOAsO_4$ (RTA) [7]. These materials, especially KTA, have therefore been demonstrated to be excellent candidates for mid-infrared generation because of a transmission range up to ~ 5 μm [4]. The strong orthophosphate and OH absorption bands of KTP are also not present in its arsenate analogues [8], (see Figure 7.1) so that efficient phase-matched wavelength generation is possible throughout the infrared transmission window of KTA.

Recently, a Ti:sapphire-pumped femtosecond OPO based on KTA was demonstrated by Powers et al [10]. By using a critical phase-matching geometry in the x-z plane, average output powers of 75 mW in pulses of 93 fs duration were produced over a signal (idler) wavelength range of 1.29-1.44 (1.83-1.91) μm. To date no Ti:sapphire-pumped picosecond KTA system has been demonstrated.

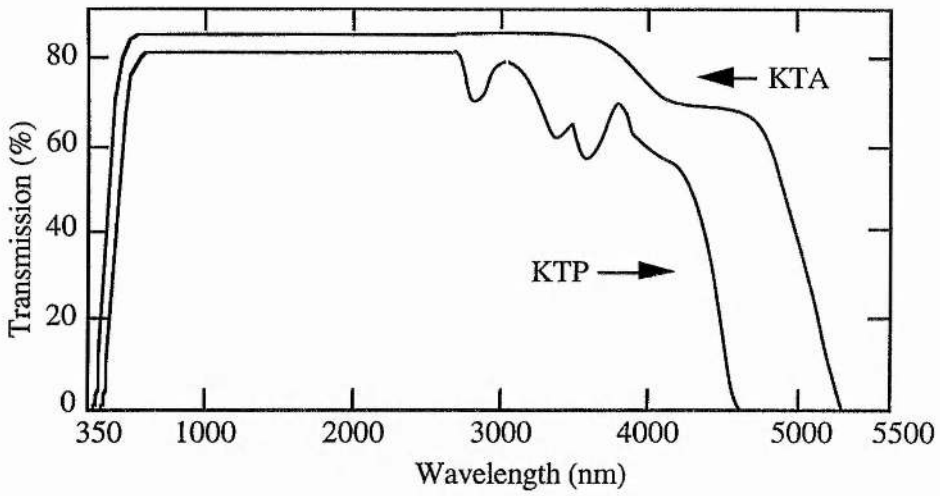

Figure 7.1
Comparison of the transmission spectra of KTA and KTP (taken from ref. [9]).

The work in this chapter describes the design, configuration and operation of a picosecond OPO using the material KTA which is pumped by a self-mode-locked Ti:sapphire laser. The chapter contains all the relevant features required to design a picosecond KTA OPO. A description of the properties of the KTP isomorphs is presented. In a similar manner to that of the LBO system important features such as phase-matching curves, group velocity dispersion, group velocity walkaway, spectral bandwidth and acceptance angle are calculated. Detailed results are then presented describing threshold, pump depletion, output power, conversion efficiencies, tuning range and pulse durations.

7.3 The KTA Crystal

In this section the reasons for choosing KTA as the nonlinear gain medium are discussed. KTA is an orthorhombic crystal with point group symmetry *mm2*. It is optically positive biaxial with a transmission range extending over 350-5300 nm. For parametric generation, KTA can be phase-matched in a number of geometries under both type I and type II interaction, with non-vanishing nonlinear coefficients. In particular, NCPM can be accomplished along the crystal optic axes without the deleterious effects of spatial walkoff. The effective nonlinear coefficient is maximised for the type II interaction along the optical x-axis ($\phi = 0°$, $\theta = 90°$) to a value of 3.23 pm/V. The NCPM geometry is also accompanied by large angular acceptance bandwidths so that tightly focused beams can be used without compromising conversion efficiency. These characteristics are particularly important in efficient parametric conversion of relatively low-energy, low-peak-power pump pulses with tightly focused beams.

This is the case with the high-repetition-rate pump pulses available from the picosecond Ti:sapphire laser used in these experiments, where typical pulse energies of 10-20 nJ with peak powers of around 10-20 kW are delivered in focused beam diameters of ~50 μm (FWHM).

7.4 Modelling of KTA Crystal Properties

In this section the most important crystal properties relating to the suitability of KTA for use as an OPO crystal are discussed.

7.4.1 Pump-Tuning in Type II non-critically phase-matched KTA.

For picosecond operation it is not possible to use angle-tuning due to the large crystal lengths required in the low-peak-power case. This would lead to unacceptable walk off and so pump-tuned non-critical phase-matching is the most useful crystal geometry. The crystal cut used for these experiments was type II NCPM along the x-axis and so all the following modelling will relate to this geometry.

In Figure 7.2, the calculated parametric tuning curves in type II KTA are depicted for pump wavelengths between 760 nm and 920 nm. This calculation was performed by using a similar method to that used in the previous case for LBO, using the Sellmeier equations of References [8, 11]. It is seen that for a pump wavelength range of 760 to 920 nm that the signal branch is tunable from ~1.1 to 1.4 μm with the idler branch tunable from 2.3 to 3.1 μm. This therefore implies that it will be possible to tune to beyond 3 μm using the Ti:sapphire mirror set available in the laboratory.

7.4.2 Comparison of tuning for different sets of Sellmeier equations

It is important whenever possible in any experiment to try to match a theoretical model to the obtained experimental results as a means to try and understand more fully the operation of the device in question. This will enable the device to be 'fine tuned' to obtain the optimum response for the required application. In OPOs the choice of the most appropriate Sellmeier equations for the crystal is generally found by matching the equations to the experimentally obtained tuning curves of the OPO. These equations are then used in all further modelling of the OPO properties. As an indication of how the choice of Sellmeier equations can produce substantial differences in the expected device properties, the same tuning curve calculations performed in the above section have been repeated for

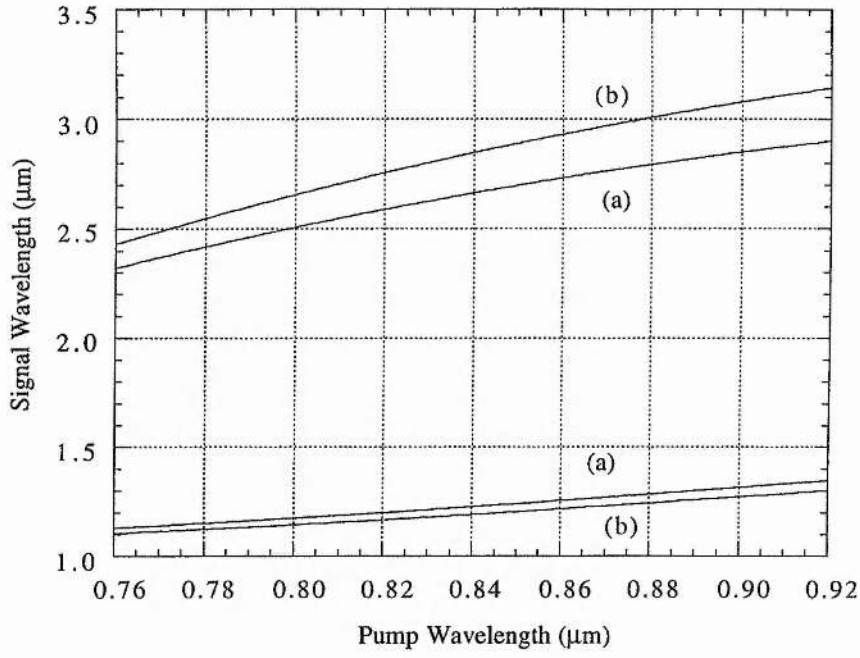

Figure 7.2
Pump-tuning for type II NCPM along the x-axis with the signal being polarised along the y-axis and the idler polarised along the z-axis, where (a) and (b) represent the calculated tuning curves using the Sellmeier equations of references [8] and [11].

four different sets of KTA Sellmeier equations. The results of these calculations are shown in Figure 7.3. The most marked difference is in the idler wavelengths obtained at a pump wavelength of 1.1 μm, in which the value changes from 3.2 μm for equations of Cheng [8] to a value of 3.6 μm for those of Bosenberg [11]. The Sellmeier equations of Cheng et al were found to produce the best match to our experimental data and so were used for all further calculations. These equations are shown below.

$$n_x = \sqrt{2.11055 + \frac{1.03177}{1 - \left(\frac{0.21088}{\lambda}\right)^2} - 0.01064\lambda^2} \qquad (7.1a)$$

$$n_y = \sqrt{2.38888 + \frac{0.77900}{1 - \left(\frac{0.23784}{\lambda}\right)^2} - 0.01501\lambda^2} \qquad (7.1b)$$

$$n_z = \sqrt{2.34723 + \frac{1.10111}{1 - \left(\frac{0.24016}{\lambda}\right)^2} - 0.01739\lambda^2} \qquad (7.1c)$$

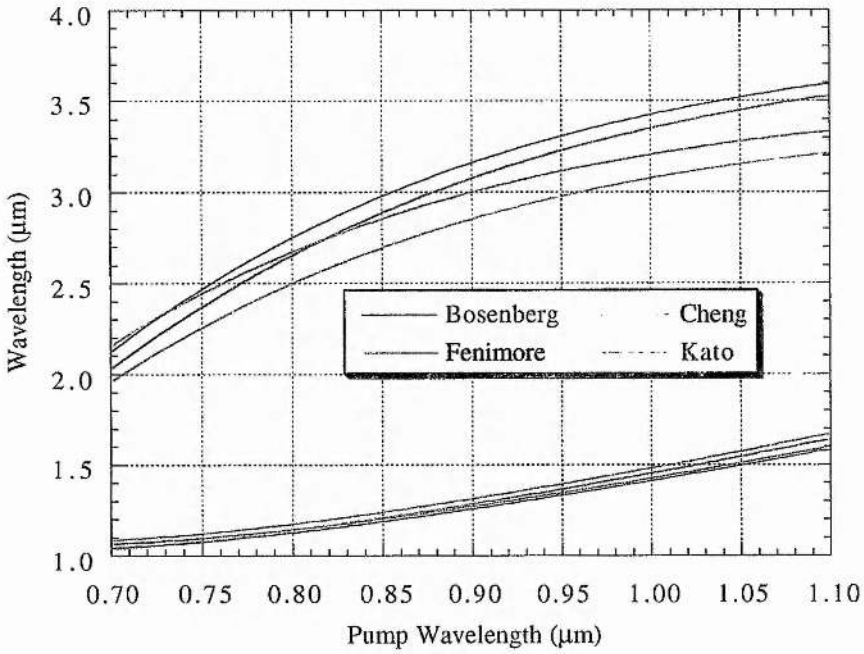

Figure 7.3
Comparison of the tuning range in type II NCPM KTA from four different sets of Sellmeier equations [8, 11, 12, 13].

7.5 Parametric conversion efficiency properties

As discussed in Chapter 4 when considering parametric generation it cannot be assumed that the phase-mismatch condition Δk, is zero. The acceptance angle and spectral bandwidth have been investigated for KTA with the calculations being performed using a similar method to that used earlier. These two parameters limit the usable crystal length for a given pump beam divergence and linewidth.

7.5.1 Acceptance angle

The acceptance angle was calculated for type II NCPM in KTA using the same method as for the LBO case. In the geometry being considered the appropriate angles are $\phi = 0°$ and $\theta = 90°$, substituting these values leads to the following equations, for Δk in the x-y (ϕ) and x-z (θ) planes.

$$\Delta k(\phi) = \left[\frac{\left(n_{x,\lambda_p}\right)^3}{\lambda_p} \left[\frac{1}{n^2_{y,\lambda_p}} - \frac{1}{n^2_{x,\lambda_p}} \right] + \frac{\left(n_{x,\lambda_s}\right)^3}{\lambda_s} \left[\frac{1}{n^2_{y,\lambda_s}} - \frac{1}{n^2_{x,\lambda_s}} \right] \right] (\Delta\phi)^2 \qquad (7.2a)$$

$$= a(\phi)(\Delta\phi)^2$$

$$\Delta k(\theta) = \frac{\left(n_{z,\lambda_i}\right)^3}{\lambda_i} \left[\frac{1}{n^2_{x,\lambda_i}} - \frac{1}{n^2_{z,\lambda_i}} \right] (\Delta\theta)^2 = a(\theta)(\Delta\theta)^2 \qquad (7.2b)$$

These expressions lead to the following solutions in the principal planes

x-y (ϕ) direction:

$$\sqrt{L}\Delta\phi = \sqrt{\frac{0.886 \times 2\pi}{a(\phi)}} \qquad (7.3)$$

$$\Delta\phi\sqrt{L} = \sqrt{\frac{0.886 \times 2\pi}{\frac{\left(n_{x,\lambda_p}\right)^3}{\lambda_p} \left[\frac{1}{n^2_{y,\lambda_p}} - \frac{1}{n^2_{x,\lambda_p}} \right] + \frac{\left(n_{x,\lambda_s}\right)^3}{\lambda_s} \left[\frac{1}{n^2_{y,\lambda_s}} - \frac{1}{n^2_{x,\lambda_s}} \right]}} \qquad (7.3a)$$

x-z (θ) direction:

$$\sqrt{L}\Delta\theta = \sqrt{\frac{0.886 \times 2\pi}{a(\theta)}} \qquad (7.4)$$

$$\Delta\theta\sqrt{L} = \sqrt{\frac{0.886 \times 2\pi}{\frac{\left(n_{z,\lambda_i}\right)^3}{\lambda_i} \left[\frac{1}{n^2_{x,\lambda_i}} - \frac{1}{n^2_{z,\lambda_i}} \right]}} \qquad (7.4a)$$

These results are plotted below in Figure 7.4

The values obtained can be observed to be considerably larger than the equivalent case for LBO, such that the acceptance angle should not prove to be a hinderance in obtaining a good overall conversion efficiency. The NCPM allows the use of tightly focused beams because of the large angular acceptance angle in this geometry compared with critical configurations.

7.5.2 Spectral acceptance bandwidth

The spectral acceptance bandwidth (see Chapter 4 §4.3.2) was also investigated for KTA. The spectral acceptance bandwidth of KTA has been calculated using equation 4.10 (see Chapter 4 §4.3.2) for type II NCPM in KTA. This produced the plot shown in Figure 7.5, where the variation in the pump acceptance

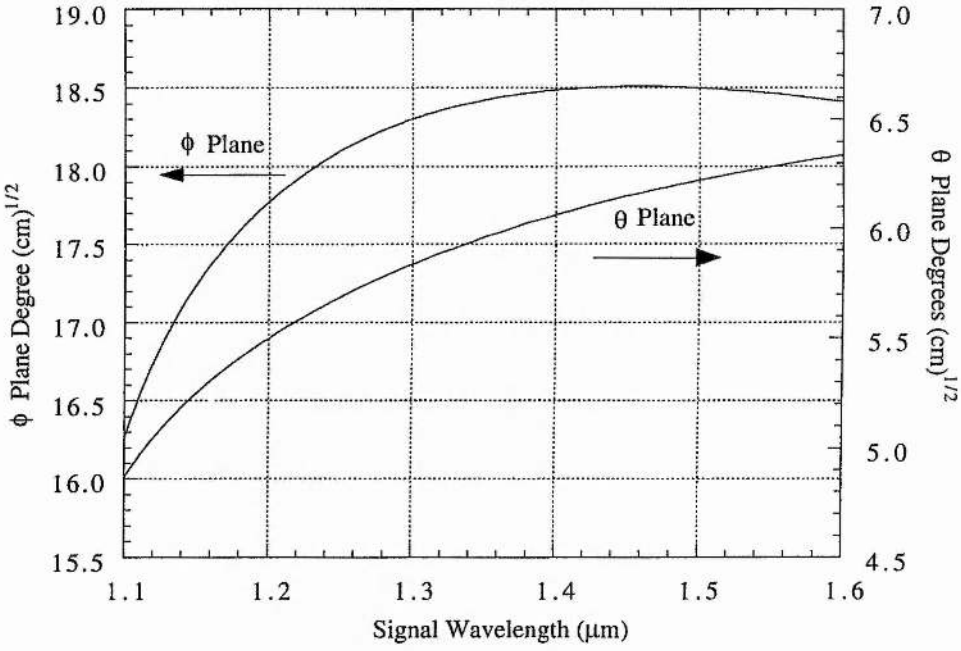

Figure 7.4
The calculated acceptance angles in the ϕ and θ direction in pump-tuned KTA for non-critical propagation along the optical x-axis.

bandwidth of KTA is shown as a function of signal wavelength. The bandwidth values are in the range 2.5-4.5 nm.cm across the available tuning range. The spectral bandwidth corresponding to a transform-limited 1 ps pulse at 800 nm is around 0.7 nm (sech^2 pulse shape assumed). Hence, for 1 ps pump pulses gain reduction due to spectral acceptance limitations in KTA is not significant even for crystals up to 25 mm or longer.

7.6 Modelling of temporal effects

The temporal effects of group velocity walkaway and group velocity dispersion have been calculated for the KTA crystal used in this experiment.

7.6.1 Group velocity walkaway

The differences in the inverse group velocity between the pump, signal, and idler pulses have been calculated using the method given in Chapter 4 §4.4.1.

The result of these calculations are shown in Figure 7.6 where the magnitude of the inverse group velocity mismatch, Δv_g^{-1}, between the pump, signal, and idler in pump-tuned KTA is plotted as a function of the signal wavelength. The

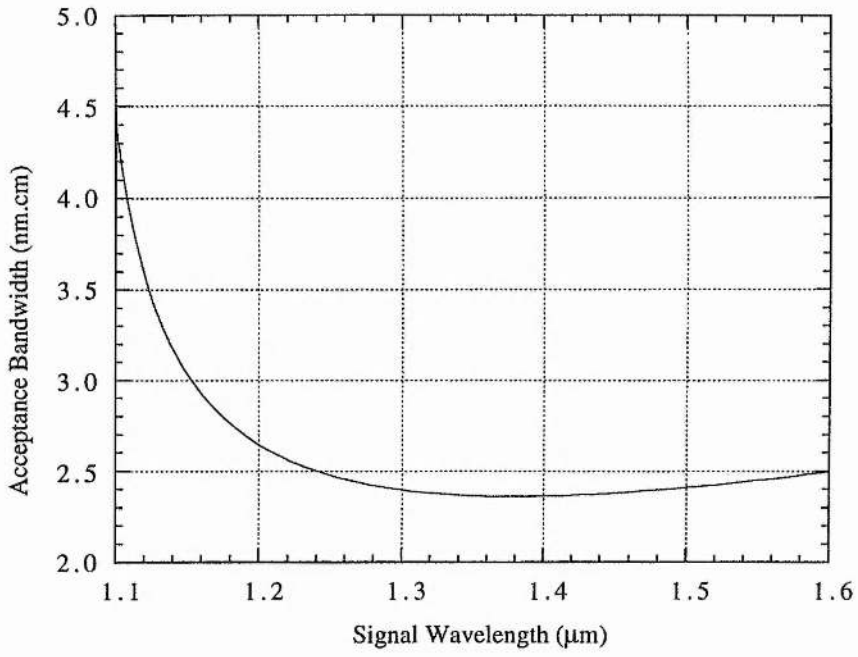

Figure 7.5
The calculated spectral acceptance bandwidth in pump-tuned KTA (θ=90°, ϕ=0°).

calculations are based on the Sellmeier equations of Cheng et al [8]. It is seen that the temporal walkaway between the resonated signal and pump is about 50-160 fs/mm across the tuning range with the corresponding signal/idler and pump/idler walkaway amounting to 240-350 fs/mm and 80-300 fs/mm, respectively. The walkaway between the pump and resonated signal has a first-order effect on OPO oscillation threshold and conversion efficiency [14] and is thus the most important parameter in determining the maximum useful interaction length. The large value of pump/signal walkaway implies that the KTA crystal length usable will be restricted to lengths far shorter than was the case for LBO.

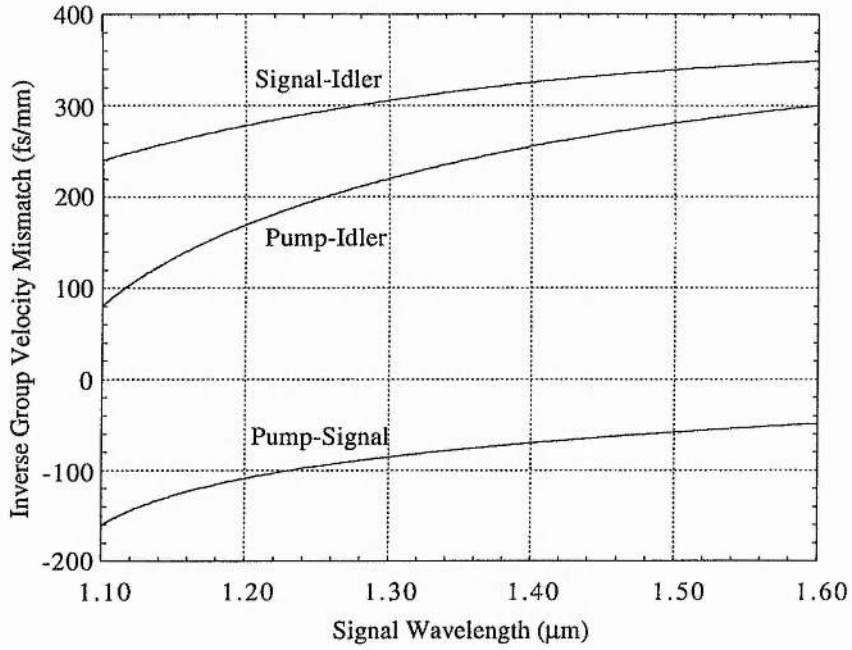

Figure 7.6
The variation in the inverse group velocity mismatch, Δv_g^{-1}, between the pump, signal and idler across the tuning range of the pump-tuned KTA (θ=90°, ϕ=0°) OPO.

7.6.2 Crystal length calculations

It is possible to calculate the maximum useful crystal lengths. This procedure was again very similar to the case for LBO (see Chapter 4, §4.4.2). This calculation was carried out for a 1 ps pulse, the results can be seen in Figure 7.7. It can be observed that the maximum crystal length permissible now varies between ~6 and 18 mm across the tuning range of the OPO. A crystal length must be chosen that is satisfactory at all signal wavelengths, i.e. walkaway must be minimal across the entire tuning range of the device. A crystal of length 10 mm is sufficient across most of the OPO tuning range. The actual crystal used in the experiment is discussed in §7.7.

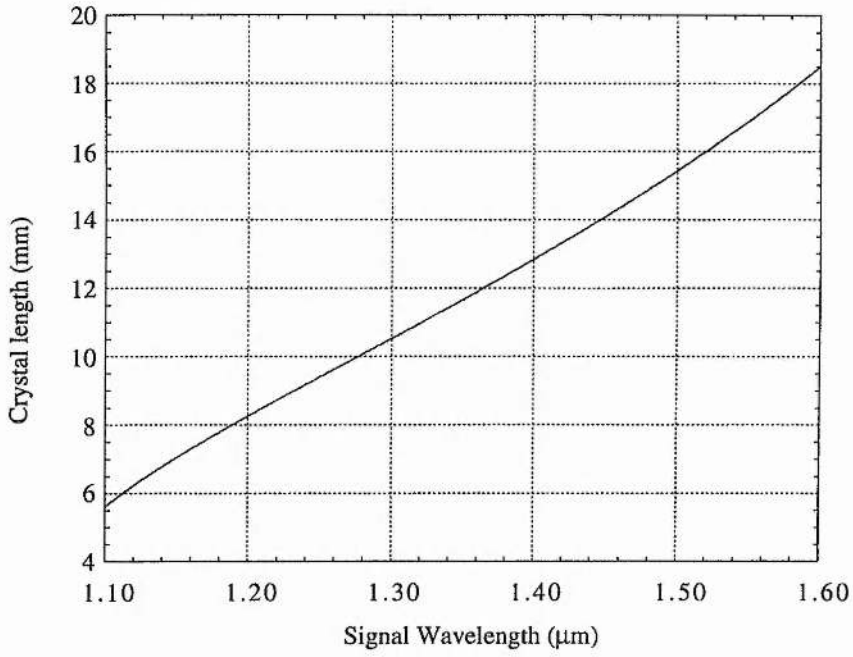

Figure 7.7
Variation in the maximum useful crystal length across the tuning range of the pump-tuned KTA (θ=90°, ϕ=0°) OPO.

7.6.3 Group velocity dispersion

Group velocity dispersion (GVD) is also a very important temporal effect. In Figure 7.8, the variation in the pump, signal and idler GVD in KTA is shown across the tuning range of the OPO. The GVD values were calculated by evaluating the dispersion parameter β'' given in Chapter 4, §4.4.3.

It is seen from the plot that the signal GVD in KTA remains in the region 25 - 120 fs²/mm. With the corresponding pump and idler values in the ranges 175 - 250 fs²/mm and 75 - 500 fs²/mm. The most important feature of the GVD values is the signal value, as this is the value governing whether or not the resonant wave will see a positive or negative GVD. The large positive GVD values encountered by the signal wave would imply that the signal pulses should be significantly chirped in nature although dispersion broadening generally becomes more significant with shorter pump pulse durations and longer interaction lengths.

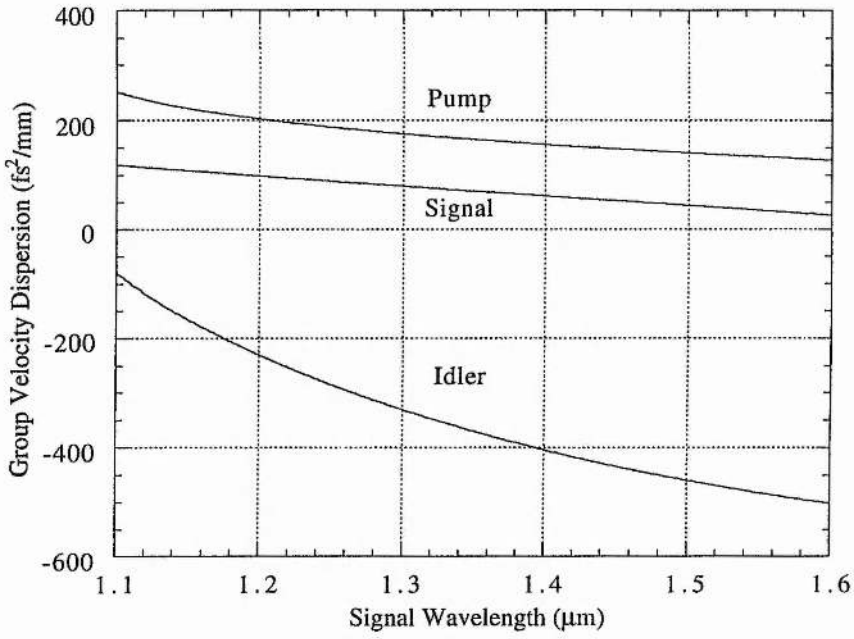

Figure 7.8
The variation in group velocity dispersion in pump-tuned KTA (θ=90°, ϕ=0°).

Therefore it may be concluded that the above considerations indicate that KTA is an excellent choice of material for use in picosecond OPOs. The following section describes the experimental configuration of the OPO.

7.7 The KTA optical parametric oscillator

The configuration of the Ti:sapphire-pumped picosecond KTA OPO is very similar to the LBO OPO and is depicted in Figure 7.9. The pump source was again a commercial self-mode-locked Ti:sapphire laser (Spectra-Physics, Tsunami) which was configured for picosecond operation. The OPO cavity was a standing-wave, three-mirror, folded arrangement formed by two concave reflectors and a plane mirror through which the output signal was collected. The resonator fold angle was kept to <3° to minimise astigmatism. The oscillator was singly-resonant and the pump was single-pass. The mirrors used were highly reflective single-layer dielectric coatings centred at 1180 nm (R>99.9%) and highly transmitting (T>95%) at 800 nm. The back surfaces of the mirrors were also antireflection-coated at the centre wavelength of 800 nm. The concave mirrors had a radius of curvature r=10 cm, resulting in a signal waist radius of 20 μm at the centre of the stability range, see section 7.8.12. No dispersion

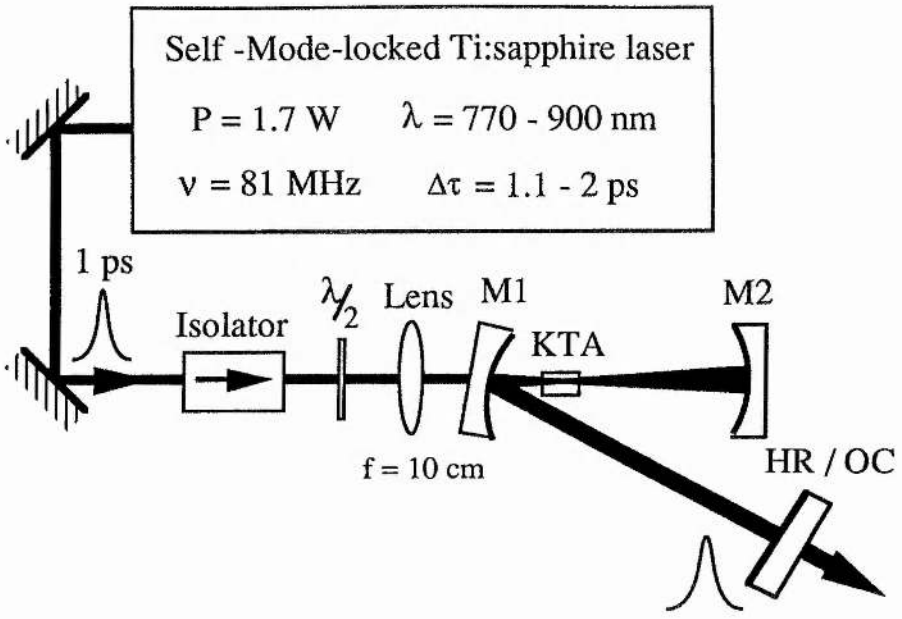

Figure 7.9
Schematic of the Ti:sapphire-pumped KTA OPO. The mirrors M_1 and M_2 have radii of curvature r=10 cm. λ/2 is a half-wave plate. HR/OC denotes a high reflector or output coupler.

compensation was included in the cavity. The KTA crystal was cut for type II non-critical phase matching along the x-axis with the pump and resonant signal wave being polarised along the y-axis and the non-resonant idler wave being polarised along the z-axis. The crystal was placed in an insulated oven so that temperature-tuning experiments could be performed. As a NCPM geometry was used no walk-off existed between the pump, signal and idler beams inside the crystal, therefore the crystal length was only restricted by the difference in the group velocity of the three wavelengths. For this cut of KTA, the group velocity walkaway (GVW) between the signal and pump is in the range 50-160 fs/mm and the group velocity dispersion (GVD) for the signal waves ranges from 25 to 120 fs^2/mm over the signal tuning range. These values when incorporated with pump pulses of 1-3 ps duration mean that the effects of GVD and GVW should not be significant for practical crystal lengths of 10-30 mm. This cut also maximises the nonlinear coefficient at 3.23 pm/V and produces a large spectral acceptance bandwidth of ~5 nm.cm, hence permitting transform-limited pulses with large output powers to be produced. The KTA crystal used was 10 mm in length with a 3 mm x 3 mm aperture. The end faces of the crystal were coated with a MgF_2 antireflection coating centred at 1200 nm (T>99.9%) with low loss (T=95%) at 800 nm. The pump beam was focused through the input concave mirror to a spot radius of ~25 μm inside the crystal, using a plano-convex lens of

focal length f=10 cm. Since the OPO was collinearly pumped, an optical isolator was used between the two cavities to avoid backreflections into the Ti:sapphire laser. A half-wave plate was also used to rotate the pump polarisation along the y-axis of the crystal. The total pump power reduction from the Ti:sapphire to the OPO was around 400 mW and is accounted for by reflection losses due to transmission optics and power loss to diagnostics. A maximum of 1.3 W was therefore available at the input to the nonlinear crystal.

7.8 Experimental results

7.8.1. Tuning Characteristics

In Figure 7.10 the measured tuning range of the KTA OPO is plotted for a range of pump wavelengths from 770 to 896 nm. With the available mirrors set, the signal covered the wavelength range 1.139 to 1.260 μm with the corresponding idler coverage being from 2.377 to 3.101 μm. The solid lines represent the

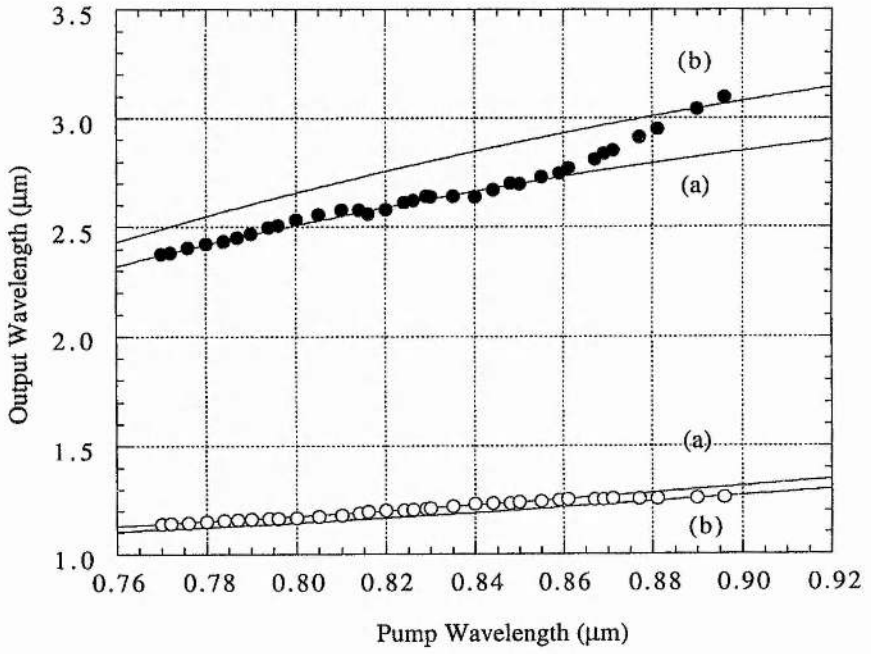

Figure 7.10
Signal wavelength data (open circles) and inferred idler data (closed circles) for pump wavelengths from 770 to 896 nm. The solid curves (a) and (b) represent the tuning predicted from the KTA Sellmeier equations of [8] and [11], respectively.

predicted tuning derived from two different sets of Sellmeier equations for KTA [8, 11] which best match the experimental data. It is interesting to note that the curves of (a) match well for pump wavelengths in the range 770-860 nm, with curves (b) producing a better fit at higher pump wavelengths, so unification of these equations to produce an improved set may be possible. The obtained tuning range provides a considerably more extensive mid-infrared coverage than the femtosecond KTA OPO reported previously [10] and that available from the picosecond OPO based on KTP [1]. Moreover, the main restriction to the demonstrated tuning range is the extent of the pump-tuning available for the Ti:sapphire laser (770-910 nm) with the existing set of optics. With an optimised mirror set, tuning of the pump to ~1 μm will extend the wavelength coverage of the signal to ~ 1.5 μm and the idler up to 3.5 μm. The tuning data in Figure 7.10 also corresponds to minimum OPO cavity length detuning.

7.8.2 Non-phase-matched processes

As with the LBO OPO it was found that in addition to the signal and idler beams, the picosecond KTA OPO also produces a further five non-phase-matched processes. Single-pass second harmonic generation occurs for the pump, signal and idler waves, which for a pump wavelength of 800 nm produces outputs at 400 nm, 584.5 nm and 1267 nm. These wavelengths were found to have polarisations in the same directions as their corresponding fundamental waves. Sum frequency mixing occurs between the pump and signal, producing output at 475 nm, and between the pump and idler, producing output at 1249 nm, both polarised along the y-axis. Figure 7.11 shows the spectra for second harmonic signal at 584.5 nm and the sum frequency output at 475 nm, if these pulses are transform-limited then the spectral widths will produce pulse durations of 1.0 and 1.02 ps for the radiation at 584.5 and 475 nm, respectively. These processes did however also occur across the entire tuning range of the OPO, with the tuning range of the doubled signal being shown in Figure 7.12. This can be seen to produce an output between 570 to 630 nm. These processes produced a range of output powers. However the strongest was the pump frequency-doubling with even this only producing 3 mW of power, and so none of these processes can be used practically due to the relatively low powers produced.

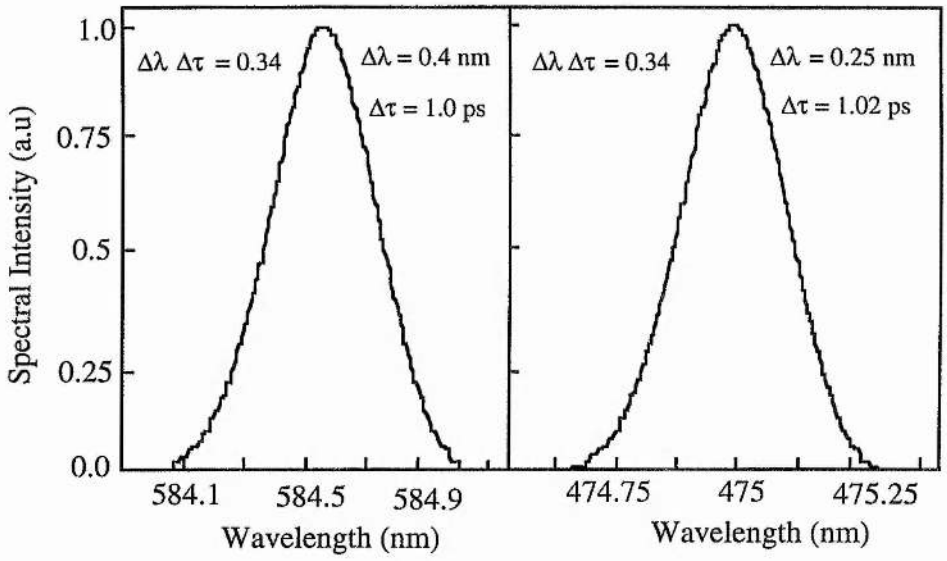

Figure 7.11

Spectra of the non-phase-matched signal pulses at 584.5 nm and sum frequency generation between the signal and pump at 475 nm.

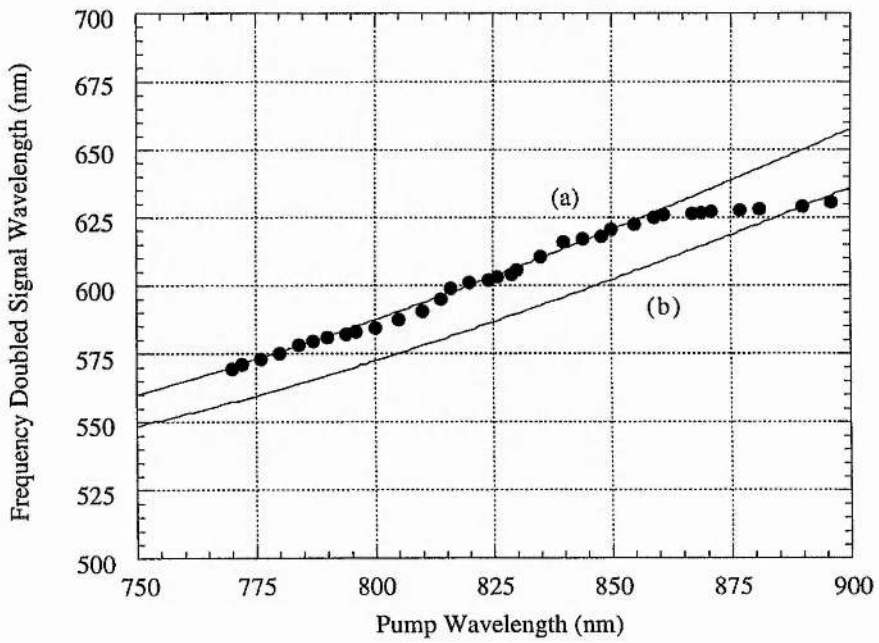

Figure 7.12

Frequency-doubled signal wavelength data (open circles) for pump wavelengths from 770 to 896 nm. The solid curves (a) and (b) represent the tuning predicted from the KTA Sellmeier equations of [8] and [11], respectively.

7.8.3 Threshold

With 1.2 ps duration input pump pulses when the cavity was configured with all highly reflecting mirrors the minimum oscillation threshold was 230 mW at the centre of the mirror reflectivity band (see Figure 7.13). Therefore, the threshold pump pulse energy was 2.5 nJ, corresponding to a peak power of 2.4 kW, and peak intensity of 240 MW/cm^2 inside the KTA crystal. Oscillation could be maintained across the entire signal tuning range for average pump powers below 600 mW. Oscillation could be maintained for an output coupling loss of up to 15%.

Optimum performance, i.e. highest power output was, however obtained for a 7.5 % output coupler. Using this 7.5% output coupler, the threshold increased to 250 mW. This small increase due to output coupling indicates that output coupling is not the dominant loss mechanism in this system. A prediction of the threshold has again been made by using the model of Guha, Wu and Falk [15], this again produced a good fit to the experimental data, as seen in Figure 7.13. The deviation away from the model is due to the lack of exact information about the variation of the mirror AR coatings and transmission across the entire tuning range. This data would allow a more accurate fit to the whole tuning range.

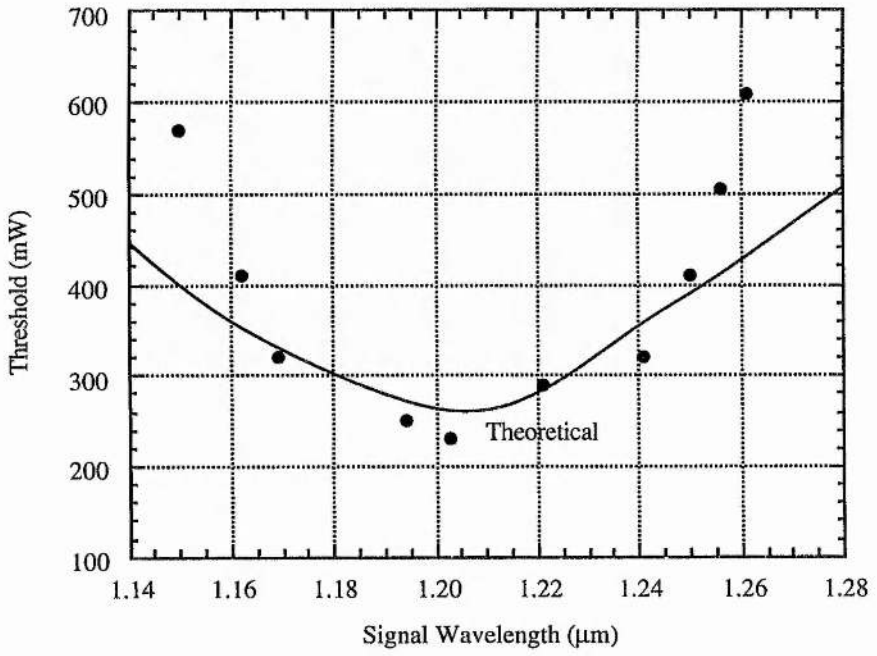

Figure 7.13
Variation in the average pump-power threshold across the tuning range of the KTA OPO.

7.8.4 Output coupling

As discussed in previous Chapters the correct choice of output coupler has a critical effect on the amount of usable energy obtainable from the system. In this section the output power from the OPO is measured for a number of different values of output coupling. The results presented in Figure 7.14 represent the signal output powers, for six different values of output coupling, namely 2, 5, 7, 7.5, 12.5 and 15 %. It can be observed in Figure 7.14 that the maximum output

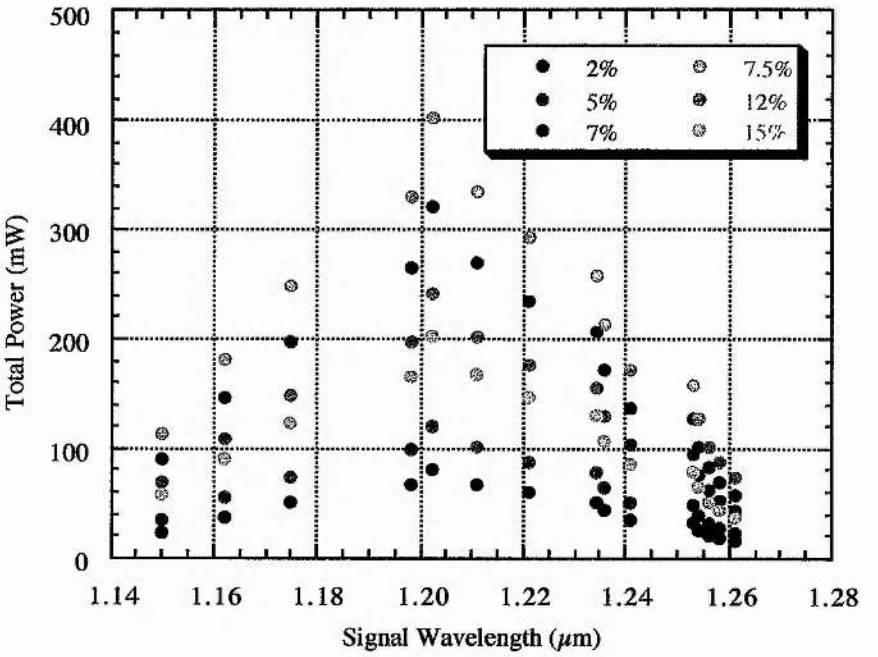

Figure 7.14
Variation in the output signal power as a function of output coupler transmission in the KTA OPO for 1.3 W of pump power.

power value of 400 mW occurs for the 7.5 % output coupler, the 12.5 and 15 % cases lead to 'overcoupling', in which a high output coupling results in a large reduction in gain leading to an associated reduction in output power. This effect is responsible for the maximum powers reducing to 250 and 200 mW for the 12.5 and 15 % cases, respectively. For the 2, 5 and 7 % cases 'undercoupling' takes place, where the lack of output power is simply due to the fact that the power is unable to 'escape' from the cavity due to a lack of transmission in the output couplers. This process results in the maximum powers reducing to 80, 120 and 320 mW for the 2, 5 and 7 % values, respectively. The 7.5 % output coupler therefore represents the best value of transmission to match the gain and

loss of the OPO cavity and leads ultimately to the highest output power. All further work in this chapter relates to the 7.5 % output coupler unless otherwise stated.

7.8.5 Output Power and Efficiency

Using the optimum 7.5% output coupler at a signal (idler) wavelength of 1.202 (2.580) μm, a total average output power of 403 mW was achieved, with this power being split into a signal power of 290 mW and a single-pass idler power of 113 mW. These values, which were generated for 1.3 W of pump power are, shown in Figure 7.15 and correspond to an external efficiency of 31% at 5.2

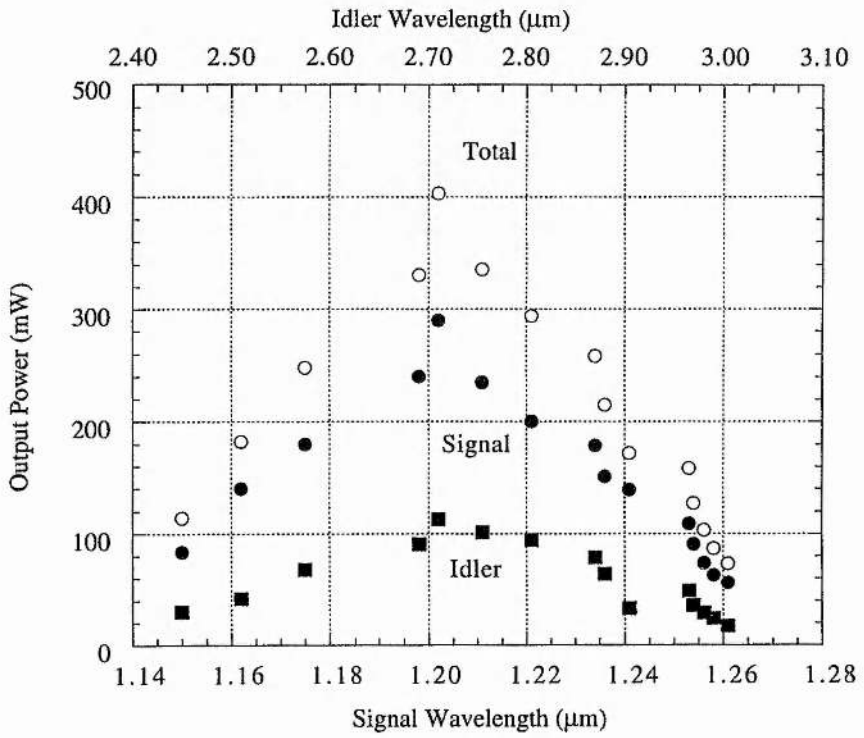

Figure 7.15
Variation of signal (closed circles), idler (squares) and total power (open circles), with a 7.5 % output coupler as a function of signal wavelength, for a pump power of 1.3 W.

times threshold. At this level the pump depletion was 49%. In the absence of optimised output coupling for all signal wavelengths, the maximum output power of 403 mW could not be maintained across the entire tuning range (see Figure 7.15). The OPO could, however, routinely deliver total output powers in excess of 200 mW over most of the available tuning range. This results in the

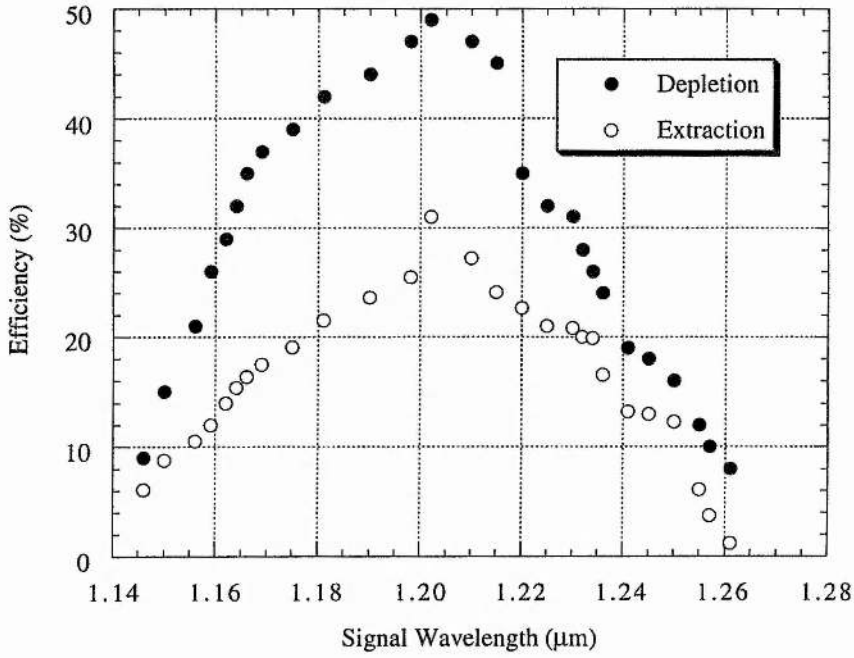

Figure 7.16
Variation in the depletion and extraction across the tuning range of the KTA OPO.

total extraction of the system remaining in the range ~10-30 % across the majority of the tuning range (see Figure 7.16). If optimum transmission output coupler coatings were available across the entire tuning range of the OPO then it would be possible to extract a far greater proportion of the depleted power over the entire tuning range. There was also found to be no evidence of saturation, which implied that significantly higher output powers and conversion efficiencies will be available with higher pump powers, longer crystals, or improvements in mode-matching. Measurement of the variation of output power of the OPO as a function of pump power was performed so that an estimate of slope the efficiency could be made. It can be observed in Figure 7.17 that the slope efficiency of this device is as high as 38%.

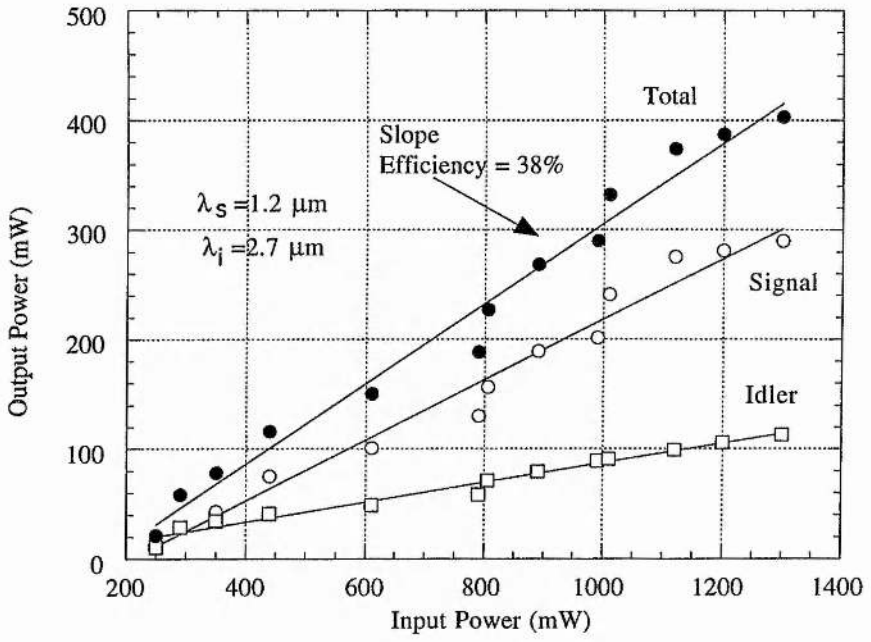

Figure 7.17
Output power of the KTA OPO as a function of input power, for a signal wavelength of 1.2 μm.

7.8.6 Amplitude noise measurements

As was the case with the LBO OPO, the KTA is also an extremely robust device. When aligned correctly, oscillation persists for several hours at a time without any form of active stabilisation. The amplitude noise present on the outputs of both the parametric oscillator and the pump laser was compared and typical oscillograms are shown in Figure 7.18. Intensity fluctuations on the Ti:sapphire pump laser are typically less than 1 %, with the OPO exhibiting amplitude fluctuations of around 2.5 %. This relatively low value is to be expected as the effects of SPM and GVD in the OPO are negligible. This result is again consistent with previous experimental and theoretical studies [16, 17] which indicated that relatively unstable output can result if there is inadequate spectral control in lasers where SPM and GVD are significant.

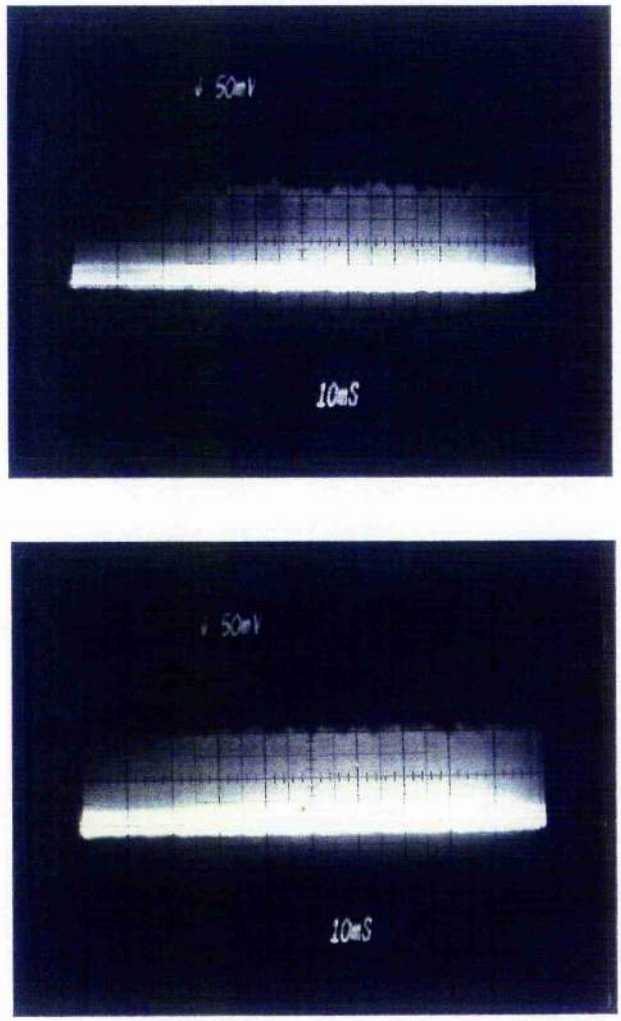

(a)

(b)

Figure 7.18
Oscillograms showing the amplitude noise (intensity fluctuations) of the self-mode-locked Ti:sapphire pump laser (a), the OPO (b). The timebase is 10 ms/division in each case.

7.8.7 Temporal Characteristics

In Figure 7.19 (a)-(c), typical intensity and interferometric autocorrelations and corresponding spectra of the signal at a wavelength of 1.248 μm are shown. The corresponding idler pulse data at a wavelength of 3.042 μm is depicted in Figure 7.19 (d)-(f). The data were recorded at minimum cavity length mismatch and at 5.2 times above oscillation threshold. The idler pulse at 3.042 μm was at the time of measurement the longest output wavelength from a synchronously-pumped OPO for which a direct intensity or interferometric autocorrelation has been reported. The pulse durations deduced from the intensity autocorrelations

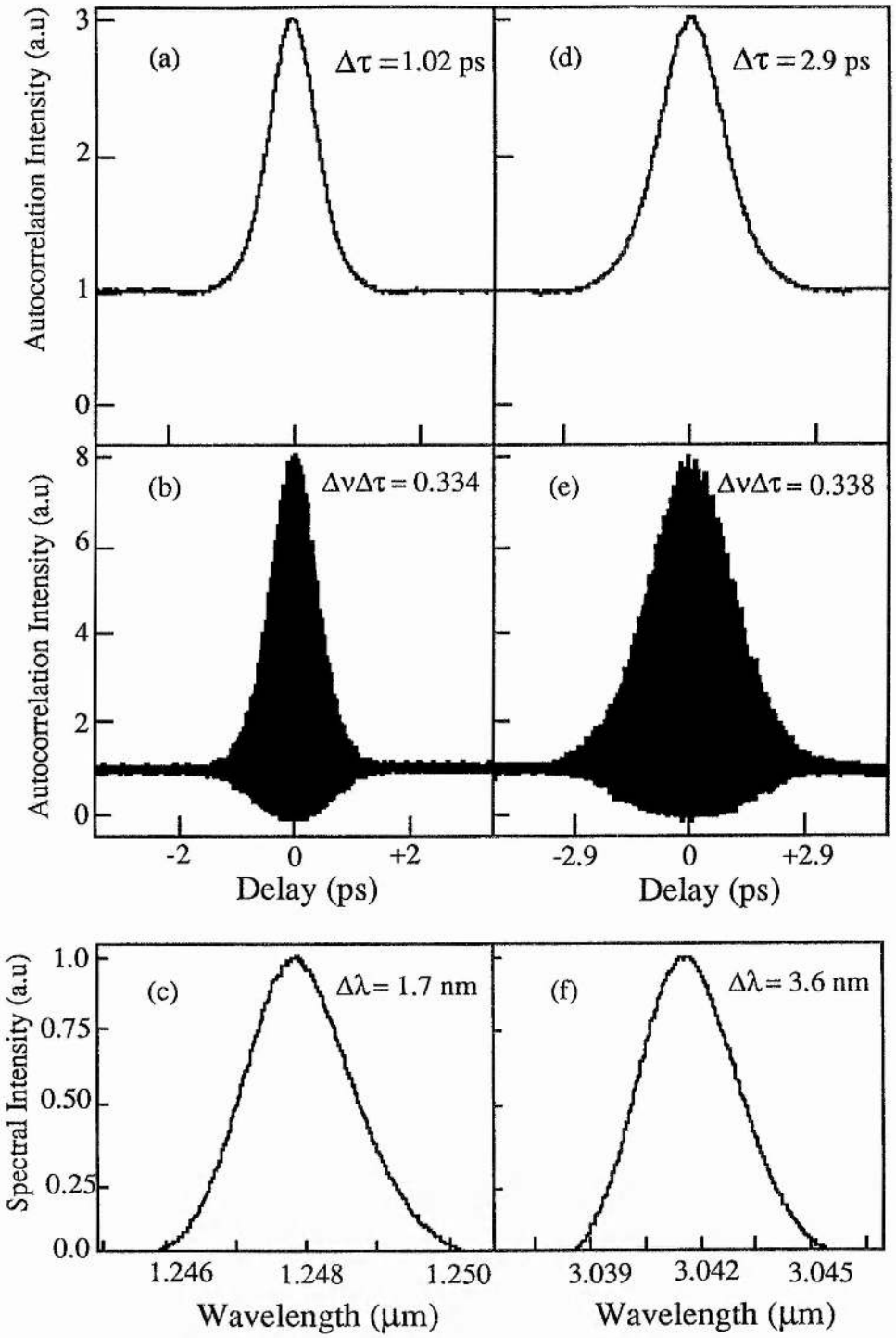

Figure 7.19

Intensity (a, d) and interferometric (b, e) autocorrelation, and the corresponding spectrum (c, f) of signal and idler pulses at 1.248 and 3.042 μm, recorded at 5.2 times pump threshold. The pulse durations determined from the intensity autocorrelation are 1.02 ps for the signal and 2.9 ps for the idler with corresponding time-bandwidth products of 0.334 and 0.338.

are 1.02 ps for the signal and 2.9 ps for the idler (assuming a $sech^2$ pulse profile) for a pump pulse duration of 1.2 ps. The shape of the interferometric autocorrelations are indicative of chirp-free pulses. The spectra of both signal and idler can be observed to have a smooth profile, with the signal having a spectral width of 1.7 nm and a time-bandwidth product of 0.334 and the idler having a spectral width of 3.6 nm and a time-bandwidth product of 0.338. These pulses are therefore essentially transform-limited. The lack of chirp in the signal autocorrelation indicates that pulse broadening due to the effects of GVD is not present here, even though in this wavelength region in KTA the GVD is significantly positive. This is to be expected because the effects of GVD are generally not so significant with picosecond pulses when using the relatively short crystal lengths, as is the case here. The smooth profile of the spectra also indicates that no self phase modulation is present. Figure. 7.20 shows the variation in the signal and idler pulse durations across the OPO tuning range. It

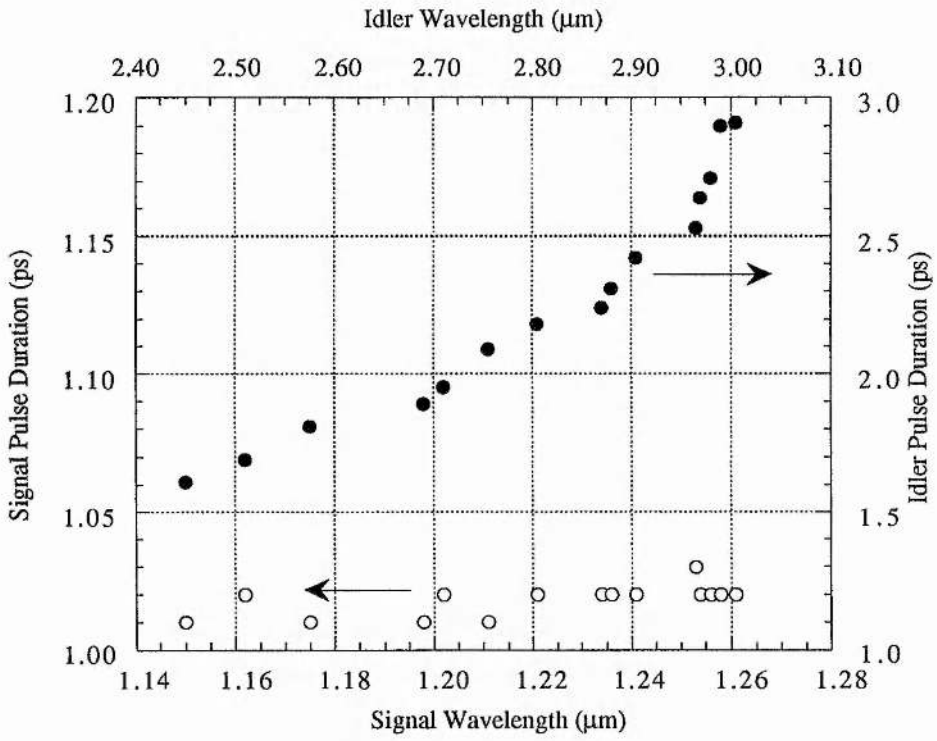

Figure 7.20
Variation in signal and idler pulse durations across the tuning range of the KTA OPO, for a pump power of 1.3 W.

can be observed that the signal pulse duration varies only minimally from 1.01 to 1.03 ps, with more extensive variation in the idler from 1.61 to 2.91 ps over the tuning range. The variation in the signal pulse durations may be accounted for

by the small differences in the output coupling across the tuning range which result in changes in the pump threshold. The increase in idler pulse durations is due to insufficient spectral bandwidth being present to support pulses of shorter duration, the idler spectral bandwidth at 3.042 μm is found to have a value of ~ 3.5 nm which corresponds to a transform-limited pulse duration of ~ 3 ps. To support a transform-limited 1 ps pulse at this wavelength would require a bandwidth of ~ 10 nm. However, it can be observed that both the signal and idler pulses remain essentially chirp-free and transform-limited across the tuning range without the need for dispersion compensation.

Investigation of the variation of signal pulse duration with pump depletion was also performed by recording autocorrelation data for a range of input pump powers from 250 mW to the maximum available of 1.3 W, the results of this study are shown in Figure 7.21. It was found that the signal pulse length

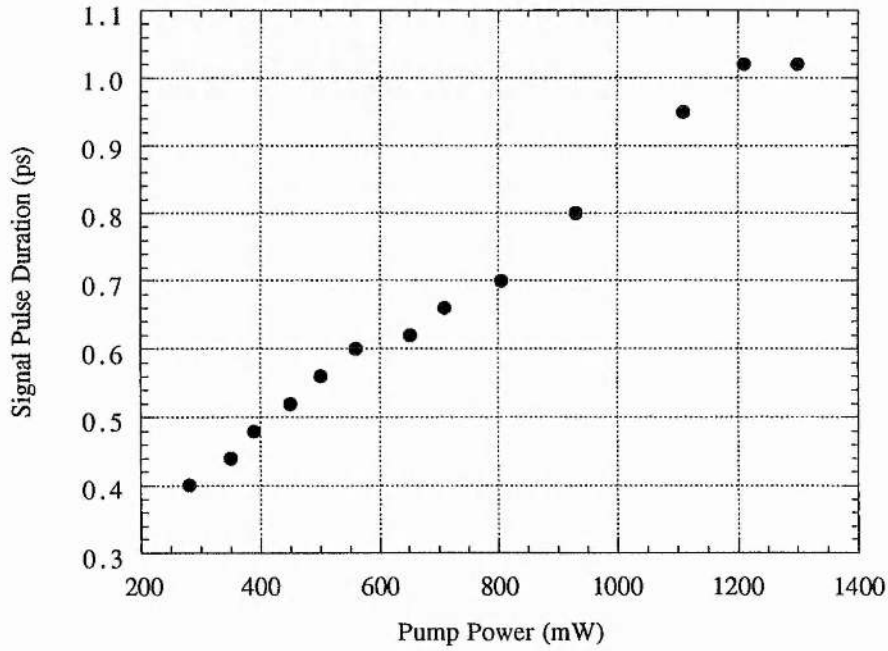

Figure 7.21
Variation in signal pulse durations as a function of pump power.

increased from 400 fs at 1.22 times threshold to 1.02 ps at 5.2 times above threshold. This behaviour is consistent with the theoretical predictions of Cheung and Liu [14] and of Becker et al [20] where the change in the curvature of the pump pulse due to depletion is suggested to be responsible for pulse broadening. However, it is interesting to note that the shortest signal pulse

duration of 400 fs measured in these experiment was slightly lower than the minimum attainable pulse width of 480 fs (~0.4 times the pump pulse width) predicted by theory [14, 18].

7.8.8 Cross correlation

As was the case for the LBO systems, cross correlation measurements were carried out between the pump, signal and idler waves, with the results indicating that again timing jitter is not significant.

7.8.9 Cavity Tuning

Operating the OPO across its cavity synchronous range of typically 25 μm (FWHM) produced a tuning in the signal of 25 nm and 122 nm in the idler (see Figure 7.22 (a)). This fine tuning occurs across the entire wavelength range of the device and extended the tuning range of the OPO to 1.116-1.281 μm and 2.260-3.160 μm for the signal and idler, respectively (see Figure 7.23). The reasons for this wavelength tuning were discussed in detail in Chapter 5. For this OPO, a detuning range of 25 μm (FWHM) was observed when pumping at around 5.2 times threshold. At higher pump powers longer detuning ranges will be available because of the increase in the signal pulse duration with pump depletion and higher instantaneous gains. It is also important to note that the signal wavelength shift of 25 nm in this OPO is much larger than other picosecond systems based on KTP [1] and is in fact similar to that observed in femtosecond oscillators [19-28].

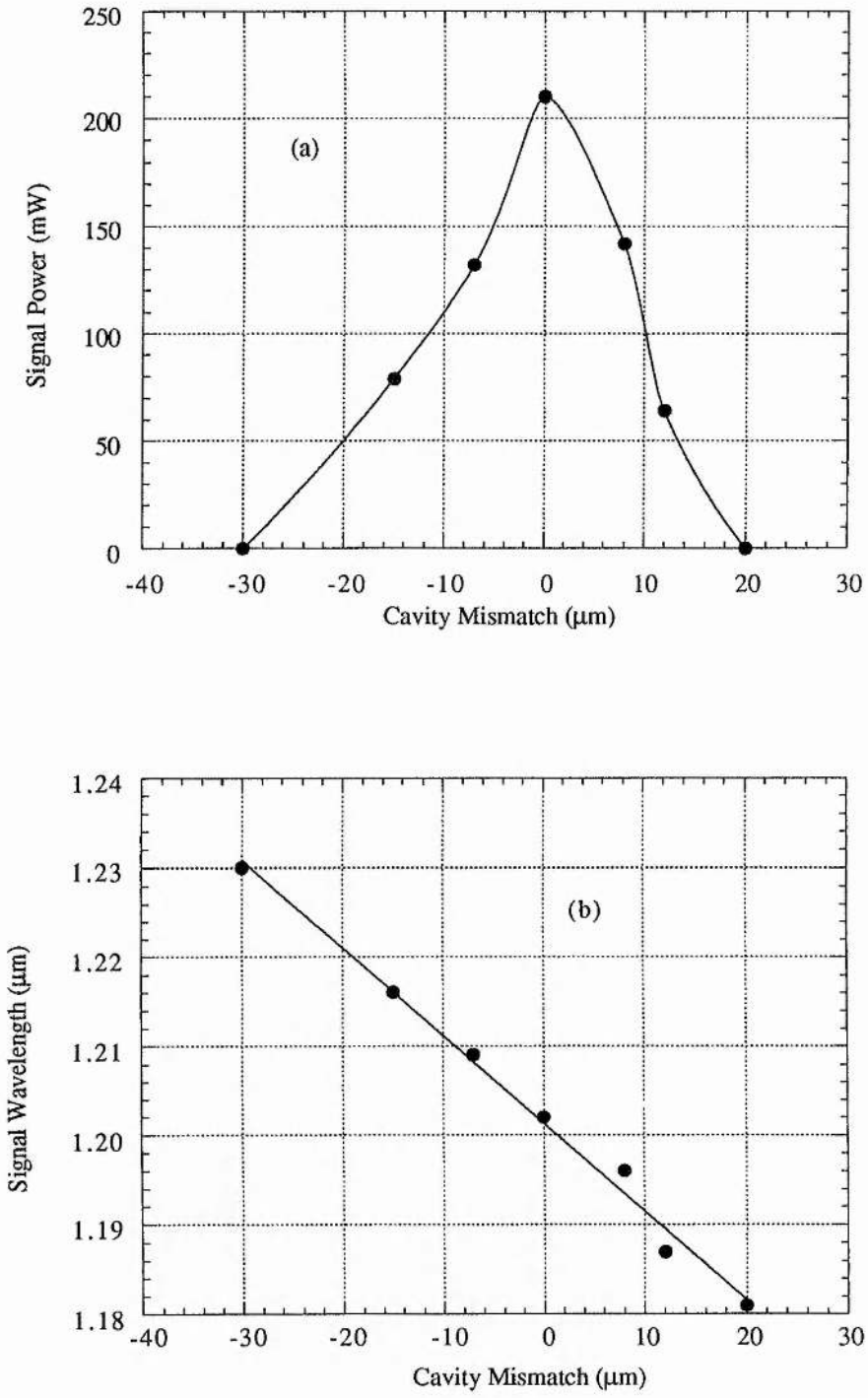

Figure 7.22

(a) Cavity synchronous range and (b) signal wavelength detuning in the KTA OPO. In (a) the FWHM synchronous range of the cavity is 25 μm. In (b) the straight line represents the best fit to the experimental data.

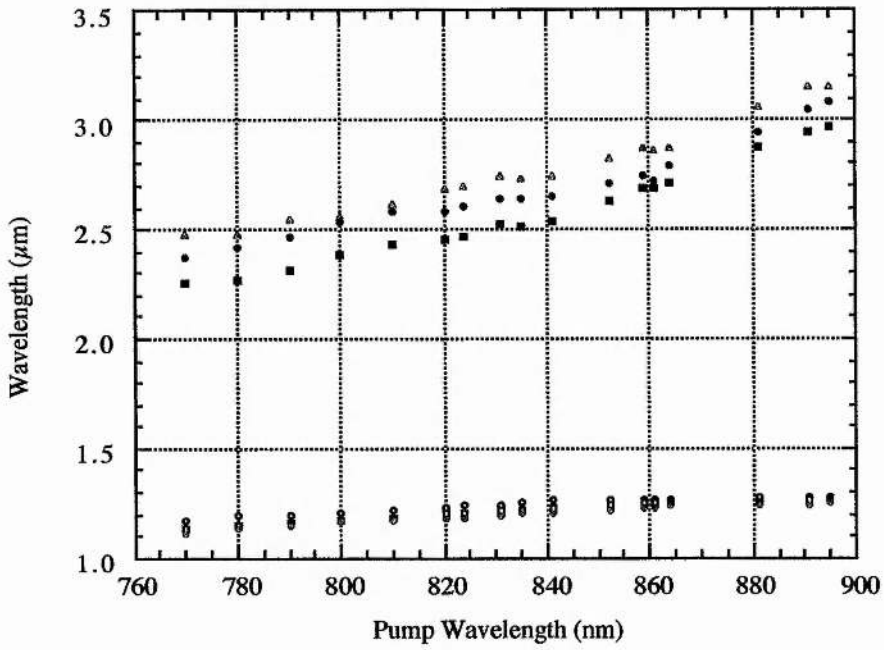

Figure 7.23
Cavity tuning extremes showing signal wavelength data and inferred idler data for pump wavelengths from 770 to 896 nm.

7.8.10 Temperature-Tuning

KTP is known to only be slowly temperature tunable, i.e. its refractive indices are not sensitive to temperature variations [29, 30]. This therefore results in a situation that if a NCPM geometry is chosen then tuning is restricted to pump-tuning only. This situation is acceptable if the pump source is tunable, as was the case in this work with the Ti:sapphire laser. If, however, the pump source was, for example a YAG laser in which pump-tuning is not possible then it would be useful if the OPO crystal being used was temperature tunable, as is the case with LBO. KTA is chemically similar to KTP and so it was thought that temperature-tuning would be unlikely in this material. However, a measurement was performed to assess the extent of the temperature tunablility which could be made. The KTA OPO was temperature-tuned as a means to ascertain if this method of tuning was practical and it was found that heating the crystal up to 100 °C yielded a shift in signal wavelength of less than 1 nm (see Figure 7.24). Although this result indicates that tuning of this kind is not practical in KTA, it also shows that this device will be impervious to variations in temperature that may occur in the laboratory, hence leading to good output stability.

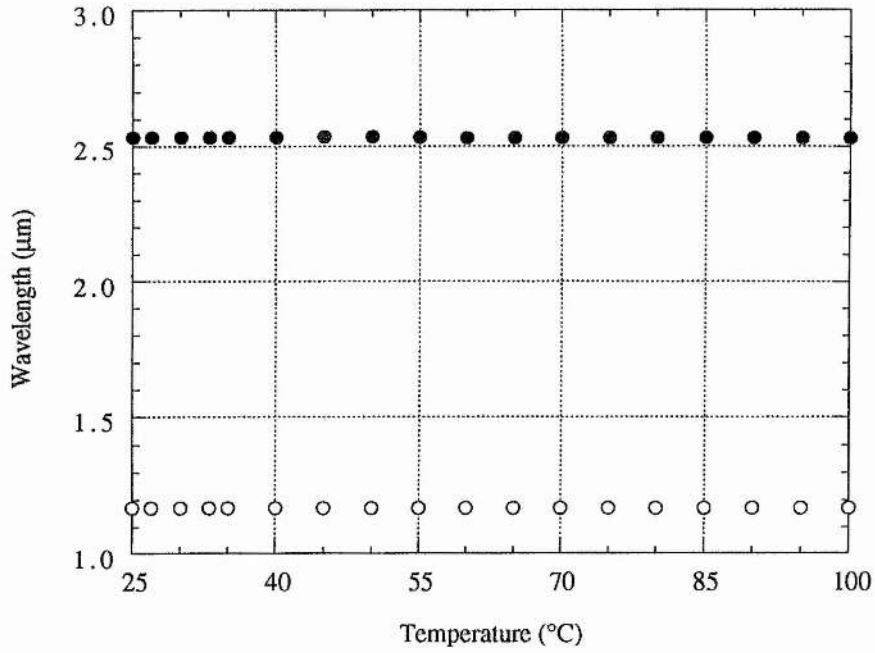

Figure 7.24
Variation in signal and idler wavelengths as the KTA OPO is temperature-tuned.

7.8.11 Angle-Tuning in KTA

It was discussed previously that angle-tuning was generally not possible for picosecond systems. However, as an exercise in extending the tunability of the system it was decided to try and angle tune the crystal in the 3 principal planes, namely x-z, x-y and y-z planes. The angle-tuning behaviour of KTA is shown below in Figure 7.25, for a pump wavelength of 800 nm. This again shows that the chosen crystal cut maximises the nonlinear coefficient. Each plane will be discussed in turn with the available tuning of each discussed, along with the measurement of the variations in thresholds and output power as the crystal is rotated.

7.8.11.1 The x-z Plane

Rotation in this plane is obtained by rotating the crystal vertically, this keep the angle ϕ constant at 0° and varies the angle θ.

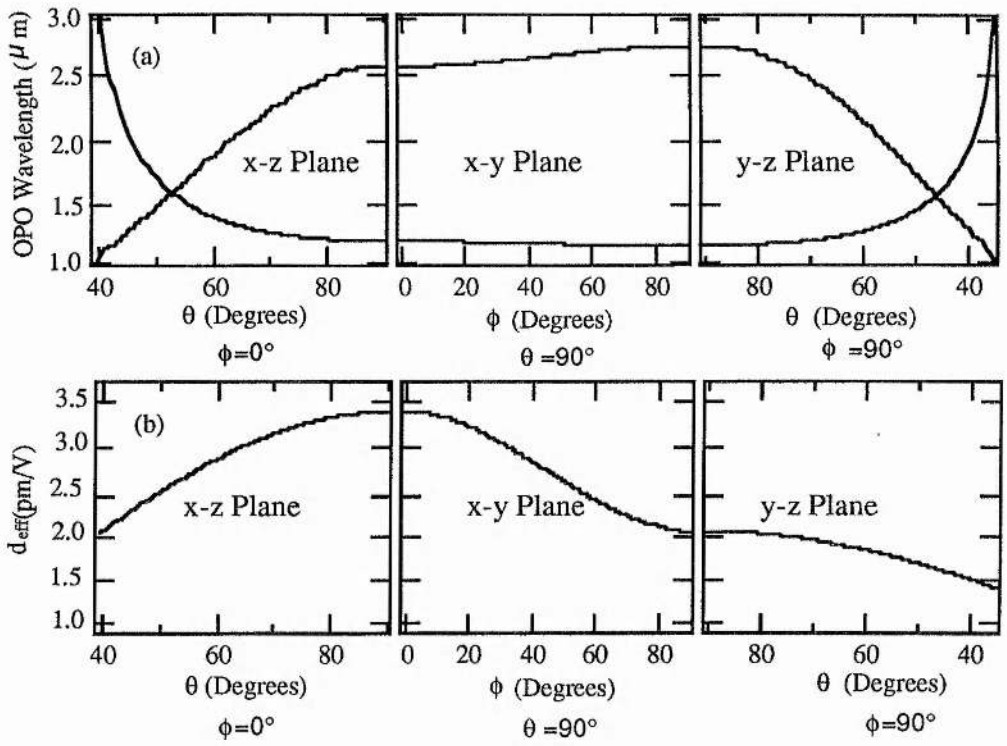

Figure 7.25

Phase-matching curves (a) and effective nonlinear coefficient (b) in the principal optical planes for type II parametric interaction in KTA with a pump wavelength of 800 nm. Refractive index data used in calculations are from Ref. [8].

Tuning characteristics

Figure 7.26 demonstrates the extent to which it is possible to angle tune in this system. From an initial θ angle of 90° it was possible to tune the OPO to an internal angle of 87.8 °, i.e. it was possible to tune the system by 2.2 °. This produced a change in the signal wavelength from an initial value of 1.169 μm to a value of 1.175 μm, representing a change in the idler from 2.54 to 2.50 μm. Several features effected the limited tunability of this arrangement. The main restriction was the limited aperture available, as the crystal was 10 mm long. Rotation resulted in rapid reduction in the available path through the crystal. Rotating the crystal also increased the walk off from the initial value of zero from the NCPM condition. A reduction in the d_{eff} will also be a factor that restricts the tunability of the system.

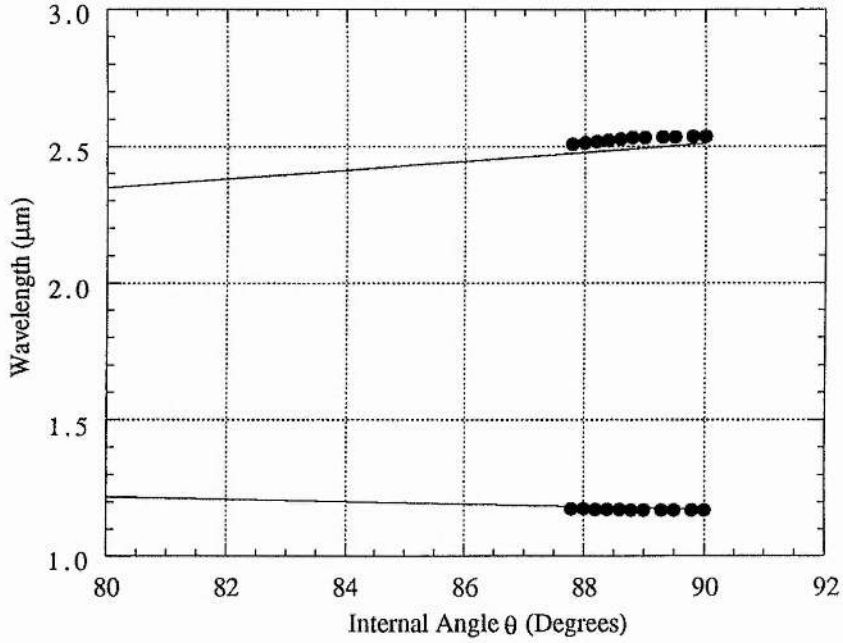

Figure 7.26
Tuning curve for type II angle-tuned parametric interaction in KTA, in the x-z plane for a pump wavelength of 800 nm. Refractive index data used in calculations are from Ref. [8].

Threshold and Output Power

The reduction in the effective nonlinear coefficient should result in an increase in threshold, as the gain of the system is reduced. The variation of the threshold of the system as the crystal is rotated can be seen in Figure 7.27 in which it can be seen that the threshold increases very rapidly from 320 mW to 710 mW, this can be attributed to the aperturing of the beam. The total output power can also be seen to drop rapidly from 275 to 38 mW. No additional variation in pulse duration was observed other than that already found to occur for pump-tuning wavelength variation. Similar results were obtained for the x-y and y-z planes, in which only small tunability was observed, coupled with a large increase in threshold and a large reduction in output power. Therefore it may be concluded that as predicted this method of tuning in picosecond systems is essentially impractical.

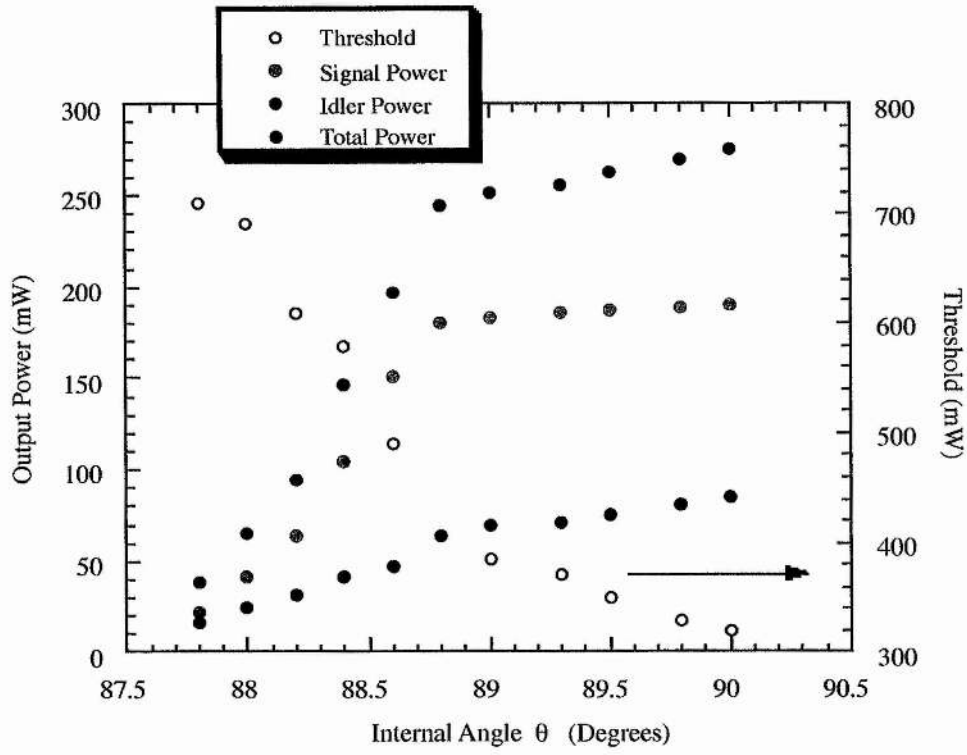

Figure 7.27

Variation in threshold and output power for type II angle-tuned parametric interaction in KTA, in the x-z plane for a pump wavelength of 800 nm.

7.8.12 Cavity Comparisons

In section 7.7 it was stated that the cavity fold mirrors had a radius of curvature of 10 cm. This value of curvature was not the only value that led to good mode-matching and cavity stability for the OPO. Mirrors of radii of curvature 10, 15 and 20 cm all produced good cavity stability parameters. However it was impossible to theoretically deduce exactly which mirrors would produce the best performance, i.e. the largest output power, etc. To this end, the cavity was configured for each set of mirrors to ascertain which produced the best performance. In this section a comparison of the operation of the KTA OPO is given for the three different sets of identically coated cavity fold mirrors, namely 10, 15 and 20 cm radii of curvature.

7.8.12.1 Threshold

With 1.2 ps duration pump pulses and the cavity configured with all highly reflecting mirrors the minimum oscillation threshold was 230 mW for the 10 cm mirrors, with the 15 and 20 cm mirrors having values of 300 and 360 mW

respectively, see Figure 7.28. These values correspond to threshold pulse energies of ~ 3, 4 and 4.7 nJ and to peak power densities of ~ 80, 104 and 125 MW/cm^2 inside the crystal. The 15 cm mirror threshold represents an increase of 30 % from the 10 cm case with the 20 cm cavity value representing a 56 %

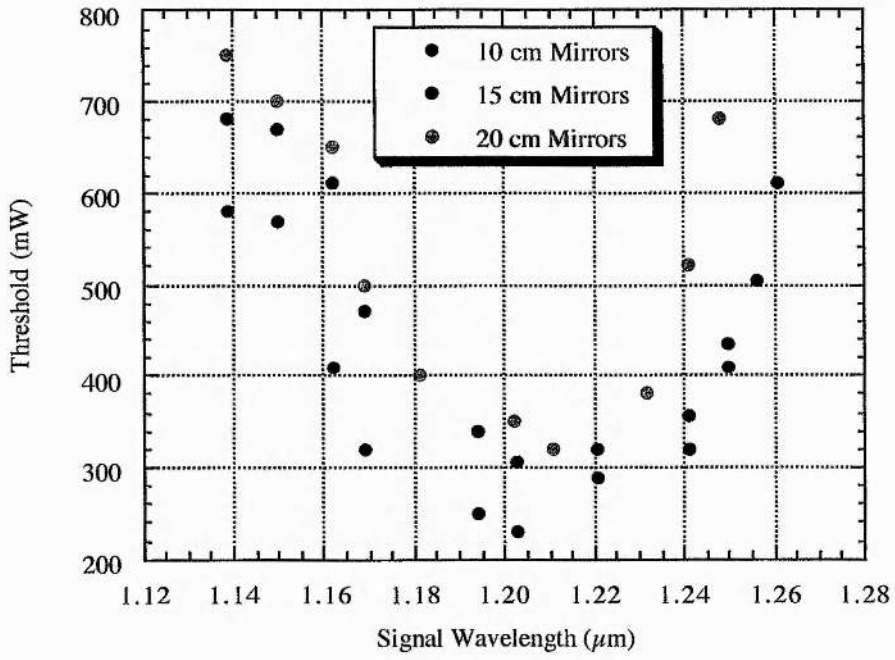

Figure 7.28
Comparison of threshold in the 3 cavity configurations.

increase from the best situation. It was these measurements that led to the decision to use the 10 cm radius of curvature mirrors for the KTA OPO cavity. The ability to operate as far as possible above threshold is very desirable as it leads to good device stability. It was also expected that the 10 cm mirrors would produce the highest output powers as the greatest depletion would be produced from this mirror set.

7.8.12.2 Tuning Characteristics

Figure 7.29 represents the difference in the extent of tuning obtained for the 3 different cavities. It can be observed that the results produced by the 15 and 20 cm mirrors sets are very similar, with the signal branches in both cases tuning from 1.139 to 1.259 μm, with corresponding idler branches of 2.377 to 2.746 μm. Greater tuning is obtained for the 10 cm mirror set with the signal branch now tuning from 1.139 to 1.261 μm. This has a corresponding idler tuning range

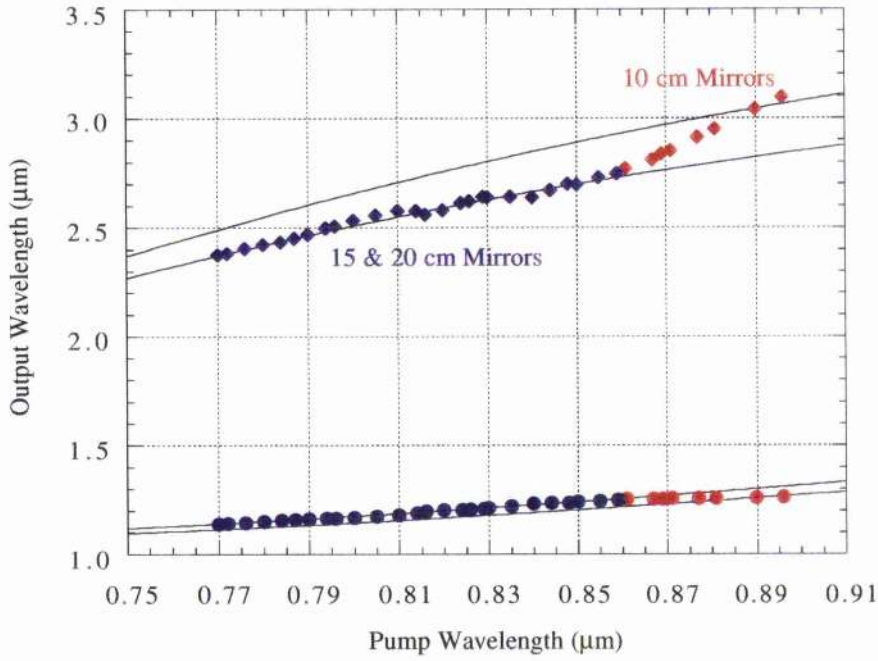

Figure 7.29
Comparison of tuning in the 3 cavity configurations.

of 2.377 to 3.095 µm so, in this case, tuning beyond the important 3 µm barrier is obtained.

7.8.12.3 Output power

Figure 7.30 represents the different power levels produced from the 3 cavity configurations. In the previous threshold section it was stated that the 10 cm mirrors would produce the largest output powers. It can be observed that the 20 and 15 cm mirrors sets produce maximum output powers of 220 and 250 mW, respectively. The 10 cm cavity produces up to 400 mW which represents an increase of 83 % from the 20 cm case. Hence the 10 cm cavity can be seen to produce a more favourable cavity properties, such as lower threshold and higher output powers and hence this is what led to the use of this curvature of mirrors in the KTA OPO cavity.

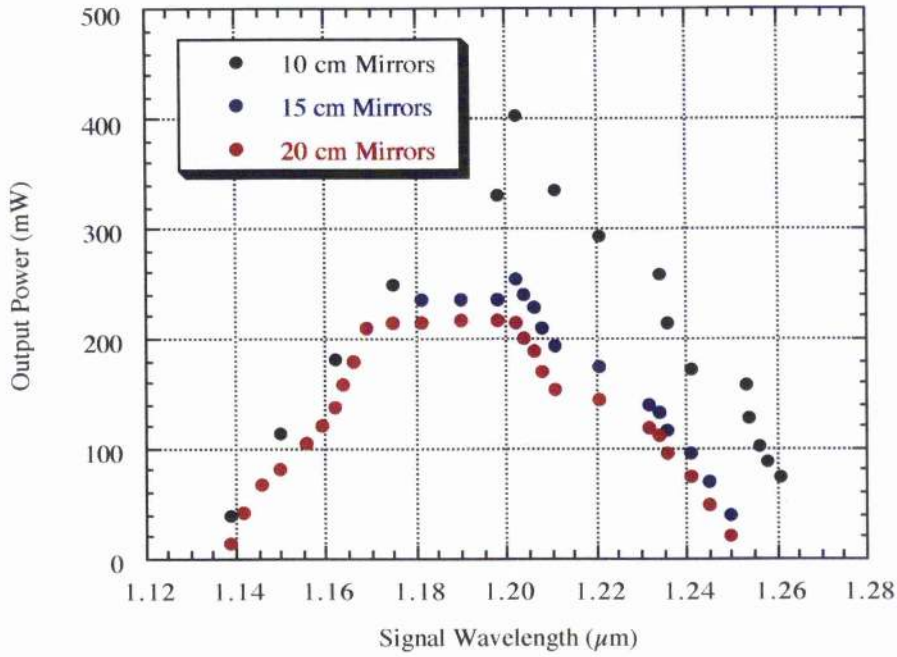

Figure 7.30
Comparison of output power in the 3 cavity configurations.

7.9 Intracavity frequency-doubled KTA OPO

In the last chapter the internal doubling of the LBO OPO was demonstrated, with wavelengths in the range 584 to 771 nm being produced. If the signal branch of the KTA OPO of 1.139 - 1.281 μm is internally-doubled, this would produce wavelengths in the range 569.5-640.5 nm. This would lower the bottom edge of the wavelengths currently available from 584 to 569.5 nm. The results for this experiment are presented in the next section.

7.9.1 Experimental configuration

The cavity configuration for the frequency-doubled picosecond KTA OPO was similar to that for the internally-doubled LBO system (see Figure 7.31). The intracavity frequency-doubling was performed using type I SHG with the LBO doubling crystal cut for non-critical propagation along the x-axis (ϕ=0°, θ=90°). The OPO mirrors were used with highly reflecting (R>99.7%) multi-layer single stack dielectric coatings centred at 1180 nm. The mirrors also had high transmission (T>95%) centred at 800 nm.

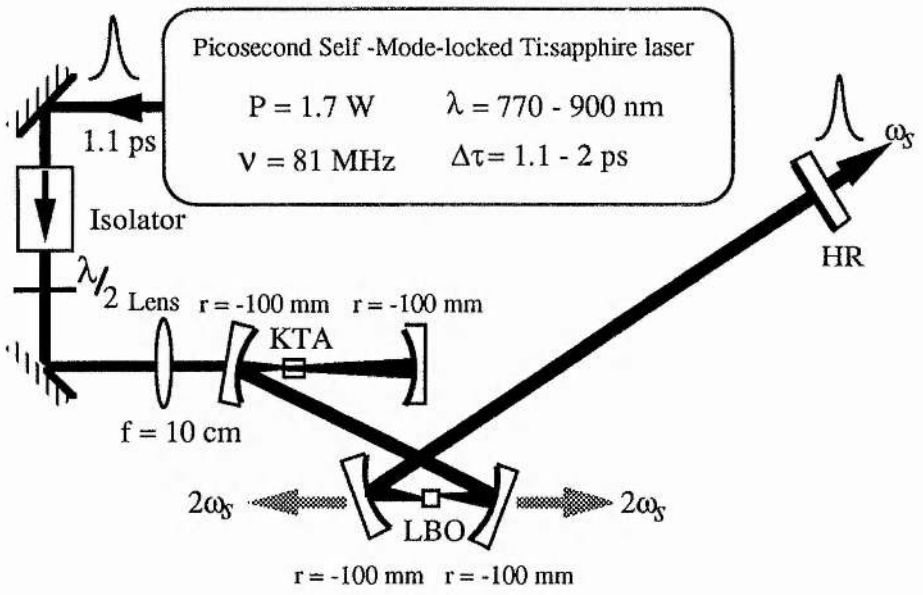

Figure 7.31
Schematic of the frequency-doubled picosecond Ti:sapphire-pumped KTA OPO, with the cavity parameters displayed.

7.9.2 Experimental results

7.9.2.1 Tuning characteristics

In Figure 7.32 the experimental tuning range of frequency-doubled KTA OPO is shown as a function of pump wavelength. The second harmonic output tuned from 569 to 640 nm, for Ti:sapphire pump wavelengths in the range 770-890 nm. The corresponding SHG phase-matching temperatures which were in the range 20 to 100 °C are shown in Figure 7.33. The solid curves represent the predicted tuning range derived from the Sellmeier equations of References [8] and [11]. The tuning could also be extended beyond 650 nm if an optimised mirror set for the Ti:sapphire laser with reflectivity above 900 nm was used.

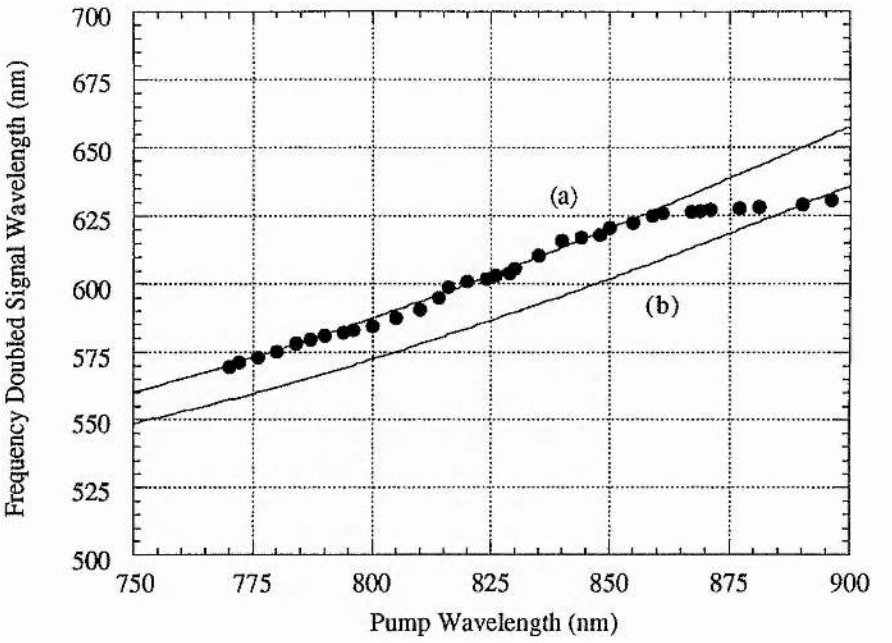

Figure 7.32
Visible range of the frequency-doubled KTA OPO, (a) and (b) as previously.

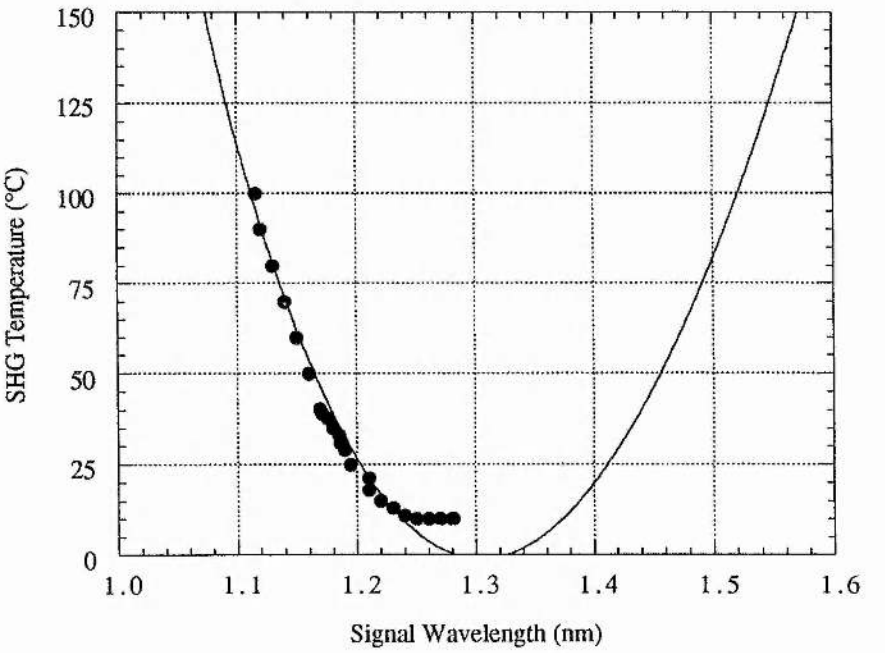

Figure 7.33
SHG temperature required to frequency double the output of the KTA OPO.

7.9.2.2 Threshold

With 1.2 ps input pump pulses and configured with all highly reflecting mirrors, the average pump power threshold for the KTA OPO was about 260 mW at the centre of the mirror reflectivity band (see Figure 7.34). Oscillation could be maintained across the entire signal tuning range for average pump powers below 700 mW. A prediction of the threshold has again been made by using the model of Guha, Wu and Falk [15], this again produces a good fit to the experimental data, as seen in Figure 7.34. The deviation between the model and the experimental results is again due to uncertainties in the variation of the value of the AR coating of the mirrors and crystal with wavelength. If these values were known more precisely then a better fit between the model and the experimental results could be made.

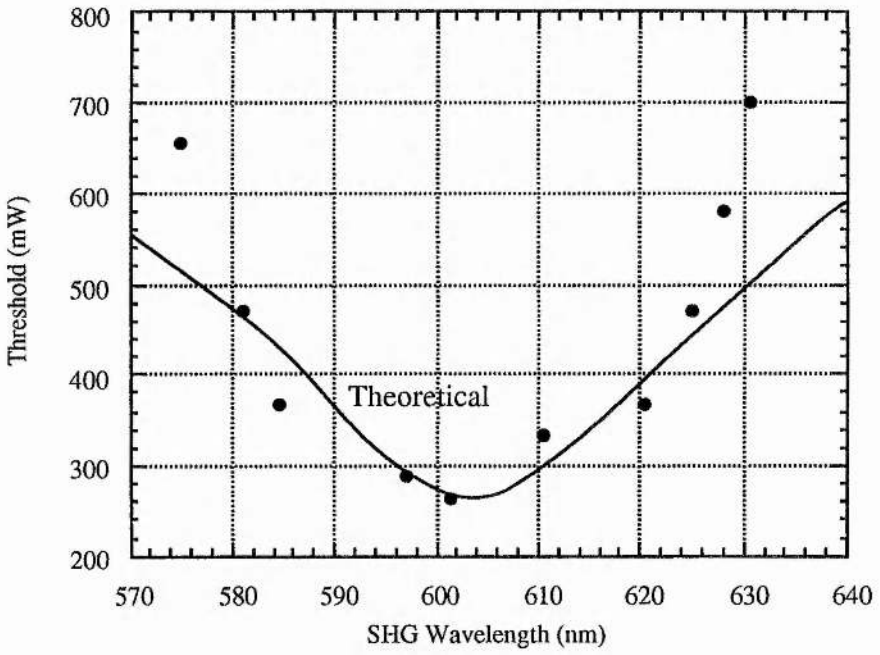

Figure 7.34
Variation in the average pump-power threshold across the tuning range of the intracavity frequency-doubled KTA OPO.

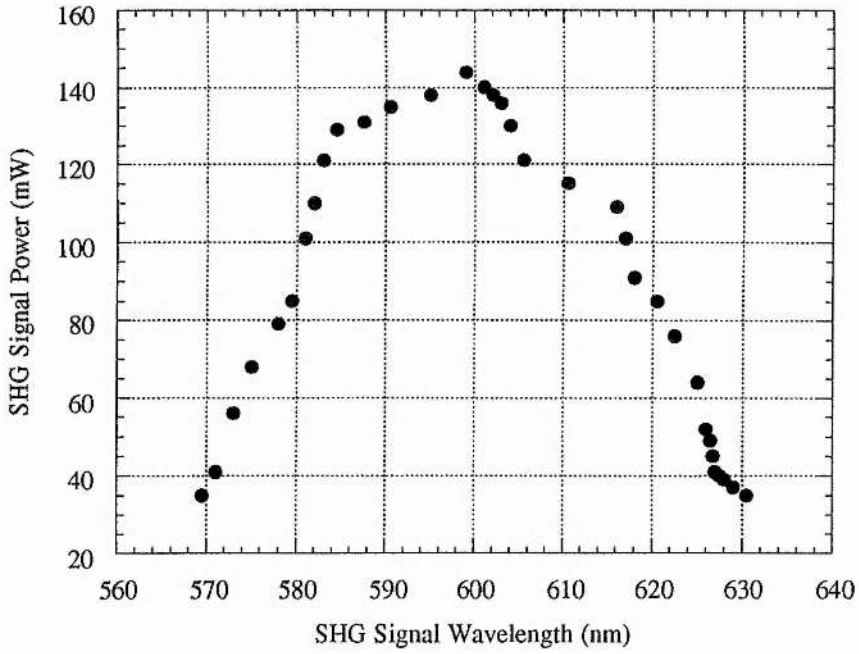

Figure 7.35
Variation of frequency-doubled signal power as a function of wavelength for a pump power of 1.3 W.

7.9.2.3 Output power and efficiency

The light was coupled out from the cavity through the r = -100mm HR mirrors (T = 50 % @ 670 nm) in two diverging beams each containing approximately 25 % of the total power.

The variation in the second harmonic output power across the visible range of the oscillator is shown in Figure 7.35. The data was obtained for 1.3 W of pump power at the input to the OPO crystal, with a cavity configured with all highly reflecting mirrors at the signal wavelength. This configuration corresponded to the maximum extraction of visible output and a minimum pump power threshold of 260 mW. It can be seen from Figure 7.35 that as much as 145 mW of output power was extracted in the second harmonic. This represents a conversion efficiency from the pump to the visible of 11.2 % .

7.9.2.4 Temporal characteristics

The temporal characteristics of the SHG pulses were determined from autocorrelation measurements. Figure 7.36 shows a typical intensity and

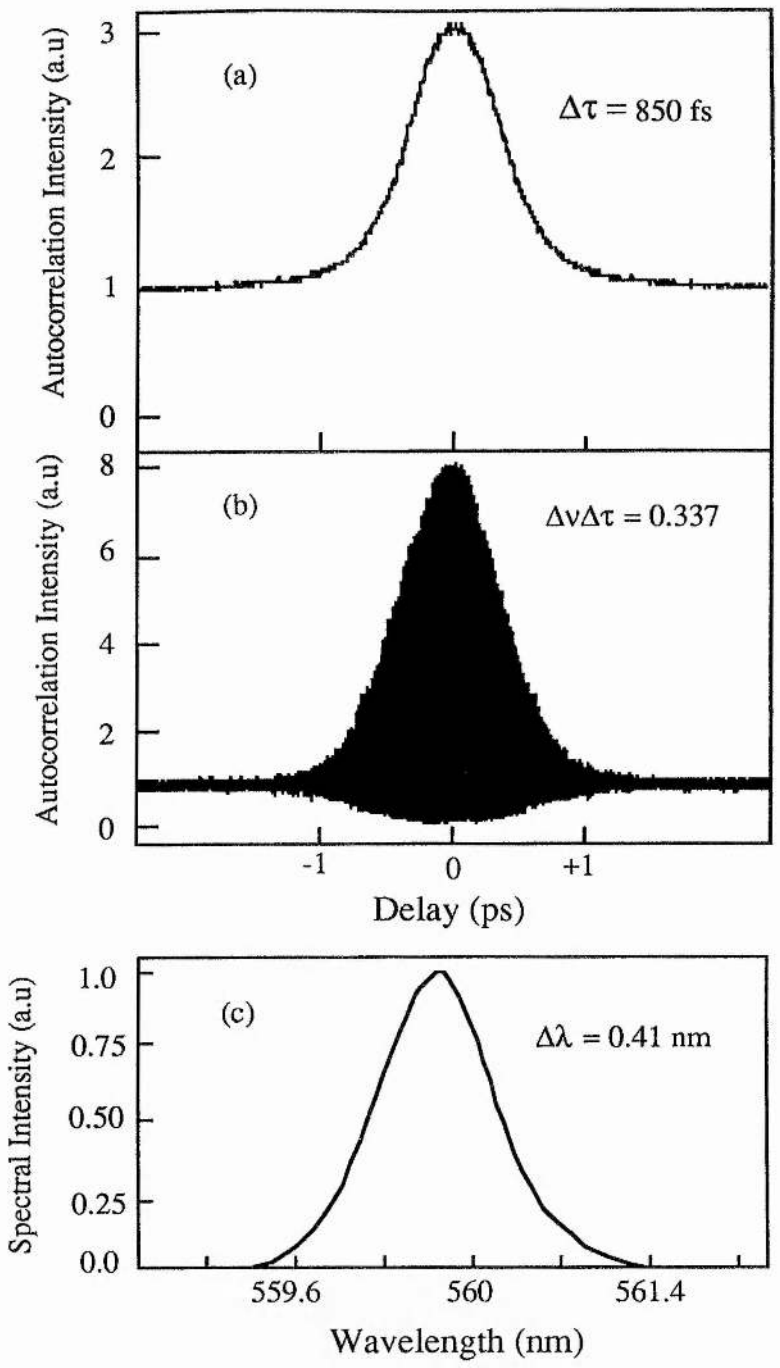

Figure 7.36

(a) Intensity and (b) interferometric autocorrelation, and (c) spectrum of frequency-doubled signal pulses at 560 nm. The pulse duration determined from the intensity autocorrelation is 850 fs, with a corresponding time-bandwidth product 0.337.

interferometric autocorrelation, and the corresponding spectrum of the frequency-doubled signal pulses at a wavelength of 560 nm. The pulse duration

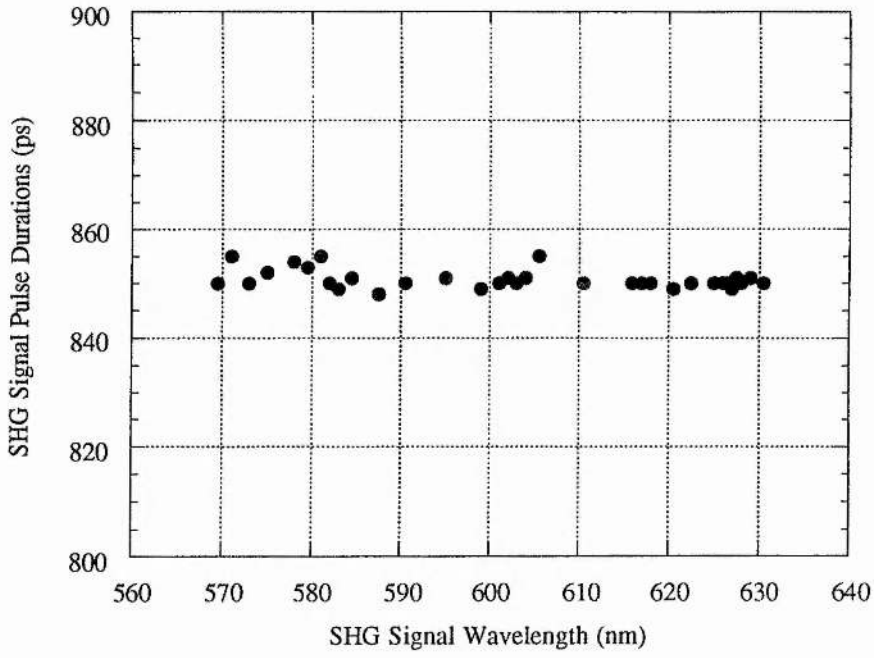

Figure 7.37
SHG signal pulse duration variation across the tuning range of the SHG KTA OPO.

deduced from the intensity autocorrelation is 850 fs (assuming a $sech^2$ pulse profile) for a pump pulse of 1.2 ps. The shape of the interferometric autocorrelation is indicative of chirp-free pulses. The spectrum has a smooth profile with a spectral width of 0.41 nm and a time-bandwidth product of 0.337. These pulses are therefore essentially transform-limited. Figure 7.37 depicts the frequency-doubled pulse durations across the entire tuning range and demonstrates that the pulse durations remain constant at approximately 850 fs. The SHG pulse duration is determined mainly by the nonlinear pulse shortening, because of the small temporal walkoff in LBO. Since the nonlinear gain remains constant across the tuning range, there is little change in the SHG pulse duration with wavelength.

7.10 Conclusions

In conclusion, this chapter has presented a characterisation of an OPO developed to access wavelengths beyond 2.5 μm. This new source of tunable picosecond pulses for the near - to mid - infrared is based on the material $KTiOAsO_4$ (KTA). Oscillation has been obtained for input pump powers as low as 230 mW. The

system produces total output powers in excess of 403 mW with conversion efficiencies of 31 % at 5.2 times threshold. Transform-limited signal and idler pulses of 1.02 and 2.9 ps have been generated over the tuning ranges 1.139-1.281 μm and 2.377-3.160 μm. The performance of the KTA OPO clearly demonstrates the potential of this material for efficient generation of high-power and transform-limited pulses in the near -to mid-infrared. This system has also been internally-doubled to produce tuning in the wavelength range 569.5 - 640.5 nm. Oscillation has been obtained for an input pump power of 260 mW with output powers in excess of 145 mW being generated, representing conversion efficiencies of as much as 11 %. The system provided transform-limited visible pulses with durations of 850 fs across the available range.

References

1. A. Nebel, C. Fallnich, R. Beigang, and R. Wallenstein, J. Opt. Soc. Am. B **10**, 2195 (1993)

2. M. Ebrahimzadeh, S. French, and A. Miller, J. Opt. Soc. Am. B **12**, 2180 (1995)

3. J. D. Bierlein and H. Vanherzeele, Appl. Phys. Lett. **54**, 783 (1989)

4. G. M. Loiacono, D. N. Loiacono, J. J. Zola, R. A. Stolzenberger, T. McGee, and R. G. Norwood, Appl. Phys. Lett. **61**, 895 (1992)

5. G. M. Loiacono, D. N. Loiacono, and R. A. Stolzenberger, J. Crys. Growth **131**, 323 (1993)

6. J. Y. Wang, Y. G. Liu, J. Q. Wei, L. P. Shi, and M. Wang, Z. Krist **191**, 231 (1990)

7. J. Han, Y. Liu, M. Wang, and D. Nie, J. Crys. Growth **128**, 864 (1993)

8. L. T. Cheng, L. K. Cheng J. D. Bierlein, and F. C. Zumsteg, Appl. Phys. Lett **62**, 346 (1993)

9. G. M. Loiacono and R. A. Stolzenberger, Private communication via Crystal Associates, Inc., Waldwick, NJ 07463, U.S.A.

10. P. E. Powers, S. Ramakrishna, C. L. Tang, and L. K. Cheng, Opt. Lett. **18**, 1171 (1993)

11. D. L. Fenimore, K. L. Schepler, U. Ramabadran, and S. R. McPherson, J. Opt. Soc. Am. B **12**, 794 (1995)

12. W. R. Bosenberg, L. K. Cheng, and J. D. Bierlein, Appl. Phys. Lett **65**, 2765 (1994)

13. K. Kato, IEEE. J. Quantum Electron. **QE-30**, 881 (1994)

14. E. C. Cheung and J. M. Liu, J. Opt. Soc. Am. B **7**, 1385 (1990)

15. S. Guha, F. Wu, and J. Falk, IEEE J. Quantum Electron. **QE-18**, 907 (1982)

16. H. Avramopoulos, P. M. W. French, G. H. C. New, M. M. Opalinska, J. R. Taylor, and J. A. R. Williams, Opt. Commun. **76**, 229 (1990)

17. W. L. Nighan, T. Gong, and P. M. Fauchet, IEEE J, Quant. Electron. **25**, 2476 (1989)

18. M. F. Becker, D. J. Kuizenga, D. W. Phillion, and A. E. Siegman, J. Appl. Phys. **45**, 3996 (1974)

19. M. J. McCarthy and D. C. Hanna, J. Opt. Soc. Am. B **10**, 2180 (1993)

20. D. C. Edelstein, E. S. Wachman, and C. L. Tang, Appl. Phys. Lett. **54**, 1728 (1989)

21. G. Mak, Q. Fu, and H. M. van Driel, Appl. Phys. Lett. **60**, 542 (1992)

22. Q. Fu, G. Mak, and H. M. van Driel, Opt. Lett. **17**, 1006 (1992)

23. W. S. Pelouch, P. E. Powers, and C. L. Tang, Opt. Lett. **17**, 1070 (1992)

24. P. E. Powers, S. Ramakrishna, C. L. Tang, and L. K. Cheng, Opt. Lett. **18**, 1171 (1993)

25. J. D. Kafka, M. L. Watts, and J. W. Pieterse, in *Conference on Lasers and Electro-Optics*, Vol. 11 of 1993 OSA Technical Digest Series (Optical Society of America, Washington, D.C., 1993), paper CPD32

26. J. M. Dudley, D. T. Reid, M. Ebrahimzadeh, and W. Sibbett, Opt. Commun. **104**, 419 (1994)

27. T. J. Driscoll, G. M. Gale, and F. Hache, Opt. Commun. **110**, 638 (1994)

28. D. T. Reid, M. Ebrahimzadeh, and W. Sibbett, Opt. Lett. **20**, 55 (1995)

29. F. C. Zumsteg, J. D. Bierlein, and T. D. Gier, J. Appl. Phys. **47**, 4980 (1976)

30. 'Crystals' catalog, JTT International Inc., 3251 Progress Drive Suite B, Orlando, Florida 32826, U.S.A.

Contents Page

8.1 Conclusions

The work in this thesis describes the design, configuration and operation of picosecond optical parametric oscillators tunable from the visible to mid-infrared. These systems were based on the materials LiB_3O_5 (LBO) and $KTiOAsO_4$ (KTA), and were pumped by a self-mode-locked Ti:sapphire laser at a repetition rate of 81 MHz. These devices were developed to be used as sources with which to perform time-resolved spectroscopy on quantum well structures. The results of measurements presented in preceding chapters indicate that ultrafast OPOs are versatile and widely tunable sources that are suitable for practical applications.

Chapter 1 provided an introduction to the field of picosecond OPOs and compared the performance of these devices with conventional mode-locked lasers producing picosecond pulses in the visible to mid-infrared. Chapter 1 also charted the progress to the present day of singly-resonant picosecond optical parametric oscillators from earlier systems which relied on pulsed or doubly-resonant operation.

The operation of the self-mode-locked Ti:sapphire pump laser was discussed in Chapter 2. This chapter gave an outline of the most salient features relating to the propagation of ultrashort pulses in transparent nonlinear optical media. A description of the apparatus used to characterise the temporal and spectral components of the picosecond pulses was also given. The Ti:sapphire laser used as the pump source for the optical parametric oscillators was continuously tunable from 770-910 nm, limited by the available mirror sets. Average output power of over 2.2 W was produced across most of the tuning range. The laser produced 1.1 ps transform-limited pulses across the entire continuous tuning range.

In Chapter 3 the design criteria required to produce an effective picosecond optical parametric oscillator were discussed. Calculations were performed to demonstrate how the determination of the appropriate choice of crystal was undertaken to meet the particular tuning or temporal requirements of specific systems.

In Chapter 4 the above criteria were used to produce the initial design of the picosecond parametric oscillator which was based on a 16 mm long crystal of LBO. This system produced transform-limited signal pulses with durations of ~720 fs. Total average output powers of up to 90 mW over the signal and idler tuning ranges of 1.374-1.530 μm and 1.676-1.828 μm were generated at 1.3 times the 900 mW threshold. Because of the small temporal walk-off and large spectral acceptance bandwidths of LBO, the use of longer crystals was expected to improve the overall performance of the oscillator. Although this device proved to be highly tunable with moderate output power levels it suffered from poor stability, which would have rendered it very difficult to use as a source for experiments and so improved stability had to be achieved.

In Chapter 5 an improved system was described which utilised a new LBO crystal of length 30 mm in contrast to the 16 mm long crystal used previously. This longer crystal became available as crystal production techniques improved since the date of the work performed on the 16 mm system. Calculations performed showed that this length was very close to the optimum length of crystal. This LBO system was found to be a powerful and versatile source of high-repetition-rate picosecond pulses for the near-infrared. It provided transform-limited 1.1 ps signal and 2.1 ps idler pulses over a wavelength range from 1.2 to 2.2 μm, without the requirement for dispersion compensation in the cavity. Transform-limited signal and idler pulses beyond these limits were also readily attainable with intracavity dispersion compensation, with little resulting degradation in performance. The addition of dispersion compensation resulted in a small increase in the threshold from 350 mW to 450 mW and a small reduction in output power of ~ 90 mW. The tuning range of the LBO OPO was continuous except close to wavelength degeneracy and the total wavelength coverage extended from 1.160 to 2.185 μm, with a single LBO crystal. This spectral range was limited by the tunability of the pump laser and could be further extended to cover the range 1-2.4 μm with a new Ti:sapphire mirror set.

Up to 690 mW of infrared average power was generated for 2 W of input pump power at 5 times threshold. For this output power a depletion of 52 % was achieved with a corresponding external extraction efficiency of 34.5 %. Despite

the requirement for cavity length synchronism, the LBO OPO was a remarkably robust and stable source, capable of routine day-to-day operation without the need for re-alignment of the resonator. In the absence of cavity length stabilisation, oscillation was maintained for extended periods of several hours at a time without re-adjustments of cavity length. The continuous wavelength coverage of LBO OPO with a single crystal is not available to similar Ti:sapphire-pumped picosecond OPOs and its output power capability, high efficiency and transform-limited performance is unmatched by most solid state pump based systems. As such, the LBO OPO represents a highly versatile, yet simple and cost-effective source of picosecond near-infrared pulses which will be useful as a source for many applications.

In Chapter 6 picosecond pulse generation in the visible by external single-pass frequency-doubling of the LBO OPO to provide picosecond pulses in the 584-771 nm range was discussed. Conversion efficiencies in excess of 20 % were demonstrated, with output powers in excess of 65 mW being measured, when utilising a combination of type I and type II temperature-tuned NCPM in LBO. The pulse width of the second harmonic was typically in the region of 840-880 fs. These pulses had bandwidths of the order of ~ 1 nm which allow time-resolved experiments to be carried out which require such a spectral and temporal resolution.

A further source of high-repetition-rate picosecond pulses for the visible was also demonstrated in Chapter 6, based on an internally-doubled, Ti:sapphire-pumped OPO that used temperature-tuned LBO both as the OPO and SHG crystal. Oscillation was obtained for an input pump power of 700 mW with output powers in excess of 320 mW being generated, corresponding to conversion efficiencies of as much as 16 %. The system was continuously tunable from 584 to 771 nm and provided transform-limited visible pulses with durations of 840-880 fs across the available range. The combination of the Ti:sapphire tuning range (770-910 nm), its second harmonic (385-455 nm), the frequency-doubled OPO (585-771 nm), and the output of the OPO itself (1.150-2.260 μm) provides an almost continuous tuning capability from 385 nm to 2.260 μm (see Figure 8.1). The use of an optimised mirror set for the Ti:sapphire laser will allow the remaining gaps to be filled. Few systems are capable of such wide tunability, high output power and transform-limited performance.

The ability to tune to wavelengths beyond 2.5 μm was also of interest in the study of intra-band transitions in quantum well structures. To this end, a new

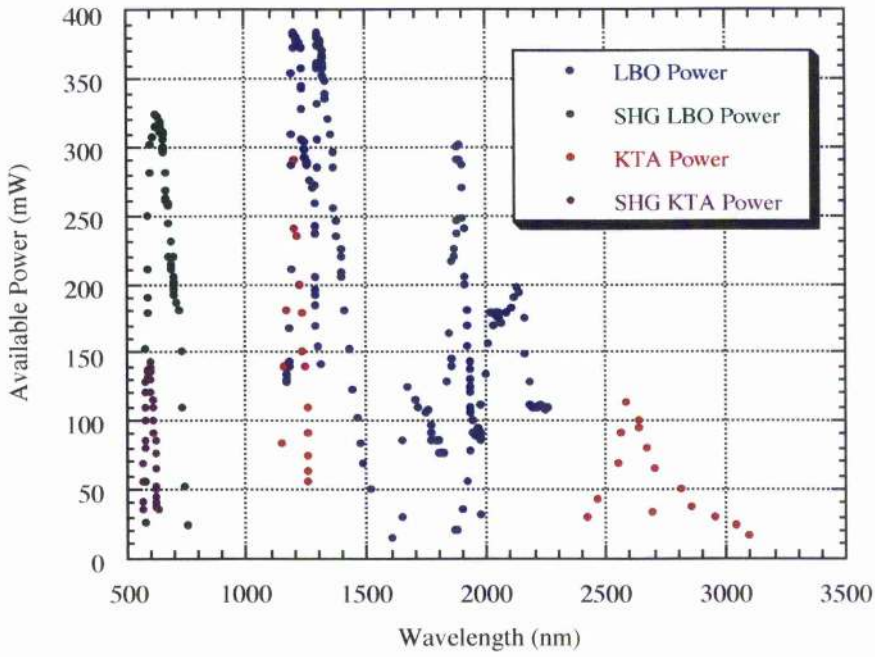

Figure 8.1
Available power from all the Ti:sapphire-laser-pumped picosecond OPOs reported in this thesis.

source of tunable picosecond pulses for the near - to mid - infrared was described in Chapter 7, which was based on the material $KTiOAsO_4$ (KTA).

Oscillation was obtained for input pump powers as low as 230 mW. The system produced total output powers in excess of 403 mW with conversion efficiencies of 31 % at 5.2 times threshold. Transform-limited signal and idler pulses of 1.02 ps and 2.9 ps duration were generated over the tuning ranges of 1.139-1.281 μm and 2.377-3.160 μm. The performance of this KTA OPO clearly demonstrates the potential of this material for efficient generation of high-power and transform-limited pulses in the near-to mid-infrared. This system was also internally-doubled to produce transform-limited pulses with durations of 850 fs in the visible wavelength range 569.5 - 640.5 nm. Oscillation was obtained for an input pump power of 260 mW with output powers in excess of 145 mW being generated corresponding to conversion efficiencies of as much as 11 %. The combination of all these devices allows the production of picosecond pulses tunable from 385 nm to 3.160 μm, as shown in Figure 8.2.

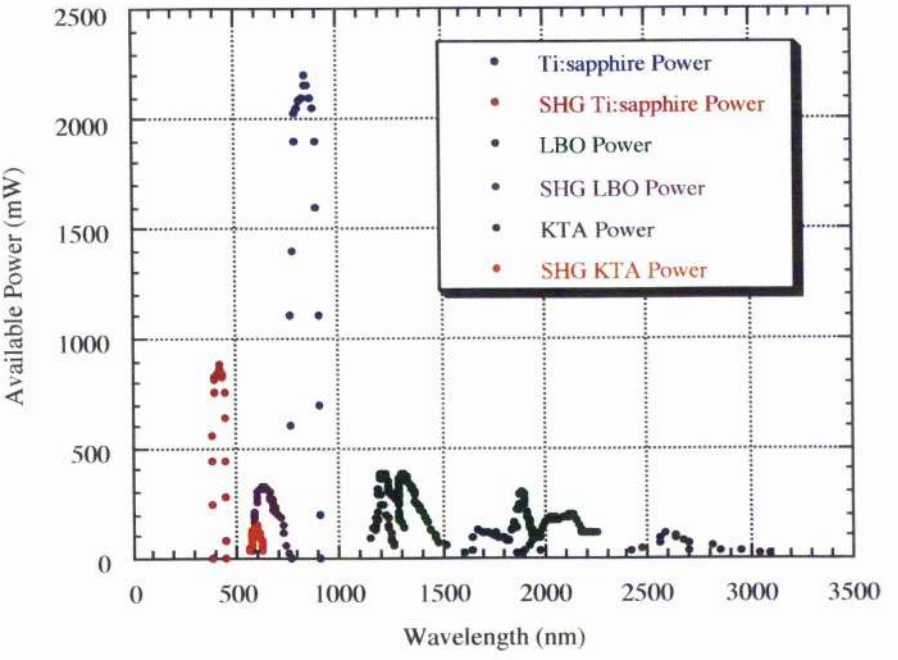

Figure 8.2
Available power from all the picosecond OPOs reported in this work as well as the fundamental and frequency-doubled output from the Ti:sapphire pump laser.

The powers required to perform pump-probe spectroscopy of semiconductor materials and devices are of the order of 1-10 mW. It can clearly be seen from Figure 8.1 that the powers available from the OPOs demonstrated in this work are in the range 100-400 mW across the extremely large tuning range. Hence these devices produce well above the required power for such applications and so should be ideally suited for their intended use. The addition of the tuning of the Ti:sapphire laser and its frequency-doubled output is demonstrated in Figure 8.2, which shows that powers of the order of 100mW-2.2W are available over almost the entire 385 nm-3.160 μm tuning range. The contributions from each system are shown in Table 8.1.

Tunable Source	Tuning Range
SHG Ti:sapphire Laser	385 - 455 nm
SHG KTA OPO	569.5 - 640.5 nm
SHG LBO Laser	584 - 771 nm
Ti:sapphire Laser	770 - 910 nm
KTA OPO	1.139 - 1.281 μm and 2.333 - 3.160 μm
LBO OPO	1.150 - 2.260 μm

Table 8.1

Wavelength ranges available from each of the tunable sources described in this thesis.

As discussed previously the compromise between spectral and temporal requirements leads to the situation that pulses of the order of a picosecond are optimal for performing pump probe spectroscopy. In Figure 8.3 the pulse durations produced by the various systems are shown and it can be observed that the available pulse durations vary between 850 fs and 1 ps, for the resonant

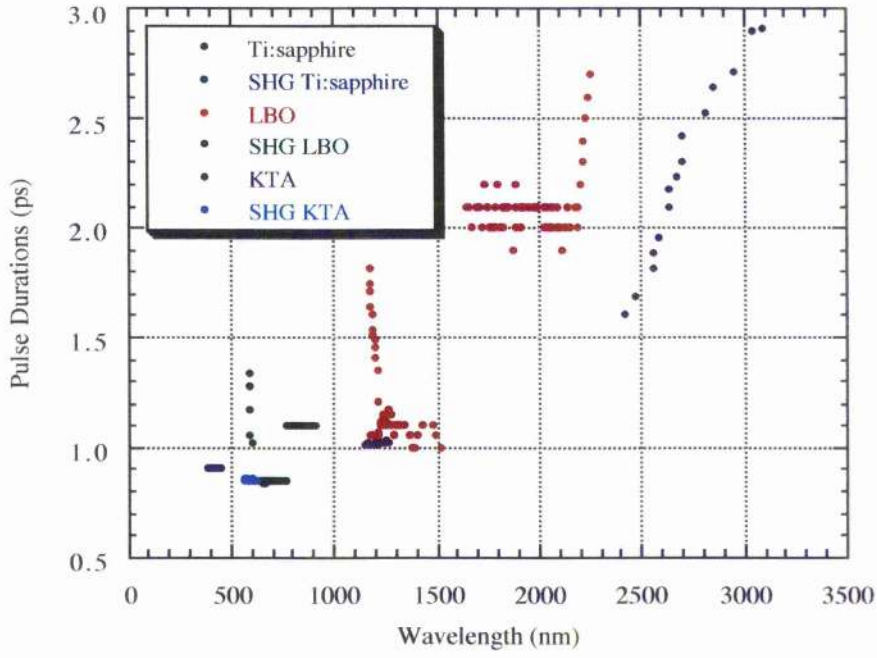

Figure 8.3

Pulse durations from all the picosecond OPOs reported here as well as the fundamental and frequency-doubled output from the Ti:sapphire pump laser.

signal waves and the frequency doubled waves (the dispersion-compensated and non-dispersion-compensated cases are shown). The non-resonant idler waves have larger pulse durations of the order of 2 ps. At 800 nm a transform-limited 1 ps pulse has a spectral width of 0.71 nm, whereas a 500 fs pulse has a spectral content of 0.84 nm. This implies that the pulses produced by the combination of devices offer the desired degree of temporal and spectral compromise. The pulse durations can be varied in a number of manners. The Ti:sapphire laser pulses can be varied from 1 ps to 2.5 ps by varying the GTI position, whereas the OPO pulse durations can be varied by changing the amount of depletion encountered by pump pulses and by the extent to which the device is operated above threshold.

8.2 Future developments

The main thrust behind the development of these picosecond optical parametric oscillators was as sources to provide tunable synchronised pulse sequences in different regions of the optical spectrum. As discussed above these sources can be used in time-resolved measurements on quantum well structures. It is possible to produce further sources in other spectral regions by the use of intracavity and extracavity nonlinear frequency-conversion techniques. Such techniques can produce picosecond pulses from the ultraviolet to the mid-infrared. The timing jitter in these systems has been shown to be very low and so they should find many more uses in applications such as, pump-probe applications. The following section discusses the development of future systems that should allow improved OPO performance as well as further increasing the available tuning range.

8.2.1 New cavity configurations

It is advantageous if cavity configurations can be developed that produce as low a threshold as possible as well as producing very high output powers. Reid et al [1] have recently developed a semi-monolithic femtosecond Ti:sapphire-pumped $RbTiOAsO_4$ (RTA) OPO that has one of the cavity mirrors on the face of the OPO crystal itself (see Figure 8.4). This produces a simplified cavity as well as reducing the losses incurred by the pump beam as it no longer has to pass through the input external cavity mirror. This arrangement also allows much tighter focussing, which means that shorter crystal lengths can be used, which is advantageous for picosecond operation. For 1.1 W of Ti:sapphire pump power, this device has produced ~300 mW in the signal around 1.3 μm and ~200 mW in the idler around 2.2 μm, therefore near 50 % conversion efficiencies are

achievable. It is proposed that the picosecond KTA system discussed in Chapter 7 shall be modified to this arrangement, to see if any system improvement results.

8.2.2 Picosecond pulse generation in the 3 - 5 μm region

The ability to access wavelengths in the 3-5 μm region is expected to become popular in the near future as the need for sources that can be used to probe intra sub-band transitions in quantum wells is expected to increase. Infrared spectroscopy in and around the 3 μm region also provides a great deal of information on chemical and biological systems. The fundamental stretching modes for the OH, CH and NH groups lie in this important spectroscopic region, see Figure 8.5 [2].

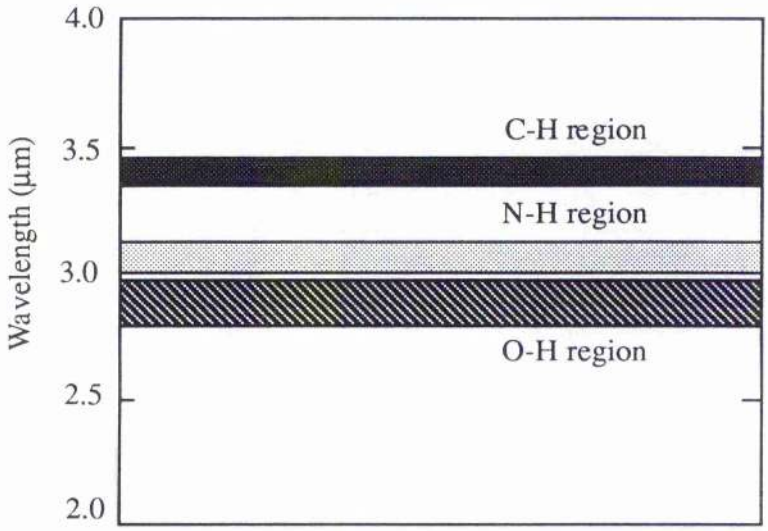

Figure 8.5
Chemically important infrared absorption bands in and around the 3 μm region.

8.2.2.1 Techniques for producing 3-5 μm radiation

A variety of techniques to produces radiation in this region exists. One proposed method is to produce these wavelengths by difference-frequency mixing the signal and idler outputs of a picosecond optical parametric oscillator in an internal difference frequency mixing scheme. The intracavity mixing scheme proposed would involve the extending of the cavity described above and is depicted in Figure 8.6.

OPO operation in the 3-5 μm region

A more direct and hence desirable approach is to build an OPO to access these wavelengths. In the mid-infrared spectral region, the number of crystals suitable for parametric generation is very limited due to the limited transparency of dielectric materials at these long wavelengths. A material that looks promising for the mid-infra-red spectral region is the chalcopyrite crystal, $AgGaSe_2$, which has a large transparency region as well as a high optical nonlinearity. The properties of this material shall now be considered.

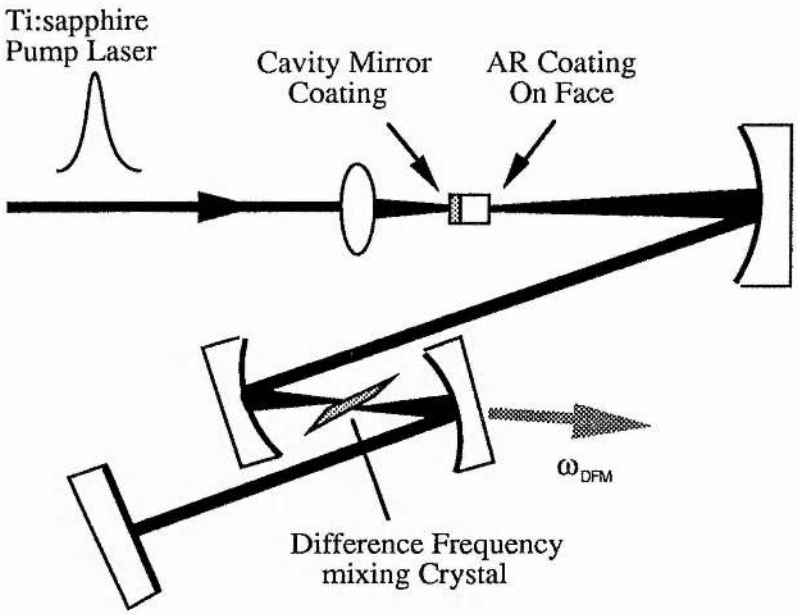

Figure 8.6
Cavity schematic of the proposed difference frequency mixing in a new simplified picosecond KTA OPO.

Type I non-critical phase-matching in $AgGaSe_2$.

The use of $AgGaSe_2$ for nonlinear infrared applications was first proposed in the early 1970s. At this time however, problems related to growth made it difficult to obtain high quality crystals of sufficient size. At this time two main problems existed; during the growth process crystals were prone to cracking, and crystals were found to display high losses in the near-infrared. In recent years, improved quality crystals have been grown which has allowed the operation of $AgGaSe_2$ OPOs to be demonstrated [3-8]. $AgGaSe_2$ has a very large transparency region, which extends as far as 13 μm.

The type I NCPM geometry in $AgGaSe_2$ was calculated in a similar manner to that of the previous LBO and KTA cases. For type I phase-matching, two separate branches exist, one for pump wavelengths in the short wavelength (band-gap) dispersive region, and the other for pump wavelengths in the long wavelength dispersive region. The short wavelength range branch is depicted in Figure 8.7.

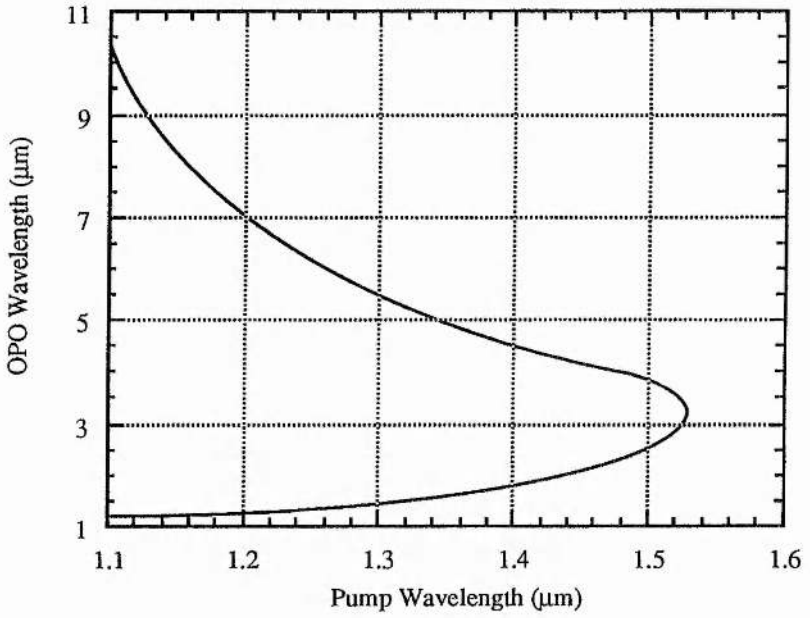

Figure 8.7
Type I NCPM in $AgGaSe_2$ with pump wavelength tuning at room temperature.

This tuning range represents type I NCPM for propagation along the y axis, with the pump polarised along the z-axis and the signal and idler polarised along the x-axis. It can be observed from this Figure that tuning from 1.2 to 10.5 μm is possible for pump wavelength tuning in the range 1.1 to 1.5 μm. This would be possible, as these wavelength are available from the LBO OPO. Only room-temperature operation is considered. It may also be possible to temperature tune this material, however no accurate temperature dependence of the refractive indices is available. However, even if the thermal dependence of the refractive indices are an order of magnitude lower than $LiNbO_3$, as inferred in reference [5], then temperature-tuning could be considered. This is important as it would increase the range of possible pump sources for OPO operation and open up the possibility of using sources such as Nd:YAG or Ti:sapphire lasers.

8.2.3 All-Solid-State Picosecond Optical Parametric Oscillators

The recent emergence of new all-solid-state sources of green radiation, most notably the Spectra Physics Millenia [9], which produces 5W of CW output power at 532 nm opens up new possibilities for the development of all-solid-state picosecond OPOs. This laser requires no external water cooling and also operates of the standard electricity supply. These features have lead to very low noise levels with < 0.1 % rms noise. This laser therefore has many advantages over the traditional green source of radiation, the Argon ion laser. This source has been demonstrated to be ideal for pumping a Ti:sapphire laser [10]. The Millenia-pumped Ti:sapphire laser produces 1W of output power with exceptionally low noise levels (<0.5% rms). The laser is tunable from 690 to 1000 nm and can produce pulse widths in the range 50 fs to 80 ps. It can therefore be predicted that the MIllenia will in time come to replace the Argon ion laser, which will lead to the production of many all-solid-state Ti:sapphire-pumped picosecond optical parametric oscillators in the near future.

References

1. D. T. Reid, C. McGowan, M. Ebrahimzadeh, and W. Sibbett, Post Deadline Paper CPD1.4 European Conference on Lasers and Electro-Optics (ECLEO), Hamburg, September 1996

2. G. R. Holton, R. A. Crowell, and X. Sunney Xie, J. Opt. Soc. Am. B **12**, 1723 (1995)

3. G. D. Boyd, H. M. Kasper, J. H. McFee, and F. G. Storz, IEEE J. Quant. Electron. **QE-8**, 236 (1972)

4. R. C. Eckardt, Y. X. Fan, R. L. Byer, R. K. Route, R. S. Feigelson, and J. van der Laan, Appl. Phys. Lett. **47**, 786 (1985)

5. R. C. Eckardt, Y. X. Fan, R. L. Byer, C. L. Marquardt, M. E. Storm, and L. Esterowitz, Appl. Phys. Lett. **49**, 608 (1986)

6. N. P. Barnes, D. J. Gettemy, J. R. Hietanen, and R. A. Iannini, Appl. Opt. **28**, 5162 (1989)

7. P. A. Budni, M. G. Knights, E. P. Chicklis, and K. L. Schepler, Opt. Lett. **18**,1068 (1993)

8. 'Crystals' catalog, JTT International Inc., 3251 Progress Drive Suite B, Orlando, Florida 32826, U.S.A.

9. Spectra-Physics *Millenia*, Spectra-Physics Lasers Inc., 1330 Terra Bella Avenue, Mountain View, California 94043, U.S.A.

10. Laser Focus World, March 1996, page 31

Appendices

Appendix 1

Calculation of the Temperature Tuned NCPM output from the LBO OPO

This program was written using the Application *Mathcad.*

The Sellmeier equations used are taken from: S. Lin, J. Y. Huang, J. Ling, C. Chen, and Y. R. Shen: Appl. Phys. Lett. **59**, 2805 (1991).

The Temperature dependence of the Refractive Indices are taken from: S. P. Velsko, M. Webb, L. Davis, and C. Huang: IEEE J. Quantum Electron. **27**, 2182 (1991).

Define Constants:

$A_z = 2.58515$ $B_z = 0.01412$ $C_z = 0.00467$ $D_z = 1.79132*10^{-2}$

$E_z = 4.17241*10^{-4}$ $F_z = 7.65183*10^{-6}$

$A_y = 2.53969$ $B_y = 0.01249$ $C_y = 0.01339$ $D_y = 0.02029$

Calculation

Guess Solution

(Temperature (T))

T:= 150

Define Equations

given

$$\frac{\sqrt{A_y + \frac{B_y}{\lambda_p^2 - C_y} - D_y\lambda_p^2}}{\lambda_p} = \frac{\sqrt{A_z + \frac{B_z}{\lambda_s^2 - C_z} - D_z\lambda_s^2 - E_z\lambda_s^4 + F_z\lambda_s^6} + (2.1\lambda_s - 6.3)\times 10^{-6}}{\lambda_s}$$

$$+ \frac{\sqrt{A_z + \frac{B_z}{\lambda_i^2 - C_z} - D_z\lambda_i^2 - E_z\lambda_i^4 + F_z\lambda_i^6} + (2.1\lambda_i - 6.3)\times 10^{-6}}{\lambda_i}$$

$\text{func}(\lambda_S,\lambda_i) = \text{find (T)}$

Define the pump wavelength and the range of signal and idler wavelengths to be phase-matched.

$\lambda_p = 0.80 \quad i = 1,2..32 \quad \lambda_{s_i} = 1.31 + 0.024(i\text{-}1) \quad \lambda_{i_i} = \left(\frac{1}{\lambda_p} - \frac{1}{\lambda_{s_i}}\right)^{-1}$

Write the data to a text file (This allows the data to be plotted in an external graphing package)

$M_{i,0} = f_i$

$M_{i,1} = \lambda_{s_i}$

WRITEPRN(LBO800) = M

This calculation has been performed for a pump wavelength of 800 nm, it can off course be performed for any pump wavelength. This produces the characteristic LBO curves as below.

The programs to calculate Acceptance angle, Spectral bandwidth, Group velocity walkaway, Maximum useful crystal length and Group velocity dispersion, as well as the pump-tuning phase-matching in the KTA system are all very similar to this program, and so it is not really of use to reproduce all of these programs.

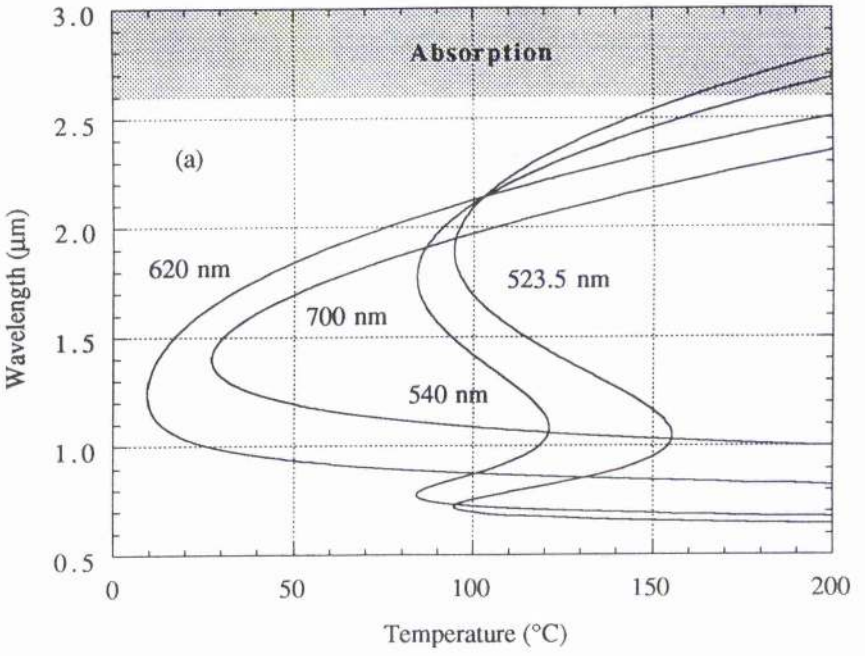

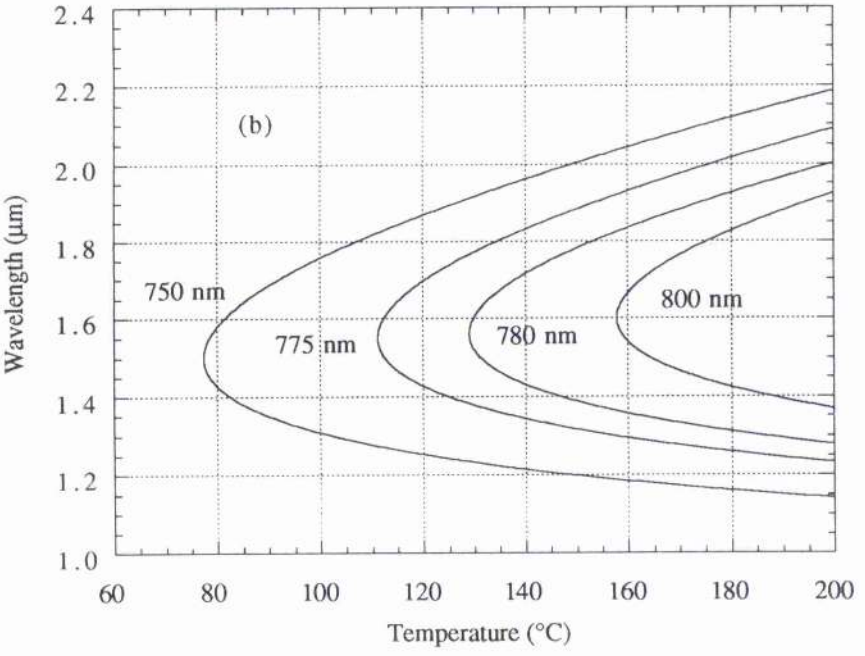

Calculated temperature-tuning range for parametric generation in type I non-critically phase-matched LBO (θ=90°, ϕ=0°) for (a) pump wavelengths between 523.5 nm and 620 nm and (b) between 750 nm and 800 nm.

Appendix 2

Glossary of Symbols

The following list of symbols does not include all the varieties formed by the addition of suffices. The subscripts *p*, *s*, and *i* refer to the pump, signal, and idler frequencies respectively.

b	confocal parameter
c	velocity of light
d_{eff}	effective nonlinear coefficient
f	focal length
h_s	focussing factor
k	wavevector
L	crystal length
n	refractive index
M	cavity mirror
P	power, polarisation, optical path length
ν	velocity
w_o	Gaussian beam waist
AR	anti-reflecting
B	magnetic field
D	dispersion constant, displacement
E	electric field
HR	highly-reflecting
I	intensity
J	displacement current
S	Poynting vector
β	propagation constant

χ	electrical susceptibility
ε_o	permittivity of free space
ε_s	cavity loss
ϕ	angle to crystallographic axis, phase shift
τ	pulse duration
λ	wavelength of light
σ	conductivity
μ_o	permeability of free space
ω	frequency
θ	angle to crystallographic axis

Appendix 3

Acknowledgements

I would like to thank Professor Alan Miller for all his help and encouragement throughout the course of this project and for giving me the opportunity to visit many foreign lands.

I am greatly indebted to Dr Majid Ebrahimzadeh who taught me a great deal about the design, operation and procedure for the characterisation of OPOs. I would also like to thank Majid for the great deal of assistance that he gave me regarding the writing and preparation of our publications and conference presentations and for always finding time to talk to me even when he was extremely busy. I would also like to thank Dr Derryck Reid for giving me many useful tips and for the countless times I borrowed his photodiode. Many thanks to both Majid and Derryck for proof reading this thesis.

I would also like to thank the boys in the office, Phillipe Riblet, Jim Hyland, Mark Holden (Popularity based on the fact that Holdens give you better value for money) and especially Alasdair Cameron for keeping me going in the dark early days when we didn't even have a lab and for his great deal of assistance in all things computers as well as the amount of work that he put into setting up the lab.

Many thanks to all my flatmates who helped through the course of this work, namely Ian Mann, Tim Bungey and especially my American touring partner David Fulton, for putting up with my dreadful fashion sense and all those red plates.

I would also like to acknowledge the help of the members of the Mechanical workshop, especially Jimmy Lindsay, Jim Clark and George Cunningham, for the construction of most of the components used in this work. Thanks also to the members of the electronics workshop and Dr Bill Sleat for all his assistance with electronics.

Thanks also to: Garry Morrison, Gordon Kennedy, Gordon Robertson, Matthew (Kaboom) Critten, David Burns, Peggy Perozzo, Peter Roberts, Sara Shepherd, Christian Rahlff, and Gareth (Super G) Valentine for their friendship and banter.

Finally, I would like to thank my Mum, Dad and Lorraine for their love and support throughout the duration of my studies.

Financial support for the duration of this project was provided by a University of St Andrews Research Studentship.